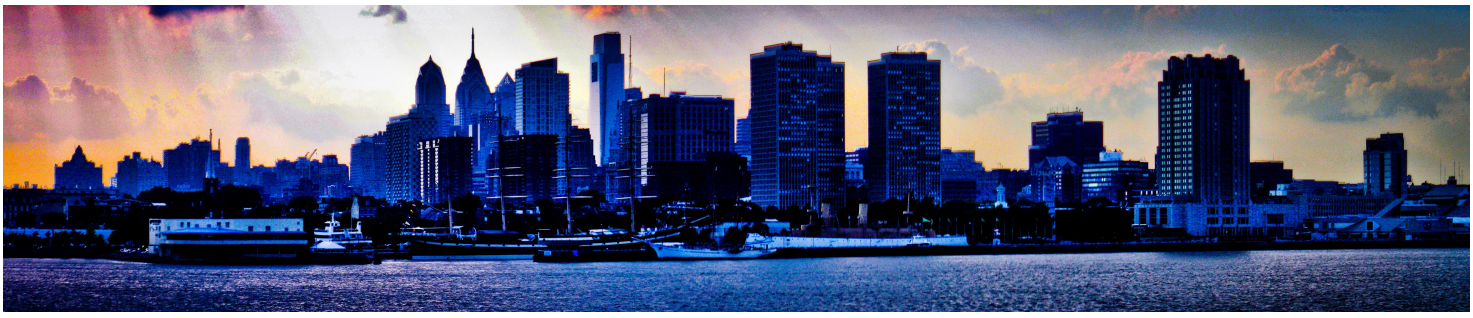

Penn
University of Pennsylvania

The 2023 International Workshop on Pulmonary Imaging

Philadelphia, PA
February 23 – 25, 2023

Hosted by:
Department of Radiology
and
Functional and Metabolic Imaging Group (FMIG)

Sponsored by:

4DMedical™

POLAREAN

Boehringer Ingelheim

VIDA™

National Heart Lung and Blood Institute

Organizing Committee:
Rahim R. Rizi, Ph.D.
Giles Santyr, Ph.D.
John P. Mugler, Ph.D.
Warren B. Gefter, M.D.

Scientific Committee:
Stephen Kadlecek, Ph.D.
Kai Ruppert, Ph.D.
Eric Hoffman, Ph.D.
Maurizio Cereda, M.D.
Hooman Hamedani, Ph.D.
Yi Xin, Ph.D.
Mitchell D. Schnall, M.D., Ph.D.

Location:
University of Pennsylvania
421 Curie Boulevard
Biomedical Research Building II/III
Philadelphia, PA, 19104

Foreword

Welcome to the 2023 International Workshop on Pulmonary Imaging. As is always the case at this multidisciplinary meeting, we have worked hard to include presenters who are able to speak authoritatively on a wide range of current topics—from lung physiology and mechanics to pulmonary imaging techniques, IPF, and recent advancements in hyperpolarization technology. This year, for this first time, we have also included sessions dedicated to photon-counting CT and pre-COPD.

The program is divided into 18 sessions consisting of 89 total presentations split between keynote lectures, presentations from leading researchers in pulmonary imaging and rising stars in the field, as well as a number of shorter presentations from postdoctoral fellows and graduate students, and a 2-hour MAD Minute poster presentation session. Presentations in each session are typically organized around an underlying method or concept. While the discussion periods at the end of each session are limited by time constraints, we hope that the numerous breaks between sessions will allow meeting participants to engage in further, informal conversation about the presentations.

Again, it is our great pleasure to welcome you to this meeting.

Warren Gefter, MD
Professor of Radiology,
University of Pennsylvania

Rahim Rizi, Ph.D.
Professor of Radiology,
University of Pennsylvania

John Mugler, Ph.D.
Professor of Radiology,
University of Virginia

Giles Santyr, Ph.D.
Professor of Medical Biophysics,
University of Toronto

XV Scanner™

Advanced Lung Scanning Technology

4DMedical™

XV Scanner

- First dedicated lung function scanner
- Optimized for XV, improved sensitivity
- Better patient experience
- Rapid, automated scan (in 1–2 breath)
- Scan during normal breathing
- Very low dose (< 1 typical chest X-ray)

The XV Scanner offers technological and competitive advantages over existing imaging modalities.

It is the first dedicated lung scanner to provide **non-invasive functional insights into breathing lungs**—providing images with unprecedented levels of clinical detail and actionable information.

4DMedical

www.4dmedical.com

21255 Burbank Blvd, Suite 120
Woodland Hills CA 91367 | +1 833 987 2267

Not yet available for commercial sale in the US.

Transform MRI Into a Lung Ventilation Imaging Platform with

XENOVIEW™

(xenon Xe 129 hyperpolarized) for oral inhalation

Evaluates regional lung ventilation

Spatially distributes to image the smallest airways

No radiation exposure to patient

Single 10 to 15 second breath hold

Non-effort dependent procedure

XENOVIEW Important Safety Information (ISI):

INDICATIONS FOR USE

XENOVIEW, prepared from the xenon Xe 129 Gas Blend, is indicated for use with magnetic resonance imaging (MRI) for evaluation of lung ventilation in adults and pediatric patients aged 12 years and older. Limitations of Use: XENOVIEW has not been evaluated for use with lung perfusion imaging

WARNINGS AND PRECAUTIONS

Risk of Decreased Image Quality from Supplemental Oxygen: Supplemental oxygen administered simultaneously with XENOVIEW inhalation can cause degradation of image quality. For patients on supplemental oxygen, withhold oxygen inhalation for two breaths prior to XENOVIEW inhalation, and resume oxygen inhalation immediately following the imaging breath hold.

Risk of Transient Hypoxia: Inhalation of an anoxic gas such as XENOVIEW may cause transient hypoxemia in susceptible patients. Monitor all patients for oxygen saturation and symptoms of hypoxemia and treat as clinically indicated.

ADVERSE REACTIONS

Adverse Reactions in Adult Patients: The adverse reactions (> one patient) in efficacy trials were oropharyngeal pain, headache, and dizziness.

Adverse Reactions in Pediatric Patients: In published literature in pediatric patients aged 6 to 18 years, the following transient adverse reactions were reported: blood oxygen desaturation, heart rate elevation, numbness, tingling, dizziness, and euphoria. In at least one published study of pediatric patients aged 6 to 18 years, transient decrease in SpO2% and transient increase in heart rate were reported following hyperpolarized xenon Xe 129 administration. XENOVIEW is not approved for use in pediatric patients less than 12 years of age.

Please see www.XENOVIEW.net for full Prescribing Information.

POLAREAN

XV-PRNT-2301 01/23

WiFi Connection Instructions

1. Select the **AirPennNet-Guest** SSID
2. Open a browser
3. Review and accept the Acceptable Use Policy terms and conditions
4. Enter a valid email address
5. Click **Submit**

Note:

1. Registration of devices on the AirPennNet-Guest wireless network will need to be **renewed daily**.
2. Only basic Internet connectivity will be provided, including web browsing and secure protocols, such as standard VPN and RDP.
3. Bandwidth usage limits are in effect providing 3Mbps up/down per device.
4. The AirPennNet-Guest wireless network will block hosts that may serve malicious content.
5. In case of abuse, repeat offenders will be blocked from using the AirPennNet-Guest wireless network.

Thursday, February 23rd, 2023	
6:50 – 7:40 am	**Continental Breakfast**
7:40 – 7:50 am	**Introductory Remarks** Rahim R. Rizi, Ph.D. University of Pennsylvania
7:50 – 8:00 am	**Welcome Remarks** Mitchell D. Schnall, M.D., Ph.D. University of Pennsylvania
Session I: Keynote Lectures – Part I Moderator: Warren Gefter, M.D.	
8:00 – 8:25 am	**A Birds-eye View of Pulmonary Challenges and How Imaging Might Help** Fernando Martinez, M.D. Weill Cornell Medicine
8:25 – 8:45 am	**Imaging Needs to Guide Interventional Treatments for COPD Patients** Gerard J. Criner, M.D. Temple University
8:45 – 9:05 am	**Origins of Quantitative Functional X-ray Computed Tomography of the Lung and What's Next** Eric A. Hoffman, Ph.D. University of Iowa
9:05 – 9:25 am	**MRI in Cystic Fibrosis: Successful Translation of Functional MRI into Clinical Medicine** Hans-Ulrich Kauczor, M.D. University Hospital Heidelberg, Germany
9:25 – 9:45 am	**The Small Airways: A Key Target for Quantitative, Functional Lung Imaging** Warren Gefter, M.D. University of Pennsylvania
9:45 – 10:00 am	**Discussion**
10:00 – 10:15 am	**Break**
Session II: Keynote Lectures – Part II Moderator: Hans-Ulrich Kauczor, M.D.	
10:15 – 10:35 am	**Artificial Intelligence in Chest Imaging: Is the Future Really Here?** Edwin van Beek, M.D., Ph.D. University of Edinburgh, U.K.
10:35 – 10:55 am	**Latest Advances in Imaging in Asthma – Targeted Therapy** Mario Castro, M.D. University of Kansas Medical Center
10:55 – 11:15 am	**Role of Imaging in COPD, in 2023 and Beyond** MeiLan Han, M.D. University of Michigan
11:15 – 11:35 am	**Sarcopenia: The Multiple Pathways of Muscle Loss** George R. Washko, M.D.

	Brigham and Women's Hospital
11:35 – 11:55 am	**Towards Routine Quantitative Lung Imaging** Joon Beom Seo, M.D., Ph.D. University of Ulsan, South Korea
11:55 – 12:10 pm	**Defining Human Specific Mechanisms of Lung Development, Injury & Regeneration** Maria Basil, M.D., Ph.D. University of Pennsylvania
12:10 – 12:20 pm	**Discussion**
12:20 – 1:10 pm	**Lunch**
Session III: Early Investigators Moderator: Stephen Kadlecek, Ph.D.	
1:10 – 1:20 pm	**Tracking Intratidal Blood Volume Redistribution with Dynamic Dual-energy CT** Jacob Herrmann, Ph.D. University of Iowa
1:20 – 1:30 pm	**Translating ^{129}Xe MRI to Clinical Practice: Preliminary Experience** Robert Thomen, Ph.D. University of Missouri
1:30 – 1:40 pm	**Optimizing Dynamic Contrast Analysis for Imaging Pulmonary Perfusion in Injured Lungs** Yi Xin, Ph.D. Massachusetts General Hospital
1:40 – 1:50 pm	**Emerging MRI Techniques and Insights for the Neonatal Lung** Nara Higano, Ph.D. Cincinnati Children's Hospital Medical Center
1:50 – 2:00 pm	**Polymorphic Deep Learning for Robust Segmentation Across Species and Diseases** Sarah E. Gerard, Ph.D. University of Iowa
2:00 – 2:15 pm	**Discussion**
2:15 – 2:30 pm	**Break**
Session IV: Lung Cancer Moderator: David Mankoff, M.D., Ph.D.	
2:30 – 2:45 pm	**Molecular Imaging of Lung Cancer: Metabolism and Proliferation** David Mankoff, M.D., Ph.D. University of Pennsylvania
2:45 – 3:00 pm	**The Role of Surgery in the Treatment of Mesothelioma** Joseph Friedberg, M.D. Temple University
3:00 – 3:15 pm	**Quantitative Imaging for Lung Cancer in the Era of Immuno-oncology** Ho Yun Lee, M.D., Ph.D. Sungkyunkwan University, South Korea
3:15 – 3:30 pm	**Intraoperative Molecular Imaging of Lung Cancer** Sunil Singhal, M.D. University of Pennsylvania
3:30 – 3:45 pm	**Lung Cancer Screening Efficacy Enhanced Through Radiomic Biomarkers**

	Jessica C. Sieren, Ph.D. University of Iowa
3:45 – 3:55 pm	**Discussion**
3:55 – 4:05 pm	**Break**
Session V: COVID and Post-COVID Lung Imaging Moderator: Maurizio Cereda, M.D.	
4:05 – 4:20 pm	**Are ^{129}Xe MRI Ventilation Abnormalities Clinically Relevant in Post-acute COVID-19 Syndrome, 3 and 15 Months Post-infection?** Grace Parraga, Ph.D. Western University, Canada
4:20 – 4:35 pm	**Leveraging CXR and CT Advanced Quantitative Imaging and Machine Learning Beyond COVID-19 Diagnosis to Quantification and Prognostication** Eduardo J. Mortani Barbosa Jr., M.D. University of Pennsylvania
4:35 – 4:50 pm	**Longitudinal Monitoring of Lung Function and Structure Post-COVID-19 Hospitalisation with Multinuclear Lung MRI** Jim Wild, Ph.D. University of Sheffield, U.K.
4:50 – 5:05 pm	**Visualizing Gas Exchange Defects Using Hyperpolarized ^{129}Xe MRI in Patients with Post-acute COVID-19 Respiratory Symptoms** Peter Niedbalski, Ph.D. University of Kansas Medical Center
5:05 – 5:15 pm	**Discussion**
5:15 – 5:30 pm	**Break**
Session VI: Assessment of Structural and Functional Changes in ARDS Moderator: Marcos Vidal Melo, M.D., Ph.D.	
5:30 – 5:45 pm	**Regional Blood Flow and Inflammation During Low Tidal Volume Mechanical Ventilation** Marcos Vidal Melo, M.D., Ph.D. Columbia University
5:45 – 6:00 pm	**Imaging Lung Perfusion to Guide ARDS Care** Maurizio Cereda, M.D. Massachusetts General Hospital
6:00 – 6:15 pm	**Ventilating the Injured Lung: Insights from Quantitative CT Imaging** David Kaczka, M.D., Ph.D. University of Iowa
6:15 – 6:30 pm	**New Approaches to Lung Repair** Nicolino V. Dorrello, M.D. Columbia University
6:30 – 6:45 pm	**Leveraging Imaging to Inform Molecular Subphenotypes of ARDS** Nadir Yehya, M.D. Children's Hospital of Philadelphia
6:45 – 7:00 pm	**Discussion**
Friday, February 24th, 2023	

7:00 – 8:00 am	**Continental Breakfast**
Session VII: Interstitial Lung Disease Moderator: Michael Beers, M.D.	
8:00 – 8:15 am	**Leveraging Novel Preclinical Models, Big Data Omics, and New Paradigms to Drive Discovery in Idiopathic Pulmonary Fibrosis** Michael F. Beers, M.D. University of Pennsylvania
8:15 – 8:30 am	**Regional Patterns of Fibrosis, Gas Exchange and Perfusion in IPF Using Chest CT and MRI** Sean B. Fain, Ph.D. University of Iowa
8:30 – 8:45 am	**Molecular Imaging of Fibrosis and Fibrogenesis in ILD** Peter Caravan, Ph.D. Massachusetts General Hospital
8:45 – 9:00 am	**Discussion**
9:00 – 9:15 am	**Break**
Session VIII: Machine Learning and Deep Learning – Imaging in COPD Moderator: Saurabh Jha, MD	
9:15 – 9:35 am	**Unsupervised Machine Learning of Quantitative CT Emphysema Subtypes** R. Graham Barr, M.D., DrPH Columbia University
9:35 – 9:50 am	**AI in Chest Imaging: From Detection to Prediction** Joon Beom Seo, M.D., Ph.D. University of Ulsan, South Korea
9:50 – 10:05 am	**Synthesizing Lung Functional Images Using Deep Learning** Joseph M. Reinhardt, Ph.D. University of Iowa
10:05 – 10:20 am	**Assessments of Emphysema and Pulmonary Fibrosis on CT Using Deep Learning** Stephen Humphries, Ph.D. National Jewish Health
10:20 – 10:35 am	**Recent Advances in Assessing Vascular Morphology and Perfusion in Pulmonary Vascular Disease** Raul San Jose Estepar, Ph.D. Brigham and Women's Hospital
10:35 – 10:50 am	**Discussion**
10:50 – 11:05 am	**Break**
Session IX: Post-Doctoral Fellow and Graduate Student Presentations Moderator: Kai Ruppert, Ph.D.	
11:05 – 11:13 am	**Denoising Diffusion-weighted Hyperpolarized ^{129}Xe Images with Patch-based Higher-order Singular Value Decomposition** Stephanie A. Soderlund Cincinnati Children's Hospital Medical Center
11:13 – 11:21 am	**Time-resolved Dynamic Lung Water Magnetic Resonance Imaging During Exercise Stress** Felicia Seemann National Institutes of Health

11:21 – 11:29 am	**3D Quantification of Clustered Lung Volume Defects in Different Lung Diseases Utilizing Hyperpolarized Gas MR Images** Gabriela Delgado University of Missouri
11:29 – 11:37 am	**Effect of CFTR Modulator Therapy with Elexacaftor/Tezacaftor/Ivacaftor on Pulmonary Ventilation Derived by 3D Phase-resolved Functional Lung MRI in Cystic Fibrosis Patients** Filip Klimeš Hannover Medical School, Germany
11:37 – 11:45 am	**Quantitative Mapping of Cardiopulmonary Oscillations Using Hyperpolarized ^{129}Xe Gas Exchange MRI** Junlan Lu Duke University
11:45 – 11:53 am	**Pulmonary Vascular Redistribution Following 2.5-year Anti-IL-5Rα Treatment in Eosinophilic Asthma** Marrissa J. McIntosh Robarts Research Institute and Western University, Canada
11:53 – 12:01 am	**Lung Volume Dependence and Repeatability of Hyperpolarized ^{129}Xe MRI Gas Uptake Metrics in Healthy Volunteers and Patients with COPD** William J. Garrison University of Virginia
12:01 – 12:10 pm	**Discussion**
12:10 – 1:00 pm	**Lunch**
Session X: Pre-COPD and Small Airways Moderator: Eric Hoffman, Ph.D.	
1:00 – 1:15 pm	**Investigating COPD Progression Through Quantitative CT** Craig J. Galbán, Ph.D. University of Michigan
1:15 – 1:30 pm	**Dysanapsis: Origins and Clinical Significance Thanks to Pulmonary Imaging** Benjamin M. Smith, M.D. McGill University and Columbia University
1:30 – 1:45 pm	**PET Imaging of Pulmonary Vasculitis** Delphine L. Chen, M.D. University of Washington
1:45 – 2:00 pm	**Physiologic Characterization of Respiratory Function Using Fluoroscopy-based X-ray Velocimetry** Naresh M. Punjabi, M.D., Ph.D. University of Miami
2:00 – 2:15 pm	**New Metrics for Quantification of Airway Disease in COPD** Surya P. Bhatt, M.D. University of Alabama at Birmingham
2:15 – 2:30 pm	**Reliable Lung Quantification via CT Using Virtual Imaging Trials** Ehsan Abadi, Ph.D. Duke University
2:30 – 2:45 pm	**Mucus Plugs Occluding COPD Airways: A Review of Their Clinical Impact**

	Alejandro A. Diaz, M.D., MPH Brigham and Women's Hospital
2:45 – 2:55 pm	**Discussion**
2:55 – 3:10 pm	**Break**
Session XI: Assessment of Pulmonary Disorders in the Pediatric Population and Imaging Asthmatic Patients Moderator: Zackary Cleveland, Ph.D.	
3:10 – 3:25 pm	**Structural and Functional Proton MRI in Pediatric Lung Disease** Giles Santyr, Ph.D. The Hospital for Sick Children, Canada
3:25 – 3:40 pm	**Translational Xe MRI in Pediatrics** Jason Woods, Ph.D. Cincinnati Children's Hospital Medical Center
3:40 – 3:55 pm	**Body Composition CT Metrics and Lung Function in Asthma Participants: Analyses from the Severe Asthma Research Program** Mark L. Schiebler, M.D. University of Wisconsin, Madison
3:55 – 4:10 pm	**Phenotyping Asthma/COPD Overlap in Patients with Mild Lung Disease with Xenon MRI and Lung Function - Results from the Novelty Cohort** Laurie Smith, Ph.D. University of Sheffield, U.K.
4:10 – 4:25 pm	**Discussion**
4:25 – 4:40 pm	**Break**
Session XII: Proton MRI of the Lung Moderator: John Mugler, Ph.D.	
4:40 – 4:55 pm	**Phase Resolved Functional Lung (PREFUL) MRI: Latest Developments and Clinical Translation** Jens Vogel-Claussen, M.D. Hannover Medical School, Germany
4:55 – 5:10 pm	**4D Proton MRI of the Lung at High Spatiotemporal Resolution** Wilson Miller, Ph.D. University of Virginia
5:10 – 5:25 pm	**Proton MR Imaging at 0.55T** Adrienne Campbell, Ph.D. National Institutes of Health
5:25 – 5:40 pm	**Quantitative Measures of Ventilation, Perfusion, and Ventilation-perfusion in the Human Lung Using Proton MRI** Rui Carlos Sa, Ph.D. National Institutes of Health
5:40 – 5:55 pm	**Discussion**
6:00 – 8:30 pm	**Poster Session**

Saturday, February 25th, 2023

7:00 – 7:45 am	**Continental Breakfast**
Session XIII: Imaging of Lung Transplant and Cell Therapy Moderator: Joel Cooper, M.D.	
7:45 – 8:00 am	**Predicting the Outcome of Lung Transplantation Using Machine Learning** Pratik Chaudhari, Ph.D. University of Pennsylvania
8:00 – 8:15 am	**The Role of CT Imaging in Lung Transplant** Micheal McInnis, M.D. University of Toronto, Canada
8:15 – 8:30 am	**Hyperpolarized ^{129}Xe Ventilation and Gas Exchange as Markers for Lung Transplantation** Faraz Amzajerdian University of Pennsylvania
8:30 – 8:45 am	**Lung Metabolism and Graft Preservation on Ex Vivo Lung Perfusion** Kentaro Noda, Ph.D. University of Pittsburgh
8:45 – 9:00 am	**Metabolic Changes in the Donor Lung During Ischemia as a Function of Time and Temperature** Zachary Schug, Ph.D. Wistar Institute
9:00 – 9:15 am	**Contemporary Challenges and Opportunities to Improve Equity and Use of Organs for Lung Transplant** Edward Cantu, M.D. University of Pennsylvania
9:15 – 9:30 am	**Neutrophil Trafficking After Lung Transplantation** Daniel Kreisel, M.D., Ph.D. Washington University in St. Louis
9:30 – 9:45 am	**Discussion**
9:45 – 10:00 am	**Break**
Session XIV: Advances in CT Imaging and Photon Counting Moderator: Peter B. Noël, Ph.D.	
10:00 – 10:15 am	**Photon-Counting CT – Opportunities for Interdisciplinary Preclinical and Clinical Research** Peter B. Noël, Ph.D. University of Pennsylvania
10:15 – 10:30 am	**Fundamentals of Photon Counting CT and Experiences with the First Clinically Available System** Juan Carlos Ramirez-Giraldo, Ph.D. Siemens Healthineers
10:30 – 10:45 am	**End-to-end Radiomics Standardization Framework** Grace Gang, Ph.D. University of Pennsylvania
10:45 – 11:00 am	**Hierarchical Phase Contrast Tomography: A Method for Imaging Multiscale Three-dimensional Structures in Whole Human Lung** Claire Walsh, Ph.D.

	University College London, U.K.
11:00 – 11:15 am	**Discussion**
11:15 – 11:30 am	**Break**
Session XV: Lung Imaging with Hyperpolarized ^{129}Xe Moderator: Rosa Tamara Branca, Ph.D.	
11:30 – 11:45 am	**Dissecting Pulmonary Gas Exchange and Hemodynamics with ^{129}Xe MRI** Bastiaan Driehuys, Ph.D. Duke University
11:45 – 12:00 am	**Combining HP ^{129}Xe and UTE MRI with Proteomics to Phenotype Cystic Fibrosis Lung Disease** Zackary I. Cleveland, Ph.D. Cincinnati Children's Hospital Medical Center
12:00 – 12:15 pm	**Sensing the Heat with Spin Polarized ^{129}Xe** Rosa Tamara Branca, Ph.D. University of North Carolina at Chapel Hill
12:15 – 12:30 pm	**How to Capture an Atom: Developing Molecular Sensors with Useful Xenon-binding Properties** Ivan Dmochowski, Ph.D. University of Pennsylvania
12:30 – 12: 45 pm	**Role of ^{129}Xe MRI in Determining the Significance of Pulmonary Pathology in Challenging Cases (Examples of COPD, E-cigarette, and Aging)** Y. Michael Shim, M.D. University of Virginia
12:45 – 1:00 pm	**^{129}Xe MRI Phenotypes of Post-HSCT Pulmonary Complications** Laura L. Walkup, Ph.D. Cincinnati Children's Hospital Medical Center
1:00 – 1:15 pm	**Assessing Lung Structure via Hyperpolarized ^{129}Xe MR Spectroscopy: Peeking into Peaks** Kai Ruppert, Ph.D. University of Pennsylvania
1:15 – 1:30 pm	**Discussion**
1:30 – 2:15 pm	**Lunch**
Session XVI: COPD and AI Moderator: Grace Parraga, Ph.D.	
2:15 – 2:30 pm	**Data Harmonization on Large Cohorts of Lung CT Scans** Andrew F. Laine, Ph.D. Columbia University
2:30 – 2:45 pm	**Image-based Multiscale Modeling of the Lung to Quantify Regional Mechanical Stress In Vivo** Reza Avaz, Ph.D. Texas A&M University
2:45 – 2:55 pm	**Dynamic Imaging of the Lung with Hyperpolarized ^{129}Xe** Hooman Hamedani, Ph.D. University of Pennsylvania
2:55 – 3:05 pm	**Airway Aerodynamics: MRI-based Modeling and Validation**

	Alister Bates, Ph.D. Cincinnati Children's Hospital Medical Center
3:05 – 3:15 pm	**AI-based Detection of COPD on Computed Tomography** Sandeep Bodduluri, Ph.D. University of Alabama at Birmingham
3:15 – 3:30pm	**Discussion**
3:30 – 3:45 pm	**Break**
Session XVII: Lung Imaging with ^{19}F Moderator: Brandon Zanette, Ph.D.	
3:45 – 4:00 pm	**^{19}F Lung Imaging with Octafluorocyclobutane** Mitchell Albert, Ph.D. Thunder Bay Regional Health Research Institute, Canada
4:00 – 4:15 pm	**Imaging Change in Ventilation Properties with ^{19}F-MRI: Quantitative, Repeatable and Accessible Imaging of Lung Function** Peter Thelwall, Ph.D. Newcastle University, U.K.
4:15 – 4:30 pm	**Beyond FEV1: Dynamic Perfluorinated Gas MRI in Cystic Fibrosis** Jennifer Goralski, M.D. University of North Carolina at Chapel Hill
4:30 – 4:45 pm	**Discussion**
Session XVIII: Clinical Translation and Latest Technical Developments Moderator: G. Wilson Miller, Ph.D.	
4:45 – 5:00 pm	**Late Breaking News: FDA Approval and Launch of Hyperpolarized Xenon MRI** Alex Dusek, Chief Commercial Officer Polarean
5:00 – 5:15 pm	**Next-generation Gas Hyperpolarization and HP Imaging on Point-of-care MRI Scanners** Boyd Goodson, Ph.D. Southern Illinois University
5:15 – 5:30 pm	**Next-generation Enabling Hyperpolarized Clinical Technologies Using Parahydrogen** Eduard Chekmenev, Ph.D. Wayne State University
5:30 – 5:45 pm	**Closing Remarks**
5:45 pm	**Adjourn**

Thursday

February 23rd, 2023

Workshop: Day 1

Origins of Quantitative Functional X-ray Computed Tomography of the Lung and What's Next

Eric A. Hoffman, PhD

University of Iowa Carver College of Medicine

In this talk, we will explore the origins of functional CT and track its evolution towards higher temporal, spatial and contrast resolution. With the emergence of multi-spectral CT imaging including dual energy utilizing energy integrating technology and multi-energy binning utilizing photon counting and function tagged via use of blood-born or inhaled contrast agents. Lung disease phenotypes have previously been lumped together by the limitations of spirometry and plethysmography. Quantitative CT (QCT) and its functional embodiments have been imbedded into studies seeking to characterize COPD, severe asthma, interstitial lung disease and more. With reductions in radiation dose by an order of magnitude or more and significant increases in spatial resolution coupled together with reductions in imaging artifacts such as beam hardening, scatter and electronic noise, attention has turned towards more mild forms of disease and younger populations.

In early applications, clinical CT concentrated on anatomic details of the lung. However, from the earliest days of CT, experimental and limited production scanners, such as Mayo's Dynamic Spatial Reconstructor or Imatron's Electron Beam CT, have sought to inter-relate regional anatomic details of the lung together with function. Structural details extracted at multiple lung volumes offer indices of lung mechanics. Additionally, single or multiple volumetric images, if acquired at standardized lung volumes and body posture, can be used to model function by employing such engineering techniques as computational fluid dynamics. QCT offers assessment of functional small airways disease (fSAD) as well as regional ventilation-perfusion matching (V/Q) and more.

Summary: Quantitative/functional CT has and continues to evolve so as to offer new insights into normal and pathophysiology of the cardiopulmonary system through the non-invasive exploration of the dynamic three-dimensional functioning of the breathing lung and beating heart within the unique negative pressure intrathoracic environment of the intact chest.

Adapted from: Hoffman EA. Origins of and lessons from quantitative functional X-ray computed tomography of the lung. Br J Radiol. 2022 Apr 1;95(1132):20211364. doi: 10.1259/bjr.20211364. Epub 2022 Mar 1. PMID: 35193364; PMCID: PMC9153696.

MRI in Cystic Fibrosis: Successful Translation of Functional MRI into Clinical Medicine

Hans-Ulrich Kauczor

Disease severity and mortality in patients with cystic fibrosis (CF) is mainly determined by (progressive) pulmonary lung disease. Early diagnosis, such as newborn screening, and therapy are important and of prognostic value to conserve lung function. Novel specific therapies with elexacaftor/tezacaftor/ivacaftor have evolved as a real game changer leading to a significant longer life expectancy of CF patients.

Primary imaging techniques for lung imaging are x-ray and computed tomography (CT) to monitor disease severity and regional distribution. They also have been used widely in CF in the past. Radiation-free imaging techniques such as magnetic resonance imaging (MRI) have gained increasing interest over the last decade in order to prevent radiation damage. In multiple institutions, MRI has been successfully introduced into clinical routine, e.g. annual surveillance examinations as well as diagnosis of exacerbations and therapy response assessment. MRI is well suited to demonstrate infiltrations, consolidations, bronchial wall thickening, bronchiectasis and mucus retention as proton rich structures ("plus"-pathologies). Chest MRI in preschoool children is also capable to assess the concomitant involvement of the paranasal sinuses and its response to therapy.

However, MRI can do more. Dynamic contrast-enhanced MRI will visualize and quantify regional lung perfusion, which is regarded as a surrogate marker of hypoxic pulmonary vasoconstriction reflecting regional ventilation. These images also allow for the assessment of the growth, dilation and respective therapy response of the bronchial arteries, which indicate hypertrophy of systemic blood supply to the lungs and an increased risk for hemoptysis. Regional assessment is a major advantage when compared to pulmonary function testing which will only provide global measures.

Using hyperpolarized gases, e.g. 129Xe, addresses the disease from the opposite side: direct visualization of ventilation and its defects as well as additional measures of the dissolved phase in order to assess perfusion and gas exchange using chemical shift imaging. A stroke of genius was the introduction a regional measurement of ventilation and perfusion without the requirement of any contrast agent by using Fourier decomposition. This technology benefits from the facts that the weak signal of the ventilated lung increases and decreases regularly at two different rhythms. One is the respiratory movement, less signal in inspiration, more signal in expiration, the other one is the cardiac action with the highest signal at the moment of highest pulmonary blood volume.

MRI is now established for routine, regular, repeated assessment (surveillance) of CF patients from newborns (before being symptomatic) to advanced age (exacerbations and longitudinal progress of the disease). MRI is also capable to visualize and quantify the effect of mucolytic or antibiotic therapy. Additional functional MRI demonstrates impairment of perfusion or ventilation even if morphological changes are not obvious. Thus, imaging can prevent

complications, support individual therapy decisions and be used as an endpoint within the framework of clinical studies.

Suggested reading

Graeber SY et al. Effects of Lumacaftor-Ivacaftor on Lung Clearance Index, Magnetic Resonance Imaging, and Airway Microbiome in Phe508del Homozygous Patients with Cystic Fibrosis. Ann Am Thorac Soc. 2021;18:971-980.

Sommerburg O et al. Magnetic Resonance Imaging Detects Chronic Rhinosinusitis in Infants and Preschool Children with Cystic Fibrosis. Ann Am Thorac Soc. 2020;17:714-723.

Woods JC et al. Current state of the art MRI for the longitudinal assessment of cystic fibrosis. J Magn Reson Imaging. 2020; 52:1306-1320.

Stahl M et al. Preventive Inhalation of Hypertonic Saline in Infants with Cystic Fibrosis (PRESIS). A Randomized, Double-Blind, Controlled Study. Am J Respir Crit Care Med. 2019;199:1238-1248.

Wielpütz MO et al. Multicentre standardisation of chest MRI as radiation-free outcome measure of lung disease in young children with cystic fibrosis. J Cyst Fibros. 2018;17:518-527.

The Small Airways: A Key Target for Quantitative, Functional Lung Imaging

Warren B. Gefter, M.D.
University of Pennsylvania

The small airways are less than 2mm in diameter, beginning at the 8th generation. They comprise close to 99% of the lungs. While decreasing in length and diameter going distally, they increase exponentially in cross-sectional area. The small airways have been referred to as the "Quiet Zone", since as much as 75% of the small airway cross-sectional area may be obliterated before airflow obstruction is detectable by spirometry.

Accumulating evidence indicates that the small airways are a primary site of involvement in virtually all of the major lung disorders, and often the initial site of pathology. Collaborative research between UPenn and Dr. James Hogg's group at the University of British Columbia using micro-CT confirmed that these are the airways involved in the early stages of COPD, even prior to the development of emphysema [1]. They are also increasingly recognized for their importance in asthma, either in early disease or as a phenotype. Asthma therapies utilizing ultrafine particles which can be delivered to the small airways have improved therapeutic efficacy. The small airways play a principal role in lung disease due to smoking (tobacco, cannabis, vaping), air pollution, respiratory disease due to climate change, ozone and other toxic inhalational exposures, pre-COPD, viral infections and post-COVID-19 pneumonia, hypersensitivity pneumonitis, immunological/inflammatory conditions, and even in idiopathic pulmonary fibrosis. Thus, there is a highly important need to assess early abnormalities in small airway morphology and function, enabling early disease detection and therapeutic intervention. Advancing knowledge of small airway epithelial cellular/molecular processes and small airway biomechanics can lead to novel and individualized therapies and their delivery systems.

The objectives of this presentation are the following: 1. Define the anatomic and functional characteristics of the small airways. 2. Discuss non-imaging and imaging methods to assess the small airways, focusing upon recent developments in image-based detection of small airway abnormalities. The latter include non-rigid registration of inspiratory/expiratory CT (parametric response mapping) [2,3,4], micro-CT [1,4] multiparametric imaging using HP-gas MRI, deep learning identification of air trapping, and the improved spatial resolution of airway images using recently introduced photon counting CT. 3. Illustrate the important role played by small airway disease in specific major lung disorders. 4. Demonstrate the importance of small airway pathophysiology for development of more effective therapeutic agents and delivery systems to target the small airways. 5. Describe recent approaches to studying molecular/cellular small airway epithelial processes, including cell culture, precise-cut lung slices and "airway-on-a chip." 6. Discuss important ongoing challenges in evaluating small airways disease, current knowledge gaps, and fruitful directions for future research [5].

Selected references:

1. McDonough JE, Yuan R, Suzuki M, Seyednejad N, Elliot WM, Sanchez PG, Wright AC, Gefter WB, et al. Small-Airway Obstruction and Emphysema in Chronic Obstructive Pulmonary Disease. N Engl J Med 2011; 365:1567-1575

2. Torigian DA, Gefter WB, Affuso JD, Emami K, Dougherty L. Application of an optical flow method to inspiratory and expiratory lung MDCT to assess regional air trapping: a feasibility study. AJR 2007; 188: W276-W280.

3. Galban CJ, Han MK, Boes JL, Chughtai KA, Meyer CR, et al. Computed tomography-based biomarker provides unique signature for diagnosis of COPD phenotypes and disease progression. Nat Med 2012; 18: 1711-1715.

4. Vasilescu DM, Martinez FJ, Marchetti N, Galban CJ, Hatt C, et al. Noninvasive imaging biomarker identifies small airway damage in severe chronic obstructive pulmonary disease. Am J Respir Crit Care Med 2019; 200: 575–581.

5. Usmani OS, Han MK, Kaminsky DA, Hogg J, Hjoberg J, et al. Seven pillars of small airways disease in asthma and COPD. Supporting opportunities for novel therapies. CHEST 2021; 160: 114-134.

Artificial Intelligence in chest imaging: is the future really here?

Edwin J.R. van Beek MD PhD

SINAPSE Chair of Clinical Radiology, University of Edinburgh, UK

There has been an enormous focus on various applications and developments of machine learning (ML) and artificial intelligence (AI) tools (often these terms are used indiscriminatory) for medical imaging. The initial "hype" led to a certain fear among radiologists that there domain was under pressure, but more recently, the development of these tools has been embraced for various reasons (e.g. lack of manpower, enhanced reporting information, automation of more tedious tasks, etc.).

For chest imaging, various diagnostic questions have been at the forefront of developing computer algorithms to enable more rapid and precise diagnosis. Initially these computer aided diagnosis algorithms were relatively crude, and focused on lung nodule detection, detection of pulmonary embolism and segmentation tasks, such as airways and quantification of parenchymal lung disease, such as pulmonary fibrosis and emphysema.

The newer technologies that are now being developed go beyond the original techniques, as they make greater use of convolutional neural networks, with or without expert annotation, and many of these systems have the ability to perform "self-directed" learning and get better over time. That is, of course, the aim of the game!

However, if one delves into what is now feasible, there is a distinct lack of validation of most new proposed ML/AI tools. This is, of course, ultimately required to provide the necessary evidence that these tools can be trusted. In addition, most of the current tools are developed on either well-characterised databases (e.g. LIDC for lung nodules; COPDGene for emphysema and airways) or are based on single center populations. This makes introduction into other clinical environments and populations more difficult.

Finally, one needs to remember that the tools that are currently available or under development are mostly focussed on performing a single task, e.g. lung nodule detection. And even then, one needs to remember that threshold settings may vary depending on the population being studies: for CT lung cancer screening a threshold of 2-3 mm may be required, whereas for detection of incidental pulmonary nodules a threshold of 4-5 mm is considered sufficient).

In conclusion, although the field is generally moving into a patchwork of dedicated ML/AI tools for assessment of lung disease, the radiologist will be tasked with ensuring the correct algorithms are applied in the right context. Many of the tools that are being published still lack validation and therefore are not directly applicable for introduction into the clinical domain. It is anticipated that it will be another 5-10 years before these tools are more widely clinical acceptable and applicable.

References:

Ajmera P, Kharat A, Seth J, et al. A deep learning approach for automated diagnosis of pulmonary embolism on computed tomographic pulmonary angiography. BMC Med Imaging 2022;22:195.

Annarumma M, Withey SJ, Bakewell RJ, Pesce E, Goh V, Montana G. Automated triaging of adult chest radiographs with deep artificial neural networks. Radiology 2019;291:196-202.

Barnes H, Humphries SM, George PM, et al. Machine learning in radiology: the new frontier in interstitial lung disease. Lancet Digit Health 2023;5:e41-e50.

Chassagnon G, Vakalopolou M, Paragios N, Revel M-P. Deep learning : definition and perspectives for thoracic imaging. Eur Radiol 2020;30:2021-2030.

Chetan MR, Dowson N, Waterfield Price N, Ather S, Nicolson A, Gleeson FV. Developing an understanding of artificial intelligence lung nodule risk prediction using insights from the Brock model. Eur Radiol 2022;32:5330-5338.

Daye D, Wiggins WF, Lungren MP, et al. Implementation of clinical artificial intelligence in Radiology: who decides and how? Radiology 2022;305:555-563.

Diaz AA, Nardelli P, Wang W, et al. Artificial intelligence-based CT assessment of bronchiectasis: The COPDGene study. Radiology 2022; Dec 13:221109. doi: 10.1148/radiol.221109. Online ahead of print.

Hsu HH, Ko KH, Chou YC, et al. Performance and reading time of lung nodule identification on multidetector CT with or without an artificial intelligence-powered computer-aided detection system. Clin Radiol 2021;76:e23-e32.

Humphries SM, Yagihashi K, Huckleberry J, et al. Idiopathic pulmonary fibrosis: data-driven textural analysis of extent of fibrosis at baseline and 15-month follow-up. Radiology 2017; 285:270-278.

Kim RY, Oke JL, Pickup LC, et al. Artificial intelligence tool for assessment of indeterminate pulmonary nodules detected with CT. Radiology 2022;304:683-691.

McNitt-Gray MF, Armato SG 3rd, et al. The lung image database consortium (LIDC) data collection process for nodule detection and annotation. Acad Radiol 2007;12:1464-1474.

Murchison JT, Ritchie G, Senyszak D, et al. Validation of a deep learning computer aided system for CT based lung nodule detection, classification, and growth rate estimation in a routine clinical population. PLOS One 2022;17:e0266799.

Nam JG, Hwang EJ, Kim DS, et al. Undetected lung cancer at posteroanterior chest radiography: potential role of a deep learning-based detection algorithm. Radiol Cardiothoracic Imaging 2020;2:e190222.

Salisbury ML, Lynch DA, van Beek EJR, et al. Idiopathic pulmonary fibrosis: the association between the adaptive multiple features method and fibrosis outcomes. Am J Respir Crit Care Med 2017;195:921-929.

Van Beek EJR, Ahn JS, Kim MJ, Murchison JT. Validation study of machine-learning chest radiograph software in primary and emergency medicine. Clin Radiol 2023 ;78 :1-7.

Wataya T, Yanagawa M, Tsubamoto M, et al. Radiologists with and without deep learning-based computer-aided diagnosis: comparison of performance and interobserver agreement for characterizing and diagnosing pulmonary nodules/masses. Eur Radiol 2023;33:348-359.

Ziegelmayer S, Graf M, Makowski M, Gawlitza J, Gassert F. Cost-effectiveness of artificial intelligence support in computed tomography-based lung cancer screening. Cancers 2022;14:1729.

Latest Advances in Imaging in Asthma – Targeted Therapy

Mario Castro, M.D., University of Kansas Medical Center

Imaging of the lungs in patients with asthma has evolved dramatically over the last two decades with sophisticated techniques, including quantitative CT (qCT) and hyperpolarized gas (HP) MRI (using ^{3}He and ^{129}Xe), and quantitative software applications to assess airway anatomy, regional lung mechanics and associated function (gas exchange/diffusion). Previous reports in asthma have been primarily limited to gross anatomic abnormalities, such as the presence of bronchiectasis, atelectasis or bronchial wall thickening, noted in asthma, especially in severe disease, compared to normal individuals.[1-3] qCT analysis objectively quantifies airway, parenchymal, and pulmonary vascular characteristics,[4,5] and its use has led to the successful identification of novel phenotypes in both COPD and asthma.[6-8] Herein, we describe its application in a new mucus plugging (MP) phenotype and its role in airflow obstruction and air trapping in persistent asthma and subsequent decline in lung function. Dunican et al., demonstrated the presence of MP in all severities of asthma and that there was an inverse correlation between this phenotype and lung function that was not reversed by inhaled corticosteroids.[9] Interestingly, the MP seemed to be driven by airway eosinophilia and type 2 inflammation with marked upregulation of MUC5AC in the airway. Subsequently, Tang et al., demonstrated that this MP phenotype is persistent for at least 3 years in the same bronchopulmonary segments and correlated with loss of lung function.[10] In addition, we demonstrate that adult asthma patients with more severe airway remodeling, more small airways disease, and less regional change in lung expansion, based on quantitative imaging analyses, suffered more severe future lung function decline and a greater frequency of future asthma exacerbations.[11]

Imaging of lung function using HP MRI has discovered local areas of airway obstruction in asthma that are heterogeneous and occur more frequently in severe asthma.[12,13] Ventilation defect percentage correlates with several clinical parameters including spirometry, severity, control and predicts severe exacerbation. In a recent pilot study of 30 subjects with severe asthma refractory to current therapies, we demonstrated that a single bronchial thermoplasty (BT) treatment guided by ^{129}Xe MRI provided similar quality of life improvements after 12 weeks as standard three-session BT.[14] One of the most notable benefits of a single treatment is reduced peri-procedure adverse events, making it a more favorable option for this therapy.

Application of these new functional lung imaging techniques in asthma present new opportunities for enhanced phenotyping, early-stage disease detection and diagnosis, and provides insights into the pathophysiologic causes of airway remodeling and disease progression in severe asthma. Ultimately qCT and XeMRI techniques have allowed us to move to the next stage of guiding therapeutic interventions by mapping regional function and allowing measurement of therapeutic response.

References

1. Benayoun L, Druilhe A, Dombret M-C, Aubier M, Pretolani M. Airway structural alterations selectively associated with severe asthma. Am J Respir Crit Care Med 2003;167:1360-8.
2. Boulet L, Belanger M, Carrier G. Airway responsiveness and bronchial-wall thickness in asthma with or without fixed airflow obstruction. Am J Respir Crit Care Med 1995;152:865-71.
3. Paganin F, Seneterre E, Chanez P, et al. Computed tomography of the lungs in asthma: Influence of disease severity and etiology. Am J Respir Crit Care Med 1996;153:110-04.
4. Sieren JP, Newell JD, Jr., Barr RG, et al. SPIROMICS Protocol for Multicenter Quantitative Computed Tomography to Phenotype the Lungs. Am J Respir Crit Care Med 2016;194:794-806.
5. Trivedi A, Hall C, Hoffman E, Woods J, Gierada D, Castro M. Using imaging as a biomarker for asthma. J Allergy Clin Immunol 2017;139:1-10.
6. Choi S, Haghighi B, Choi J, et al. Differentiation of Quantitative Computed Tomography Imaging Phenotypes in Asthma vs. COPD. BMJ Open Resp Res 2017;4:e000252.
7. Ash S, Harmouche R, Putman R, et al. Clinical and Genetic Associations of Objectively Identified Interstitial Changes in Smokers. Chest 2017;152:780-91.
8. Trivedi A, Hall C, Goss C, et al. Quantitative Computed Tomographic Characteristics of Cluster Phenotypes in the Severe Asthma Research Program Cohorts. Radiology 2022;304:450-9.
9. Dunican E, Elicker B, Gierada D, et al. Mucus plugs in patients with asthma linked to eosinophilia and airflow obstruction. J Clin Invest 2018;epub.
10. Tang M, Elicker B, Henry T, et al. Mucus plugs persist in asthma and changes in mucus plugs associate with chages in airflow over time. Am J Respir Crit Care Med 2022;205:1036-45.
11. Krings J, Goss C, Lew D, et al. Quantitative CT analysis can predict future lung function decline and asthma exacerbations: results from SARP-3. J Allergy Clin Immunol 2021;148:752-62.
12. de Lange E, Altes T, Patrie J, et al. Evaluation of asthma with hyperpolarized helium-3 MRI: correlation with clincial severity and spirometry. Chest 2006;130:1055-62.
13. Fain S, Gonzalez-Fernandez G, Peterson E, et al. Evaluation of Structure-Function Relationships in Asthma using Multidetector CT and Hyperpolarized He-3 MRI. Acad Radiol 2008;15:753-62.
14. Hall C, Quirk J, Goss C, et al. Single-Session Bronchial Thermoplasty Guided by 129Xe MRI. Am J Respir Crit Care Med 2020;202:524-34.

Role of Imaging in COPD, In 2023 and Beyond

MeiLan Han, M.D.
University of Michigan

In recent years, computed tomography (CT) has become increasingly available, both as a research tool and in clinical practice, providing additional insights into the structural and pathologic abnormalities present in COPD. This has led to enhanced understanding of disease phenotypes and outcomes. However, traditionally CT imaging has not considered part of routine diagnostic criteria or management for COPD. The diagnosis of COPD has centered on establishing the presence of airflow obstruction using spirometry. Yet spirometry is grossly underutilized. Most patients with COPD are diagnosed only when the disease has significantly advanced. At the same time, CT imaging is being increasingly routinely, particularly among individuals with risk factors for COPD given the routine use of CT imaging for lung cancer screening. Here, both traditional quantitative analytic methods in addition to deep learning approaches have the potential to increase the value of CT imaging for identification of individuals with COPD.[1-3]

CT can also be important for aiding with differential diagnosis. Patients with excessive cough and sputum, despite maximal medical therapy, may have concomitant bronchiectasis or atypical infection that require specific therapies. Roughly 30% of COPD patients have bronchiectasis visible on CT, which is now the examination of choice when bronchiectasis is suspected. Bronchiectasis is associated with increased risk for exacerbations and mortality.[4] Both lung volume reduction surgery and bronchoscopic lung volume reduction reduce hyperinflation and improve symptoms. Hence, if emphysema is suspected, CT imaging can identify location and severity of emphysema as well as fissure integrity, helping to identify patients that might be appropriate for one of these therapies. While historically this has been performed based on expert radiologist visual analysis, particularly for LVRS, increasingly quantitative analysis for emphysema extent, location and fissure integrity is being performed to assist with treatment decision making. The presence of emphysema is also associated with more rapid progression of FEV_1 decline, increased mortality and increased risk for development of lung cancer. Finally, it should be noted that CT imaging of the chest can also provide a wealth of information about COPD comorbidities including coronary artery calcium, bone density and muscle mass. Such CT assessed comorbidities have been associated with all-cause mortality.[5]

While current recommendations suggest imaging in COPD should be focused on patients eligible for lung cancer screening, those with persistent exacerbations or symptoms out of proportion to spirometric severity and those individuals with FEV_1 less than 45% and hyperinflation[6], in the future CT may be used at a health system level for COPD screening and phenotyping.

1. Mets OM, Buckens CF, Zanen P, Isgum I, van Ginneken B, Prokop M, et al. Identification of chronic obstructive pulmonary disease in lung cancer screening computed tomographic scans. JAMA 2011;306(16):1775-1781.
2. Gonzalez G, Ash SY, Vegas-Sanchez-Ferrero G, Onieva Onieva J, Rahaghi FN, Ross JC, et al. Disease Staging and Prognosis in Smokers Using Deep Learning in Chest Computed Tomography. Am J Respir Crit Care Med 2018;197(2):193-203.
3. Han MK, Tayob N, Murray S, Woodruff PG, Curtis JL, Kim V, et al. Association between Emphysema and Chronic Obstructive Pulmonary Disease Outcomes in the COPDGene and SPIROMICS Cohorts: A Post Hoc Analysis of Two Clinical Trials. Am J Respir Crit Care Med 2018;198(2):265-267.
4. Martinez-Garcia MA, de la Rosa-Carrillo D, Soler-Cataluna JJ, Catalan-Serra P, Ballester M, Roca Vanaclocha Y, et al. Bronchial Infection and Temporal Evolution of Bronchiectasis in Patients With Chronic Obstructive Pulmonary Disease. Clin Infect Dis 2021;72(3):403-410.
5. Ezponda A, Casanova C, Divo M, Marin-Oto M, Cabrera C, Marin JM, et al. Chest CT-assessed comorbidities and all-cause mortality risk in COPD patients in the BODE cohort. Respirology 2022;27(4):286-293.
6. GOLD. Global Strategy for Prevention, Diagnosis and Management of COPD: 2023 Report

Sarcopenia: The Multiple Pathways of Muscle Loss

George R. Washko, M.D.
Brigham and Women's Hospital

Low muscle mass is associated with numerous adverse outcomes independent of other associated comorbid diseases. In smokers, the loss of muscle mass may be due to inflammation and disuse atrophy. Our goal is to predict and understand an individual's risk for developing low muscle mass using proteomics and machine learning. Muscle mass was objectively assessed on computed tomographic imaging by measuring the cross-sectional area of the pectoralis major and minor muscles at the level of the aortic arch. This metric has previously been demonstrated to be associated with fat free mass as well as clinically relevant outcomes such as exercise capacity and survival.

We identified 8 biomarkers associated with low pectoralis muscle area (PMA). We built 3 random forest classification models that used either clinical measures, feature selected biomarkers, or both to predict development of low PMA. The area under the receiver operating characteristic curve for each model was: clinical-only = 0.646, biomarker-only = 0.740, and combined = 0.744. We displayed the heterogenetic nature of an individual's risk for developing low PMA and identified 2 distinct subtypes of participants who developed low PMA. While additional validation is required, our methods for identifying and understanding individual and group risk for low muscle mass could be used to enable developments in the personalized prevention of low muscle mass.

Towards Routine Quantitative Lung Imaging

Joon Beom Seo

From early stage of clinical implementation, chest imaging, particularly CT has played an important role in the diagnosis and treatment of various lung diseases. Thin section CT images provide excellent information on the structural change of the disease lung, so that we can understand the underlying pathophysiologic changes. However, most of information was given by subjective assessment by radiologists and the extent and severity of the disease elements were given in qualitative or semi-quantitative ways.

With use of various image processing technologies, many disease elements can be quantitatively assessed using computer software. These components include radiomics of lung cancer, emphysema, air trapping, airway wall thickening, extent of localized disease patterns of interstitial lung disease, and so on. Many researches have shown that those quantitative information will be useful in clinical practices, since it can be used in early disease detection in preclinical stage, assessment of disease severity, choice of treatment options, and assessment of treatment responses and so on.

Even with many promising results on quantitative lung imaging, the implementation of real clinical practice has been delayed. Aside the necessity of proving real value of quantitative imaging in clinics, there are severe technical issues to be overcome to accelerate the clinical adoption. Firstly most of image processing algorithms are not perfect; it often requires human interaction such as minor correction or confirmation, which is usually time consuming and hinders timely presentation of information. Secondly, most of software algorithms are very sensitive to imaging parameters such as radiation dose, reconstruction kernels, slice thickness and so on. This limitation generate serious variation of measurements and the results and thresholds of clinical researches by using standardized imaging protocols cannot be applied in clinical practice. It also hampers transfer of quantitative results to other hospital, in comparison to the results of clinical studies such as CBC or PFT. Thirdly, there is a concern of radiation exposure of the routine use of CT for measuring disease changes. Finally, the quantitative results include too many measures and there should be a way to summarize or visualize the results to be accessible by general physicians and patients.

With the recent introduction of deep learning algorithm and many researches, all of the technical problems mention above can be solved, at least in part. Full automation without human interaction of quantitative assessment is possible by replacing human interactive steps with deep

learning algorithms. Measurement variation can be minimized by using image style conversion algorithm. Further reduction of radiation dose has become possible by applying deep learning algorithm either in raw data or image domain.

With additional technical development and clinical validation, routine clinical use of quantitative lung imaging will be possible in the future and will open a new era of thoracic imaging big data.

1. Yun J, Park J, Yu D, Yi J, Lee M, Park HJ, Lee JG, Seo JB, Kim N. Improvement of fully automated airway segmentation on volumetric computed tomographic images using a 2.5 dimensional convolutional neural net. Med Image Anal. 2019 Jan;51:13-20.
2. Lee SM, Lee JG, Lee G, Choe J, Do KH, Kim N, Seo JB. CT Image Conversion among Different Reconstruction Kernels without a Sinogram by Using a Convolutional Neural Network. Korean J Radiol. 2019 Feb;20(2):295-303
3. Choe J, Lee SM, Do KH, Lee G, Lee JG, Lee SM, Seo JB. Deep Learning-based Image Conversion of CT Reconstruction Kernels Improves Radiomics Reproducibility for Pulmonary Nodules or Masses. Radiology. 2019 Aug;292(2):365-373
4. Park J, Yun J, Kim N, Park B, Cho Y, Park HJ, Song M, Lee M, Seo JB. Fully Automated Lung Lobe Segmentation in Volumetric Chest CT with 3D U-Net: Validation with Intra- and Extra-Datasets. J Digit Imaging. 2020 Feb;33(1):221-230
5. Kim H, Oh G, Seo JB, Hwang HJ, Lee SM, Yun J, Ye JC. Multi-domain CT translation by a routable translation network. Phys Med Biol. 2022 Oct 17;67(21). doi: 10.1088/1361-6560/ac950e. PMID: 36162401

The Human Respiratory Airways – a Regenerative Niche in Lung Development, Injury, and Regeneration

Maria C. Basil, MD PhD
Perelman School of Medicine at the University of Pennsylvania

Chronic Obstructive Pulmonary Disease (COPD) is one of the leading causes of morbidity and mortality worldwide. Despite this intense disease burden, no novel molecular therapies have been developed in over a decade. For COPD, as is true for nearly all forms of lung injury and disease, therapies are aimed at stopping destruction, not at repair and regeneration of the injured lung. Recent work has advanced our knowledge of the pathways and processes at work in lung regeneration, but much of this work has been done in murine models, and has yet to be translated into human disease. The molecular pathways dysregulated during lung repair in COPD, however, have been difficult to study because the anatomical site of the inciting injury in this disease – the distal human respiratory airways – is absent in mice.

The distal airways of human lungs contain respiratory bronchioles (RBs), which are a unique anatomic structure where regions of low cuboidal airway epithelium are interdigitated with regions of alveolar epithelium, the sites of gas exchange. The RBs have been shown to be a site of injury in several respiratory diseases including COPD, Bronchiolitis Obliterans Syndrome (BOS), various forms of interstitial lung disease, and aging. Despite their immense clinical relevance, the cellular composition, function, molecular regulation, and response to injury of this region are poorly understood. We have characterized a novel progenitor cell type in the RBs of human lungs that we term Respiratory Airway Secretory Cells (RAS cells).

Using advanced genomic techniques, high-resolution imaging, a novel bi-lineage human embryonic stem cell (hESC) reporter system, ferret models of disease, and human primary cell organoid modeling we have shown that RAS cells act as progenitors for Alveolar Type 2 (AT2) epithelial cells in a rapid and unidirectional manner, also act as progenitors for other airway epithelial cells types in the distal lung, and these progenitor relationships are regulated, in part, by Notch and WNT signaling. These findings support the RB has a regenerative niche within the distal human lung. Furthermore, we identified the emergence of an abnormal AT2 state that expresses markers of RASCs in multiple human disease and injury states including cigarette smoke injury, COPD and BOS, suggestive of aberrant regenerative response in human lung injury.

Through the interrogation of the molecular pathways that govern development, injury response, and repair in human respiratory bronchioles, we hope to further our understanding of the molecular regulation of RAS cell function, the signals that maintain the human RB niche, and how this region responds to injury. Combined, this will allow for the development of new treatment modalities in COPD and other devastating respiratory diseases.

Tracking Intratidal Blood Volume Redistribution with Dynamic Dual-Energy CT

Jacob Herrmann, PhD

Purpose: High airway pressures applied during mechanical ventilation of injured lungs can be beneficial for recruiting atelectatic lung regions, yet can also impose hemodynamic challenges. In this study, we present a novel experimental method for imaging intratidal variations in pulmonary perfused blood volume (PBV) during uninterrupted mechanical ventilation, using dynamic contrast-enhanced dual-energy computed tomography (DECT) with retrospective gating [1].

Methods: CT imaging was performed during pressure-controlled ventilation in one pig with iodinated liposomal contrast [2], using inspiratory:expiratory ratios of 1:2.2 and 6.2:1, typical timings used in pressure-control ventilation (PCV) and airway pressure release ventilation (APRV) modalities, respectively. For each modality, two consecutive 20-second axial scans (57.6 mm axial coverage) were acquired at 70 kVp and 150 kVp. X-ray projections were retrospectively sorted according to the phases of the respiratory and/or cardiac cycles to reconstruct 4D and 5D dynamic DECT image sequences [1]. PBV and virtual noncontrast images were computed by three-material decomposition. Lung regions were segmented automatically using a convolutional neural network [3].

Results & Discussion: Increased gas pressures during inspiratory phases of mechanical ventilation were associated with intratidal increases in aeration and reductions in PBV, similar to findings of dynamic imaging studies performed using single-slice CT [4] and synchrotron radiation [5]. There was a phase lag between changes in aeration and changes in PBV, measured in 4D-DECT at 240 ms during PCV, and 150 ms during APRV. PBV from 4D-DECT exhibited no consistent signal associated with the heart rate. However, cardiac-associated PBV fluctuations measured in 5D-DECT during PCV and APRV were on average 49% and 28% of corresponding respiratory-associated PBV fluctuations measured in 4D-DECT, respectively.

Conclusion: During positive pressure ventilation, inspiratory reductions in pulmonary perfused blood volume lagged changes in lung aeration, with substantial hysteresis in measured PBV-aeration curves. PBV fluctuations due to ventilator cycles were 2- to 4-fold larger than those due to cardiac cycles, depending on the ventilation modality and phase of the ventilator cycle. These results highlight the dynamic interactions between pulmonary blood and gas volumes, and the influence of mechanical ventilation modality.

References:

[1] J Herrmann et al. *IEEE Trans Med Imaging* 36(8):1722-1732, 2017.
[2] S Mukundan Jr et al. *Am J Roentgenol* 186(2):300-307, 2006.
[3] SE Gerard et al. *Med Image Anal* 60:101592, 2020.
[4] JN Cronin et al. *Crit Care Med* 48(3):e200-e208, 2020.
[5] L Porra et al. *Am J Respir Cell Mol Biol* 57(4):459-467, 2017.

Translating ^{129}Xe MRI to Clinical Practice: Preliminary Experience

Robert P Thomen, PhD

With the recent FDA approval of ^{129}Xe MRI, practical questions related to clinical implementation and hospital adoption must be addressed. Creating patient orders, CPT coding, reimbursement, pharmacy involvement, radiologist reads, and polarizer operation are just a few aspects of clinical operation which must be given consideration. Whether clinicians adopt or abandon a new technique can depend greatly on the ease with which it can be implemented and executed; thus, establishing concrete standards of operation is essential in the early stages of a clinical program. In this discussion, I will present these aspects of clinical implementation including successes and struggles experienced in University of Missouri healthcare system. We will also examine aspects of ^{129}Xe MRI which will require changes and augmentations for true clinical adoption separate from research laboratories including the requirements/responsibilities of technologists, polarizer operators, dose administrators, and nurses.

Optimizing Dynamic Contrast Analysis for Imaging Pulmonary Perfusion in Injured Lungs

Yi Xin

Background: Acute respiratory distress syndrome (ARDS) is characterized by a maldistribution of pulmonary blood flow (*PBF*) but the clinical impact of perfusion changes is under-investigated due to limitations in available imaging methods. Dynamic contrast-enhanced (DCE) CT captures first-pass kinetics of intravenously injected dye during continuous scan acquisitions. Injection of concentrated contrast, which has several folds higher viscosity than blood yields a better signal to noise ratio in static imaging but the effects of contrast dilution in dynamic imaging have never been explored. We aimed to 1) evaluate the effects of contrast viscosity on imaging *PBF*; 2) perform comparative evaluation of difference *PBF* models in healthy lungs and after lung injury, validating their results against cardiac output by thermodilution.

Methods: 10 Yorkshire pigs (5 with lung injury, 5 healthy) were anesthetized, intubated, and mechanically ventilated. In the lung injury group, 3.5 ml/kg of HCl was divided into 5 ml aliquots and instilled via bronchoscopy into the lobar bronchi of each lung. Each DCE CT scan was obtained during a 30 second end-expiratory breath-hold. A 57.6 mm slab was imaged continuously at the temporal resolution of 0.25 seconds. After a 5-second inspiratory hold, 16 ml of each contrast agent - Isovue-370 and diluted Isovue-370 (3:2 ratio contrast:0.9% saline) - were separately injected via internal jugular vein catheter at a rate of 4 ml/s with a washout of 10 minutes. Density-time curves were analyzed via both the steepest slope (SS) and peak enhancement (PE) models. *PBF* measurements was compared to cardiac output via thermodilution as gold standard for whole-lung perfusion using regression analysis. In two healthy pigs, three slabs of image covering the entire lung were acquired to determine cumulative *PBF* in comparison to cardiac output.

Results: Slab-averages of *PBF* in SS model had a better correlation with cardiac output (R^2=0.82) than the PE model (R^2=0.64). Moreover, whole lung perfusion was also shown to be closer to the cardiac output value in the SS model compared to the PE model. Both methods have the prerequisite assumption that contrast injection is fast enough that tissue venous outflow can be ignored. The SS model detects the maximum gradient of enhancement in the middle of the upsloping density-time curve, which occurs earlier than the peak value captured in the PE model. This characteristic implies that the SS method may be less influenced by venous outflow than the PE model, and it may explain why PE estimates of *PBF* were underestimated compared with cardiac output. In addition, injecting diluted isovue-370 did not significantly alter peak enhancement in the pulmonary artery (p=0.156) and in lung tissue (p=0.108). However, mean transit time (MTT) was smaller with diluted vs. undiluted contrast in pulmonary vessels, suggesting faster passage of contrast through the lungs. With diluted contrast, calculated *PBF* values were larger than with undiluted dye (3.03±1.05 vs. 3.24±1.05, P<0.001).

Conclusion: DCE CT using the SS model and diluted contrast agent provided reliable quantitative estimates of *PBF*.

Emerging MRI Techniques and Insights for the Neonatal Lung

Nara Higano, Ph.D.

Division of Pulmonary Medicine and Department of Radiology, Cincinnati Children's Hospital

The underlying structure, function, and microstructure of pulmonary disease in neonates who are born preterm (bronchopulmonary dysplasia, BPD) or with congenital abnormalities (e.g. pulmonary hypoplasia) remains poorly characterized, with unclear links to later morbidity and mortality. There is a lack of suitable techniques to reliably assess lung disease in this population; infant PFT, chest x-ray radiography, and chest CT are limited by technical challenges, low sensitivity, or safety concerns. Recent advances in both ^{1}H and hyperpolarized ^{129}Xe pulmonary MRI in infants allow for refined characterization of neonatal lung pathologies, particularly in BPD, with minimal safety concerns.

^{1}H ultrashort echo-time (UTE) MRI can sensitively characterize abnormal structures in infant lungs and can quantify lung tissue density with CT-like metrics, due to proton-density weighting. UTE MRI has revealed clinical relevance in BPD when applying a modified Ochiai reader score, with the ability to predict short-term respiratory outcomes better than current clinical measures (R^2 = 0.77–0.91).[1] Hyperinflation in BPD (whole-lung volumes normalized by body size) is a strong marker of severe BPD (P = 0.001) and poor clinical trajectories (P = 0.0004), similar to PFT findings of obstructive lung disease, and may provide image-based phenotyping of obstructed pulmonary function.[2] Early work exploring lung ventilation via k_0-gated UTE MRI during tidal breathing may map the spatiotemporal features relevant in multifaceted neonatal lung diseases such as BPD, with minimal patient risks.[3]

Application of hyperpolarized ^{129}Xe gas MRI in infants is early, with preliminary experience demonstrating feasibility and challenges for future consideration.[4] Patients with severe BPD were imaged with breath-hold ^{129}Xe MRI near term-age (~40 weeks gestation). Spiral ventilation acquisitions (N = 6) showed good image quality and sufficient sensitivity to detect mild defects that were mostly, but not exclusively, attributable to structural findings on ^{1}H UTE. Observed ADC values (N = 4) were similar to those seen in healthy adults (~0.04 cm^2/s), and in an extremely pre-term patient, ADC was notably high (~0.06 cm^2/s). Dynamic spectroscopy (N = 7) revealed an RBC/M ratio that would be considered abnormally low (~0.14) in adults and school-aged children (0.46 and 0.31, respectively).[5]

Over the past decade, ^{1}H MRI has begun to mature as a sensitive technique with true clinical relevance to characterize neonatal lung structure and function, with strong potential for early outcomes prognostication, monitoring disease progression via serial imaging with minimal risk, and informing clinical management decisions on an individual patient basis. Initial feasibility and safety findings of ^{129}Xe MRI in infants are emerging; early results hint at sufficient sensitivity for measuring multiple aspects of functional and microstructural impairment in BPD.

1. Higano NS, Spielberg DR, Fleck RJ, et al. Neonatal pulmonary magnetic resonance imaging of bronchopulmonary dysplasia predicts short-term clinical outcomes. *Am J Respir Crit Care Med*. 2018;198(10):1302-1311. doi:10.1164/rccm.201711-2287OC
2. Higano N, Mukthapuram S, Hysinger E, Fleck RJ, Woods JC. Obstructive Versus Restrictive Lung Disease in Neonatal Bronchopulmonary Dysplasia: Surrogate MRI Metrics Reveal Differences in Clinical Relevance. In: *Proceedings of the American Thoracic Society*. ; 2022:A5298-A5298. doi:10.1164/ajrccm-conference.2022.205.1_MeetingAbstracts.A5298
3. Bates A, Higano N, Schuh A, et al. Neonatal Lung Ventilation Mapping from Proton Ultrashort Echo-Time MRI. In: *Proceedings of the International Society for Magnetic Resonance in Medicine*. ; 2020.
4. Higano NS, Stewart NJ, Mukthapuram S, et al. Initial Experience with Hyperpolarized Xenon-129 Gas MRI in Neonates with Bronchopulmonary Dysplasia. In: *Proceedings of the American Thoracic Society*. ; 2022:A4356-A4356. doi:10.1164/ajrccm-conference.2022.205.1_MeetingAbstracts.A4356
5. Willmering MM, Walkup LL, Niedbalski PJ, et al. Pediatric (129) Xe Gas-Transfer MRI-Feasibility and Applicability. *J Magn Reson Imaging*. 2022;56(4):1207-1219. doi:10.1002/jmri.28136

Polymorphic Deep Learning for Robust Segmentation Across Species and Diseases

Sarah E. Gerard, PhD

Chest computed tomography (CT) produces spatially resolved maps of pulmonary anatomy, enabling detection and characterization of disease with greater specificity compared to global measures of lung function from spirometry. Segmentation of pulmonary structures in CT images is important for efficient and reliable quantification of disease phenotypes. Deep learning has achieved ubiquitous improvements in accuracy and efficiency of image segmentation across different organs and medical imaging modalities. However, training neural networks require large annotated datasets with consistent labeling, which are tedious and expensive to produce. The ability to combine annotated datasets from different sources would expedite new network development and improve network generalizability, however, inconsistencies in label specificity between datasets can impose challenges. As a result, many research efforts rely on small bespoke training datasets.

We propose a novel neural network training paradigm called polymorphic deep learning which combines differently labeled datasets to produce a network that is capable of labeling images at any desired specificity level. This is a form of weak supervision for partially labeled training data. Polymorphism in this context refers to a property of labels with multiple hierarchical meanings. For example, voxels specifically labeled as “left lower lobe” in one dataset also implicitly belong to the “left lung” label as well as the most general “lung” label. The polymorphic training paradigm allows inclusion of multiple datasets with heterogeneous labeling specificity, by injecting supervision at multiple layers and enforcing hierarchical label constraints.

Our recent work used polymorphic training to achieve lobe-specific segmentation in thoracic CT images of critically ill COVID-19 patients without any training data from the COVID-19 dataset. This was achieved by combining training data from different sources, including humans with COPD, IPF, and lung cancer and experimental animal models of acute lung injury. We are extending this network to achieve lobar segmentation across multiple species using specifically labeled human datasets and non-specifically labeled animal datasets. The results demonstrate that polymorphic training enables unified training on heterogenous datasets which can enable network generalizability across species and diseases. This talk will present an overview of the polymorphic training paradigm. We will then present our recent study performed in COVID-19 patients. We will conclude with future directions for polymorphic training to improve CT lung segmentation.

SE Gerard, J Herrmann, Y Xin, KT Martin, E Rezoagli, D Ippolito, G Bellani, M Cereda, J Guo, EA Hoffman, DW Kaczka, JM Reinhardt. CT image segmentation for inflamed and fibrotic lungs using a multi-resolution convolutional neural network. Scientific Reports 2021;11:1455.

PET/CT Molecular Imaging of Lung Cancer - Metabolism and Proliferation

David A. Mankoff, M.D., Ph.D.

The ability to measure biochemical and molecular processes to guide cancer treatment represents a potentially powerful tool for trials of targeted cancer therapy. These assays have traditionally been performed by analysis of tissue samples. More recently, functional and molecular imaging allows in vivo assay of cancer biochemistry and molecular biology that is highly complementary to tissue-based assay. Molecular imaging can be used as a biomarker inform targeted cancer clinical trials and clinical decision making by (1) measuring regional expression of the therapeutic target, (2) testing the ability of drugs to interact with their intended targets, and (3) by measuring cancer response early in the course of treatment, and (4) relating response to the risk of relapse.

This talk will review basic principals of molecular imaging in cancer, with an emphasis on those methods that have been tested in patients. The talk will review the current state of molecular imaging in lung cancer patients, including methods in routine clinical use, those undergoing advanced clinical trials, and those in early-phase testing. Topics covered will including imaging lung cancer metabolism with a focus on glucose metabolism, and cellular proliferation as a tool assessing tumor response. The talk will also briefly touch on new targets for lung cancer treatment, including immunotherapy. Current trials and future directions will also be highlighted, as will the application of new technology advances, including total-body PET.

References

1. Mankoff DA, Farwell MD, Clark AS, Pryma DA. Making molecular imaging a clinical tool for precision oncology: a review. JAMA Oncol. 2017 May 1;3(5):695-701.
2. Sellmyer MA, Lee IK, Mankoff DA. Building the Bridge: Molecular Imaging Biomarkers for 21st Century Cancer Therapies. J Nucl Med. 2021 Aug 26;62(12):1672-6.
3. Pantel AR, Viswanath V, Daube-Witherspoon ME, Dubroff JG, Muehllehner G, Parma MJ, Pryma DA, Schubert EK, Mankoff DA, Karp JS. PennPET Explorer: Human Imaging on a Whole-Body Imager. J Nucl Med. 2020 Jan;61(1):144-151.
4. Farwell MD, Gamache RF, Babazada H, Hellmann MD, Harding JJ, Korn R, Mascioni A, Le W, Wilson I, Gordon MS, Wu AM, Ulaner GA, Wolchok JD, Postow MA, Pandit-Taskar N. CD8-Targeted PET Imaging of Tumor-Infiltrating T Cells in Patients with Cancer: A Phase I First-in-Humans Study of 89Zr-Df-IAB22M2C, a Radiolabeled Anti-CD8 Minibody. J Nucl Med. 2022 May;63(5):720-726.

The Role of Surgery in the Treatment of Pleural Mesothelioma

Joseph S. Friedberg, MD FACS

Pleural Mesothelioma (PM) remains one of the most virulent cancers known to man. It is still considered incurable and typically portends a life expectancy in the one-year range. It is an orphan disease, only several percent as common as lung cancer, and is associated with asbestos exposure in the majority of cases. The standard of care is palliative systemic therapy, either pemetrexed-platin doublet chemotherapy or, more recently, nivolumab-ipilimumab immunotherapy (1).

Surgery, at this time, remains an investigational treatment for PM. The reason for this is that it is not possible to achieve a microscopically complete (R0) resection for diffuse pleural cancers. When employed, the role of surgery is to a achieve a *macroscopically* complete resection as part of a multimodal treatment plan that should also include standard of care systemic therapy.

There are two surgical approaches to achieving a macroscopic complete resection, both involve resecting or treating all parietal pleural surfaces. The visceral pleural surface can be addressed by either performing a pneumonectomy or preserving the lung. Over the past two decades the general international trend has been toward lung preservation, but there is no standard surgical approach at this time. In either case it is a colossal operation, arguably the most extensive palliative procedure in the field of medicine.

The reason surgery does appear to have a role in the treatment of PM is because carefully selected patients seem to exhibit a significantly longer survival than would be anticipated with systemic therapy alone. Oncologic indications for surgery are well established for most solid tumors, like NSCLC, with the staging system clearly identifying the patients likely to benefit from surgery. This is not the case for PM. While the staging system for PM continues to be improved and revised, two of the most significant prognosticators that inform the expected oncologic benefit of surgery, histologic subtype and tumor volume, are not included in the staging system. Histologic subtype, with epithelioid being the most likely to be positively impacted by surgical extirpation, is readily determined with a biopsy. Accurate estimates of tumor volume, presumably from CT scans, as proved more elusive. A number of approaches have been employed to render estimates of tumor volume, but a standardized volumetric system has yet to emerge.

It seems likely that if a validated and universally accessible instrument becomes available to measure tumor volume from a CT scan, that this technique will become standard of care for PM. Volumetric estimation would prove not only useful for general prognostication, but would be invaluable in helping with patient selection for surgery.

1 First-line nivolumab plus ipilimumab in unresectable malignant pleural mesothelioma (CheckMate 743): a multicentre, randomised, open-label, phase 3 trial. Lancet, 2021 Jan 30;397(10272):375-386.

Quantitative Imaging for Lung Cancer in the Era of Immuno-oncology

Ho Yun Lee

Clinical oncology is experiencing rapid growth in data that are collected to enhance cancer care, where quantitative imaging has been proposed as the next frontier in radiology as part of an effort to improve patient care through precision medicine. Especially with recent advances in the field of artificial intelligence (AI), there is now a computational basis to integrate and synthesize this growing body of multi-dimensional data, deduce patterns, and predict outcomes to improve shared patient and clinician decision making.

What's more, another paradigm shift in treatment of cancer has been brought by immune-checkpoint inhibitors achieved impressive success. Yet, unfortunately, only a subset of unselected cancer patients responds to these therapies. Thus, an important area of ongoing research is to identify biomarkers that can predict which patients are most likely to derive clinical benefits.

In this lecture, the rationale for and the key facts related to the application of these quantitative imaging biomarkers in the recent era of immune-oncology are presented.

1. Thai AA, Solomon BJ, Sequist LV, Gainor JF, Heist RS. Lung cancer. Lancet. 2021;398(10299):535-554.
2. Gerlinger M, Rowan AJ, Horswell S, et al. Intratumor heterogeneity and branched evolution revealed by multiregion sequencing. N Engl J Med. 2012;366(10):883-892.
3. Memmott RM, Wolfe AR, Carbone DP, Williams TM. Predictors of response, progression-free survival, and overall survival in patients with lung cancer treated with immune checkpoint inhibitors. J Thorac Oncol. 2021;16(7):1086-1098.
4. Abbosh C, Birkbak NJ, Wilson GA, et al. Phylogenetic ctDNA analysis depicts early-stage lung cancer evolution. Nature. 2017;545(7655):446-451.
5. Lee G, Park H, Bak SH, Lee HY. Radiomics in lung cancer from basic to advanced: current status and future directions. Korean J Radiol. 2020;21(2):159-171.

Intraoperative Molecular Imaging of Lung Cancer

Sunil Singhal, MD

Lung cancer remains the most common cause of cancer death in the United States with more than 235,000 new cases last year. Surgery remains the most effective approach to manage lung cancer if the patient's tumor is completely resectable and the patient can tolerate an operation. However, despite seemingly successful surgery, 20% of patients develop a local recurrence due to surgical failure. This local recurrence rate is due to positive margins during resection and missed synchronous or discontinuous cancers.

Intraoperative molecular imaging (IMI) has developed rapidly over the past decade to address this challenge. IMI utilizes optical tracers that target malignant lesions through a variety of means. These tracers fluoresce and can easily be visualized using optical imaging instrumentation, making it possible to accurately identify tumors intraoperatively, remove them with negative margins, and even identify additional lesions that were not visualized preoperatively. Recent studies have also used fluorescent tracers to help surgeons identify and avoid vital structures like nerves and vasculature.

Fluorescent tracers generally act through one of three mechanisms: passive, active, and activatable. Passive targeting relies on the enhanced permeability and retention effect, which leverages the increased vascular permeability and decreased lymphatic drainage of cancerous tissue. More recently developed tracers actively target abnormally expressed receptors on malignant cells, enhancing labeling specificity and permitting higher resolution imaging. Our group has been studying targeting folate-receptor alpha (FRα) with a near-infrared targeted tracer that has allowed real-time visualization of radiologically occult lung tumors and contrast between tumor cells and normal lung.

Over the last decade, our group has performed preclinical work and clinical trials testing this strategy. In the presentation, we will discuss the results of the preclinical studies and the resulting Phase I, Phase II and Phase III studies. In this Phase III, 12-center randomized trial, 111 subjects with suspected or biopsy-confirmed cancer in the lung scheduled for sublobar pulmonary resection were administered a single intravenous infusion of pafolacianine within 24 hours before surgery. Subjects were randomly assigned (10:1) to surgery with (n=100) or without (n=11) IMI. The primary endpoint was the proportion of subjects with a clinically significant event (CSE), defined as a clinical change in the surgical operation attributed to enhanced visualization of tumors.

No drug-related serious adverse events occurred. One or more CSE's occurred in 54/100 subjects (54%, 95% CI 43.7 – 64.0, $p < 0.0001$) randomly assigned to IMI. There were 38 patients with margins < 10 mm from the resected primary nodule (38%, 95% CI 28.5 – 48.3) with 32 confirmed by concordant pathology measurement. In 19 subjects (19%, 95% CI 11.8 – 28.1), IMI located the primary nodule that the surgeon could not locate. IMI revealed 11 occult synchronous malignant lesions in 9 subjects (9%, 95% CI 4.2 – 16.4) unknown to the surgeon. A change in the overall scope of surgical procedure occurred for 29% of the subjects (22% increase, 7% decrease). Most (73%) IMI-discovered synchronous malignant lesions were outside the planned resection field. In 10% of the cases, the use of IMI up-staged the patients due to new information.

Based on these results, this past December 2022, this molecule was granted FDA approval and will be the first targeted fluorescent probe in humans.

Predina J. D., Newton A. D., Connolly C., Dunbar A., Baldassari M., Deshpande C., Cantu E., 3rd, Stadanlick J., Kularatne S. A., Low P. S. and Singhal S. "Identification of a Folate Receptor-Targeted Near-Infrared Molecular Contrast Agent to Localize Pulmonary Adenocarcinomas." Mol Ther. 26(2): 390-403. Feb 7, 2018. PMCID: 29241970.

Predina J. D., Newton A. D., Keating J., Dunbar A., Connolly C., Baldassari M., Mizelle J., Xia L., Deshpande C., Kucharczuk J., Low P. S. and Singhal S. "A Phase I Clinical Trial of Targeted Intraoperative Molecular Imaging for Pulmonary Adenocarcinomas." Ann Thorac Surg. 105(3): 901-908. Mar, 2018. PMCID: 29397932.

Azari F., Kennedy G., Bernstein E., Delikatny J., Lee J. Y. K., Kucharczuk J., Low P. S. and Singhal S. "Evaluation of OTL38-Generated Tumor-to-Background Ratio in Intraoperative Molecular Imaging-Guided Lung Cancer Resections." Mol Imaging Biol. Jun 8, 2021. PMCID: 34101106.

Gangadharan S., Sarkaria I. N., Rice D., Murthy S., Braun J., Kucharczuk J., Predina J. and Singhal S. "Multiinstitutional Phase 2 Clinical Trial of Intraoperative Molecular Imaging of Lung Cancer." Ann Thorac Surg. 112(4): 1150-1159. Oct, 2021. PMCID: 33221195.

Lung Cancer Screening Efficacy Enhanced Through Radiomic Biomarkers

Jessica Sieren

Smoking is the largest risk factor for both lung cancer and obstructive lung disease. The National Lung Screening Trial (NLST) enrolled subjects who reported a cigarette smoking history of at least 30 pack years and showed that annual low-dose computed tomography (LDCT) screening could reduce mortality from lung cancer by approximately 16%, compared to conventional chest x-ray[1]. However, it remains clinically challenging to efficiently distinguish the small number of malignant nodules from the many benign lung nodules detected with screening.

CT imaging creates a wealth of information. We have previously demonstrated the potential of radiomic features in predicting lung cancer risk in a cohort of 460 subjects, with an accuracy of 100% in testing and 98% in validation[2]. In that study, computer extracted features capturing the radiological intensity, texture, and shape of the imaging identified pulmonary nodules were utilized, along with features extracted from an optimized perimeter of peri-nodular lung parenchyma. However, these preliminary results focused on high-resolution CT data in a diverse cohort of research subjects. Hence, the approach requires testing and validation using LDCT data and in a cohort specifically meeting the criteria for lung cancer screening.

A comparator to risk prediction models created with radiomic features, are existing mathematical risk prediction models using multivariate logistic regression and incorporating demographic, clinical and radiologist assessed nodule features from imaging data. We have tested the performance of four such models (including the Brock University model[3] recommended by the British Thoracic Society[4]), pre- and post-calibration of the thresholds[5], on a subset of subjects from the NLST. We compare the performance of the mathematical risk prediction models in the context of the Lung-RADS criteria. The performance of these simpler prediction models forms a baseline for which the radiomics model in development must outperform.

References

1. Aberle DR, Adams AM, Berg CD, Black WC, Clapp JD, Fagerstrom RM, Gareen IF, Gatsonis C, Marcus PM, Sicks JD. Reduced lung-cancer mortality with low-dose computed tomographic screening. N Engl J Med. 2011;365(5):395-409. Epub 2011/07/01. doi: 10.1056/NEJMoa1102873. PubMed PMID: 21714641; PMCID: PMC4356534.

2. Uthoff J, Stephens MJ, Newell JD, Jr., Hoffman EA, Larson J, Koehn N, De Stefano FA, Lusk CM, Wenzlaff AS, Watza D, Neslund-Dudas C, Carr LL, Lynch DA, Schwartz AG, Sieren JC. Machine learning approach for distinguishing malignant and benign lung nodules utilizing standardized perinodular parenchymal features from CT. Med Phys. 2019;46(7):3207-16. Epub 2019/05/16. doi: 10.1002/mp.13592. PubMed PMID: 31087332.

3. McWilliams A, Tammemagi MC, Mayo JR, Roberts H, Liu G, Soghrati K, Yasufuku K, Martel S, Laberge F, Gingras M, Atkar-Khattra S, Berg CD, Evans K, Finley R, Yee J, English J, Nasute P, Goffin J, Puksa S, Stewart L, Tsai S, Johnston MR, Manos D, Nicholas G, Goss GD, Seely JM, Amjadi K, Tremblay A, Burrowes P, MacEachern P, Bhatia R, Tsao MS, Lam S. Probability of cancer in pulmonary nodules detected on first screening CT. N Engl J Med. 2013;369(10):910-9. Epub 2013/09/06. doi: 10.1056/NEJMoa1214726. PubMed PMID: 24004118; PMCID: PMC3951177.

4. Baldwin DR, Callister ME. The British Thoracic Society guidelines on the investigation and management of pulmonary nodules. Thorax. 2015;70(8):794-8. Epub 20150701. doi: 10.1136/thoraxjnl-2015-207221. PubMed PMID: 26135833.

5. Uthoff J, Koehn N, Larson J, Dilger SKN, Hammond E, Schwartz A, Mullan B, Sanchez R, Hoffman RM, Sieren JC. Post-imaging pulmonary nodule mathematical prediction models: are they clinically relevant? Eur Radiol. 2019;29(10):5367-77. Epub 2019/04/03. doi: 10.1007/s00330-019-06168-x. PubMed PMID: 30937590; PMCID: PMC6717521.

Are ^{129}Xe MRI ventilation abnormalities clinically relevant in post-acute COVID-19 syndrome, 3- and 15-months post infection?

Grace Parraga PhD FCAHS

The COVID-19 pandemic has compelled the intentional development and optimization of new ways to directly evaluate the effects of acute viral infection in patients with mild (requiring home-based care only) and more severe symptoms (requiring hospital and intensivist care). Whilst a myriad of body/organ systems were affected, the respiratory system was the main entry and viral replication space; severe, acute respiratory symptoms obligated the necessity for the application of rapid chest imaging methods and measurements in patients. Chest CT and CT pulmonary angiography certainly dominated for those patients experiencing severe acute chest infection requiring hospital-based care.[1] As the pandemic evolved however, it became clear that many COVID-19 survivors reported new and ongoing symptoms of unexplained dyspnea, tachypnea, malaise, exercise limitation and quality-of-life deficits, in the absence of measurable virus and with normal or only mildly abnormal chest CT and pulmonary function tests. Defined as post-acute COVID-19 syndrome[2], substantial numbers of infected patients experienced long-term symptoms 12 weeks+ post-infection. The possibility was raised that some of these symptoms may be due to small airways disease.[3] To test this hypothesis and demonstrate feasibility, we evaluated 53 patients with symptoms and poor quality-of-life scores consistent with post-acute COVID-19 syndrome, 3- and 15-months post-infection using hyperpolarized ^{129}Xe ventilation MRI.

In this prospective study at two centres in the province of Ontario, Canada, ^{129}Xe MRI ventilation defect percent (5.4±7.1%, 4.2±6.8%; *P*=.003), forced expiratory volume in 1s (85±20%$_{pred}$, 90±19%$_{pred}$ *P*=.001), diffusing capacity of the lung for carbon-monoxide (DL_{CO}; 89±29%$_{pred}$, 99±22%$_{pred}$; *P*=.002) and quality-of-life-score (35±18, 25±20, *P*<.001) significantly improved at 15-months as compared to 3-months post-infection. In multivariable models, abnormal MRI ventilation defect percent at 3-months post-infection predicted the change in six-minute-walk-distance, 15-months post-infection (β=-.643, *P*=.001), while the changes in both DL_{CO} and forced-vital-capacity explained the change in quality-of-life score. Treatment with inhaled airways disease medication at 3-months post-COVID correlated with improved quality-of-life score (odds ratio=4.0, 95%CI:1.2,13.8, *P*=.03) 15-months post-COVID.

Pulmonary function, exercise capacity, quality-of-life, and ^{129}Xe MRI ventilation defect percent improved in participants with post-acute COVID-19 syndrome 15-months post-infection. Participants prescribed airways-disease therapy were four-times (OR=4.0, p=.03) more likely to experience quality-of-life-score improvements. We are currently exploring the relationship of ventilation and gas-exchange abnormalities in those participants evaluated using both approaches.

1 Kanne, J. P. *et al.* COVID-19 Imaging: What We Know Now and What Remains Unknown. *Radiology* **299**, E262-E279 (2021). https://doi.org:10.1148/radiol.2021204522

2 Nalbandian, A. *et al.* Post-acute COVID-19 syndrome. *Nat Med* **27**, 601-615 (2021). https://doi.org:10.1038/s41591-021-01283-z

3 Adeloye, D. *et al.* The long-term sequelae of COVID-19: an international consensus on research priorities for patients with pre-existing and new-onset airways disease. *Lancet Respir Med* **9**, 1467-1478 (2021). https://doi.org:10.1016/S2213-2600(21)00286-1

Leveraging CXR and CT Advanced Quantitative Imaging and Machine Learning Beyond COVID-19 Diagnosis to Quantification and Prognostication

Eduardo J. Mortani Barbosa Jr., M.D.

University of Pennsylvania

At the dawn of COVID-19 pandemic, pulmonary involvement was acknowledged as the primary contributor to morbidity and mortality. While the diagnosis of COVID-19 infection relies on detection of viral proteins or its genetic material, detecting COVID-19 pneumonia requires medical imaging, such as radiographs (CXR) or chest CTs. Nonetheless, the simple binary detection of pneumonia relinquishes a substantial amount of latent information on imaging, which can be unleashed through quantitative methods to inform predictive prognostic models and assess therapeutic response. Therefore, imaging pattern detection, classification, quantification, and prognostication driven by a combination of automated algorithms and human expert input should be holistically integrated.

This presentation will discuss original research on novel methods and applications utilizing artificial intelligence algorithms in the clinical setting of patients with suspected COVID-19 pneumonia. The first[1] is a novel method that leverages the superior 3D quantification of airspace disease (AD) on chest CTs, which is encoded in planar projections through the creation of synthetic DRRs (digitally reconstructed radiographs), allowing superior 2D quantification on paired chest radiographs by a deep convolutional neural network (CNN). The CNN, learning from the DRRs, was able to achieve expert level performance to quantify the area of AD on chest radiographs, with mean absolute error of [8.8 – 10.2%] and correlation of [0.73 - 0.85] with the reference standard of volumetric AD quantification on chest CTs. The second[2] is a multicenter study applying machine learning methods (both supervised and unsupervised) to classify different 3D patterns of lung disease on chest CTs, which achieved AUC (area under the ROC curve) of 0.93, sensitivity of 0.90 and specificity of 0.83 to diagnose COVID-19 pneumonia. Furthermore, the deep-learning classifier achieved a moderate to high performance to correctly classify non-COVID-19 pneumonias (64%), interstitial lung diseases (91%) and normal CT scans (94%). The third[3] is a retrospective observational study comparing the utility of both 3D AD quantification by CT and 2D AD quantification by CXR with established prognostic markers in patients with COVID-19, such as demographics, vital signs (Sat O2, respiratory rate) and laboratory metrics (d-dimer, ferritin, WBC), for prognostication of COVID-19, separating mild/moderate from severe disease that required ICU admission. Models using imaging derived quantitative markers outperformed models utilizing demographics, vital signs, and laboratory values (AUC of 0.78 vs 0.67, $p<0.05$), and importantly, performed equally well when 2D AD data replaced 3D AD data.

Taken together, these research results indicate that CT and CXR imaging derived quantitative measurement of AD, performed by automated algorithms which learned from expert humans, not only allow accurate detection and classification of COVID-19 pneumonia, but also enable superior prognostication when compared to clinical metrics. Hence, these

provide valuable guidance to proactively identify and aggressively manage COVID-19 patients at the greatest risk for poor outcomes.

1. Mortani Barbosa EJ Jr, Gefter WB, Ghesu FC, Liu S, Mailhe B, Mansoor A, Grbic S, Vogt S. Automated Detection and Quantification of COVID-19 Airspace Disease on Chest Radiographs: A Novel Approach Achieving Expert Radiologist-Level Performance Using a Deep Convolutional Neural Network Trained on Digital Reconstructed Radiographs from Computed Tomography-Derived Ground Truth. Invest Radiol. 2021 Aug 1;56(8):471-479. doi: 10.1097/RLI.0000000000000763. PMID: 33481459.

2. Mortani Barbosa EJ Jr, Georgescu B, Chaganti S, Aleman GB, Cabrero JB, Chabin G, Flohr T, Grenier P, Grbic S, Gupta N, Mellot F, Nicolaou S, Re T, Sanelli P, Sauter AW, Yoo Y, Ziebandt V, Comaniciu D. Machine learning automatically detects COVID-19 using chest CTs in a large multicenter cohort. Eur Radiol. 2021 Nov;31(11):8775-8785. doi: 10.1007/s00330-021-07937-3. Epub 2021 May 1. PMID: 33934177; PMCID: PMC8088310.

3. Jung HM, Yang R, Gefter WB, Ghesu FC, Mailhe B, Mansoor A, Grbic S, Comaniciu D, Vogt S, Mortani Barbosa EJ Jr. Value of quantitative airspace disease measured on chest CT and chest radiography at initial diagnosis compared to clinical variables for prediction of severe COVID-19. J Med Imaging (Bellingham). 2022 May;9(3):034003. doi: 10.1117/1.JMI.9.3.034003. Epub 2022 Jun 17. PMID: 35721308; PMCID: PMC9203354.

Longitudinal lung function assessment of patients hospitalised with COVID-19 using ^{1}H and ^{129}Xe lung MRI

Laura C Saunders[1], Guilhem J Collier[1], Ho-Fung Chan[1], Paul J C Hughes[1], Laurie J Smith[1] , James Watson[2], James Meiring[2], Zoë Gabriel[2], Thomas Newman[2], Megan Plowright[2], James A Eaden[1], Jody Bray[1], Helen Marshall[1], David J Capener[1], Leanne Armstrong[1], Jennifer Rodgers[1], Martin Brook[1], Alberto M Biancardi[1], Madhwesha R Rao[1], Graham Norquay[1], Oliver Rodgers[1], Ryan Munro[1], Neil J Stewart[1], Alan Lawrie[1], Gisli Jenkins[3], James Grist[4], Fergus Gleeson[4], Frederick Wilson[5*], Anthony Cahn[5] , Andrew J Swift[1], Smitha Rajaram[2], Gary H Mills[1], Lisa Watson[2], Paul J Collini[1], Rod Lawson[2], A A Roger Thompson[1], and **Jim M Wild[1]**

1 Department of Infection, Immunity; Cardiovascular Disease, University of Sheffield, Sheffield, United Kingdom 2 Sheffield Teaching Hospitals, NHS Foundation TRUST, Sheffield, United Kingdom,

Abstract

Introduction: Microvascular abnormalities and impaired ^{129}Xe gas transfer have been observed in patients with COVID-19. The progression of pathophysiological pulmonary changes during the post-acute period in these patients remains unclear.

Methods: Patients who were hospitalised due to COVID-19 pneumonia underwent a pulmonary ^{1}H and ^{129}Xe MRI protocol at 6, 12, 25 and 51 weeks after hospital admission. The imaging protocol included: ultra-short echo time, dynamic contrast enhanced lung perfusion, ^{129}Xe lung ventilation, ^{129}Xe diffusion weighted and ^{129}Xe 3D spectroscopic imaging of gas exchange.

Results: 9 patients were recruited and underwent MRI at 6 (n=9), 12 (n=9), 25 (n=6) and 51 (n=8) weeks after hospital admission. At 6 weeks after hospital admission, patients demonstrated impaired ^{129}Xe gas transfer (RBC:M) but normal lung microstructure (ADC, Lm_D). Minor ventilation abnormalities present in four patients were largely resolved in the 6–25 week period. At 12 week follow up, all patients with lung perfusion data available (n=6) showed an increase in both pulmonary blood volume and flow when compared to 6 weeks, though this was not statistically significant. At 12 week follow up, significant improvements in ^{129}Xe gas transfer were observed compared to 6-week examinations, however ^{129}Xe gas transfer remained abnormally low between 12 and 51 weeks.

Conclusions: This study demonstrates that multinuclear MRI is sensitive to functional pulmonary changes in the follow up of patients who were hospitalised with COVID-19. Persistent impairment of xenon transfer may represent a physiological mechanism underlying ongoing symptoms in some patients and may indicate damage to the pulmonary microcirculation.

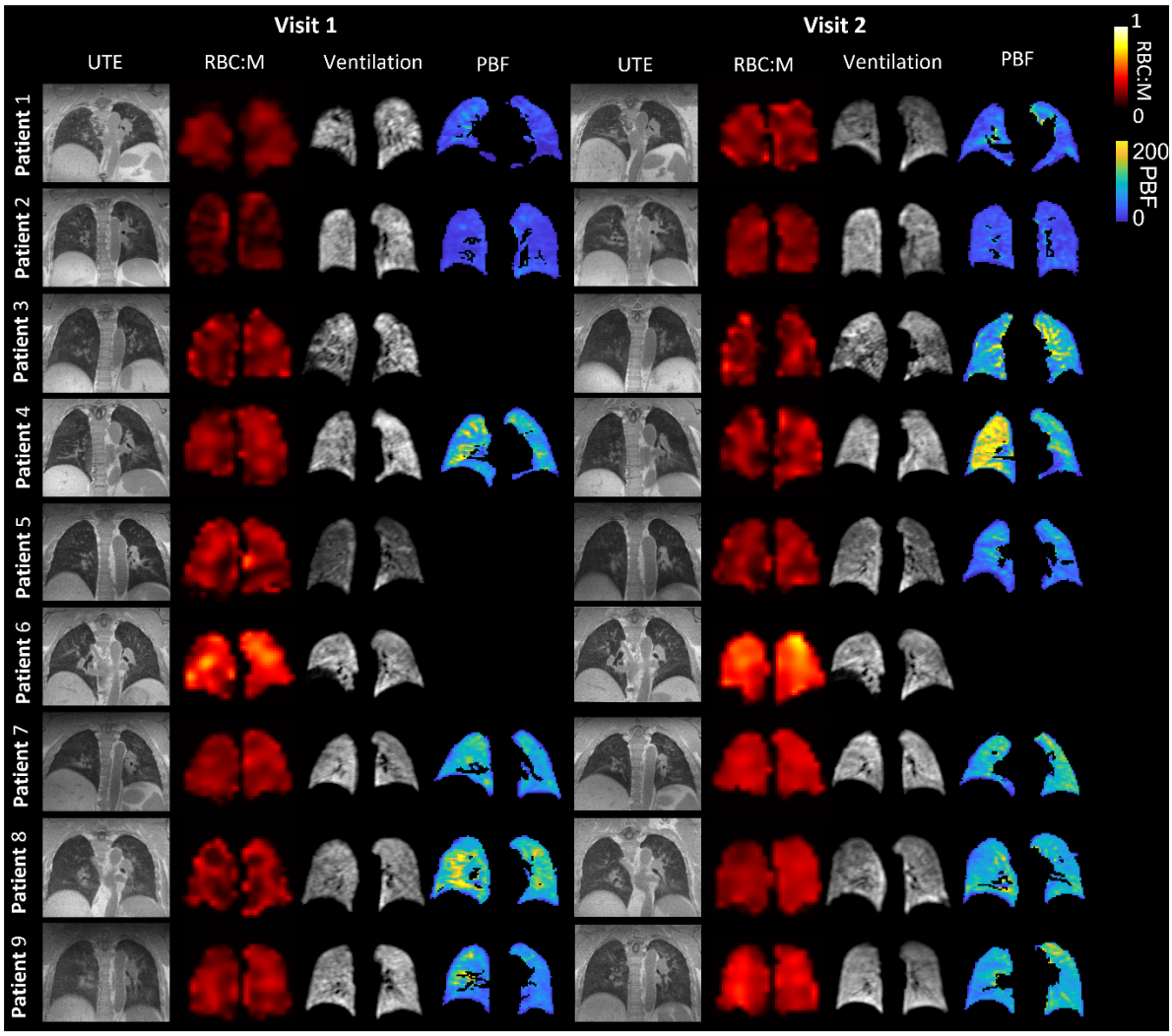

Figure 1: Example ultra-short echo time (UTE) images, RBC:M maps, ^{129}Xe ventilation images and maps of pulmonary blood flow at visit 1 and visit 2, for each patient. The white arrow shows a segmental perfusion defect visible at visit 1 which improves at visit 2. UTE: ultra-short echo time. RBC: red blood cell. M: membrane. PBF: pulmonary blood flow.

Visualizing Gas Exchange Defects Using Hyperpolarized ^{129}Xe MRI in Patients with Post-acute COVID-19 Respiratory Symptoms

Peter Niedbalski

Since the beginning of the COVID-19 pandemic, >660 million people (>100 million in United States) have been infected, leading to the death of >7.5 million (>1 million in US). Over time, it has become clear that acute COVID-19 is only part of the story, with 54% of hospitalized COVID-19 patients and 34% of non-hospitalized patients exhibiting lingering symptoms at least 28 days after acute COVID-19 infection.[1] Respiratory (or respiratory-related) symptoms are among the most prevalent post-COVID-19 complaints. In particular, 23% of COVID-19 patients report fatigue, 13% report dyspnea, 7% report cough, and 5% report chest pain.[1] These symptoms are often associated with radiologic and lung function abnormalities. However, there are also many cases in which imaging and lung function are normal or symptoms are disproportionate to radiologic and lung function abnormalities.[2] Hyperpolarized ^{129}Xe MRI (Xe-MRI) can elucidate impaired lung function with a high degree of sensitivity, and thus is a compelling modality to use in the post-acute COVID-19 population.

Xe-MRI can be used to collect images reflecting ventilation and the transfer of gas to red blood cells (RBCs) through the pulmonary interstitium ("membrane"), commonly referred to as gas exchange imaging.[3] We collected ventilation and gas exchange Xe-MRI images in 35 patients who had COVID-19 (mean 333 ± 188 days diagnosis). Imaging was performed using 3D spiral acquisition ("FLORET") for ventilation imaging and radial 1-point Dixon imaging for gas exchange.[4] At the time of imaging, we collected information regarding respiratory symptoms in all participants. A subset of participants (N = 15) were imaged at a second timepoint 6 months after the initial imaging timepoint. Images were quantified to calculate mean RBC/membrane, membrane/gas, and RBC/gas ratios.[5] We then examined the association between respiratory symptoms and Xe-MRI markers. Following this single-site study, we examined Xe-MRI data collected using similar protocols in post-acute COVID-19 patients across 2 other sites in the United States and Canada (Duke University, University of British Columbia).

Participants with respiratory symptoms trended toward having lower RBC/Membrane (0.32 ± 0.09 vs. 0.37 ± 0.10, $p = 0.13$) and RBC/Gas (0.28 ± 0.1 vs. 0.34 ± 0.09, $p = 0.1$) ratios than participants with no long-term respiratory symptoms. When examining prominent symptoms (dyspnea, fatigue, cough) individually, only fatigue was associated with a significant difference in Xe-MRI markers (RBC/Gas: 0.26 ± 0.09 vs. 0.35 ± 0.11, $p = 0.01$). Membrane/Gas was widely variable across participants and ventilation defect percent was not associated with respiratory symptoms. There was no significant change in Xe-MRI markers from baseline to 6-month imaging ($p > 0.15$ for all markers). This was the case in participants who continued to experience respiratory symptoms and those who reported resolution of symptoms.

In the larger, multi-site cohort (N = 104, N = 67 with symptoms, 37 recovered), similar results are observed. Participants reporting respiratory symptoms show significantly reduced RBC/Membrane (0.37 ± 0.12 vs. 0.45 ± 0.12, $p < 0.001$) and RBC/Gas (0.29 ± 0.09 vs. 0.33 ± 0.1, $p = 0.01$) as compared to those without respiratory symptoms. Similar to the single-site results, Membrane signal was widely variable and not significantly associated with symptoms.

These results demonstrate that Xe-MRI is sensitive to lung damage associated with post-acute COVID-19 respiratory symptoms. Moreover, these results are suggestive of primarily vascular pathophysiology in post-acute COVID-19, based on reductions to RBC signal with no corresponding elevation in membrane signal. Preliminary results examining patients over 6 months suggest that the functional impairment associated with symptoms persists over long time scales. Finally, the Xe-MRI results observed at a single-site were consistent with results observed previously[2] and when examining a larger, multi-site Cohort. Ultimately, Xe-MRI is an effective method to assess pulmonary functional impairment in patients experiencing post-acute COVID-19 respiratory symptoms.

1. Chen C, Haupert SR, Zimmermann L, Shi X, Fritsche LG, Mukherjee B. Global Prevalence of Post-Coronavirus Disease 2019 (COVID-19) Condition or Long COVID: A Meta-Analysis and Systematic Review. The Journal of Infectious Diseases 2022.
2. Grist JT, Collier GJ, Walters H, et al. Lung Abnormalities Depicted with Hyperpolarized Xenon MRI in Patients with Long COVID. Radiology 2022;0:220069.
3. Niedbalski PJ, Hall CS, Castro M, et al. Protocols for multi-site trials using hyperpolarized 129Xe MRI for imaging of ventilation, alveolar-airspace size, and gas exchange: A position paper from the 129Xe MRI clinical trials consortium. Magn Reson Med 2021;86:2966-86.
4. Niedbalski PJ, Lu J, Hall CS, et al. Utilizing flip angle/TR equivalence to reduce breath hold duration in hyperpolarized 129Xe 1-point Dixon gas exchange imaging. Magn Reson Med 2022;87:1490-9.
5. Wang Z, Robertson SH, Wang J, et al. Quantitative analysis of hyperpolarized 129Xe gas transfer MRI. Med Phys 2017;44:2415-28.

Imaging Lung Perfusion to Guide ARDS Care

Maurizio Cereda, MD

Treatment of acute respiratory distress syndrome (ARDS) focuses primarily on monitoring and protecting the pulmonary airspaces: dialing lower tidal volumes, targeting lower driving pressures, and using prone positioning to reduce lung stress during mechanical ventilation. Pharmacological options are limited by insufficient characterization of heterogeneous ARDS populations.

Early angiographic and autopsy studies revealed simultaneous reversible (pulmonary vasoconstriction, thromboembolism, interstitial edema) and irreversible (intimal proliferative lesions progressing to permanent vascular obstruction and remodeling) impairment of lung perfusion in early ARDS[1]. Because of this, blood is variably diverted to well perfused lung regions, where in addition to worsening hypoxemia, elevated intravascular volumes and pressures damage the vascular endothelium, compounding pulmonary edema and stress-induced injury[2]. However, little has been done to preserve and improve pulmonary vascular function.

Imaging regional lung perfusion may help characterize ARDS patients: abnormal blood flow distributions and locally altered vasoregulation are likely associated with important biological characteristics, treatment responses, and outcomes of ARDS. Furthermore, mapping regional blood flows can help interpret the relationship between gas exchange impairment and severity of lung injury in each patient, improving individualized outcome predictions.

4D dynamic contrast-enhancement (DCE) computed tomography (CT)[3], and dual energy CT (DECT)[4] contribute to pre-clinical and clinical research by providing high-resolution maps of pulmonary blood flow (PBF) and volume (PBV). In experimental ARDS, we used these instruments to quantify regional changes in pulmonary perfusion related to treatments such as prone positioning, inhaled nitric oxide (iNO), and cardiac stimulants.

Electrical impedance tomography (EIT) is a bedside imaging modality which enables frequent joint assessments of regional lung mechanics and perfusion without requiring patient transport. EIT injects electric microcurrents through 16-32 electrodes to monitor the distribution of thoracic impedance in an axial plane. Regional PBF is measured after intravenous injection of small boluses of hypertonic saline tracer[5]. In experimental ARDS, we test correlations of EIT-derived and CT-derived PBF values. Furthermore, we used this technique in human ARDS to demonstrate individual variability of responses to iNO.

Moving forward, integrating techniques of perfusion imaging in ARDS research and care will likely allow a paradigm shift to targeting the vascular physiology and biology in addition to airspace mechanics.

1. Greene R, et al. Early bedside detection of pulmonary vascular occlusion during acute respiratory failure. Am Rev Respir Dis 1981; 124:593-601
2. Hotchkiss JR, et. al Relative roles of vascular and airspace pressures in ventilator-induced lung injury. Crit Care Med 2001;29:1593–8.
3. Wolfkiel CJ, Rich S. Analysis of regional pulmonary enhancement in dogs by ultrafast computed tomography. Invest Radiol 1992;27:211–6.
4. Fuld MK, et al. Pulmonary perfused blood volume with dual-energy CT as surrogate for pulmonary perfusion assessed with dynamic multidetector CT. Radiology 2013;267:747–56
5. Borges JB, et al. Regional lung perfusion estimated by electrical impedance tomography in a piglet model of lung collapse. J Appl Physiol 1985 2012;112:225–36

Ventilating the Injured Lung: Insights from Quantitative CT Imaging

David W. Kaczka, MD, PhD

The acute respiratory distress syndrome (ARDS) is a deadly form of respiratory failure associated with high mortality, and places significant burdens on public health resources. Patients suffering from ARDS have few treatment options available to them, other than supportive mechanical ventilation. However, mechanical ventilation itself also has the potential to increase mortality, due to the maldistribution of ventilation and lung parenchymal strain, as well as repetitive alveolar collapse and expansion. Together, these phenomena may contribute to unintended ventilator-induced lung injury (VILI). Lung protective mechanical ventilation attempts to mitigate the risk for VILI, while simultaneously providing life-sustaining gas exchange of the failing respiratory system. Traditional strategies for protective ventilation rely on appropriate levels of positive end-expiratory pressure (PEEP) to limit end-expiratory derecruitment, and low tidal volumes or driving pressures to limit overdistention. However, since ventilation distribution in ARDS is governed by a heterogeneous distribution of regional mechanics, the most appropriate distending pressure, ventilation frequency, or tidal volume for one lung region may not necessarily be the same for another, even within the same patient. This may result in poor ventilation-to-perfusion matching and ineffective gas exchange.

We have previously demonstrated that ventilation of a mechanically heterogeneous lung using multiple simultaneous frequencies, improves gas exchange and maintains lung recruitment at lower distending pressures compared to traditional "single-frequency" ventilation (3). We have termed this unique modality of mechanical ventilation "multi-frequency ventilation" (MFV), and have postulated that such improvements in physiological outcomes may arise from a more even distribution of ventilation to different lung regions, in accordance with local mechanical properties. Since specific lung regions may be characterized by different "preferred" frequencies of ventilation, MFV is uniquely capable of enhancing gas exchange in the mechanically heterogeneous lung, including more efficient oxygenation and CO_2 elimination. MFV may also be a more efficacious approach to minimizing VILI in the heterogeneously injured lung, by reducing parenchymal strain heterogeneity. In this presentation, we will discuss the theoretical rationale for the use of MFV in structurally heterogeneous pathologies such as ARDS. Based on our previous work using dynamic xenon-enhanced computed tomographic (CT) imaging (1) and four-dimensional image registration (2), we will elucidate mechanisms by which MFV improves regional ventilation distribution, aeration, and parenchymal strain in a porcine model of ARDS. We expect that these pre-clinical studies of MFV will have a high likelihood of establishing the foundation for the further exploration of novel modes of conventional and oscillatory ventilation in a broad range of patients with acute respiratory failure.

1. **Herrmann J, Gerard SE, Reinhardt JM, Hoffman EA, and Kaczka DW**. Regional gas transport during conventional and oscillatory ventilation assessed by xenon-enhanced computed tomography. *Ann Biomed Eng* 2021.

2. **Herrmann J, Gerard SE, Shao W, Hawley ML, Reinhardt JM, Christensen GE, Hoffman EA, and Kaczka DW**. Quantifying regional lung deformation using four-dimensional computed tomography: A comparison of conventional and oscillatory ventilation. *Frontiers in physiology* 11: 14, 2020.

3. **Kaczka DW, Herrmann J, Zonneveld CE, Tingay DG, Lavizzari A, Noble PB, and Pillow JJ**. Multifrequency oscillatory ventilation in the premature lung: Effects on gas exchange, mechanics, and ventilation distribution. *Anesthesiology* 123: 1394-1403, 2015.

Lung repair by alveolar type II epithelial cells in surfactant protein C deficient mice

N. Valerio Dorrello, MD PhD
Columbia University

Childhood interstitial lung disease (chILD) secondary to pulmonary surfactant deficiency is a devastating chronic lung disease in children. The incidence of ChILD ranges from 0.1 to 16.2 per 100,000 people (12,13) with a prevalence of 1.3-3.8 per million and mortality as high as 35% (6,9–11,14–16). Some forms of chILD are lethal in the neonatal period while others cause respiratory disease ranging from neonatal respiratory failure to childhood- or adult-onset interstitial lung disease. There is no specific treatment, except lung transplantation, which is hampered by a severe shortage of donor organs, especially for young patients.

Repair of lungs with chILD represents a longstanding therapeutic challenge but cellular therapy is a promising strategy. As surfactant is produced by alveolar type II epithelial (ATII) cells, engraftment with normal or gene-corrected ATII cells might provide an avenue to cure. Here we used a chILD disease-like model, *Sftpc*$^{-/-}$ mice, that lack surfactant protein C (SPC), to provide proof-of-principle for this approach.
Sftpc$^{-/-}$ mice were followed up to 12 months of age. They developed progressive interstitial lung disease with age and lack of SPC resulted in morphological and stereological changes of the lungs similar to histological patters observed in chILD.

We next explored whether bleomycin, a chemotherapeutic and radiomimetic agent, could be used to ablate endogenous ATII cells. We treated mice with 3 increasing doses of bleomycin. *Sftpc*$^{-/-}$ mice were more susceptible to bleomycin injury than *Sftpc*$^{+/+}$ and bleomycin depleted ATII cells in *Sftpc*$^{-/-}$ mice already at the lowest dose.

Finally, we investigated engraftment of ATII cells in bleomycin-treated *Sftpc*$^{-/-}$ mice. 4-, 8-, and 12-month-old *Sftpc*$^{-/-}$ mice were conditioned with low- or high-dose bleomycin and 10 days later received $1x10^6$ *Sftpc*$^{+/+}$ ATII cells i.t. We detected the higher number of transplanted *Sftpc*$^{+/+}$ cells in younger mice (4 and 8 months) compared to older mice (12 months) and after low compared to high bleomycin dose or vehicle. Transplanted ATII cells produced mature SPC and attenuated bleomycin-induced lung injury up to four months post-transplant.

In conclusion, our data demonstrates that partial replacement of mutant ATII cells can promote lung repair in *Sftpc*$^{-/-}$ mice. Our study lays the foundation for cell therapy in chILD, offering an alternative approach to lung transplantation.

Leveraging Imaging to Inform Molecular Subphenotypes of ARDS

Nadir Yehya, MD MSCE

Heterogeneity of critical illness syndromes, such as sepsis and acute respiratory distress syndrome (ARDS), has contributed to negative clinical trials, as therapies effective in some subtypes may be harmful in other subtypes (1). Prior attempts at subphenotyping ARDS have relied on clinical characteristics, such as direct (pulmonary) versus indirect (extra-pulmonary) inciting etiologies, or infectious (pneumonia or sepsis) versus non-infectious. Imaging has been proposed as a method to subphenotype ARDS, with a single trial testing the efficacy of standard lung-protective ventilation versus ventilator strategies personalized according to whether subjects had focal (consolidations only in the inferoposterior lung) or non-focal (diffuse pulmonary edema) on chest radiograph or computed tomography (CT)(2). However, clinical and radiographic subphenotyping is subject to high risk of misclassification, making this an imperfect solution for mitigating heterogeneity.

Biomarkers have also been proposed to mitigate heterogeneity in ARDS, with clustering methodology applied to combinations of clinical variables and biomarkers to identify subphenotypes (3). Secondary analyses of multiple ARDS trials and cohorts has consistently demonstrated the presence of two subphenotypes, dubbed hyper- and hypoinflammatory (3-6). Hyperinflammatory ARDS is characterized by higher levels of inflammatory biomarkers, more shock, and higher prevalence of sepsis. However, these subphenotypes are not specific for ARDS, and generalize to other critical illness syndromes (7, 8). However, molecular subphenotypes have not been systematically analyzed alongside imaging subphenotypes, and the degree of overlap is unknown.

Imaging in ARDS is often hampered by the degree of patient illness, limiting the frequency, type, and resolution of available imaging to inform care. The majority of imaging studies in ARDS have relied on (readily available and portable) plain radiographs and (snapshot in time) CTs. Advances in novel imaging technologies, such as dynamic chest radiography, electrical impedance tomography (EIT), and lung ultrasound can now provide viable portable alternatives, with longitudinal and spatial resolution, to fill in the gaps of plain radiographs and CT.

As a first step, biomarker-based subphenotypes should be thoroughly characterized using multimodal imaging, both at ARDS onset and longitudinally. Second, reproducible imaging characteristics can be used as inputs for future subphenotyping strategies, both alone and alongside biomarkers and clinical characteristics, in order to determine subtypes more specific to ARDS. Finally, some aspects of image analysis can be automated for real-time subphenotype determination in the electronic health record, helping operationalize these concepts for use in cohort recruitment, randomized trials, and eventually for clinical care.

References

1. Prescott HC, Calfee CS, Thompson BT, Angus DC, Liu VX. Toward Smarter Lumping and Smarter Splitting: Rethinking Strategies for Sepsis and Acute Respiratory Distress Syndrome Clinical Trial Design. Am J Respir Crit Care Med. 2016;194(2):147-55.
2. Constantin JM, Jabaudon M, Lefrant JY, Jaber S, Quenot JP, Langeron O, et al. Personalised mechanical ventilation tailored to lung morphology versus low positive end-expiratory pressure for patients with acute respiratory distress syndrome in France (the LIVE study): a multicentre, single-blind, randomised controlled trial. The Lancet Respiratory medicine. 2019;7(10):870-80.
3. Calfee CS, Delucchi K, Parsons PE, Thompson BT, Ware LB, Matthay MA, et al. Subphenotypes in acute respiratory distress syndrome: latent class analysis of data from two randomised controlled trials. The Lancet Respiratory medicine. 2014;2(8):611-20.
4. Famous KR, Delucchi K, Ware LB, Kangelaris KN, Liu KD, Thompson BT, et al. Acute Respiratory Distress Syndrome Subphenotypes Respond Differently to Randomized Fluid Management Strategy. Am J Respir Crit Care Med. 2017;195(3):331-8.
5. Calfee CS, Delucchi KL, Sinha P, Matthay MA, Hackett J, Shankar-Hari M, et al. Acute respiratory distress syndrome subphenotypes and differential response to simvastatin: secondary analysis of a randomised controlled trial. The Lancet Respiratory medicine. 2018;6(9):691-8.
6. Sinha P, Delucchi KL, Thompson BT, McAuley DF, Matthay MA, Calfee CS, et al. Latent class analysis of ARDS subphenotypes: a secondary analysis of the statins for acutely injured lungs from sepsis (SAILS) study. Intensive Care Med. 2018;44(11):1859-69.
7. Bhatraju PK, Zelnick LR, Herting J, Katz R, Mikacenic C, Kosamo S, et al. Identification of Acute Kidney Injury Subphenotypes with Differing Molecular Signatures and Responses to Vasopressin Therapy. Am J Respir Crit Care Med. 2019;199(7):863-72.
8. Wiersema R, Jukarainen S, Vaara ST, Poukkanen M, Lakkisto P, Wong H, et al. Two subphenotypes of septic acute kidney injury are associated with different 90-day mortality and renal recovery. Crit Care. 2020;24(1):150.

Friday

February 24th, 2023

Workshop: Day 2

Leveraging Novel Preclinical Models, Big Data Omics, and New Paradigms to Drive Discovery in Idiopathic Pulmonary Fibrosis

Michael F. Beers, M.D Perelman School of Medicine at The University of Pennsylvania

Despite considerable research effort and investment, median survival following a diagnosis of Idiopathic Pulmonary fibrosis (IPF) remains 3 to 5 years and has remained remarkably refractory to current "gold-standard" anti-fibrotic strategies (i.e., Pirfenidone; Nintedanib). The lack of preclinical model systems that effectively reproduce the pathologic features of human IPF and can also be exploited to assess drug efficacy is a significant impediment to the realization of clinical treatments stemming from basic IPF research. The most frequently used model to study IPF involves intratracheal delivery of the DNA-damaging agent bleomycin to mice. This model is characterized by widespread acute inflammation and rapidly forming fibrosis that spontaneously resolves. In stark contrast, human IPF is marked by the absence of overt inflammation and defined by non-resolving, progressive pathology classified as usual interstitial pneumonia (UIP). Other less commonly used animal models of IPF similarly reproduce some but not all disease features and the effects are often strain-specific. As such, there is a critical and unmet need for improved research tools and resources that facilitate the study of IPF and further the development and testing of novel therapeutics to treat this devastating disease.

The weight of current evidence suggests that the pathogenesis of IPF involves the aberrant intersection of diverse cellular and molecular pathways. Repetitive injury to a vulnerable alveolar epithelium is thought to initiate the processes that have been observed in the lungs of patients with mild to moderate IPF: increased apoptosis/senescence of the alveolar epithelium, localized proliferation of repair-associated myofibroblasts, and excess extracellular matrix including collagen deposition. Slowly over time and in association with the aging process, an accumulation of these events is believed to produce the histopathological features of advanced IPF, such as patchy subpleural and basilar-predominant interstitial thickening, fibroblastic foci, and cystic dilation of the alveoli and bronchioles that eventually lead to a progressive decline in lung function and clinically apparent symptoms. Studying the insidious onset of these wide-ranging pathological features is further complicated by spatial and temporal heterogeneity among fibrotic zones, with areas of normal lung architecture interspersed with regions of dense fibroblastic foci even within the same lobe.

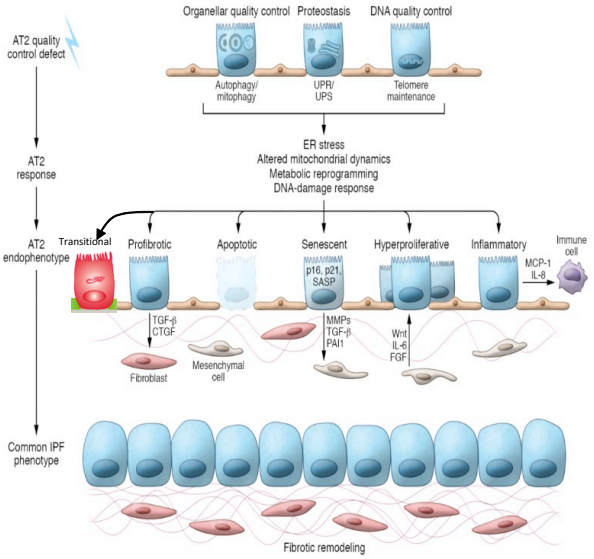

The identification of rare IPF associated genetic variants has provided valuable insight into cells and pathways that participate in fibrotic lung remodeling. Mutations in the alveolar epithelial type 2 cell (AT2) restricted Surfactant Protein C (SP-C) gene (*SFTPC*) have been identified in a subset of these patients. We described 2 major classes of disease-associated *SFTPC* mutations based upon AT2 stress phenotypes evoked by the mutant SP-C isoforms: (i) **"Trafficking"** mutants evoke lysosomal stress, and inhibit autophagy; (ii) misfolded, aggregation-prone **"BRICHOS"** mutants elicit endoplasmic reticulum (ER) stress and AT2 apoptosis. These findings, coupled with signatures of autophagy dysfunction and ER stress in the epithelium of patients with sporadic IPF, illustrate that AT2 centric pathways are capable of driving PF. As proof of concept, we then generated two novel knock-in murine models expressing either a trafficking (**SP-C^{I73T}**)[1] or a BRICHOS misfolding (**SP-C^{C121G}**) mutation[2]. Expression of either mutation in adult mice results in **spontaneous** fibrosis and recapitulation of many disease defining elements including: i) activation of lung tissue repair-associated pathways; ii) heterogeneous fibrotic histology with features of usual interstitial pneumonia; iii) restrictive lung physiology; iv) relevant IPF biomarkers (SP-D, Osteopontin, MMP7, CCL17, MCP-1).

As a preclinical platform these models have been successfully leveraged as a Discovery/ Target ID tool to explore multiple aspects of IPF pathogenesis including: (i) early immune cell (monocyte/macrophage) recruitment[3]; (ii) AT2 cell ER stress[2]; (iii) the emergence of a novel pathological AT2 derived transitional cell state[4]; (iv) AT2 metabolic reprogramming and mitochondrial dysfunction[5]. In preclinical testing, the *Sftpc* models also respond to standard of care "antifibrotics (e.g. Nintedanib) and have been utilized to index effect sizes of various therapeutic strategies including TGFB inhibition, prostaglandin signaling, and Unfolded Protein Response pathways. In summary, *Sftpc* mouse models offer an additional and disease relevant preclinical platform to explore IPF pathogenesis and therapeutic discovery.

References

1. Nureki SI, Tomer Y, Venosa A, et al. Expression of mutant Sftpc in murine alveolar epithelia drives spontaneous lung fibrosis. The Journal of Clinical Investigation 2018;128(9):4008-4024.
2. Katzen J, Wagner BD, Venosa A, et al. An SFTPC BRICHOS mutant links epithelial ER stress and spontaneous lung fibrosis. JCI Insight 2019;4(6). DOI: 10.1172/jci.insight.126125.
3. Venosa A, Cowman S, Katzen J, et al. Role of CCR2+ Myeloid Cells in Inflammation Responses Driven by Expression of a Surfactant Protein-C Mutant in the Alveolar Epithelium. Frontiers in Immunology 2021;12(1348) (Original Research) (In English). DOI: 10.3389/fimmu.2021.665818.
4. Katzen J, Rodriguez LR, Tomer Y, et al. Disruption of Proteostasis Causes IRE1 Mediated Reprogramming of Alveolar Epithelial Cells. Proceedings National Academy Sciences 2022;119.
5. Alysandratos K-D, Russo SJ, Petcherski A, et al. Patient-specific iPSCs carrying an SFTPC mutation reveal the intrinsic alveolar epithelial dysfunction at the inception of interstitial lung disease. Cell Reports 2021;36(9):109636.

Regional Patterns of Fibrosis, Gas Exchange and Perfusion in IPF Using Chest CT and MRI

Sean B. Fain, PhD

Departments of Radiology, Biomedical Engineering, Electrical and Computer Engineering, and Human Physiology,
University of Iowa

Hyperpolarized (HP) Xenon MRI can be used to measure the transfer of gas from the alveoli into the lung tissue and blood and has shown promise for characterizing regional pathophysiology in ILD [1] and progression in Idiopathic Pulmonary Fibrosis (IPF) [2]. Quantitative measures of lung perfusion using dynamic contrast enhanced (DCE) MRI have shown similar promise in IPF [2-5]. Here, we explore the regional relationship between HP Xe MRI of gas exchange and DCE MRI of perfusion in patients with IPF and how these patterns co-localize to fibrotic injury on chest CT.

At total of 5 participants were studied with spectroscopic HP Xenon imaging performed using a 1-pt Dixon sequence to estimate the regional uptake of Xenon into the lung tissue/plasma ("Membrane") and into the red blood cells ("RBC"). The ratio of these two measurements (RBC:Membrane) was used as a surrogate for gas exchange. Pulmonary blood flow (PBF), blood volume (PBV), and mean transit time (MTT) were calculated using indicator-dilution theory. Functional gas exchange and perfusion images were spatially registered using Advanced Normalization Tools (ANTs). The lung volume was sub-segmented into 12 components composed of Left/Right, Upper/Middle/Lower, and Anterior/Posterior regions. The median value of each metric was then calculated in each region for each subject. Regional correlations between gas exchange and perfusion estimates were calculated. Finally, a linear mixed effects model was used to account for the random effects between participants.

Significant and moderate regional correlations were found between RBC:Membrane and PBF (r = 0.44, *P*=5.7e-4), PBV (r = 0.42, *P*=8e-4), but not MTT (r = .11, *P*=0.42). Correlation analysis indicates some variability in the relationship between these metrics across the different participants. However, the linear mixed effect models show PBF and PBV remain strong explanators of RBC:Membrane (PBF: *P*=4.7e-4; PBV: *P*=6.7e-4), and similarly do not support an association of RBC:Membrane and MTT (*P*=0.41). In most cases texture analysis on chest CT indicates patterns of reduced RBC:Membrane and PBF that are regionally heterogeneous and are located in normal appearing, non-fibrotic lung (Figure).

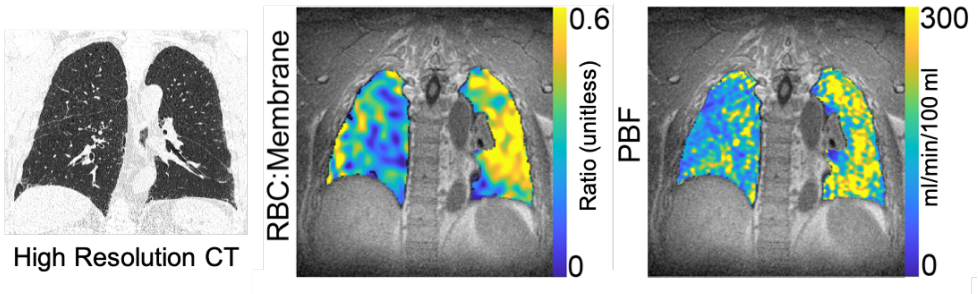

MRI based estimates of gas exchange made with HP Xenon MRI are moderately correlated regionally with both PBF and PBV in patients with IPF. Although a larger sample size is needed to confirm, the observed regional association of PBF and PBV, but not MTT, with the RBC:Membrane measure suggests patterns of pathophysiology in gas exchange on HP Xenon MRI may be due to the regional matching of pulmonary ventilation and pulmonary blood volume.

References

1. Mummy, D.G., et al., *Hyperpolarized (129)Xe MRI and Spectroscopy of Gas-Exchange Abnormalities in Nonspecific Interstitial Pneumonia.* Radiology, 2021. **301**(1): p. 211-220.
2. Hahn, A.D., et al., *Hyperpolarized (129)Xe MR Spectroscopy in the Lung Shows 1-year Reduced Function in Idiopathic Pulmonary Fibrosis.* Radiology, 2022. **305**(3): p. 688-696.
3. Weatherley, N.D., et al., *Quantification of pulmonary perfusion in idiopathic pulmonary fibrosis with first pass dynamic contrast-enhanced perfusion MRI.* Thorax, 2021. **76**(2): p. 144-151.
4. Montesi, S.B., et al., *Dynamic contrast-enhanced magnetic resonance imaging of the lung reveals important pathobiology in idiopathic pulmonary fibrosis.* ERJ Open Res, 2021. **7**(4).
5. Torres, L.A., et al., *Dynamic contrast enhanced MRI for the evaluation of lung perfusion in idiopathic pulmonary fibrosis.* Eur Respir J, 2022. **60**(4).

Molecular Imaging of Fibrosis and Fibrogenesis in ILD

Peter Caravan

There remains an unmet need for better methods to predict disease progression in interstitial lung disease and to monitor treatment response. Our lab has developed molecular MR and PET imaging probes, first to type I collagen, and then to oxidized collagen as quantitative markers of fibrosis and fibrogenesis.[1-4] In animal models we have shown that the collagen-targeted PET probe ^{68}Ga-CBP8 is specific for fibrosis and that probe uptake in the lung correlates strongly with the collagen concentration in the lungs in both a murine model of pulmonary fibrosis (r^2 = 0.93) and in explanted human lungs from IPF patients (r^2 = 0.94).[1] We have also been developing PET and MR probes that bind to allysine, an amino acid side chain formed by the action of lysyl oxidase enzyme on collagen and other matrix proteins. These probes show promise in monitoring disease activity and in distinguishing active fibrosis from stable scar.

We performed the first-in-human studies of ^{68}Ga-CBP8 PET-MRI in healthy volunteers (n = 4) and subjects with IPF (n = 9) and showed that this probe detects increased lung collagen in IPF subjects.[2] Here we will describe our continued work with ^{68}Ga-CBP8 PET-MRI in IPF subjects and in non-IPF ILD subjects. Our preliminary data indicates that ^{68}Ga-CBP8 lung uptake can predict 12 month change in pulmonary function tests like change in forced vital capacity.

We have also been exploring the potential of dynamic contrast enhanced MRI to characterize ILD and predict disease progression.[5] In a study comparing DCE-MRI in IPF subjects and healthy volunteers we found that DCE measures of perfusion could distinguish the two groups. Interestingly the rate of contrast washout from the lung appears to predict outcome in the IPF group with rapid progressors exhibiting markedly slower tissue washout. Taken together these molecular and functional lung imaging approaches show promise in improving prognostication in ILD.

1. Désogère P, Tapias LF, Hariri LP, Rotile NJ, Rietz TA, Probst CK, Blasi F, Day H, Mino-Kenudson M, Weinreb P, Violette SM, Fuchs BC, Tager AM, Lanuti M, Caravan P. Type I collagen–targeted PET probe for pulmonary fibrosis detection and staging in preclinical models. Sci. Transl. Med. 2017 Apr 5;9(384). pii: eaaf4696.
2. Montesi SB, Izquierdo-Garcia D, Désogère P, Abston E, Liang LL, Digumarthy S, Seethamraju R, Lanuti M, Caravan P, Catana C. Type I Collagen-Targeted PET Imaging in Idiopathic Pulmonary Fibrosis: First-in-Human Studies. Am J Resp Crit Care Med. 2019;200(2):258-261.
3. Chen HH, Waghorn PA, Wei L, Tapias LF, Schühle DT, Rotile NJ, Jones CM, Looby RJ, Zhao G, Elliott JM, Probst CK, Mino-Kenudson M, Lauwers GY, Tager AM, Tanabe KK, Lanuti M, Fuchs BC, Caravan P. Molecular imaging of oxidized collagen quantifies pulmonary and hepatic fibrogenesis. JCI Insight. 2017 Jun 2;2(11). pii: 91506.
4. Ning Y, Zhou IY, Roberts Jr JD, Rotile NJ, Akam E, Barrett SC, Sojoodi M, Barr MN, Punshon T, Pantazopoulos P, Drescher H, Jackson BP, Tanabe KK, Caravan P. Molecular MRI quantification of extracellular aldehyde pairs for early detection of liver fibrogenesis and response to treatment. Sci Trans Med. 2022;14(663): eabq6297.
5. Montesi SB, Zhou I, Liang LL, Digumarthy SR, Mercaldo S, Mercaldo N, Seethamraju RT, Rosen B, Caravan P. Dynamic contrast-enhanced magnetic resonance imaging of the lung reveals important pathobiology in idiopathic pulmonary fibrosis. ERJ Open Research 2021;7:00907-2020.

Unsupervised Machine Learning of Quantitative CT Emphysema Subtypes

R Graham Barr, MD DrPH
Columbia University Medical Center

Treatment advances for chronic obstructive pulmonary disease (COPD) have been slowed due, in part, to limited subphenotypes. New subphenotypes, for example learned on massive data in research computed tomographic (CT) scans, might provide more specific targets for personalized therapies. We hypothesized that large-scale unsupervised machine learning on CT images would discover CT emphysema subtypes.

New CT emphysema subtypes were identified using unsupervised machine learning on the texture and location of emphysematous regions on CT scans from 2,853 participants in the Subpopulations and Intermediate Outcome Measures in COPD Study (SPIROMICS), a COPD case-control study, followed by data reduction. Subtypes were compared to symptoms and physiology among 2,949 participants in the population-based Multi-Ethnic Study of Atherosclerosis (MESA) Lung Study, which acquired lung CTs following the SPIROMICS protocol. Prognosis and incident COPD were examined among 6,658 MESA participants followed for up to 18 years with baseline cardiac scans, which were labeled using a deep-learned algorithm. Structure of CT emphysema subtypes was assessed using hyperpolarized ^{3}He MRI with co-registration to CT scans. Associations with genome-wide single-nucleotide-polymorphisms were examined.

The algorithm discovered six CT emphysema subtypes with a high degree of reproducibility of learning at regional and subject levels. The most common subtype in SPIROMICS, the *combined bronchitis-apical emphysema* subtype, was associated with chronic bronchitis, accelerated lung function decline, hospitalizations, deaths, and incident airflow limitation. The second, the *diffuse* subtype was associated with lower weight, respiratory hospitalizations and deaths, and incident airflow limitation. The *senile* subtype was associated with age only. The fourth and fifth visually resembled *combined pulmonary fibrosis emphysema* and had distinct symptoms, physiology, and prognosis. The sixth visually resembled *vanishing lung* syndrome. Lung microstructure, assessed by apparent diffusion capacity (ADC) varied by CT emphysema subtype. Regional heterogeneity of PAO_2 and ventilation defects were increased in lung regions labeled as *combined bronchitis-apical emphysema* and *vanishing lung* subtypes compared to normal lung. There were distinct, replicated, biologically relevant genetic associations for three subtypes.

Large-scale unsupervised machine learning on CT scans defined six reproducible and familiar CT emphysema subtypes with distinct symptomatology, prognoses, genetic associations and lung microstructure. Quantitative CT emphysema subtypes suggest paths to more specific diagnosis and personalized therapies in COPD and preCOPD.

Funding: NIH/NHLBI R01-HL121700, R01-HL076612, R01-HL093081

AI in Chest Imaging: From Detection to Prediction

Joon Beom Seo

Recently application of artificial intelligence, particularly deep learning algorithm has opened the new chances of use of chest imaging in clinical practices. From early stage, many researches has focused on applying AI in interpretation of chest radiographs and chest CT particularly lung cancer screening setting, because those are typical labor intensive task requiring expert radiologists. Many studies have proved that deep learning is very useful in this task of detecting various disease patterns on chest radiographs and detecting lung nodules on chest CT. In addition many studies have shown that it is also useful in classifying disease, such as determination of likelihood of malignancy of detected lung nodules.

Although detection and diagnosis of disease is important clinical task in chest radiology, there are multiple clinical works in practice, which can be improved by using AI. For example many technical obstacles of using quantitative lung imaging analysis can be overcome by using deep learning technology. In addition, deep learning method can provide novel information which was not possible before. For example, by using quantitative assessment and deep learning algorithm, retrieval of cases of similar imaging pattern is possible from the imaging database, which will help correct diagnosis of disease, choice of right treatment options by reviewing similar chases and so on. Secondly, image based prediction of disease progression of interstitial lung disease, genetic mutation of lung cancer, survival of patients is possible, which will be useful in choice of treatment. Finally, novel additional information of patients can be extracted from the image, for example predictive value of FVC or FEV1 from chest CT to be used for screening purposes to triage patients of early stage of decreased lung function requiring PFT examination.

With further researches and development, AI will be useful tool of chest imaging practice, improving quality of care and expanding indication of imaging beyond simple detection of abnormalities.

1. Choe J, Lee SM, Do KH, Kim S, Choi S, Lee JG, Seo JB. Outcome prediction in resectable lung adenocarcinoma patients: value of CT radiomics. Eur Radiol. 2020 Sep;30(9):4952-4963
2. Choe J, Lee SM, Kim W, Do KH, Kim S, Choi S, Seo JB. CT radiomics-based prediction of

anaplastic lymphoma kinase and epidermal growth factor receptor mutations in lung adenocarcinoma. Eur J Radiol. 2021 Jun;139:109710

3. Yun J, Cho YH, Lee SM, Hwang J, Lee JS, Oh YM, Lee SD, Loh LC, Ong CK, Seo JB, Kim N. Deep radiomics-based survival prediction in patients with chronic obstructive pulmonary disease. Sci Rep. 2021 Jul 26;11(1):1

4. Choe J, Lee SM, Hwang HJ, Lee SM, Yun J, Kim N, Seo JB. Artificial Intelligence in Lung Imaging. Semin Respir Crit Care Med. 2022 Dec;43(6):946-960. doi: 10.1055/s-0042-1755571. Epub 2022 Sep 29. PMID: 36174647

Estimating CT Biomarkers of Lung Disease Using Deep Learning

Joseph M. Reinhardt, PhD

Purpose: Inspiratory-expiratory CT image pairs can be used to characterize lung disorders such as COPD. Emphysematous regions can be identified on the inspiratory scan, air trapping regions can be detected on the expiratory scan, and by registering the inspiratory and expiratory images, functional small airways disease (fSAD), local lung volume change, and biomechanical parameters can be computed. However, acquiring multiple CT images increases time, cost, and radiation dose. We describe a deep-learning approach that can directly estimate multi-volume, lung biomarkers from a single inspiratory CT image.

Methods: Our approach uses a style-based generative adversarial network called Lung2Lung for translating CT images from end-inspiratory to end-expiratory volume. The input to the network is a CT image at inspiration and the network synthesizes the corresponding expiratory image. The expiratory image is created in the shape of the inspiratory image, so effectively, the two images are in registration and local lung volume change and parametric response mapping biomarkers can be directly computed.

The network is trained and evaluated using CT data from a diverse set of 1567 subjects in the SubPopulations and Intermediate Outcome Measures in COPD Study (SPIROMICS). Subjects from all GOLD stages and non-smokers were included. Each subject in SPIROMICS had total lung capacity (TLC) and residual volume (RV) scans at baseline. The TLC and RV scans were registered using a mass preserving B-spline-based lung registration method. The CT data was split into training and testing subgroups, with 1055 subjects used for training and 512 subjects used for testing. Lung2Lung was implemented using the open-source PyTorch framework and was trained on a single NVIDIA RTX8000 GPU. Training time was approximately 72 hours with a batch size of four.

Results: After training, the network can synthesize an artificial expiratory image from a real inspiratory image in about 40 seconds. In the testing subgroup, air trapping estimated from the synthetic RV image was close to the ground truth values; the average Lung2Lung estimate of air trapping was 24.2% vs. 25.5% ground truth. The average PRM fSAD estimate using the Lung2Lung RV image was 15.4% vs 17.4% fSAD using the actual RV image.

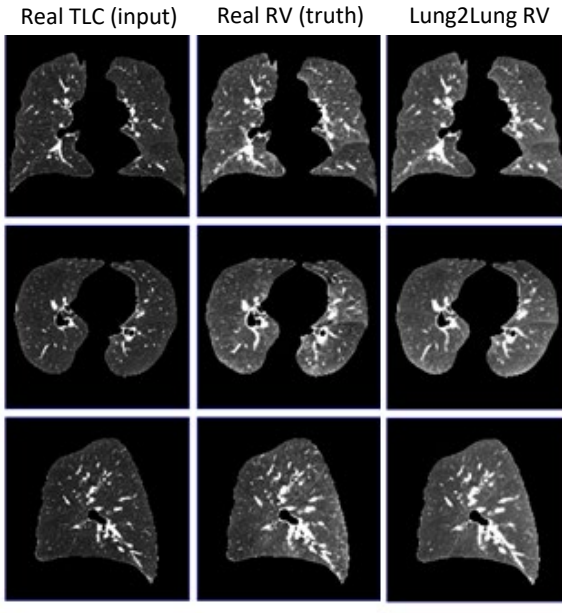

Summary: A generative adversarial network called Lung2Lung was trained to synthesize expiratory CT images from an inspiratory scan, thus allowing estimates of air trapping, fSAD, and local volume change. Lung2Lung can enable air trapping, fSAD, and lung volume change analysis in existing data sets that only contain inspiratory images, and reduce time, cost, and radiation dose by allowing new studies to collect only inspiratory scans. The biomarker estimates derived from the Lung2Lung synthetic expiration image match closely with ground truth data in the COPD subjects in SPIROMICS. It may be possible to extend this approach to other image translation tasks, such as estimating a hyperpolarized gas images directly from a CT image or proton MRI image.

Assessments of Emphysema and Pulmonary Fibrosis on CT Using Deep Learning

Stephen Humphries

CT plays an essential role in the evaluation of patients with diffuse lung disease. Capitalizing on the inherent tissue contrast of aerated lung, CT captures the presence, pattern, and extent of phenotypic abnormalities associated with chronic obstructive pulmonary disease (COPD) and various forms of interstitial lung disease (ILD). However, visual assessment of images is limited by interobserver variation and is often considered insufficiently precise for longitudinal evaluation. Deep learning (DL) has been successful in a wide range of challenging image analysis tasks including segmentation, pattern classification and quantification and has provided improved tools for objective assessments of emphysema and pulmonary fibrosis on CT.

We developed a DL model, consisting of convolutional neural network (CNN) and long-short term memory (LSTM) components, capable of automatic classification of CT emphysema severity according to the Fleischner Society scoring system[1]. We used the CNN-LSTM to classify emphysema at baseline and 5-year follow-up in n=5056 participants in the COPDGene study and showed that 26% (n=1293) had an increase in emphysema grade at 5 years. These inviduals had progressive airflow obstruction, greater decline in 6-minute walk distance, and greater progression in emphysema extent (based on CT lung densitometry) than those with nonprogressive emphysema. Further, emphysema progression was associated with increased mortality[2].

In separate work we developed DL methods for detection and quantification of fibrotic abnormality on CT. In multiple independent cohorts of patients with pulmonary fibrosis we have shown that extent of fibrosis, measured objectively at baseline CT using DL, is associated with disease progression and mortality, independent of pulmonary function[3]. DL is also capable of detecting clinically significant early fibrotic abnormality in patients at risk of developing fibrotic ILD. In separate cohorts we showed that DL-based fibrosis extent score was associated with lower lung function, more breathlessness and poorer survival, suggesting that DL may be more sensitive than visual assessment for identifying early lung abnormalities[4], [5].

DL enables enhanced, objective assessments of chest CT that can provide clinically meaningful markers of severity and progression of emphysema and pulmonary fibrosis.

References

[1] S. M. Humphries *et al.*, “Deep Learning Enables Automatic Classification of Emphysema Pattern at CT,” *Radiology*, vol. 294, no. 2, pp. 434–444, Feb. 2020, doi: 10.1148/radiol.2019191022.

[2] A. S. Oh *et al.*, “Emphysema Progression at CT by Deep Learning Predicts Functional Impairment and Mortality: Results from the COPDGene Study,” *Radiology*, vol. 304, no. 3, pp. 672–679, Sep. 2022, doi: 10.1148/radiol.213054.

[3] S. M. Humphries *et al.*, “Quantitative computed tomography predicts outcomes in idiopathic pulmonary fibrosis,” *Respirol. Carlton Vic*, vol. 27, no. 12, pp. 1045–1053, Dec. 2022, doi: 10.1111/resp.14333.

[4] S. M. Matson *et al.*, “Prospective Identification of Subclinical Interstitial Lung Disease in a Rheumatoid Arthritis Cohort Is Associated with the MUC5B Promoter Variant,” *Am. J. Respir. Crit. Care Med.*, vol. 205, no. 4, pp. 473–476, Feb. 2022, doi: 10.1164/rccm.202109-2087LE.

[5] M. P. Steele *et al.*, “Incidence and Progression of Fibrotic Lung Disease in an At-Risk Cohort,” *Am. J. Respir. Crit. Care Med.*, Sep. 2022, doi: 10.1164/rccm.202206-1075OC.

Recent Advances in Assessing Vascular Morphology and Perfusion in Pulmonary Vascular Disease

Raul San Jose Estepar, Ph.D.

The pulmonary vasculature is the primary system coupling the lungs with the heart and is directly involved in the gas exchange. Pulmonary Vascular Disease is a broad term that refers to multiple conditions affecting the lungs. From Pulmonary Hypertension (PH) to vascular remodeling and injury due to chronic lung disease, changes affecting the pulmonary vasculature play a fundamental role in the etiology of multiple pathological conditions of the lung.

Among the imaging technologies that target the lung, imaging of pulmonary vascular structural complexity using X-ray computed tomography has been empowered by recent advances in computational imaging and deep learning [1]. Emerging approaches to segment, classify and resolve small vessels at the limit of the resolution are enabling end-to-end automatic imaging phenotyping of pulmonary vascular disease [2,3]. During this talk, we will review some of those advances propelling the clinical utilization of quantitative imaging of the lung vasculature. We will overview the relevant vascular metrics proposed to characterize vascular remodeling and pruning and present some recent studies showing the impact of quantifying small arterial and venous simplification in relation to COPD and PH [4,5].

Finally, we will briefly overview some of the upcoming advances in characterizing microvasculature and perfusion from single, dual, and multispectral CT imaging using photon counting technology that can address some imaging gaps at the alveolar level.

Reference

1. Harder EM, Vanderpool R, Rahaghi FN. Advanced Imaging in Pulmonary Vascular Disease. Clin Chest Med. 2021 Mar;42(1):101-112.

2. Nardelli P, Jimenez-Carretero D, Bermejo-Pelaez D, Washko GR, Rahaghi FN, Ledesma-Carbayo MJ, San Jose Estepar R. Pulmonary Artery-Vein Classification in CT Images Using Deep Learning. IEEE Trans Med Imaging. 2018 Nov;37(11):2428-2440.
3. Nardelli P, Ross JC, San José Estépar R. Generative-based airway and vessel morphology quantification on chest CT images. Med Image Anal. 2020 Jul;63:101691
4. San José Estépar R, Kinney GL, Black-Shinn JL, Bowler RP, Kindlmann GL, Ross JC, Kikinis R, Han MK, Come CE, Diaz AA, Cho MH, Hersh CP, Schroeder JD, Reilly JJ, Lynch DA, Crapo JD, Wells JM, Dransfield MT, Hokanson JE, Washko GR; COPDGene Study. Computed tomographic measures of pulmonary vascular morphology in smokers and their clinical implications. Am J Respir Crit Care Med. 2013 Jul 15;188(2):231-9.
5. Rahaghi FN, Nardelli P, Harder E, Singh I, Sánchez-Ferrero GV, Ross JC, San José Estépar R, Ash SY, Hunsaker AR, Maron BA, Leopold JA, Waxman AB, San José Estépar R, Washko GR. Quantification of Arterial and Venous Morphologic Markers in Pulmonary Arterial Hypertension Using CT Imaging. Chest. 2021 Dec;160(6):2220-2231.

Denoising Diffusion-Weighted Hyperpolarized ^{129}Xe Images with Patch-Based Higher-Order Singular Value Decomposition

Stephanie A. Soderlund[1], Abdullah S. Bdaiwi[1], Joseph W. Plummer[1,2], Jason C. Woods[1], Laura L. Walkup[1,2], Zackary I. Cleveland[1,2]
[1]Center for Pulmonary Imaging Research, Division of Pulmonary Medicine, Cincinnati Children's Hospital Medical Center, Cincinnati, OH 45229,
[2]Department of Biomedical Engineering, University of Cincinnati, Cincinnati, OH 45221

Purpose: Gas exchange is limited by the surface area provided by alveolar microstructure, making the dimensions of acinar units of fundamental interest. Hyperpolarized (HP) ^{129}Xe MRI, when combined with diffusion encoding, provides a powerful and non-invasive method to probe these dimensions. Within the acini, collisions with the alveolar walls restrict ^{129}Xe motion, resulting in an apparent diffusion coefficient (ADC) that is reduced relative to free diffusion. When alveolar compliance and elastance are disrupted (e.g., by disease processes such as emphysema), ADC increases. Thus, HP ^{129}Xe ADC has been used to evaluate lung disease severity in a range of disorders, including chronic obstructive pulmonary disease (COPD) and lymphangioleiomyomatosis (LAM).(1) However, diffusion is negative form of image contrast (i.e., contrast is generated by decaying signal as a function of diffusion weighting) and HP gas ADC measurements are biased by low signal-to-noise (SNR).(2) In many regions of clinical importance—cysts in LAM or bullae in COPD—ventilation is reduced, resulting in lower ^{129}Xe signal due to gas dilution and elevated ADC.(3) Thus, ADC accuracy is lowest in regions where clinical value is greatest. Here, we seek to increase SNR across diffusion weightings (b values) and improve ADC estimates via patch-based Global-Local Higher-Order Singular Value Decomposition (GLHOSVD) denoising.(4) GLHOSVD was validated in simulated and physical free-diffusion phantoms with known ADC values and then applied in-vivo in four subject cohorts (healthy, cystic fibrosis [CF], asthma, and LAM).

Methods: Patients with CF (N=39, age=14.9±8.9 years, range=6-37), asthma (N=19, age=14.1±7.9 years, range=7-45), LAM (N=27, age=45.7±10.3 years, range=25-64), and healthy controls (N=38 age=17.9±11.2 years, range=6-40) underwent diffusion-weighted ^{129}Xe MRI under FDA and IRB approved protocols after obtaining informed consent (adults and parents) or age-appropriate ascent (children). HP ^{129}Xe was polarized to 15-40% (Polarean, PLC; Model 9820A). Images were acquired during ≤16s breath-holds (^{129}Xe dose=1/6th total lung capacity up to 1L) with a 3T Philips Achieva or Ingenia scanner [resolution=5×5 mm^2, BW=264.8 Hz/pixel, TE=2.9 ms, TR=6.1 ms, FOV=250-350 mm, 3-8 slices, slice thickness=15 mm, b = (0, 6.25, 12.5, 18.75, 25) s/cm^2]. Images were reconstructed and processed in MATLAB (Mathworks) before denoising using GLHOSVD. Briefly, the algorithm first applies a global smoothing filter (k_{global}) across all the images. Voxels are then binned into patches of a designated size (patch), grouped based on signal within applied search windows (SW) that move with a specified step size (step), and finally filtered on a local level (k_{local}).(4) GLHOSVD parameters included: k_{global}=0.4, k_{local}=0.8, step=2, patch=6, and SW=12. A variance stabilizing transformation was applied to magnitude data before GLHOSVD to generate Gaussian rather than Rician-distributed noise, and the inverse transformation was applied to restore the data afterwards.(5) ADC was calculated by weighted linear fitting. Differences before/after denoising were assessed via Wilcoxon signed-rank tests.

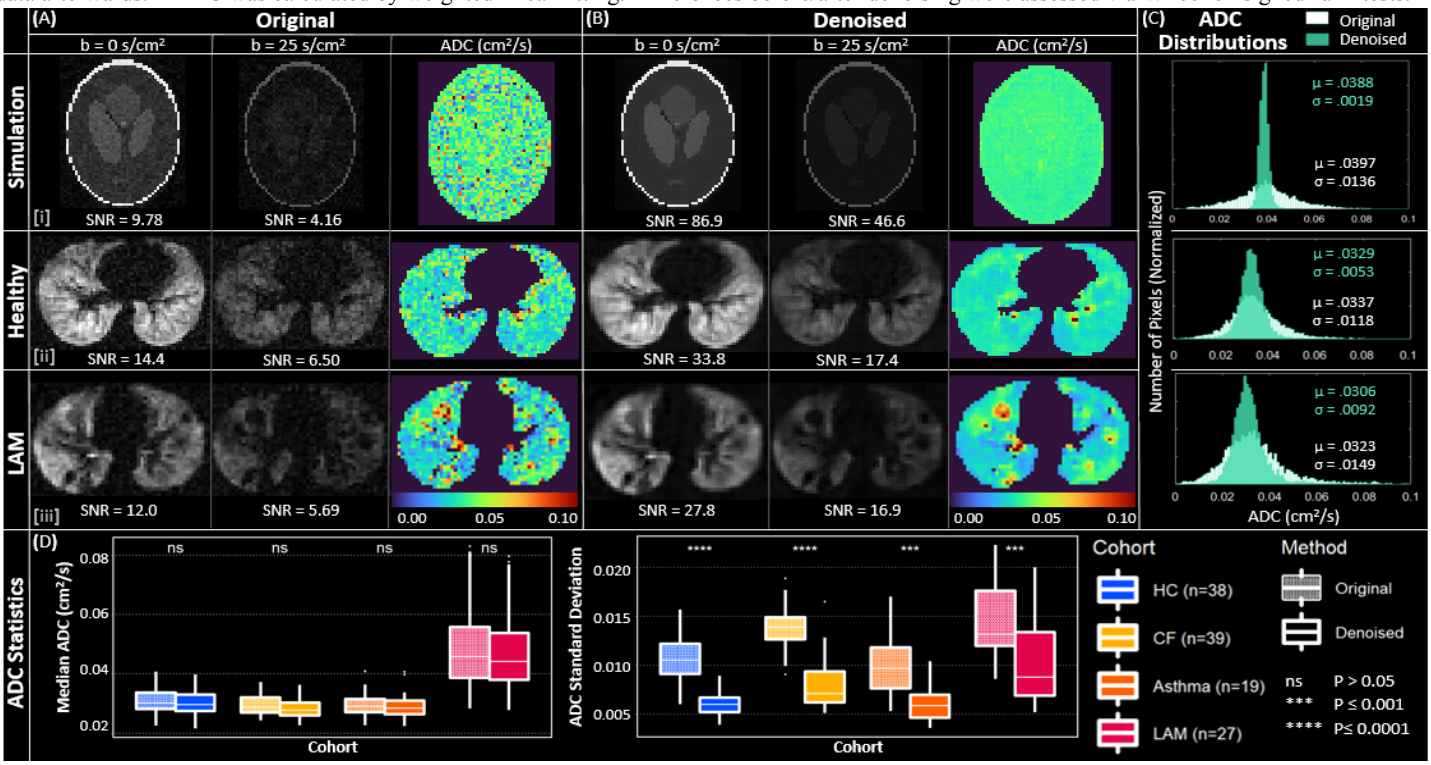

Fig 1. **(A)** Diffusion-weighted images with corresponding ADC maps before **(A)** and after **(B)** GLHOSVD denoising for a **(i)** Shepp-Logan simulated phantom (ADC=0.04), **(ii)** healthy control (HC), age=20, and **(iii)** LAM patient, age=25. **(C)** ADC histograms of all voxels before (***white***) and after (***green***) denoising with ADC median (μ) and standard deviation (σ) provided. **(D)** Boxplots showing no significant change in median ADC (***left***) but significant reductions in the ADC standard deviation (***right***) after denoising.

Results & Discussion: GLHOSVD effectively increased the SNR across diffusion images by 156 ± 98% with the greatest relative increases observed in the highest b values originally suffering the lowest signal. For example, a nearly a three-fold increase in SNR was observed (5.69 to 16.9) in the in vivo b=25 s cm^{-2} images shown in Figure 1. There was no significant difference in the median ADC ($p \geq 0.05$), but significant reductions in the ADC standard deviation ($p < 0.001$) after denoising—often by >50%. These metrics indicate that GLHOSVD improves the precision—and therefore physiological relevance—of ADC measurements without compromising accuracy.

Conclusions: When applied to diffusion HP ^{129}Xe imaging, GLHOSVD denoising generates more precise ADC measurements—particularly in lung regions with low SNR. Improved precision thus increases the utility of ^{129}Xe ADC measurements for assessing microstructural changes in the lungs.

References: [1] Walkup LL, Woods JC. NMR in Biomed 2014;27(12):1429-1438. [2]O'Halloran RL, et al., JMR (1997) 2007;185(1):42-49. [3]Walkup LL, et al., AnnalsATS 2019;16(8):1008-1016. [4]Kim Y., et al., MRM 2021; 86(5):2497-2511. [5]Azzari L. & Foi A. IEEE Signal Proces (2016); 23(8):1086-1090.

Time-resolved dynamic lung water magnetic resonance imaging during exercise stress

Felicia Seemann PhD, Ahsan Javed PhD, Jaffar M Khan BM BCh PhD, Christopher G Bruce MBChB, Rachel Chae, Korel Yildirim PhD, Amanda Poternak RT(MR), Haiyan Wang RT(MR), Scott Baute PA-C, Rajiv Ramasawmy PhD, Robert J Lederman MD, Adrienne E Campbell-Washburn PhD
Cardiovascular Branch, Division of Intramural Research, National Heart, Lung, and Blood Institute, National Institutes of Health, Bethesda MD, USA

Purpose: Exertional dyspnea caused by accumulation of lung water is an early symptom of heart failure. Quantification of lung water dynamics during exercise stress is therefore of interest to unmask latent heart failure[1]. In this study, we develop a continuous 3D magnetic resonance imaging (MRI) method to quantify lung water dynamics between rest and exercise stress.
Methods: Free-breathing data was acquired at 0.55T[2] using a continuous 3D stack-of-spirals proton density weighted MRI sequence with isotropic resolution[3]. Time-resolved images were derived using a motion compensated sliding-window reconstruction with 90s temporal resolution and 20s temporal increment. The method was evaluated in a porcine model of dynamic lung water accumulation through mitral regurgitation (n=5), and in 15 healthy subjects and 2 patients with compensated heart failure imaged in transitions between rest and exercise stress. A supine MRI-compatible pedal ergometer was used for exercise. Time-resolved global and regional lung water density (LWD) and percent change in LWD (ΔLWD), and accumulation rates dLWD/dt were quantified using an automated pipeline[4] (Fig 1). The measured LWD were corroborated with cardiac output by phase contrast MRI. Pulmonary arterial wedge pressure (PAWP) was measured simultaneously to imaging in pigs.
Results: An increase in LWD was observed in conjunction with induction of lung water in all pigs, with a peak lung water accumulation rate of 1.01±0.81%/min. Over the course of 10 minutes ΔLWD increased by 3.3±1.5%, from 0.34±0.05 L to 0.35±0.05 L of lung water volume, p=0.02. PAWP increased by 6.6±3.1 mmHg (101±112%, p=0.009), and cardiac output decreased by -28±15%, from 3.7±0.7 L/min to 2.6±0.8 L/min (p=0.01), suggesting that measured ΔLWD was predominantly extravascular (Fig. 2). Healthy subjects developed a ΔLWD of 7.8±5.0% during moderate exercise, peaked at 16±6.8% during vigorous exercise, and remained unchanged over 10 minutes at rest (-1.4±3.5%, p=0.18). Cardiac output increased from 4.5±1.5 L/min at rest to 7.5±2.6 L/min at moderate exercise, p=0.0004. Regional LWD were higher posteriorly compared the anterior lungs (rest: 33±3.7% vs 20±3.1%, p<0.0001; peak exercise: 36±5.5% vs 25±4.6%, p<0.0001). Patient and healthy subject LWD were similar at rest (28±10% and 28±2.9%), respectively, as was peak vigorous ΔLWD (17±10% vs 16±6.8%) (Fig 3). Accumulation rates were slower in patients than in healthy subjects (2.0±0.1%/min vs 2.6±0.9%/min).
Discussion: This study presents a continuous MRI method which was capable of depicting and quantifying LWD dynamics in a controlled porcine lung water model, and in healthy subjects and heart failure patients during supine exercise stress. The 3D images have isotropic resolution, allowing re-slicing in any orientation. The method does, however, not distinguish between intravascular and extravascular fluid and the measured LWD-increase in healthy subjects is attributed to an exercise-induced increase in intravascular lung fluid. We hypothesize that the predominant posteriorly accumulated LWD, but higher anterior ΔLWD-increase, reflects a global increase in pulmonary perfusion during exercise. Additional patient studies are warranted to determine if this method can unmask latent heart failure, where an extravascular lung water accumulation is expected, in line with the pig model results where the LWD increased despite a decrease in cardiac output.
Conclusion: Dynamic changes in LWD can be quantified during exercise using a continuous 3D acquisition and a sliding-window, motion compensated image reconstruction.

.

References. 1. Thompson et al, JCMR 2019; 2. Campbell-Washburn et al, Radiology 2019; 3. Javed et al, MRM 2022; 4. Seemann et al, JCMR 2022.

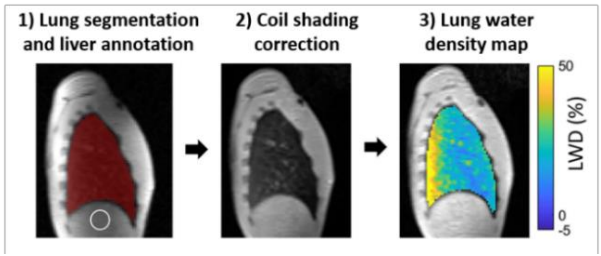

Figure 1. Illustration of image processing steps in a sagittal slice. 1) Automated lung segmentation (red mask) and liver annotation (white) used for quantitative purposes. 2) Coil shading correction. 3) Derivation of quantitative lung water density (LWD) maps.

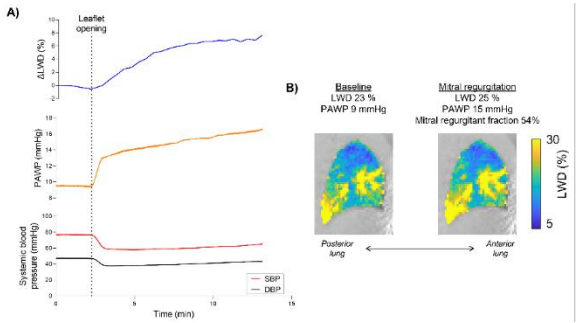

Figure 2. A) Example of concurrent increase in lung water density (ΔLWD) and PAWP, and decrease in SBP and DBP upon induction of mitral regurgitation in a porcine model. B) Lung water density maps in a sagittal slice at baseline and after 10 mins of mitral regurgitation.

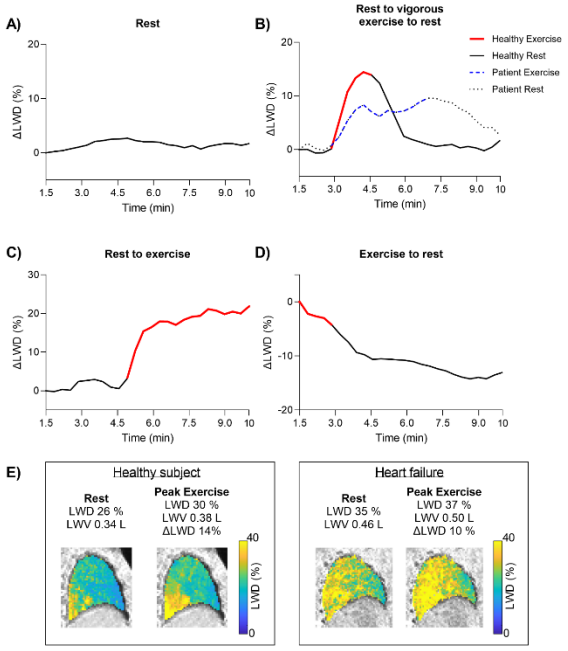

Figure 3. Changes in lung water density (ΔLWD) in a heathy subject (solid line) and a patient with heart failure (dashed line) at rest (black) and exercise stress (red). A) ΔLWD at rest. B) ΔLWD starting at rest, followed by vigorous exercise targeting maximum heart rate, and then rest again. C) ΔLWD at rest, followed by exercise. D) Dynamic ΔLWD starting at moderate exercise then rest. E) LWD-maps in a sagittal slice at rest and after 10 minutes of moderate exercise in a healthy subject and a patient with heart failure. LWV, lung water volume.

3D Quantification of Clustered Lung Volume Defects in Different Lung Diseases Utilizing Hyperpolarized Gas MR Images

Garcia Delgado, Gabriela M[1], Shammi, Ummul Afia[1], Altes, Talissa[2], Mugler III, John P[3, 4], Thomen, Robert P[1, 2]

[1] Biomedical, Biological, and Chemical Engineering, University of Missouri, Columbia, MO 65201
[2] Radiology, School of Medicine, University of Missouri, Columbia, MO 65201
[3] Radiology and Medical Imaging, School of Medicine, University of Virginia, Charlottesville, VA 22908
[4] Biomedical Engineering, University of Virginia, Charlottesville, VA 22908

Purpose: In this study, we developed a 3D cluster quantification algorithm that was used to compare the spatial distribution of defects in hyperpolarized gas magnetic resonance images of subjects with asthma, cystic fibrosis, and chronic obstructive pulmonary disease.

Introduction: Hyperpolarized gas MR imaging (HPG) is a non-ionizing tool that demonstrates lung function and structure with regional specificity which allows for the quantification of a patient's lung volume that is poorly ventilated: a ventilation defect percentage (VDP)[1]. Although informative, VDP does not provide information regarding spatial distribution information of defects which could reflect underlying pathophysiology of lung disease. For example, small vs large, localized defect patterns may reflect the relative contributions of small vs large airways to disease presentation. Expanding on an approach introduced by Valk et al.[2], we have developed an algorithm that quantifies the relative spatial congregation of defect voxels within the lung. This algorithm returns a patient's whole-lung clustering index (CI): sparser defects yield low CI, more focal defects yield high CI. We hypothesized that lung CI may provide valuable spatial information related to lung disease where VDP is uninformative. We compared CIs among different lung diseases with their corresponding VDP.

Methods: The CI algorithm (Figure 1a) inputs a 3D binary array of defect voxels calculated from subject's HPG images (60% of mean as defect threshold). At each identified defect voxel, a sphere was expanded until the quantity of defect voxels within the sphere was less than 50% of the total voxels inside the sphere. The final sphere volume was then recorded as the cluster value (CV) for the active voxel; the process was repeated for all defect voxels. Voxel CVs were normalized to the subject's total lung volume, and the 95th percentile CV value was returned as the subject's whole-lung CI. Artificial defect arrays of 100 binary dense and scattered spherical defects with radii of 3 to 14 voxels were created to assess and confirm accurate results are returned (max CV value for sphere = $2^{1/3}$R). CI analysis was then performed on 16 sets of HPG images in subjects with asthma and cystic fibrosis (CF) (mean age 46.4± 18.7): 2D multi-slice GRE[3] (Figure 3a, b): TR=9.7-12 ms, TE=1 ms, flip angle=9-11°, voxel size=2.5-3.9 mm in-plane, 15 mm slice thickness, bandwidth of 170-391 Hz/pixel.

Results: Linear regression of maximum CI for synthesized defect arrays of dense spheres a slope of $\sqrt[3]{2}$ (m = 1.25) as excepted, while the slope of the scattered defects had a lower, but linear, slope (m = 0.7053). Example HPG images and CI maps from 3 subjects are presented in Figure 1b where similarities and differences in VDP and CI are observed. Pearson correlation coefficients between CI and VDP were r = 0.4492 (p=0.0809) when evaluated through all 16 subjects. Example HPG images and CI maps of 3 subjects with corresponding VDP and CI are found in Figure 1b. A scatterplot of all subjects and their corresponding CI versus VDP is found in Figure 1c.

Discussion: As seen in Figure 1b, subjects with similar VDP values (~5.9%) can have CI differences: 0.35% in Subject 1, 2.37% in Subject 2. Additionally, subjects with higher VDP (14.14%) values can also have CI differences (4.10%) like Subject 3. These differences in CI are supported by visual inspection of defect morphometry: defects in the asthma subject are smaller and sparsely distributed whereas defects in the CF subject are large and focal. As expected, CI and VDP are positively though not perfectly correlated (r = 0.4492, p = 0.0809). This may be useful to clinicians weighing potential benefits of treatments which target different pathways, or which may be globally vs locally targeted (e.g., biologic vs thermoplastic treatment of severe asthma).

Conclusion: The spatial distribution of defects and how these agglomerate in HPG MRI could be caused by different underlying pathophysiological features among lung diseases which is something that cannot be quantified with VDP calculations. Having the ability to not only observe how they cluster but also the quantification of these defects may be helpful in quantifying differences in defect clusters throughout different diseases, etiologies, or regional treatment response in longitudinal studies. Future work will involve further analysis in larger sample sizes, especially those with higher VDP, and how these possibly differ among more lung diseases and the possible evaluation of regional defects in smaller and larger airways.

References: [1] Thomen RP, et al., J Cyst Fibros. 2017;16(2):275-82., [2] Valk, A, et al., Magn Reson Med. 2021; 86: 3224– 3235., [3] Mugler, J.P., III, et al., J. Magn. Reson. Imaging. 2013;37: 313-331

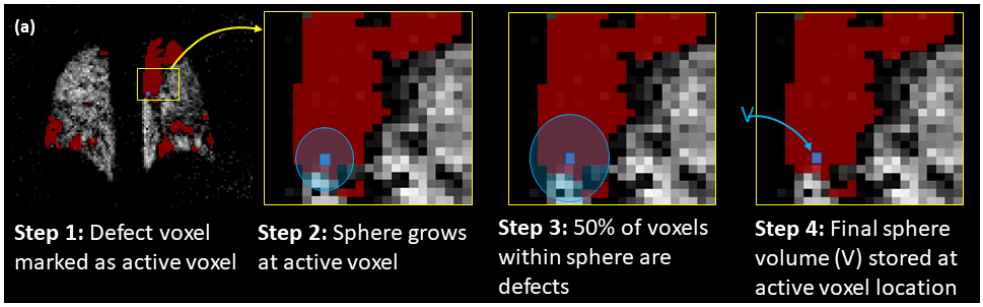

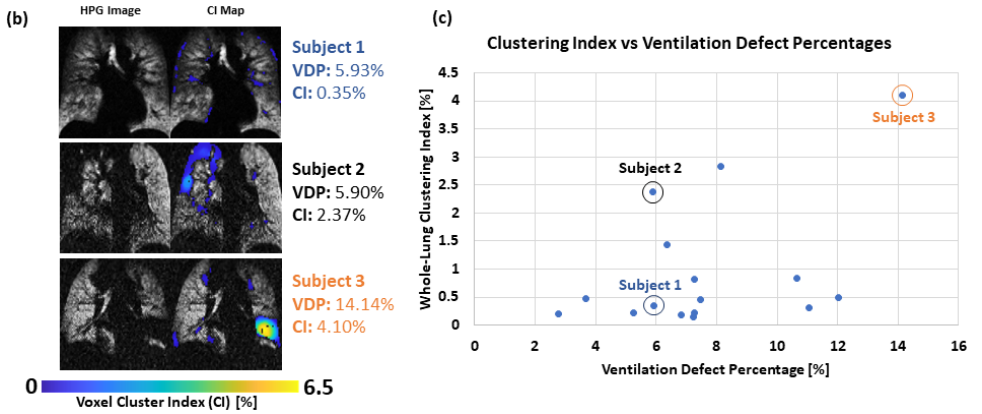

Figure 1. (a) Process diagram of the cluster quantification algorithm. (b) Example HPG ventilation images in 3 subjects with VDP and corresponding whole-lung CI. VDP and whole-lung CI are reported on the right. (c) Plot of CI versus VDP of all lung disease data.

EFFECT OF CFTR MODULATOR THERAPY WITH ELEXACAFTOR/TEZACAFTOR/IVACAFTOR ON PULMONARY VENTILATION DERIVED BY 3D PHASE-RESOLVED FUNCTIONAL LUNG MRI IN CYSTIC FIBROSIS PATIENTS

F. Klimeš[1,2]; A. Voskrebenzev[1,2]; M. Gutberlet[1,2]; M. Speth[1,2]; R. Grimm[3]; M. Dohna[1]; G. Hansen[2,4]; F. Wacker[1,2]; D. Renz[1]; A. Dittrich[2,4]; J. Vogel-Claussen[1,2]

[1]Institute of Diagnostic and Interventional Radiology, Hannover Medical School, Hannover, Germany

[2]Biomedical Research in Endstage and Obstructive Lung Disease Hannover (BREATH), German Center for Lung Research (DZL), Hannover, Germany

[3]MR Application Predevelopment, Siemens Healthcare GmbH, Erlangen, Germany

[4]Department for Pediatric Pneumology, Allergology and Neonatology, Hannover Medical School, Hannover, Germany

Purpose: To investigate whether 3D phase-resolved functional lung (PREFUL) MRI parameters are suitable to measure response to elexacaftor/tezacaftor/ivacaftor (ETI) therapy and their association with clinical outcomes in cystic fibrosis (CF) patients.

Methods: 23 patients with CF underwent MRI examination at baseline and 8-16 weeks after initiation of ETI therapy. In addition to morphological sequences, a functional 3D PREFUL measurement assessed pulmonary ventilation. Morphological images were evaluated using a semi-quantitative scoring system, and 3D PREFUL functional scans were evaluated by ventilation defect percentage (VDP) values derived from regional ventilation (RVent) and cross-correlation maps. Improved ventilation volume (IVV) and IVV normalized to body-surface area (BSA) between baseline and post-treatment visit were assessed. Along with spirometry, lung clearance index (LCI) was assessed by nitrogen multiple breath washout technique. Treatment effects were analyzed using paired Wilcoxon signed rank tests. Treatment changes and post-treatment agreement between 3D PREFUL and clinical parameters were evaluated by Spearman correlation analyses.

Results: After therapy with ETI all 3D PREFUL ventilation markers (all $P < 0.0056$) improved significantly, except for mean RVent parameter. The IVV_{RVent} and IVV_{RVent} normalized to BSA were significantly correlated to relative treatment changes of MEF25 and mucus plugging score (all $|r| > 0.44$, all $P < 0.0350$). In post-treatment analyses, 3D PREFUL VDP values significantly correlated with spirometry, LCI, MRI global, morphology and perfusion scores (all $|r| > 0.44$, all $P < 0.0348$).

Discussion: 3D PREFUL MRI derived VDP maps show significantly reduced ventilation defects (19-28%) after ETI therapy. The significant post treatment correlations of 3D PREFUL ventilation measures especially with LCI, FEV_1 % pred, and global MRI score suggest that 3D PREFUL MRI is sensitive to measure improved regional ventilation of the lung parenchyma due to reduced inflammation induced by ETI therapy in CF patients. 3D PREFUL MRI derived improved ventilation volume (IVV) correlated with MRI mucus plugging score changes suggesting that reduced endobronchial mucus is predominantly responsible for regional ventilation improvement 8-16 weeks after ETI therapy. This may show the complementary value of 3D PREFUL MRI to global clinically established measures such as FEV_1 and LCI.

Conclusion: 3D PREFUL ventilation MRI is a very promising tool to monitor CFTR modulation induced regional dynamic ventilation changes in CF patients.

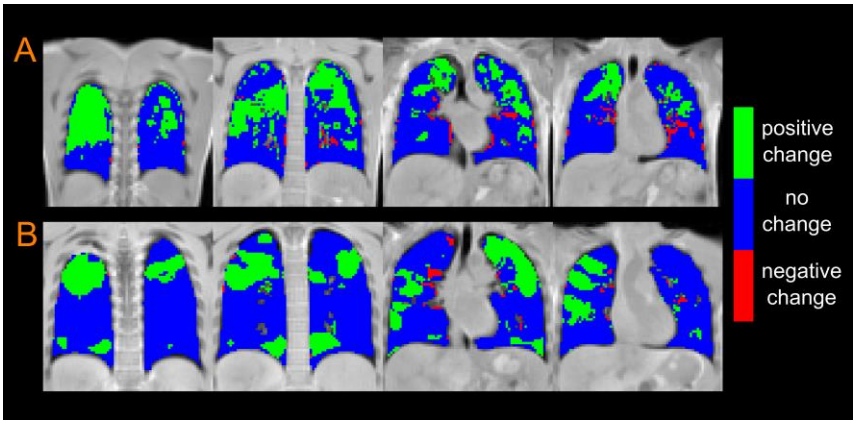

Figure 1. In (A) exemplary treatment response maps for a 26-year-old female derived from VDP_{RVent} maps are observed. The positive change of 24.2% (IVV_{RVent} / BSA = 442 ml/m^2) compared to the negative change of 3.1 %, resulted in an improvement of 21.1%. In (B) examples of coronal treatment response maps for a 19-year-old male derived from VDP_{CC} maps are shown. Subtracting the negative change of 1.3 % from the positive change of 16.1% (IVV_{CC} / BSA = 358 ml/m^2) results in an improvement of 14.8%.

REFERENCES

1. Graeber SY et al. *Am J Respir Crit Care Med*. 2022; 2. Klimeš F et al. *MRM* 2021; 3. Klimeš F et al. *JMRI* 2021; 4. Eichinger M et al. *Eur J Radiol*. 2012; 5. Forsberg D. image-registration; 6. Klimeš F et al. *NMR Biomed*. 2019; 7. Voskrebenzev A et al. *MRM* 2018; 8. Miller MR et al. *Eur Respir J*. 2005; 9. Quanjer PH et al. *Eur Respir J*. 2012; 10. Robinson PD et al. *Eur Respir J*. 2013.

Quantitative mapping of cardiopulmonary oscillations using hyperpolarized ^{129}Xe gas exchange MRI

Junlan Lu[1], Fawaz Alenezi[5], Suphachart Leewiwatwong[2], David Mummy[3], Sakib Kabir[3], Sudarshan Rajagopal[5], Scott Robertson[6], Peter J. Niedbalski[4], and Bastiaan Driehuys[1, 2, 3]

[1]Medical Physics Graduate Program, Duke University, Durham, North Carolina, United States,[2]Biomedical Engineering, Duke University, Durham, North Carolina, United States, [3]Radiology, Duke University Medical Center, Durham, North Carolina, United States, [4]Division of Pulmonary, Critical Care, and Sleep Medicine, University of Kansas Medical Center, Kansas City, Kansas, USA, [5]Division of Cardiology, Department of Medicine, Duke University Medical Center, Durham, NC, USA, [6]Clinical Imaging Physics Group, Duke University Medical Center, Durham, NC, USA

Purpose: The interaction of ^{129}Xe atoms with pulmonary capillary red blood cells (RBCs) exhibits cardiogenic oscillations that are sensitive to pre- and post-capillary pulmonary hypertension (PH)[1]. However, current measurements using whole-lung spectroscopy are unable to discern spatial heterogeneity and the previously established cardiogenic oscillation mapping methods[2] are not robust to radial undersampling artifacts. Here, we use digital phantom simulations to optimize keyhole reconstruction of oscillation imaging. We apply this method to establish proposed healthy reference values and to evaluate CTEPH subjects before and after thromboendarterectomy.

Methods: We designed a 6-zone digital lung phantom to investigate the effects of radial views, key radius, and SNR. We acquired standard 1-point Dixon ^{129}Xe gas exchange MRI[3] in a healthy cohort (n=17), from which we proposed reference distributions mapping thresholds. These were used to map RBC oscillation amplitudes in 10 CTEPH subjects, 6 of whom were scanned again after endarterectomy.

Results: Undersampling with 1,000 radial views introduces significant heterogeneity, but this can be reduced by decreasing the key radius. Subjects with CTEPH at baseline exhibited lower mean oscillation amplitudes, (4.8±2.9%) than healthy volunteers (11.2±3.4%, $p < .001$). Those who also underwent PTE exhibited mean oscillation amplitudes that increased from 4.0±3.5% to 7.5±5.2% ($p = 0.04$).

Discussion: RBC oscillation imaging using keyhole reconstruction is sensitive to the choice of radial projection binning, keyhole radius, and voxel intensity calculation. Applying these updated methods to a well-curated healthy cohort yielded a narrower healthy reference distribution while also demonstrating the ability to spatially localize regions of low oscillations for subjects with CTEPH.

Conclusions: Digital phantom simulations demonstrate both the veracity of the keyhole reconstruction technique and limitations of standard 1-point Dixon imaging parameters. The improvements introduced here for image preprocessing and reconstruction permit more robust quantitative mapping of cardiogenic oscillation amplitudes.

Figures

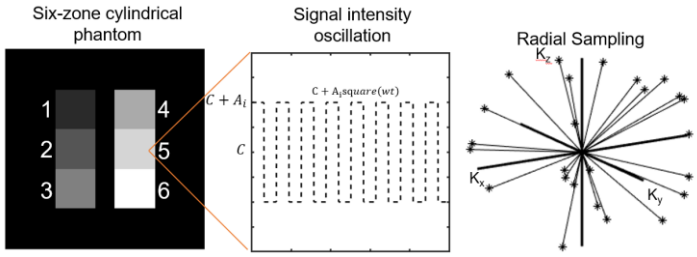

Figure 1. Six-zone cylindrical phantom design and simulation of signal intensity oscillation. Each zone i is assigned an oscillation amplitude A_i. For each TR, a single radial projection is acquired as signal evolves according to the function $C + A_i square(wt)$.

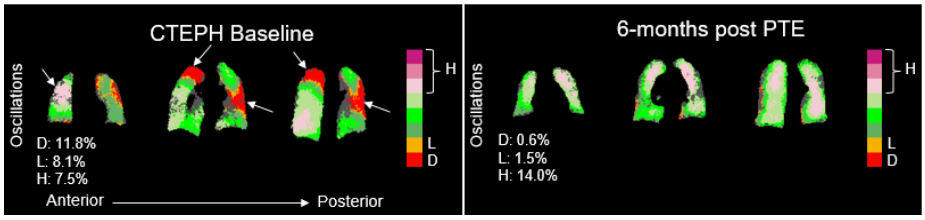

Figure 2. ^{129}Xe RBC oscillation imaging for a representative subject with CTEPH and no extensive obstructive or interstitial disease. Conventional whole-lung dynamic spectroscopy showing a 10.9% oscillation amplitude would falsely classify this subject as having no PH[4]. However, spatially resolving the oscillations appears to correctly indicate the presence of decreased perfusion (areas of decreased oscillations) and at baseline and an improvement in perfusion post-PTE.

References

1. Bier, E.A., et al., NMR Biomed, 2019. 32(1): p. e4029.
2. Niedbalski, P.J., et al. J Appl Physiol (1985), 2020. 129(2): p. 218-229.
3. Wang, Z., et al., Med Phys, 2017. 44(6): p. 2415-2428.
4. Bier, E.A., et al., ERJ Open Res, 2022. 8(2).

Pulmonary Vascular Redistribution following 2.5-years anti-IL-5Rα treatment in Eosinophilic Asthma

Marrissa J McIntosh,[1,2] Alexander M Matheson,[1,2] Harkiran K Kooner,[1,2] Rachel L Eddy,[3,4] Cory Yamashita[5] and Grace Parraga[1,2,5]

[1]Robarts Research Institute, [2]Department of Medical Biophysics, Western University, London, Canada; [3]Centre for Heart Lung Innovation, St. Paul's Hospital; [4]Division of Respiratory Medicine, Department of Medicine, University of British Columbia, Vancouver, Canada; [5]Division of Respirology, Department of Medicine, Western University, London, Canada

PURPOSE: Chest CT investigations from the Severe Asthma Research Program revealed pulmonary vascular remodelling in asthma,[1] which was suggested to be mediated via hypoxic vasoconstriction.[1,2] Ventilation distribution in asthma may be non-invasively quantified using hyperpolarized noble gas magnetic resonance imaging (MRI).[3] Both vascular[1] and ventilation abnormalities[4,5] have been linked to abnormal airway and systemic eosinophilia and poor asthma control. In eosinophilic asthma anti-IL-5Rα treatment eliminates airway and systemic eosinophils,[6] and was shown to improve MRI ventilation defects.[7] Based on these previous findings, we evaluated CT pulmonary vascular tree small-vessel volume and density in eosinophilic asthma participants prior to anti-IL-5Rα initiation and following 2.5-years of continuous treatment. We also compared these measurements to those of healthy, elderly never-smokers.

METHODS: Participants with eosinophilic asthma provided written informed consent (NCT03733535, NCT02351141) to CT, ^{129}Xe MRI and spirometry just prior to anti-IL-5Rα treatment initiation and after 2.5-years of continuous treatment. Healthy, elderly never-smokers (NCT02483403) were retrospectively evaluated as controls. The Chest Imaging Platform[8] was used to generate total blood volume (TBV) and the blood volume for vessels with cross sectional area less than 5 mm^2 (BV_5), between 5-10 mm^2 ($BV_{5\text{-}10}$) and greater than 10 mm^2 (BV_{10}). CT mucus-score[9] and MRI ventilation defect percent (VDP) were quantified as previously described.[10] Differences were evaluated using paired or independent samples t-tests and non-parametric relationships were evaluated using Spearman (ρ) correlation coefficients.

RESULTS: Of 28 participants with poorly-controlled, eosinophilic asthma evaluated with CT at Day-0,[7] 12 (10 females, 61±15y) completed a visit after 2.5-years of continuous anti-IL-5Rα therapy. In eosinophilic asthma, as compared to Day-0, BV_5/TBV (Δ=0.06±0.03, p=.02) and BV_{10}/TBV (Δ=-0.05±0.02, p=.03) were significantly different (improved) after 2.5 years while TBV (p=.09) was not. In eosinophilic asthma, as compared to 42 healthy controls (22 females, 73±6y), BV_5/TBV (p<.001) and BV_{10}/TBV (p=.002) were significantly worse at Day-0, but not different at 2.5-years (p=.3, p=1.0, respectively). The change in BV_5/TBV after 2.5-years in eosinophilic asthma was related to Day-0 blood eosinophils (ρ=.78, p=.004), FEV_1 (ρ=-.64, p=.03), VDP (ρ=.83, p=.001) and mucus-score (ρ=.91, p<.001).

DISCUSSION: In a small group of patients with poorly-controlled, eosinophilic asthma, CT small-vessel volume was worse than in healthy controls at baseline, but increased (improved) alongside decreased large-vessel volume after 2.5-years of continuous anti-IL-5Rα treatment. This novel finding suggests that pulmonary vascular small vessels increased in volume and/or density as a direct or indirect response to anti-IL-5Rα-driven eosinophil depletion. Worse ventilation and more airway mucus measured just prior to therapy initiation predicted small-vessel volume increases after 2.5-years of treatment. To our knowledge this is the first demonstration of pulmonary vascular differences after biologic therapy in eosinophilic asthma. These findings agree with previous suggestions of pulmonary vascular remodeling in asthma.[1,2]

CONCLUSIONS: CT small-vessel volume was worse in eosinophilic asthma than healthy, elderly never-smokers at baseline, but improved in eosinophilic asthma and was similar to measurements in healthy controls following 2.5-years of continuous anti-IL-5Rα treatment.

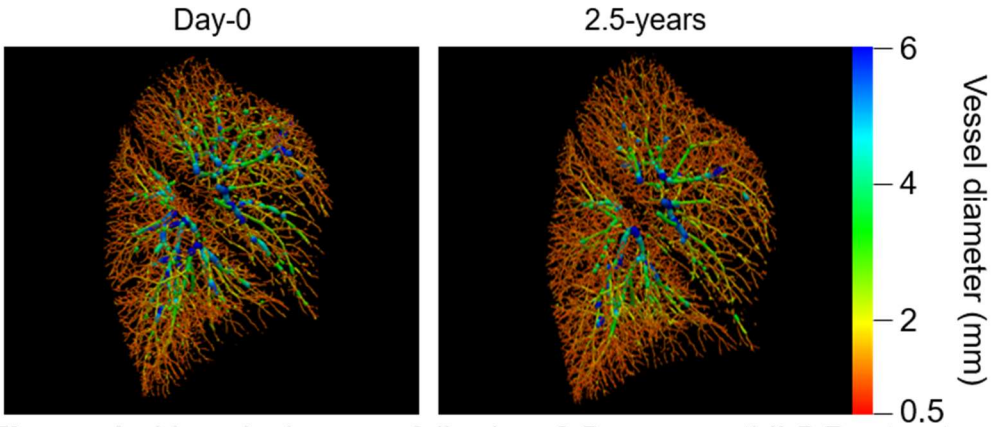

Figure 1: Vessel changes following 2.5-years anti-IL5-Rα treatment. Visually more small vessels (red) at 2.5-years.

REFERENCES:
1. Ash, *AJRCCM* (2018); 2. Sverzellati & Silva *AJRCCM* (2018); 3. Altes *JMRI* (2001); 4. Svenningsen *AJRCCM* (2018); 5. Svenningsen *ERJ* (2016); 6. Skolnik & Carnahan *Curr Med Res Opin* (2019); 7. McIntosh & Kooner *Chest* (2022); 8. Estepar *Proc IEEE Int Symp Biomed Imaging* (2012); 9. Dunican *J Clin Invest* (2018); 10. Kirby *Acad Radiol* (2012).

Lung Volume Dependence and Repeatability of Hyperpolarized ^{129}Xe MRI Gas Uptake Metrics in Healthy Volunteers and Patients with COPD

William J Garrison[1], Kun Qing[2,3], Mu He[4], Li Zhao[5], Nicholas J Tustison[2], Jaime F Mata[2], Y Michael Shim[4], Alan M Ropp[2], Talissa A Altes[6], John P Mugler III[1,2], and G Wilson Miller[1,2,7]

[1]Biomedical Engineering, University of Virginia; [2]Radiology and Medical Imaging, University of Virginia; [3]Radiation Oncology, City of Hope National Medical Center; [4]Medicine, University of Virginia; [5]Biomedical Engineering, Zhejiang University; [6]Radiology, University of Missouri; [7]Physics, University of Virginia

Purpose: MRI of dissolved-phase ^{129}Xe can be used to derive spatially-resolved metrics characterizing gas uptake by the lung, by taking advantage of the distinct ^{129}Xe chemical shifts when dissolved in alveolar membrane and blood plasma (Mbr) and bound to hemoglobin in red blood cells (RBC) [1,2]. Signal ratios derived from dissolved-phase ^{129}Xe MRI demonstrate sensitivity to changes in lung function associated with disorders including COPD [3,4]. Previous work has noted that lung volume during ^{129}Xe MRI significantly impacts gas-uptake metrics [3,5]. This observation holds potential implications for dissolved-phase ^{129}Xe MRI study design, particularly in pathological contexts in which lung volume differs from the healthy population, such as in COPD. The purpose of this work was therefore to robustly characterize the relationships between lung volume and ^{129}Xe MRI-derived gas-uptake metrics in healthy individuals and individuals with COPD, and to assess the impact of scan-to-scan volume differences on measurement variability.

Methods: Dissolved-phase ^{129}MRI was performed in 49 participants (five young healthy, 25 older healthy, 19 COPD). All participants received scans at 1/3 FVC and TLC, and 17/49 participants additionally received scans at RV. All scans were performed using a 1 L ^{129}Xe dose, with buffer gases inhaled (or inhaled ^{129}Xe/air exhaled) in order to reach the target inflation level. Multi-echo, IDEAL-based ^{129}Xe MRI was performed as previously described [3,4]. The effect of scan-to-scan lung volume changes on measured signal ratios was quantified by performing pairwise comparisons of scans within each participant. A linear relationship was assumed between the relative signal-ratio difference and relative volume difference between any two such scans, as described in Eq. 1:

$$\frac{R_2 - R_1}{(R_1 + R_2)/2} = -\alpha \cdot \frac{V_2 - V_1}{(V_1 + V_2)/2} \qquad (1)$$

where R_1 (R_2) and V_1 (V_2) represent the mean signal ratio and lung volume, respectively, from the chronologically earlier (later) of the two scans, and α represents the slope of the linear correlation, similar to a relationship previously studied in repeated scans in healthy individuals [5].

Results: Mbr/Gas and RBC/Gas increased with decreasing lung volume, and the slope of this dependence was highest at lower lung volumes (Fig. 1a-b). Strong linear correlations were found between relative ratio difference and relative volume difference between scans for Mbr/Gas (R=-0.97) and RBC/Gas (R=-0.93) (Fig. 1d-e). A weaker relationship was found between RBC/Mbr and lung volume (R=-0.66) (Fig. 1c,f). Lung volumes achieved during ^{129}Xe MRI were higher for participants with COPD than older healthy participants at RV (p=0.02) and 1/3 FVC (p<0.001) (Fig. 2a). Mbr/Gas ratios were lower for participants with COPD than older healthy participants at RV (p=0.03) and 1/3 FVC (p<0.001), but after regressing out volume contribution using Eq. 1, these groupwise differences were no longer significant (p=0.15 at RV, 0.29 at 1/3 FVC) (Fig. 2b-c).

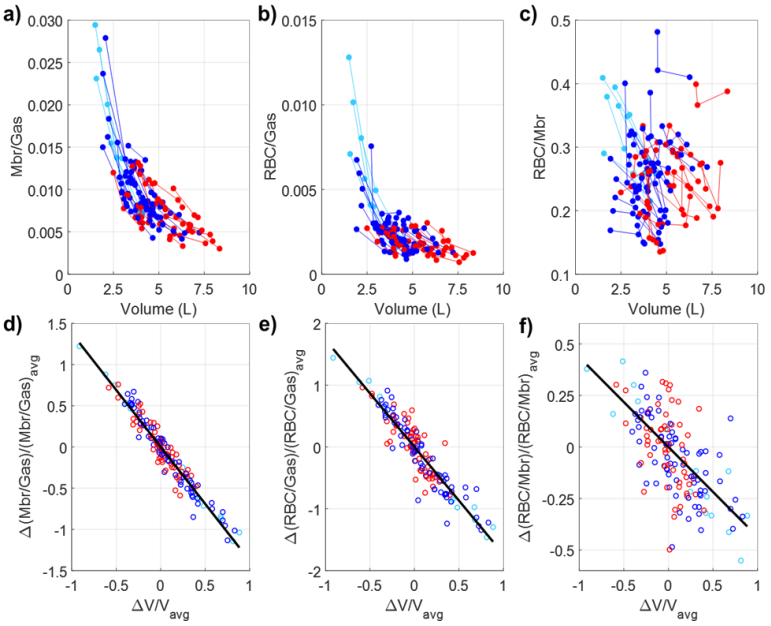

Figure 1: a) Mbr/Gas, **b)** RBC/Gas, and **c)** RBC/Mbr vs. lung volume. Lines connect scans from the same participant. **d)** Relative Mbr/Gas, **e)** relative RBC/Gas, and **f)** relative RBC/Mbr differences vs. ΔV/V. Each data point in **d)**, **e)**, and **f)** corresponds to a pair of points from the same participant in **a)**, **b)**, and **c)**, respectively. Light blue = young healthy, dark blue = older healthy, red = chronic obstructive pulmonary disease (COPD). Lines in **d)**, **e)**, and **f)** are linear fits to Eq. 1.

Discussion and Conclusion: These results implicate volume differences between scans as an important source of variability for Mbr/Gas and RBC/Gas in both healthy and diseased individuals. Given the prevalence of hyperinflation in individuals with COPD, it is apparent that care must be taken when comparing gas-uptake metrics across healthy individuals and individuals with COPD, particularly as groupwise differences in Mbr/Gas and RBC/Gas in our study population diminished when corrections for lung volume were applied. The weaker volume dependence at higher lung volumes suggests that TLC may be the optimal inflation level for these measurements with regard to repeatability and reduction of groupwise volume-driven differences between healthy individuals and individuals with COPD. However, dose volume during experiments remains an important concern, and high inflation levels may not provide optimal sensitivity to disease [1]. These results therefore present an interesting subject of future discussion regarding dissolved-phase ^{129}Xe MRI best practices.

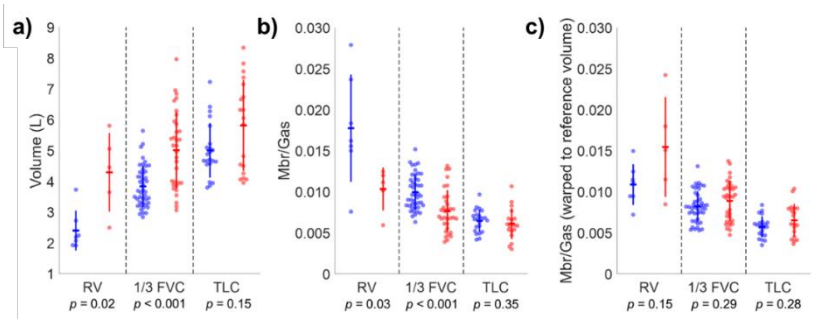

Figure 2: a) Lung volumes, **b)** Mbr/Gas, and **c)** Mbr/Gas projected at reference lung volumes for each inflation level using Eq. 1, separated by inflation level, in participants with chronic obstructive pulmonary disease (COPD, red) and older healthy participants (blue). Lines depict means and standard deviations.

Acknowledgments: This work was supported by NIH grants R01 HL109618, R01 HL105586, R01 HL132177, and R01 CA172595.

References:

[1] Niedbalski PJ *et al*. Magn Reson Med. 2021;86(6):2966–86.
[2] Cleveland ZI *et al*. PLoS One. 2010;5(8):e12192.
[3] Qing K *et al*. NMR Biomed. 2014;27(12):1490–501.
[4] Qing K *et al*. Acad Radiol. 2019;26(3):326–34.
[5] Hahn AD *et al*. J Magn Reson Imaging. 2019;50(4):1182–90.

Investigating COPD Progression Through Quantitative CT

Craig J. Galban

Chronic obstructive pulmonary disease (COPD) is a leading cause of death and healthcare burden in the United States and worldwide. Major causes of airflow obstruction are attributed to chronic bronchiolitis, a.k.a small airways disease (SAD), and emphysema. Although SAD and emphysema are treated as separate COPD subtypes, studies have shown strong quantitative evidence that SAD exists as an intermediate state between healthy lung tissue and emphysema—i.e., irreversible lung damage—in COPD pathogenesis[1-3]. At present, little has been done to exploit SAD as a predictor of emphysema. Our group investigates how the Parametric Response Map (PRM) may be used to harness the predictive potential of SAD. PRM is a CT-based voxel-wise computational technique that can identify and quantify functional small airways disease (fSAD) even in the presence of emphysema[4]. The percent volume of PRM-derived fSAD (PRM^{fSAD}), i.e., the amount of fSAD in the lungs, has improved COPD phenotyping and the prediction of spirometric decline in subjects at risk of COPD[5]. We improved the sensitivity of PRM for quantifying fSAD by applying topological techniques to PRM as an extension of the PRM algorithm. These topological readouts were shown to improve upon commonly used whole-lung PRM measures with respect to COPD characterization[6].

Of particular interest is the Euler-Poincaré characteristic (χ). This topological readout, for which positive values are associated with pocket formations of fSAD[6], may serve as a surrogate of lung parenchymal transition from healthy to emphysema through SAD. In recent studies, we found that volume density for PRM^{fSAD} was sensitive to overall burden of diseased tissue, whereas χ was sensitive to the coalescing of diseased tissue into pocket formations. Comparing χ^{fSAD} and χ^{Norm}, we observed a strong correlation between these two readouts. We postulate that mild COPD consists of PRM^{fSAD} pockets (high χ^{fSAD}) that reside within normal lung tissue (low χ^{Norm}).

These two readouts transition for COPD stages GOLD 2 and 3. In addition, we have observed a unique COPD subset, associated with emphysema progression, using an unsupervised clustering approach applied to χ of PRM^{Norm} and PRM^{fSAD}.

The topological PRM readout χ^{fSAD} provides an index of COPD severity by quantifying the extent of SAD pocket formation. Further, χ^{fSAD} may be used to assess disease subtypes associated with emphysema progression and predict spirometric decline. Our approach shows promise for using both the presence and pattern of PRM fSAD as biomarkers of emphysema onset.

1. Boes JL, Hoff BA, Bule M, et al. Parametric Response Mapping Monitors Temporal Changes on Lung CT Scans in the Subpopulations and Intermediate Outcome Measures in COPD Study (SPIROMICS). *Academic Radiology*. February 1, 2015 2015;22(2):186-194. doi:10.1016/j.acra.2014.08.015
2. Labaki WW, Gu T, Murray S, et al. Voxel-Wise Longitudinal Parametric Response Mapping Analysis of Chest Computed Tomography in Smokers. *Acad Radiol*. Feb 2019;26(2):217-223. doi:10.1016/j.acra.2018.05.024
3. McDonough JE, Yuan R, Suzuki M, et al. Small-Airway Obstruction and Emphysema in Chronic Obstructive Pulmonary Disease. *New England Journal of Medicine*. October 27, 2011 2011;365(17):1567-1575. doi:10.1056/NEJMoa1106955
4. Galbán CJ, Han MK, Boes JL, et al. Computed tomography–based biomarker provides unique signature for diagnosis of COPD phenotypes and disease progression. *Nature Medicine*. 11/2012 2012;18(11):1711-1715. doi:10.1038/nm.2971
5. Bhatt SP, Soler X, Wang X, et al. Association between Functional Small Airway Disease and FEV1 Decline in Chronic Obstructive Pulmonary Disease. *American Journal of Respiratory and Critical Care Medicine*. 2016-7-15 2016;194(2):178-184. doi:10.1164/rccm.201511-2219OC
6. Hoff BA, Pompe E, Galbán S, et al. CT-Based Local Distribution Metric Improves Characterization of COPD. *Scientific Reports*. 2017-06-07 2017;7(1):2999. doi:10.1038/s41598-017-02871-1

Dysanapsis: Origins and clinical significance
Benjamin M Smith MD

Dysanapsis refers to a mismatch between airway tree caliber and lung size that arises early in life (Greek: "dys" = unequal "anaptixy" = growth).[1] The term was first introduced by Green and colleagues in 1974 to describe the hypothesized source of inter-individual differences in lung function among healthy adults.

Advances in pulmonary imaging have since enabled direct and reproducible assessment of dysanapsis *in vivo*.[2,3] Imaging-assessed dysanapsis is evident in the general population,[2] is established by early adulthood,[4] extends to from trachea to terminal bronchioles[5,6] and is strongly associated with chronic obstructive pulmonary disease (COPD) risk later in life[2] (as was originally hypothesized by Green et al in 1974!)

More than just a static trait, emerging evidence suggests that dysanapsis may interact with the environment to influence susceptibility to air pollutants[7] and efficacy of inhaled therapeutics.[8]

In this talk I will present some recent findings on the early life origins and later life outcomes of dysanapsis. Hope you enjoy!

References

1. Green M, Mead J, Turner JM. Variability of maximum expiratory flow-volume curves. *J Appl Physiol*. Jul 1974;37(1):67-74. doi:10.1152/jappl.1974.37.1.67
2. Smith BM, Kirby M, Hoffman EA, et al. Association of Dysanapsis With Chronic Obstructive Pulmonary Disease Among Older Adults. *JAMA*. Jun 9 2020;323(22):2268-2280. doi:10.1001/jama.2020.6918
3. Maetani T, Tanabe N, Terada S, et al. Physiological impacts of computed tomography airway dysanapsis, fractal dimension and branch count in asymptomatic never smokers. *J Appl Physiol (1985)*. Oct 21 2022;doi:10.1152/japplphysiol.00385.2022
4. Vameghestahbanati M, Hiura GT, Barr RG, Sieren JC, Smith BM, Hoffman EA. CT-Assessed Dysanapsis and Airflow Obstruction in Early and Mid Adulthood. *Chest*. Aug 12 2021;161(2):389-391. doi:10.1016/j.chest.2021.08.038
5. Vameghestahbanati M, Kirby M, Tanabe N, et al. Central Airway Tree Dysanapsis Extends to the Peripheral Airways. *Am J Respir Crit Care Med*. Feb 1 2021;203(3):378-381. doi:10.1164/rccm.202007-3025LE
6. Smith BM, Wiemken A, Hoffman EA, et al. Upper and Lower Airway Dysanapsis and Airflow Obstruction Among Older Adults. *Am J Respir Crit Care Med*. Jun 9 2022;doi:10.1164/rccm.202202-0353LE
7. Bourbeau J, Doiron D, Sharmistha B, et al. Ambient air pollution and dysanapsis: associations with lung function and COPD in the CanCOLD study. *Am J Respir Crit Care Med*. 2022;In pressdoi:doi.org/10.1164/rccm.202106-1439OC
8. Vameghestahbanati M, Kirby M, Maltais F, et al. Dysanapsis and the Spirometric Response to Inhaled Bronchodilators. *Am J Respir Crit Care Med*. Oct 15 2021;204(8):997-1001. doi:10.1164/rccm.202107-1574LE

Physiologic Characterization of Respiratory Function Using Fluoroscopy-based X-ray Velocimetry

Naresh M. Punjabi, MD, PhD; University of Miami)

Rationale: X-ray velocimetry (XV) has been utilized in preclinical models to assess lung motion and regional ventilation, though no studies have compared XV-derived physiologic parameters to measures derived through conventional means.

Objectives: To assess agreement between XV-analysis of fluoroscopic lung images and pitot tube flowmeter measures of ventilation.

Methods: XV- and pitot tube-derived ventilatory parameters were compared during tidal breathing and with bilevel-assisted breathing. Levels of agreement were assessed using the Bland-Altman analysis. Mixed models were used to characterize the association between XV- and pitot tube-derived values and optimize XV-derived values for higher ventilatory volumes.

Measurements and Main Results: Twenty-four healthy volunteers were assessed during tidal breathing and 11 were reassessed with bilevel-assisted breathing. No clinically significant differences were observed between the two methods for respiratory rate (average Δ: 0.58; 95% 95% limits of agreement: -1.55, 2.71) or duty cycle (average Δ: 0.02; 95% limits of agreement: 0.01, 0.03). Tidal volumes and flow rates measured using XV were lower than those measured using the pitot tube flowmeter, particularly at the higher volume ranges with bilevel-assisted breathing. Under these conditions, a mixed-model based adjustment was applied to the XV-derived values of tidal volume and flow rate to obtain closer agreement with the pitot tube-derived values.

Conclusion: Radiographically obtained measures of ventilation with XV demonstrate a high degree of agreement with parameters of ventilation. These results open the potential for using XV in the regional assessment of ventilatory abnormalities that is not possible with conventional pulmonary function tests or static radiographic assessments.

New Metrics for Quantification of Airway Disease in COPD

Surya P. Bhatt, MD, MSPH

The structural underpinnings chronic obstructive pulmonary disease (COPD) include both parenchymal destruction and airway remodeling. Emphysema has been consistently quantified using lung density but airway disease is more difficult to quantify, given the non- uniformity of the airway structure. Wall area thickness and wall area percentage at the segmental and sub-segmental levels have been commonly used to quantify airway wall thickness but these reflect changes at only one level. Pi10 is the square root of the wall area of a theoretical airway with internal perimeter 10 mm, derived by plotting the internal perimeters of all measured airways against the square root of the wall area of airways. Pi10 is a useful summary measure of airway wall thickness that is adjusted for airway size. A major limitation of Pi10 however is the assumption that there is a linear relationship between wall thickness of larger central airways and smaller peripheral airways. We show that the slope of the relationship between airway lumen perimeter and wall thickness is not the same in all individuals and that quantifying this slope (PiSlope) is a new method of quantifying airway wall thickness. PiSlope decreases with worsening disease severity. We show that, after adjustment for age, sex, race, BMI, smoking status, pack-years of smoking, and lung function, PiSlope is associated inversely with shortness of breath and quality of life and positively with 6-minute walk distance. PiSlope is also associated inversely with exacerbation frequency and survival. These associations were significant even after adjusting for Pi10.

There is repetitive reduction in airway lumen diameter of daughter airways at each generation (as compared to the parent) allowing for maximum efficiency in airflow with minimum resistance. This ratio of child-to-parent lumen diameter at each generation is termed the Airway Homothety Ratio (AHR). We hypothesized that airway narrowing in adults with COPD results in a reduction in the mean AHR, thus increasing overall peripheral airway resistance, and that the mean AHR is associated with respiratory morbidity, lung function decline, and mortality. The mean AHR decreases progressively with worsening disease. After adjusting for age, sex, race, smoking status, BMI, pack-years of smoking, CT scanner type, CT emphysema, and segmental airway wall thickness, AHR was independently associated with FEV_1 and FEV_1/FVC, quality of life, dyspnea, lung function decline, and mortality.

Reliable lung quantification via CT using virtual imaging trials

EHSAN ABADI

Computed Tomography (CT) has notable potential to quantify the severity and progression of diseases in the lungs. Such quantification should ideally reflect the true attributes and pathologies of subjects, not scanner parameters or makes and models. To achieve such an objective, the effects of the scanner conditions need to be understood so the influence can be mitigated.

These assessments cannot be fully made using patient images as they lack the underlying ground truth. In addition, patients cannot be imaged repeatedly across multiple conditions due to radiation dose concerns. Alternative assessment of the effects via physical phantoms is further limited because they do not represent the diverse anatomy and pathology of real patients. Alternatively, these imaging trials can be explored using realistic simulations of targeted patients and imaging scanners, a process known as *in silico* or virtual imaging trials (VITs).

The purpose of this talk is to present our recent developments in virtual imaging trials and to demonstrate their utility in reliable lung quantifications via CT. We will introduce the developments of a library of anthropomorphic, computational human models with COPD abnormalities (i.e., emphysema and bronchitis), representing diverse severity and patient attributes. We will also introduce the developments of a scanner-specific CT simulator (i.e., DukeSim) with extensive validations against experimental measurements of various scanner models.

These human and scanner models have been recently utilized to investigate the effects of CT imaging parameters and technologies on COPD quantifications (i.e., emphysema and airway measurements). In particular, we will present the effects of dose level (mAs), tube current modulation, reconstruction algorithms (filtered backprojection vs. iterative reconstruction), reconstruction kernel sharpness, pixel size, and slice thickness. In terms of technology, we will present our findings for both energy-integrating and the emerging photon-counting detectors.

This presentation will demonstrate that while CT quantification is possible, its reliability is impacted by the choice of imaging parameters and technologies. The developed virtual imaging trial platform enables comprehensive evaluation of CT methods in reliable quantifications, an effort that cannot be readily made with patient images or simplistic physical phantoms

Mucus Plugs Occluding COPD Airways: A Review of Their Clinical Impact

Alejandro Diaz MD, MPH –Brigham and Women's Hospital

COPD is a heterogenous, complex disease. Changes to the mucociliary system are central airway pathology of COPD. The airway pathology is characterized by excess mucus production, hypersecretion, and reduced clearance, leading to accumulation in the airways as plugs.[1] Mucus plugs completely occluding the medium-to-large-sized airways (i.e., ~2-10 mm-lumen diameter) are observed on computed tomography (CT) scans in up to 67% of individuals with COPD and are associated with airflow obstruction, lower oxygen saturation, and reduced exercise capacity.[2,3] Further, up to 30% of individuals with COPD who do not report cough or phlegm, typical symptoms of mucus pathology, present with mucus plugs occluding airway lumen.[2] As mucus plugs provide a potential target for therapeutical intervention, further preliminary studies have investigated whether this airway pathology is associated with clinically relevant outcomes, such as exacerbations, mortality, and changes in lung function.

In participants with COPD from the COPDGene cohort, during a median follow-up of over 9 years, the incidence of exacerbations per 100 person-years was 43.7, 62.4, and 74.6 for participants with 0, 1-2, and ≥3 lung segments with mucus plugs, respectively. In adjusted models, airway mucus plugs were associated with increased frequency of total exacerbations during follow-up (rate ratio [RR] [95% confidence interval], 1.07 [1.03 – 1.11] and RR 1.14 [1.10 – 1.19] for those with 1-2 vs 0 and ≥3 vs 0 lung segments with mucus plugs). The all-cause mortality rate in participants with COPD without mucus plugs and 1-2 and ≥3 lung segments with mucus plugs was 34%, 47%, and 54%, respectively. In adjusted models, the presence of mucus plugs was associated increased risk of all-cause mortality (adjusted hazard ratio of death of 1.15 [95% CI, 1.02 – 1.29] and 1.24 [95% CI, 1.10 – 1.41] for those with 1-2 vs. 0 and ≥3 vs. 0 lung segments with mucus plugs, respectively). Finally, in participants with both baseline and 5-yr CT scans evaluated, persistently positive vs. persistently negative mucus plug status was associated with a greater decline in FEV_1 (-65.5 mL [SE 20.7], p=0.002; -2.66 % predicted [SE 0.74], p<0.001) and higher odds of rapid decline in FEV_1, i.e., drop in FEV_1>40 mL per year (OR [95% CI] 1.59 [1.19 – 2.12]). When compared to persistently positive, resolved mucus plugs status was associated with improvement in FEV_1 (97.6 mL [SE 23.2], p<0.001; 4.07% predicted [SE 0.83], p<0.001). The results suggest that mucus pathology is associated with important COPD outcomes and support further investigation of therapeutic interventions targeting mucus plugs.

References

1. Boucher RC. Muco-Obstructive Lung Diseases. N Engl J Med 2019;380:1941-53.
2. Okajima Y, Come CE, Nardelli P, et al. Luminal Plugging on Chest CT Scan: Association With Lung Function, Quality of Life, and COPD Clinical Phenotypes. Chest 2020;158:121-30.
3. Dunican EM, Elicker BM, Henry T, et al. Mucus Plugs and Emphysema in the Pathophysiology of Airflow Obstruction and Hypoxemia in Smokers. Am J Respir Crit Care Med 2021;203:957-68.

Structural and Functional Proton Magnetic Resonance Imaging in Pediatric Lung Disease

Giles Santyr PhD
Senior Scientist, The Hospital for Sick Children
Professor, Department of Medical Biophysics, University of Toronto

The value of proton Magnetic Resonance Imaging (MRI) for assessing lung disease has increased steadily in recent years due to improvements in image quality and the emergence of new structural and functional biomarkers. Furthermore, compared to X-ray based methods (eg. computed tomography; CT), MRI does not involve ionizing radiation thereby permitting multiple scans without accumulated dose. This is particularly advantageous when serial or longitudinal imaging is required to assess disease progression or determine the effects of interventions. For these reasons, it is anticipated that proton MRI will take on a growing role in diagnosis and monitoring of pediatric lung disease. Two particularly useful approaches are ultrashort echo time (UTE) and free-breathing (FB) proton MRI. UTE can mitigate signal losses in the lung permitting structural imaging of the lung parenchyma and airways rivaling CT. FB MRI gathers image data through multiple cycles of quiescent tidal breathing to reconstruct motion-free lung images at arbitrary respiratory and cardiac phases. Using non-rigid image registration, these images can then be used to calculate functional maps of ventilation and perfusion without the need for gaseous or intravenous contrast agents, important for imaging of very young or very sick children. This presentation will describe advances in UTE and FB proton MRI with a particular emphasis on structural and functional imaging of the pediatric lung. Promising applications of proton MRI for the evaluation of early obstructive lung disease (eg. cystic fibrosis; CF) will be high-lighted.

Body Composition CT Metrics and Lung Function in Asthma Participants: Analyses from the Severe Asthma Research Program

Mark L. Schiebler, M.D.
University of Wisconsin, Madison

Sponsorship: NHLBI SARP III, IV

Introduction

Recent work by Peters et al (**PMID:** 27283230**)** showed that plasma IL-6 levels were increased in asthmatics. It is known that low grade inflammation occurs in obesity and is correlated with insulin resistance. They showed that the inflammatory cytokine IL-6 was strongly associated with severe asthma and that those participants also had higher rates of diabetes and systemic hypertension.

We aimed to determine if body composition, as measured from routine non-contrast chest CT, was related to lung function and IL-6 cytokine levels in SARP participants (PMID: 36194556)

Methods

SARP participants with baseline CT Chest exams were secondarily reviewed for their paraspinous muscle density (PSMD) and their longitudinal change in lung function. The PSMD was determined from the mean Hounsfield unit (HU) value of the right and left erector spinae muscles at T12 obtained with a region of interest (500-510mm2) placed in the center of the muscle. The longitudinal change in lung function was the post-bronchodilator FEV1%-predicted over a median follow-up period of five years. A linear multivariable mixed effects model was used to determine the association of PSMD and lung function decline for males and females.

Results

A total of 219 asthmatics (147 Females) were studied. We found that PSMD predicted lung function decline for female SARP participants, [(β= -0.47 Δ-slope per 10 HU decrease), p= 0.03], but not males [(β= 0.11 Δ-slope per 10 HU decrease), p= 0.77]. In females, the highest PSMD tertile predicted a 2.9% improvement in lung function after five years while the lowest tertile predicted a 1.8% decline in FEV1%-predicted. The Spearman correlations of PSMD with IL-6 were also significant (males- ρ .4, p value 0.3; females- ρ .36, p value <.001).

Conclusion

In female asthma participants, a CT metric of body composition, was independently associated with lung function decline.

Phenotyping Asthma/COPD Overlap in Patients with Mild Lung Disease with Xenon MRI and Lung Function - Results from the NOVELTY ADPro Cohort

Laurie Smith PhD, University of Sheffield, UK

Asthma and chronic obstructive pulmonary disease (COPD) are both highly prevalent respiratory diseases affecting >600 million people worldwide and place a large burden on healthcare providers. There is a large degree of overlap between the two diseases and therefore distinguishing features of both conditions are often prevalent in patients. This becomes a challenge to accurately diagnose, phenotype and treat individuals who may have overlap of two highly heterogeneous respiratory diseases. Patients with asthma + COPD have poorer quality of life and more hospitalisations than patients with asthma or COPD alone. 2015 GINA and GOLD report on asthma+COPD concluded an 'urgent need for more research on this topic'. Patients are predominantly managed in primary care whereby, alongside symptoms, spirometry is the primary objective assessment of lung health. Spirometry however is insensitive to early signs of small airways disease and spirometry phenotypes are not specific to either asthma or COPD. In addition, spirometry cannot provide detail on other physiological characteristics specific to the diseases such as ventilation heterogeneity, gas trapping and impaired gas exchange. Tests of physiological function specific to disease and lung function characteristics are therefore desirable in order to best manage individuals with asthma and/or COPD.

The NOVEL observational longiTudinal studY (NOVELTY) study is an observational longitudinal global study of ~12000 patients with a broad range of asthma and/or COPD (ClinicalTrials.gov identifier: NCT02760329) and is funded by AstraZeneca. The study broadly aims to phenotype and characterise these conditions in order to better understand the differences and similarities. As part of NOVELTY, the Advance Diagnostic Profiling (ADPro) sub-study is a collaboration between York primary care trust and the University of Sheffield in the UK. The aim of ADPro is to physiologically phenotype patients from NOVELTY using ^{129}Xe-MRI of the lung and advanced lung function testing. Patients already taking part in NOVELTY in York, were invited to attend Sheffield at two time points approximately 1 year apart. At visit one, post-bronchodilator, patients performed hyperpolarised ^{129}Xe MRI ventilation imaging, diffusion-weighted imaging and gas transfer imaging, in addition to ^{1}H structural imaging. Following the imaging session patients also performed, airwave oscillometry, transfer factor for carbon monoxide, body plethysmography, spirometry and FeNO. A second visit was performed approximately 1-year post visit one where the same methods were repeated both pre and post bronchodilator.

In total 164 patients were assessed at visit one using the methods outlined above. 82 of these had a diagnosis of asthma, 27 had a diagnosis of COPD and 55 had a combined diagnosis of asthma and COPD. As this study was performed during the COVID-19 pandemic, our resultant population were a mild cohort, with 127/164 patients having 'normal' spirometry at visit 1. 140 patients were then also followed up at visit 2.

This talk will detail the cross-sectional findings to date from the analysis of visit 1. The talk will focus on the physiological phenotypes observed between the three diagnosis groups, the increased sensitivity of ^{129}Xe-MRI and advanced lung function to detect lung disease in patients with normal spirometry and the impact of airways dysanapsis on ^{129}Xe-MRI.

Phase Resolved Functional Lung (PREFUL) MRI: Latest Developments and Clinical Translation

Jens Vogel-Claussen, MD

Fourier decomposition (FD) is a contrast agent–free 1H MR image acquisition and postprocessing method for lung perfusion (Q) and ventilation (V) assessment. Conventionally, after image registration, the time series of each voxel is analyzed with regard to the signal amplitude of the cardiac and breathing frequency component, and further quantified by using either the amplitude of a full blood voxel or the expiratory signal. This analysis offers the possibility to acquire radiation-free V/Q maps simultaneously.

Using a standard 2D spoiled gradient-echo (GRE) sequence with a temporal resolution of 288 to 324 ms an image-sorting algorithm was developed to produce phase resolved functional lung imaging (PREFUL) with an interpolated temporal resolution of about 50 ms. With this method it is feasible to evaluate flow volume loops during tidal volume free breathing on a voxel level. PREFUL also depicts the propagation of the pulse wave during the cardiac cycle due to the pulsatile inflow of fresh blood into the 2D slice.

In recent years PREFUL ventilation MRI has been validated using ^{129}Xe and ^{19}F gas imaging with good regional agreement. For perfusion weighted imaging the cardiac phase is used at the time of maximum flow related enhancement in the lung parenchyma. Perfusion weighted PREFUL MRI has been validated using SPECT imaging as well as dynamic contrast enhanced (DCE) MRI. PREFUL has been tested in a dual center dual vendor setting and is currently applied in several ongoing multicenter trials. Furthermore, it has been shown to be feasible across a range of field strengths (0,55T-3T) and across all age groups.

Quantitative V/Q PREFUL MRI has been used in patients with CF, COPD, PH and COVID 19 to quantify disease and monitor treatment change after therapy. Furthermore, PREFUL V/Q imaging has been shown to predict transplant loss due to chronic lung allograft dysfunction (CLAD) in patients after lung transplantation. It seems that the dynamic flow-volume loop ventilation parameter have a higher predictive power and sensitivity to detect treatment changes compared to the “static” ventilation parameter, which only take the end inspiratory and end expiratory phases into account.

Recently, 3D PREFUL ventilation weighted MRI has been developed to cover the whole lung volume using a stack of stars GRE sequence. 3D PREFUL MRI achieves higher image resolution compared to 2D PREFUL MRI, which might be more sensitive to detect small ventilation changes in early lung disease.

In summary, PREFUL MRI is an exciting maturing development for quantitative ventilation and pulmomary pulse wave/perfusion imaging for regional pulmonary disease detection, quantification and treatment monitoring with added value to the current clinical routine.

References:

1. Voskrebenzev A, Gutberlet M, Klimeš F, Kaireit TF, Schönfeld C, Rotärmel A, Wacker F, Vogel-Claussen J. Feasibility of quantitative regional ventilation and perfusion mapping with phase-resolved functional lung (PREFUL) MRI in healthy volunteers and COPD, CTEPH, and CF patients. Magn Reson Med. 2018 Apr;79(4):2306-2314.

2. Voskrebenzev A, Gutberlet M, Kaireit TF, Wacker F, Vogel-Claussen J. Low-pass imaging of dynamic acquisitions (LIDA) with a group-oriented registration (GOREG) for proton MR imaging of lung ventilation. Magn Reson Med 2017;78:1496–1505.

3. Bauman G, Puderbach M, Deimling M, Jellus V, Chefd'hotel C, Dinkel J, Hintze C, Kauczor HU, Schad LR. Non-contrast-enhanced perfusion and ventilation assessment of the human lung by means of fourier decomposition in proton MRI. Magn Reson Med 2009;62:656–664.

4. Voskrebenzev A, Kaireit TF, Klimeš F, Pöhler GH, Behrendt L, Biller H, Berschneider K, Wacker F, Welte T, Hohlfeld JM, Vogel-Claussen J.PREFUL MRI Depicts Dual Bronchodilator Changes in COPD: A Retrospective Analysis of a Randomized Controlled Trial. Radiol Cardiothorac Imaging. 2022 Apr 21;4(2):e210147.

5. Kaireit TF, Kern A, Voskrebenzev A, Pöhler GH, Klimes F, Behrendt L, Gutberlet M, Moher-Alsady T, Dittrich AM, Wacker F, Hohlfeld J, Vogel-Claussen J. Flow Volume Loop and Regional Ventilation Assessment Using Phase-Resolved Functional Lung (PREFUL) MRI: Comparison With 129 Xenon Ventilation MRI and Lung Function Testing. J Magn Reson Imaging. 2021 Apr;53(4):1092-1105.

6. Behrendt L, Voskrebenzev A, Klimeš F, Gutberlet M, Winther HB, Kaireit TF, Alsady TM, Pöhler GH, Derlin T, Wacker F, Vogel-Claussen J. Validation of Automated Perfusion-Weighted Phase-Resolved Functional Lung (PREFUL)-MRI in Patients With Pulmonary Diseases. J Magn Reson Imaging. 2020 Jul;52(1):103-114.

7. Kaireit TF, Voskrebenzev A, Gutberlet M, Freise J, Jobst B, Kauczor HU, Welte T, Wacker F, Vogel-Claussen J. Comparison of quantitative regional perfusion-weighted phase resolved functional lung (PREFUL) MRI with dynamic gadolinium-enhanced regional pulmonary perfusion MRI in COPD patients. J Magn Reson Imaging. 2019 Apr;49(4):1122-1132

8. Pöhler GH, Klimeš F, Behrendt L, Voskrebenzev A, Gonzalez CC, Wacker F, Hohlfeld JM, Vogel-Claussen J. Repeatability of Phase-Resolved Functional Lung (PREFUL)-MRI Ventilation and Perfusion Parameters in Healthy Subjects and COPD Patients. J Magn Reson Imaging. 2021 Mar;53(3):915-927.

9. Munidasa S, Zanette B, Couch M, Grimm R, Seethamraju R, Dumas MP, Wee W, Au J, Braganza S, Li D, Woods J, Ratjen F, Santyr G. Inter- and intravisit repeatability of free-breathing MRI in pediatric cystic fibrosis lung disease. Magn Reson Med. 2022 Dec 28.

10. Lévy S, Heiss R, Grimm R, Grodzki D, Hadler D, Voskrebenzev A, Vogel-Claussen J, Fuchs F, Strauss R, Achenbach S, Hinsen M, Klett D, Schmid J, Kremer AE, Uder M, Nagel AM, Bickelhaupt S. Free-Breathing Low-Field MRI of the Lungs Detects Functional Alterations Associated With Persistent Symptoms After COVID-19 Infection. Invest Radiol. 2022 Nov 1;57(11):742-751.

11. Moher Alsady T, Voskrebenzev A, Greer M, Becker L, Kaireit TF, Welte T, Wacker F, Gottlieb J, Vogel-Claussen J. MRI-derived regional flow-volume loop parameters detect early-stage chronic lung allograft dysfunction. J Magn Reson Imaging. 2019 Dec;50(6):1873-1882.

12. Voskrebenzev A, Vogel-Claussen J. Proton MRI of the Lung: How to Tame Scarce Protons and Fast Signal Decay. J Magn Reson Imaging. 2021 May;53(5):1344-1357.

13. Pöhler GH, Löffler F, Klimeš F, Behrendt L, Voskrebenzev A, González CC, Westhoff-Bleck M, Wacker F, Vogel-Claussen J. Validation of Phase-Resolved Functional Lung (PREFUL) Magnetic Resonance Imaging Pulse Wave Transit Time Compared to Echocardiography in Chronic Obstructive Pulmonary Disease. J Magn Reson Imaging. 2022 Aug;56(2):605-615.

14. Glandorf J, Klimeš F, Voskrebenzev A, Gutberlet M, Behrendt L, Crisosto C, Wacker F, Ciet P, Wild JM, Vogel-Claussen J. Comparison of phase-resolved functional lung (PREFUL) MRI derived perfusion and ventilation parameters at 1.5T and 3T in healthy volunteers. PLoS One. 2020 Dec 30;15(12):e0244638.

15. Couch MJ, Munidasa S, Rayment JH, Voskrebenzev A, Seethamraju RT, Vogel-Claussen J, Ratjen F, Santyr G. Comparison of Functional Free-Breathing Pulmonary 1H and Hyperpolarized 129Xe Magnetic Resonance Imaging in Pediatric Cystic Fibrosis. Acad Radiol. 2021 Aug;28(8):e209-e218.

16. Klimeš F, Voskrebenzev A, Gutberlet M, Kern A, Behrendt L, Kaireit TF, Czerner C, Renne J, Wacker F, Vogel-Claussen J. Free-breathing quantification of regional ventilation derived by phase-resolved functional lung (PREFUL) MRI. NMR Biomed. 2019 Jun;32(6):e4088.

17. Klimeš F, Voskrebenzev A, Gutberlet M, Kern AL, Behrendt L, Grimm R, Suhling H, Crisosto CG, Kaireit TF, Pöhler GH, Glandorf J, Wacker F, Vogel-Claussen J. 3D phase-resolved functional lung ventilation MR imaging in healthy volunteers and patients with chronic pulmonary disease. Magn Reson Med. 2021 Feb;85(2):912-925.

18. Klimeš F, Voskrebenzev A, Gutberlet M, Obert AJ, Pöhler GH, Grimm R, Behrendt L, Crisosto C, Glandorf J, Moher Alsady T, Wacker F, Vogel-Claussen J. Repeatability of dynamic 3D phase-resolved functional lung (PREFUL) ventilation MR Imaging in patients with chronic obstructive pulmonary disease and healthy volunteers. J Magn Reson Imaging. 2021 Aug;54(2):618-629.

19. Marshall H, Voskrebenzev A, Smith LJ, Biancardi AM, Kern AL, Collier GJ, Wielopolski PA, Ciet P, Tiddens HAWM, Vogel-Claussen J, Wild JM. 129 Xe and Free-Breathing 1 H Ventilation MRI in Patients With Cystic Fibrosis: A Dual-Center Study. J Magn Reson Imaging. 2022 Oct 11. doi: 10.1002/jmri.28470.

20. Behrendt L, Smith LJ, Voskrebenzev A, Klimeš F, Kaireit TF, Pöhler GH, Kern AL, Gonzalez CC, Dittrich AM, Marshall H, Schütz K, Hughes PJC, Ciet P, Tiddens HAWM, Wild JM, Vogel-Claussen J. A dual center and dual vendor comparison study of automated perfusion-weighted phase-resolved functional lung magnetic resonance imaging with dynamic contrast-enhanced magnetic resonance imaging in patients with cystic fibrosis. Pulm Circ. 2022 Apr 5;12(2):e12054.

21. Pöhler GH, Klimes F, Voskrebenzev A, Behrendt L, Czerner C, Gutberlet M, Cebotari S, Ius F, Fegbeutel C, Schoenfeld C, Kaireit TF, Hauck EF, Olsson KM, Hoeper MM, Wacker F, Vogel-Claussen J. Chronic Thromboembolic Pulmonary Hypertension Perioperative Monitoring Using Phase-Resolved Functional Lung (PREFUL)-MRI. J Magn Reson Imaging. 2020 Aug;52(2):610-619.

22. Heiss R, Tan L, Schmidt S, Regensburger AP, Ewert F, Mammadova D, Buehler A, Vogel-Claussen J, Voskrebenzev A, Rauh M, Rompel O, Nagel AM, Lévy S, Bickelhaupt S, May MS, Uder M, Metzler M, Trollmann R, Woelfle J, Wagner AL, Knieling F. Pulmonary Dysfunction after Pediatric COVID-19. Radiology. 2022 Sep 20:221250.

23. Lasch F, Karch A, Koch A, Derlin T, Voskrebenzev A, Alsady TM, Hoeper MM, Gall H, Roller F, Harth S, Steiner D, Krombach G, Ghofrani HA, Rengier F, Heußel CP, Grünig E, Beitzke D, Hacker M, Lang IM, Behr J, Bartenstein P, Dinkel J, Schmidt KH, Kreitner KF, Frauenfelder T, Ulrich S, Hamer OW, Pfeifer M, Johns CS, Kiely DG, Swift AJ, Wild J, Vogel-Claussen J. Comparison of MRI and VQ-SPECT as a Screening Test for Patients With Suspected CTEPH: CHANGE-MRI Study Design and Rationale. Front Cardiovasc Med. 2020 Apr 9;7:51.

24. Kaireit TF, Gutberlet M, Voskrebenzev A, Freise J, Welte T, Hohlfeld JM, Wacker F, Vogel-Claussen J. Comparison of quantitative regional ventilation-weighted fourier decomposition MRI with dynamic fluorinated gas washout MRI and lung function testing in COPD patients. J Magn Reson Imaging. 2018 Jun;47(6):1534-1541.

25. Glandorf J, Klimeš F, Behrendt L, Voskrebenzev A, Kaireit TF, Gutberlet M, Wacker F, Vogel-Claussen J. Perfusion quantification using voxel-wise proton density and median signal decay in PREFUL MRI. Magn Reson Med. 2021 Sep;86(3):1482-1493.

4D Proton MRI of the Lung at High Spatiotemporal Resolution

Wilson Miller, University of Virginia

Robust implementation of proton lung MRI must overcome a variety of challenges, most prominently: low proton density and short T_2* of lung parenchyma, and cyclical motion of the heart and lung during image acquisition. Nonselective 3D excitation combined with ultra-short echo time (UTE) or zero echo time (ZTE) radial readouts are often employed to address the T2* limitation. Moreover, the oversampling of central k-space provided by 3D radial trajectories naturally assists in mitigating heart-motion artifacts. Further combining UTE readout with a balanced steady-state free precession (bSSFP) excitation scheme maximizes the sampled signal per unit time, thereby addressing the challenge posed by low proton density in lung parenchyma[1,2]. However, the overall advantage of bSSFP (over spoiled RF pulse trains) diminishes at higher field strengths. Image artifacts caused by lung motion can be mitigated by using breath holds or prospective respiratory gating[1]. However, breath-hold imaging places restrictive limits on scan time (and thereby image resolution and SNR), while prospective gating increases scan time and decreases sampling efficiency. Moreover, both of these approaches miss the opportunity to image throughout the breathing cycle.

There has been significant interest in recent years in developing techniques that combine continuous image acquisition during free breathing with retrospective motion sorting to produce 3D images of the lung at one or more phases of the breathing cycle. Such techniques require a signal tied to inflation level, which can be provided by a mechanical breathing sensor but can also be extracted from the imaging data itself using various strategies ranging from zero-dimensional (DC) to three-dimensional motion tracking. Following motion sorting, the nonuniformly under-sampled temporal frames can be reconstructed using any number of different model-based approaches, including CG-SENSE[3], XD-GRASP[4], L1-ESPIRiT[5], and iMoCo[6].

In short, there are many choices to make when implementing an image acquisition and reconstruction pipeline for high-resolution lung MRI. In our lab, we are particularly interested in combining proton lung MRI with hyperpolarized xenon MRI, which places further constraints on the particular scanner (and therefore magnetic field strength) used. This presentation will review our experience balancing all these different considerations, towards creating optimized free-breathing proton imaging schemes for 1.5T and 3T scanners.

1. Miller GW et al. Advances in functional and structural imaging of the human lung using proton MRI. *NMR Biomed* 27(12):1542-1556 (2014).
2. Bauman G, Bieri O. Balanced steady-state free precession thoracic imaging with half-radial dual-echo readout on smoothly interleaved archimedean spirals. *Magn Reson Med* 84(1):237-246 (2020).
3. Pruessmann KP et al. Advances in sensitivity encoding with arbitrary k-space trajectories. *Magn Reson Med* 46(4):638-651 (2001).
4. Feng L et al. XD-GRASP: Golden-angle radial MRI with reconstruction of extra motion-state dimensions using compressed sensing. *Magn Reson Med* 75(2):775-788 (2016).
5. Jiang W et al. Motion robust high resolution 3D free-breathing pulmonary MRI using dynamic 3D image self-navigator. *Magn Reson Med* 79(6):2954-2967 (2018).
6. Zhu X et al. Iterative motion-compensation reconstruction ultra-short TE (iMoCo UTE) for high-resolution free-breathing pulmonary MRI. *Magn Reson Med* 83(4):1208-1221 (2020).

Proton MR Imaging at 0.55T

Adrienne Campbell-Washburn, PhD

National Heart, Lung, and Blood Institute, National Institutes of Health, Bethesda, MD

Proton pulmonary MRI is an ongoing challenge for conventional MRI systems because the air-tissue interfaces in the lung cause magnetic susceptibility gradients that corrupt the lung tissue signal. However, using a contemporary superconducting magnet operating at a lower field strength (eg. 0.55T), these artifacts are reduced, thereby improving image quality compared to 1.5T or 3T [1]. This image quality can be leveraged for a suite of MR imaging techniques to allow imaging of lung morphology, tissue characterization, and assessment of regional lung function and physiology.

Figure 1 provides an illustration of imaging the same patient with lymphangioleiomyomatosis using CT, 1.5T MRI, and 0.55T MRI where the improvement in cyst delineation and parenchymal signal at 0.55T can be appreciated. In a pilot study, we found that 0.55T MRI and CT provided similar information content [2]. More recently, we have leveraged the prolonged T2* at 0.55T to develop a free-breathing stack-of spirals for isotropic resolution [3].

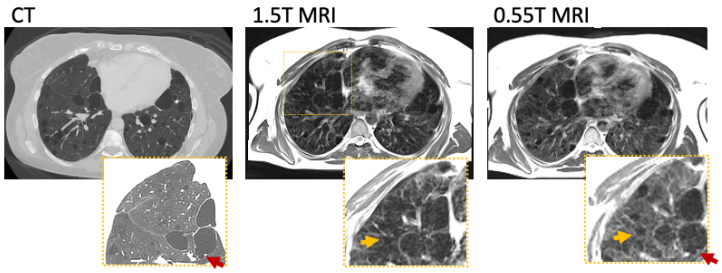

Figure 1: Patient with lymphangioleiomyomatosis imaged with CT, 1.5T MRI and 0.55T MRI. The improved parenchymal signal, cyst delineation (orange arrow) and small details (red arrow) at 0.55T can be appreciated.

In addition, we sought to develop functional imaging at 0.55T. Oxygen T1 relaxivity is higher at lower field strengths, and therefore oxygen-enhanced imaging is attractive [1]. We have demonstrated a 3D breath-hold method to quantify oxygen-enhancement and regional heterogeneity, and applied this method to assess patients with LAM. We demonstrated that the percentage of lung with low oxygen enhancement was modestly correlated with functional obstructional classification, and in the same cohort, we demonstrated the ability to quantify cyst burden from morphological MRI images with excellent correlation to CT [4]. More recently, we have demonstrated dynamic contrast enhanced pulmonary imaging with pharmacokinetic modelling to quantify perfusion at 0.55T.

The contemporary 0.55T platform is also well-suited to combined cardiopulmonary evaluations, since the heart and lung can be imaged in the same setting. Such an exam could include imaging of cardiac structure, cardiac function, pulmonary structure, pulmonary function, and cardiopulmonary physiology, with/without simultaneous hemodynamic measurements via catheters, and with/without exercise stress. For example, we have developed the capability to quantify cardiogenic pulmonary edema in patients with heart failure [5].

In summary, contemporary 0.55T MRI may provide a power platform for structural and functional proton MRI of the lung.

1. Campbell-Washburn, A.E., et al., *Opportunities in Interventional and Diagnostic Imaging by Using High-performance Low-Field-Strength MRI.* Radiology, 2019: p. 190452.
2. Campbell-Washburn, A.E., et al., *T2-weighted Lung Imaging Using a 0.55-T MRI System.* Radiol Cardiothorac Imaging, 2021. **3**(3): p. e200611.
3. Javed, A., et al., *Self-gated 3D Stack-of-Spirals Ultra-Short Echo-Time Pulmonary imaging at 0.55T. .* Magnetic Resonance in Medicine, 2021. **In Press**.
4. Bhattacharya, I., et al., *Assessment of Lung Structure and Regional Function Using 0.55 T MRI in Patients With Lymphangioleiomyomatosis.* Invest Radiol, 2021.
5. Seemann, F., et al., *Imaging gravity-induced lung water redistribution with automated inline processing at 0.55T MRI.* Under Review, 2022.

Quantitative Measures of Ventilation, Perfusion, and Ventilation-perfusion in the Human Lung Using Proton MRI

Rui C Sá
University of California, San Diego

Ventilation-perfusion matching is the most important mechanism determining gas exchange in health and disease. The ability to spatially characterize ventilation-perfusion opens a window into the study of regional functional changes originating from disease processes, as well as therapeutical interventions.

The Pulmonary Imaging Laboratory at the University of California, San Diego developed multiple quantitative proton MRI approaches that independently map ventilation and perfusion in the human lung. Ventilation is quantified using a combination of a fast gradient echo measurement of regional proton density[1] at end expiration (from which regional functional residual capacity is computed), and specific ventilation imaging[2], an oxygen enhanced MRI technique that measures specific ventilation (the regional ratio of tidal volume to local FRC). Perfusion quantification is obtained using arterial spin labelling (ASL)[3].

All these techniques have been validated and/ or cross-correlated against independent measurement [4,5,6,7]. Images are acquired as 'thick' (15mm) 2D slices, typically (but not necessarily) in the sagittal plane. Multiple slices are acquired simultaneously (up to 4 without compromising spatial resolution), covering most of the lung (typically the right lung, to maximize the sampled lung volume and minimize the noise generated by heart movements).

Ventilation-perfusion ratio quantification is achieved from the independent maps of ventilation and perfusion. To minimize potential effects of mis-registration across modalities when creating ventilation-perfusion maps, spatial maps of ventilation and perfusion are combined at a spatial resolution of ~1cm^3 (~5-6 acini). Independent ventilation-perfusion maps can be acquired ~30 min apart, an interval largely determined by the ~18min it takes to acquire specific ventilation maps. We have recently shown this time can be decreased ~7min[8].

These techniques have been deployed to understand the effects of exercise, aging, vaping, asthma, pulmonary arterial hypertension, etc, in ventilation, perfusion, and ventilation-perfusion ratio and their spatial distributions within the lung. The imaging protocol is optimally suited for longitudinal follow up and the study of functional response to interventions (e.g. bronchoconstriction / bronchodilation). Given the built-in redundancy of the human lung, characterization of regional ventilation, perfusion, and particularly, ventilation-perfusion disruptions, are potential early biomarkers of disease, as regional disruption will precede – potentially by significant and actionable intervals - detectable changes in the (blunt) integrative measurements commonly used for diagnosis.

[1] Theilmann, R. J. *et al.* Quantitative MRI measurement of lung density must account for the change in T2(*) with lung inflation. *J Magn Reson Imaging* **30,** 527–534 (2009).

[2] Sá, R. C. *et al.* Vertical distribution of specific ventilation in normal supine humans measured by oxygen-enhanced proton MRI. *J Appl Physiol* **109,** 1950–1959 (2010).

[3] Hopkins, S. R. *et al.* Vertical gradients in regional lung density and perfusion in the supine human lung: the Slinky effect. *J Appl Physiol* **103,** 240–248 (2007).

[4] Holverda, S. *et al.* Measuring lung water: ex vivo validation of multi-image gradient echo MRI. *J Magn Reson Imaging* **34,** 220–224 (2011).

[5] Sá, R. C. *et al.* Validating the distribution of specific ventilation in healthy humans measured using proton MR imaging. *J Appl Physiol* **116,** 1048–1056 (2014).

[6] Arai, T. J. *et al.* Comparison of quantitative multiple-breath specific ventilation imaging using colocalized 2D oxygen-enhanced MRI and hyperpolarized 3He MRI. *J Appl Physiol* **125,** 1526–1535 (2018).

[7] Sá, R. C. *et al.* Measurement of the distribution of ventilation-perfusion ratios in the human lung with proton MRI: comparison with the multiple inert-gas elimination technique. *J Appl Physiol* **123,** 136–146 (2017).

[8] Geier, E. T., Prisk G.K., Sá, R.C. Measuring short-term changes in specific ventilation using dynamic specific ventilation imaging. *J Appl Physiol* **132:6,** 1370–1378 (2022).

Saturday

February 25th, 2023

Workshop: Day 3

Title: Predicting the Outcome of Lung Transplantation Using Machine Learning

Speaker: Pratik Chaudhari

Purpose:
Evaluating whether a potential donor lung is a good match for a particular recipient is hard; physicians often make decisions using qualitative reasoning and incomplete information. Tools from modern Machine Learning (ML) can help by leveraging historical data from transplant surgeries to predict the outcome of a specific donor-recipient match.

Results:
We study 61 variables (selected to have less than 10% missing data and to be clinically relevant to lung transplantation) of 18,027 subjects in the United Network for Organ Sharing (UNOS) database (aged 18+ years with lung-only transplant surgeries performed since 2005). A Random Forest (RF) is used to predict missing entries for each feature given entries of all other features in the data. Imputation is performed iteratively (25 iterations) on all features to produce a dataset; five imputed datasets are created. Two Cox Proportional Hazards (Cox-PH) models, one with the hazards function modeled using RF and another with a linear model, are used to predict the post-transplant survival probability. RFs are powerful ensemble methods that can model nonlinear interactions in the data for both regression and imputation. Permutation tests and partial dependence plots are used to quantify variable importance and interpret RF-based ML models.

RF-based imputation can accurately fill in up to 10% missing entries in lung transplantation data. As a validation of the imputation method, an RF for regressing theLung Allocation Score (LAS) using imputed data obtains R2=0.73, RMSE=7.78 compared to a linear regression with median imputation that obtains R2=0.58, RMSE=14.28. Standard Cox-PH model obtains a continuous ranked probability score (CRPS, integral of Brier score) of 0.189 which is much higher than that of RF-based Cox-PH model (0.094); lower CRPS score is better. Variable importance methods reveal that age, recipient's creatinine, diagnosis and BMI are the top few strongest predictors of the transplant outcome; these are different from the top few important variables that make the LAS (O2 requirement at registration, days on waitlist, diagnosis, O2 requirement at rest).

We next pre-trained a deep neural network (DNN) with 3 layers of 1024 neurons each to predict survival one year post-transplant in order to characterize its performance on different sub-groups of the population. We focus on three features flagged as strong predictors of survival probability: age, creat_trr and ethnicity. For each feature, we sequester data into three sub-groups and for each sub-group, we fine-tune the pre-trained DNN using data from that specific sub-group. We ensured that the pre-trained model was trained with sufficient regularization (Dropout), and the fine-tuning was performed carefully using stochastic gradient descent (SGD). Such adaptation improves predictions for almost all sub-groups of the population: prediction error improves for all ages < 65 years while it is unchanged for the rest; we see improved predictions for subjects with creatinine between 0.62-1.01; we see dramatic improvements in the predictive accuracy of 1-year post-transplant survival for Hispanic and Black populations.

Discussion:
Machine learning models have shown great promise for precision diagnosis, treatment prediction, and a number of other clinical applications. This has led to increasing interest in building systems where such models can aid human experts for accurate and efficient decision making in clinical settings. But data for problems in lung transplantation, and healthcare in general, is heterogeneous and different demographic, clinical and genetic features, all play a role in the outcome. Current machine learning methods, which seek to identify salient features across the entire population, work poorly in such cases. Even if predictive models are accurate on average, they can be quite sub-optimal for specific sub-groups. In such situations, techniques to mitigate this heterogeneity and explicitly adapt trained ML models to different demographic and clinical population sub-groups can be very effective.

Conclusions:
RandomForests improve the accuracy of imputation of missing data and post-transplant survival prediction compared to existing methods in the literature. Deep learning-based methods to explicitly adapt the learned model can significantly improve predictions in under-represented sub-groups in the population.

The Role of CT Imaging in Lung Transplant

Micheal McInnis, M.D.

Computed tomography (CT) is used routinely in the post-operative monitoring of lung transplant patients. Although protocols vary, we perform CT acquired at end-inspiration and end-expiration using a low dose technique CT at 3, 6, 9, 12, 18 and 24 months which provides a wealth of imaging data. While there are many post-transplant complications, the main cause of lung transplant allograft failure is chronic lung allograft dysfunction (CLAD)[1].

There are two principal phenotypes of CLAD with distinct radiologic presentations. The first and most common is bronchiolitis obliterans syndrome (BOS) characterized by progressive and irreversible airway obstruction. Radiologically, this classically presents with progressive air trapping and CT imaging at end-expiration excels at demonstrating this[1]. Parametric response mapping (PRM) is a novel method of quantifying this air trapping on CT and is the subject of recent and ongoing studies in CLAD[2,3]. The second and less common phenotype is restrictive allograft syndrome (RAS) characterized by volume loss and fibrosis with an upper lung zone predominance[4]. The prognosis for RAS is much poorer than BOS[1].

We investigated the role of pulmonary opacities on CT at the time of CLAD onset using a commercially available quantitative lung texture analysis tool that was machine learning trained. Distinct from previously published studies, our CTs were performed close to the time of CLAD onset, in part because of our frequent CT surveillance program. The CT analysis tool segments and separates the lung into five textures: normal, hyperlucent, ground glass, reticular and honeycombing. In addition to radiologist interpretation, quantitative lung texture was found to be predictive of allograft survival at the time of CLAD onset, independent of CLAD phenotype or other factors in our multivariable model. Indeed, quantitative CT effectively discriminated between CLAD phenotypes with characteristic quantitative imaging patterns for BOS and RAS. Furthermore, pulmonary vessel volume, a measure unique to quantitative CT with no direct radiologist correlate, was found to be best in phenotyping CLAD and in prognostication[5].

1. Verleden GM, Glanville AR, Lease ED, Fisher AJ, Calabrese F, Corris PA, Ensor CR, Gottlieb J, Hachem RR, Lama V, Martinu T, Neil DAH, Singer LG, Snell G, Vos R. Chronic lung allograft dysfunction: Definition, diagnostic criteria, and approaches to treatment-A consensus report from the Pulmonary Council of the ISHLT. J Heart Lung Transplant 2019: 38(5): 493-503.
2. Belloli EA, Degtiar I, Wang X, Yanik GA, Stuckey LJ, Verleden SE, Kazerooni EA, Ross BD, Murray S, Galbán CJ, Lama VN. Parametric Response Mapping as an Imaging Biomarker in Lung Transplant Recipients. Am J Respir Crit Care Med 2017: 195(7): 942-952.
3. Belloli EA, Gu T, Wang Y, Vummidi D, Lyu DM, Combs MP, Chughtai A, Murray S, Galbán CJ, Lama VN. Radiographic graft surveillance in lung transplantation: Prognostic role of parametric response mapping. Am J Respir Crit Care Med 2021: 204(8): 967-976.
4. Sato M, Waddell TK, Wagnetz U, Roberts HC, Hwang DM, Haroon A, Wagnetz D, Chaparro C, Singer LG, Hutcheon MA, Keshavjee S. Restrictive allograft syndrome (RAS): a novel form of chronic lung allograft dysfunction. J Heart Lung Transplant 2011: 30(7): 735-742.
5. McInnis MC, Ma J, Karur GR, Houbois C, Levy L, Havlin J, Fuchs E, Tikkanen J, Chow CW, Huszti E, Marinu T. Chronic lung allograft dysfunction phenotype and prognosis by machine learning CT analysis. Eur Respir J 2022: 60(1): 2101652.

Hyperpolarized ^{129}Xe as Imaging Marker for Early Detection of CLAD

Faraz Amzajerdian

Purpose: Lung transplantation outcomes continue to be the poorest among whole organ transplants, primarily due to high rates of graft failure and a lack of treatment options, with chronic lung allograft dysfunction (CLAD) constituting the leading long-term cause of death. However, while treatments options remain limited, earlier CLAD diagnosis could enable the initiation of therapeutic management prior to the occurrence of irreversible damage. Unlike the current gold standard clinical assessment, spirometry, which cannot provide localized measures of lung function, hyperpolarized xenon-129 (HXe) MRI—and Xenon polarization Transfer Contrast (XTC) imaging in particular—is capable of quantifying regional gas uptake and exchange, and thus may be more sensitive to early restrictive or obstructive changes associated with CLAD. High-resolution maps of exchange between gas-phase (GP) xenon and xenon dissolved in the tissue membrane or red blood cells (RBC) can be calculated from the subsequent loss of GP signal after selective saturation of the desired dissolved-phase (DP) component[1] and, when combined with local measures of gas volume, provide a comprehensive evaluation of lung function.

Methods: Seven bilateral lung transplant recipients were imaged longitudinally at 3, 6 and 12 months post-transplant, with pulmonary function tests (PFTs) performed the day of imaging, in order to establish baseline metrics and trends. Images were acquired at end-exhalation using a multi-breath XTC technique consisting of three repeated schemes of 6 wash-in breaths of a HXe mixture and 4 normoxic wash-out breaths, with and without saturation of either RBC or tissue resonances. To maintain consistency throughout imaging, breathing rates and tidal volumes were guided by a coordinator; inhale and exhale flows were recorded to account for any variations in breathing. The flow measurements, along with the no-saturation, RBC-saturation, and tissue-saturation images, were fit voxel-wise to a modified fractional ventilation (FV) model[2] to generate maps of regional ventilation parameters including tidal volume (TV), functional residual capacity (FRC) and fractional ventilation (FV), in addition to the RBC- and tissue-gas exchange metrics.

Results & Discussion: For most subjects, one-second forced expiratory volume (FEV1), the clinically standard lung function metric, was at its lowest 3 months post-surgery, improving thereafter consistent with a typical recovery[3]. These trends were associated with decreasing average RBC-gas and tissue-gas exchange as well as increasing homogeneity, potentially reflecting either recovery following inflammatory responses to surgery or a gradual decline in perfusion or uptake. Comparing ventilation parameters with percent change in FEV1 revealed little change with TV, which is largely dependent on the respective sizes of donor and recipient lungs; for FRC, both heterogeneity and whole-lung averages tended to decrease with improved FEV1. These decreased expiratory gas volumes likely indicate greater lung recoil associated with improved ventilation efficiency, especially considering corresponding increases in FV. Even with this small sample of transplant subjects uncontrolled for age, gender, diagnosis or donor characteristics, strong correlations are still apparent and reflect physiological and functional changes associated with lung transplant recovery as well as potential CLAD development.

[1] Amzajerdian, Faraz, et al (2020). *Measuring pulmonary gas exchange using compartment-selective xenon-polarization transfer contrast (XTC) MRI*. MRM 85(5), 2709-2722.
[2] Hamedani, Hooman, et al (2016). *Regional fractional ventilation by using multibreath wash-in 3He MR imaging*. Radiology 279(3), 917-924.
[3] Mason, David P., et al (2012). *Effect of changes in postoperative spirometry on survival after lung transplantation*. The Journal of Thoracic and Cardiovascular Surgery, 144(1), 197-203.e2.

Lung Metabolism and Graft Preservation on *Ex Vivo* Lung Perfusion

Kentaro Noda, PhD. University of Pittsburgh

Ex vivo lung perfusion (EVLP) contributes to expanding the donor pool in lung transplantation and increases 10-15% of transplants every year.[1] The current role of EVLP is to find out available donors from a marginal donor pool through secondary evaluation. During the evaluation, lung grafts exhibit glycolysis and lactate production with progressive acidosis. Recently, our institutional data of clinical EVLP showed that the declining glucose and acidosis progression in perfusate had a significant correlation with graft quality.[2] Also, clinical data showed transplanted grafts after EVLP did not show fair outcomes compared to the standard lung transplant control cohort.[2] Nonetheless, the current EVLP system does not have any metabolic support to keep the grafts viable, thus the role of EVLP as the graft preservation as well as therapeutic platform is limited. Our research group has been focusing on graft metabolism during EVLP and investigating its regulation on graft preservation. We have been investigating to improve the EVLP graft preservation milieu by modulating graft metabolism with active oxygenation strategies and mitochondrial protection using a rat EVLP model.

Through our investigation of graft oxygenation via bronchial artery or pulmonary artery, we found the graft metabolism was significantly improved along with better graft quality and attenuated proinflammatory response compared to normal EVLP setting.[3,4] This suggests that lung grafts on current EVLP may be exposed to hypoxia therefore the grafts show high glycolysis. While EVLP incurs mitochondrial dysfunction and death in lung grafts, the active oxygenation strategies preserved mitochondria in the lungs after EVLP. We next tried to preserve the mitochondria during EVLP in a normal setting and applied cyclosporin A to prevent the opening of mitochondrial membrane transition pores in the lungs. Administration of cyclosporin A successfully preserved mitochondria in the lungs during EVLP and significantly attenuated glucose consumption and calcium release compared to control.[5] Importantly, lungs regulating graft metabolism during EVLP exhibited significantly improved posttransplant graft function compared to control.

Overall, our findings suggest that monitoring graft metabolism can be an alternative graft evaluation during EVLP, and the metabolic regulation can improve lung preservation milieu on EVLP leading to better posttransplant outcomes. The idea to keep enough energetic support or balancing the demand and support of graft metabolism on EVLP may help to develop a novel graft preservation strategy to expand the further donor pool and improve posttransplant outcomes in lung transplantation.

References

1. Noda K, Furukawa M, Chan EG, Sanchez PG. Expanding Donor Options for Lung Transplant: Extended Criteria, Donation After Circulatory Death, ABO Incompatibility, and Evolution of Ex Vivo Lung Perfusion. *Transplantation.* 2022.
2. Noda K, Chan EG, Furukawa M, et al. Single-center experience of ex vivo lung perfusion and subsequent lung transplantation. *Clinical Transplantation.* 2023;n/a(n/a): e14901.
3. Noda K, Tane S, Haam SJ, et al. Optimal ex vivo lung perfusion techniques with oxygenated perfusate. *The Journal of Heart and Lung Transplantation.* 2017;36(4): 466-474.
4. Tanaka Y, Noda K, Isse K, et al. A novel dual ex vivo lung perfusion technique improves immediate outcomes in an experimental model of lung transplantation. *American Journal of Transplantation.* 2015;15(5): 1219-1230.
5. Haam S, Noda K, Philips BJ, Harano T, Sanchez PG, Shigemura N. Cyclosporin A Administration During Ex Vivo Lung Perfusion Preserves Lung Grafts in Rat Transplant Model. *Transplantation.* 2020;104(9): e252-e259.

Metabolic Changes in the Donor Lung During Ischemia as a Function of Time and Temperature

Zachary Schug

A successful approach to organ preservation is one that can maintain cellular energy, offer osmatic support, and lower the risk of post-transplant morbidity and mortality associated with ischemia-reperfusion injury. Despite the widespread usage of static cold storage (SCS) at 4 or 10^{o}C for donor lung preservation, we still know little about the metabolic changes that are suppressed at low temperatures, those triggered by unavoidable periods of warm ischemia, or the exact pathways through which these changes proceed. We therefore sought to define the impact of both time and temperature on the metabolic state of lung tissue during SCS using a liquid chromatography-mass spectrometry (LC-MS) based metabolomic approach, we analyzed >200 polar metabolites from rat lungs stored at either the clinically standard 4^{o}C or recently explored 10^{o}C (1). As organ preservation typically lasts no longer than 8 h, lung tissue was taken from individual rat lungs every 2 h for the first 8 h of SCS, as well as at 48 h of SCS, to compare changes in metabolism at the two different temperatures. We detected immediate decreases in the tricarboxylic acid (TCA) cycle intermediate alpha-ketoglutarate suggesting decreased mitochondrial metabolism. We also noted that succinate levels increased during SCS. Succinate was significantly higher in lungs stored at 10^{o}C for 8 h compared to both 0 h normal lungs and lungs stored at 4^{o}C for 8 h. To further investigate the impact on succinate metabolism upon reperfusion and reoxygenation, we placed lungs on an EVLP system post-SCS and compared metabolites isolated from 10^{o}C SCS lungs to those taken from lungs after 30 min of EVLP at 37^{o}C. Succinate levels increased during SCS but dropped after transfer to the EVLP system. Oxidation of succinate upon reperfusion has been linked to reactive oxygen species (ROS) generation in tissues (2, 3). We therefore compared the ratio of oxidized to reduced glutathione (GSSG/GSH) in SCS vs. EVLP lungs and saw that SCS decreased the levels of oxidized glutathione, while reperfusion on EVLP increased it. These results support a model whereby reperfusion of lungs on the EVLP reoxygenates the lung tissue and stimulates the electron transport chain in the mitochondria. The consequent oxidation of the NADH and succinate that accumulated during SCS overwhelms the CoQ pool which then leads to reverse electron transfer to Complex I and ROS production (4). Overall, our metabolomic studies indicated dynamic changes in mitochondrial metabolism during SCS centered around succinate, suggesting that strategies that directly address succinate levels before, or ROS during reperfusion, may ameliorate these detrimental effects.

1. Ali A, Wang A, Ribeiro RVP, Beroncal EL, Baciu C, Galasso M, Gomes B, Mariscal A, Hough O, Brambate E, Abdelnour-Berchtold E, Michaelsen V, Zhang Y, Gazzalle A, Fan E, Brochard L, Yeung J, Waddell T, Liu M, Andreazza AC, Keshavjee S, Cypel M. Static lung storage at 10 degrees C maintains mitochondrial health and preserves donor organ function. Sci Transl Med. 2021;13(611):eabf7601. Epub 2021/09/16. doi: 10.1126/scitranslmed.abf7601. PubMed PMID: 34524862.

2. Chouchani ET, Pell VR, Gaude E, Aksentijevic D, Sundier SY, Robb EL, Logan A, Nadtochiy SM, Ord ENJ, Smith AC, Eyassu F, Shirley R, Hu CH, Dare AJ, James AM, Rogatti S, Hartley RC, Eaton S, Costa ASH, Brookes PS, Davidson SM, Duchen

MR, Saeb-Parsy K, Shattock MJ, Robinson AJ, Work LM, Frezza C, Krieg T, Murphy MP. Ischaemic accumulation of succinate controls reperfusion injury through mitochondrial ROS. Nature. 2014;515(7527):431-5. Epub 2014/11/11. doi: 10.1038/nature13909. PubMed PMID: 25383517; PMCID: PMC4255242.

3. Murphy MP, Chouchani ET. Why succinate? Physiological regulation by a mitochondrial coenzyme Q sentinel. Nat Chem Biol. 2022;18(5):461-9. Epub 2022/04/29. doi: 10.1038/s41589-022-01004-8. PubMed PMID: 35484255; PMCID: PMC9150600.

4. Robb EL, Hall AR, Prime TA, Eaton S, Szibor M, Viscomi C, James AM, Murphy MP. Control of mitochondrial superoxide production by reverse electron transport at complex I. J Biol Chem. 2018;293(25):9869-79. Epub 2018/05/11. doi: 10.1074/jbc.RA118.003647. PubMed PMID: 29743240; PMCID: PMC6016480.

Contemporary Challenges and Opportunities to Improve Equity and Use of Organs for Lung Transplant

Edward Cantu, Joshua Diamond, Jason Christie, Robert Gallup, Jesse Hsu, Douglas Schaubel

The US transplant system has seen significant growth since its inception and recently achieved a historic milestone of 1 million organ transplants. Half of all transplants performed have occurred within the last 15 years with over 400,000 recipients alive today with a functioning transplant.[1] This has occurred through changes in organ allocation, introduction of new technologies and center changes in perception of risk. Despite the success of the US transplant system, as a whole, and the individual success seen in lung transplant, in particular, the National Academies of Sciences, Engineering and Medicine (NASEM) released a report in February of 2022 in response to a request from the U.S. Congress and the National Institutes of Health. NASEM identified inequity of access to transplant, limitations in transparency of decision making, significant variation in decision making and performance across transplant centers and under use of donated organs.[2]

Within the last decade, the number of lung recipients has increased by almost 42%.[3] Recent trends in lung organ allocation have resulted in transplantation of candidates with increased severity of illness. Reported consequences of these trends include increases in procurement costs, allograft discard rate, ischemic times, primary graft dysfunction (PGD) rates.[4] In addition to these challenges, the lack of transparency between transplant centers and patients on accountability for candidacy decision making and organ offer declines.[2] As a solution, the NASEM report recommended the development, implementation, and evaluation of objective standardized metrics to track performance and evaluate results of the transplant system. [2] This talk will cover our work in the development of PGD prediction, candidate risk assessment and future work to address identified challenges in lung transplantation.

References

1. UNOS. U.S. reaches historic milestone of 1 million transplants. (https://unos.org/news/u-s-reaches-1-million-transplants/).
2. Kizer KW, English RA, Hackmann M. Realizing the Promise of Equity in the Organ Transplantation System. Washington (DC)2022.
3. UNOS. National Transplant Data. (https://optn.transplant.hrsa.gov/data/view-data-reports/national-data/#).
4. Cantu E, Diamond JM, Cevasco M, et al. Contemporary trends in PGD incidence, outcomes, and therapies. J Heart Lung Transplant 2022;41(12):1839-1849. DOI: 10.1016/j.healun.2022.08.013.

Neutrophil trafficking after lung transplantation

Daniel Kreisel

Neutrophils have been shown to be critical mediators of tissue damage during ischemia reperfusion injury (1). Primary graft dysfunction, a condition that is mediated by ischemia reperfusion injury, continues to be a key factor that adversely impacts short- and long-term outcomes after lung transplantation. Therefore, it is important to gain a better understanding of cellular and molecular requirements that guide neutrophils into transplanted lungs. Intravital two-photon imaging has allowed investigators to study dynamic leukocyte behavior in a variety of tissues. Our group has developed techniques to stabilize moving mouse organs, including ventilated lungs and beating heart grafts, and image these in vivo (2, 3). Intravital two-photon imaging of ventilated mouse lungs has enabled us to gain new insights into cues that regulate neutrophil trafficking into pulmonary grafts. We have uncovered an interplay between donor-resident non-classical and recipient spleen-derived classical monocytes that, through production of chemokines and cytokines, regulate the recruitment and extravasation of neutrophils after lung transplantation(4, 5). Using a model of severe ischemia reperfusion injury, we have shown that necroptotic death of graft cells, which results in the release of damage-associated molecular patterns and activation of a variety of donor and recipient cells, is an important upstream event that initiates neutrophil recruitment (6). Intravital two-photon imaging has also revealed differences between cues that regulate neutrophil trafficking into freshly reperfused lungs vs. hearts (7). Thus, our studies have lay a foundation for the development of new therapeutic strategies to inhibit neutrophil trafficking into lung grafts, which hold promise to prevent or ameliorate primary graft dysfunction.

1. D. Kreisel *et al.*, Bcl3 prevents acute inflammatory lung injury in mice by restraining emergency granulopoiesis. *J Clin Invest* **121**, 265-276 (2011).
2. D. Kreisel *et al.*, In vivo two-photon imaging reveals monocyte-dependent neutrophil extravasation during pulmonary inflammation. *Proc Natl Acad Sci U S A* **107**, 18073-18078 (2010).
3. W. Li *et al.*, Intravital 2-photon imaging of leukocyte trafficking in beating heart. *J Clin Invest* **122**, 2499-2508 (2012).
4. C. Kurihara *et al.*, Crosstalk between nonclassical monocytes and alveolar macrophages mediates transplant ischemia-reperfusion injury through classical monocyte recruitment. *JCI Insight* **6** (2021).
5. H. M. Hsiao *et al.*, Spleen-derived classical monocytes mediate lung ischemia-reperfusion injury through IL-1beta. *J Clin Invest* **128**, 2833-2847 (2018).
6. W. Li *et al.*, Necroptosis triggers spatially restricted neutrophil-mediated vascular damage during lung ischemia reperfusion injury. *Proc Natl Acad Sci U S A* **119**, e2111537119 (2022).
7. W. Li *et al.*, Ferroptotic cell death and TLR4/Trif signaling initiate neutrophil recruitment after heart transplantation. *J Clin Invest* **129**, 2293-2304 (2019).

Photon-Counting CT - Opportunities for Interdisciplinary Preclinical and Clinical Research

Peter B. Noël
University of Pennsylvania

Photon counting computed tomography (PCCT) is a novel imaging technology that promises improved image quality, reduced radiation dose, and increased accuracy compared to conventional Computed Tomography (CT). It is a type of x-ray imaging that uses advanced detectors and specialized imaging algorithms to measure the number of photons that pass through a patient's body. Today, PCCT is used to diagnose and monitor various diseases, including cancer, cardiovascular disease, and pulmonary disorders. In this presentation, we present a review of PCCT technology, its advantages and disadvantages, and potential clinical applications.

First, the basics of PCCT will be discussed. This includes a description of the first clinical PCCT system (Naeotom Alpha, Siemens Healthineers) which has received FDA clearance. In general, PCCT scanners are equipped with a standard x-ray source and photon-counting detectors (PCDs). PCDs, in contrast to conventional x-ray detectors, are capable of providing energy information for individual photons and dividing them into several data bins based upon their energy threshold. Second, the advantages and limitations of PCCT will be discussed. Several clinical benefits are derived from this technology including improved CNR, higher spatial resolution, fewer image artifacts (e.g., reduced blooming, beam hardening artifacts), and reduced radiation dose.

Finally, the clinical applications in pulmonary diagnostics will be discussed. PCCT has been applied in clinical studies of various pulmonary diseases, such as asthma and chronic obstructive pulmonary disease (COPD). In a study of COPD, PCCT was used to evaluate airway wall thickness and the degree of emphysema. Results showed that PCCT was able to detect subtle differences in airway wall thickness and emphysema that were not detectable with conventional CT.

Overall, photon counting CT has proven to be a valuable tool in both clinical and research settings. Its ability to provide more detailed imaging, with improved dose efficiency, has enabled it to become – in the near future – a mainstay in medical imaging.

Fundamentals of Photon Counting CT and Experiences with the First Clinically Available System

Juan Carlos Ramirez-Giraldo, PhD

Photon-counting detector (PCD)-CT is by now recognized as a strong technological trend for computed tomography in years to come with the promise to reduce dose, improve image quality and drive forward new clinical CT applications. As of 2023, most manufacturers have existing PCD CT prototypes using technologies based on CdTe, CdZTe and Silicon. In October 2021, the FDA cleared the first clinically available PCD-CT system in the US, the NAEOTOM Alpha (Siemens Healthineers, Forchheim Germany).

PCD-CT provides four major benefits including improved spatial resolution, reduced electronic noise, equal energy weighting, and concurrent spectral capabilities. In lung imaging, spatial resolution has a strong role to play. Typical spatial resolution of energy-integrating detectors (EID-CT) range from 0.5mm to 1mm. With PCD-CT the ability to scan with 0.2mm isotropic resolution, early clinical studies have found is possible to better characterize lung anatomy and texture which could be helpful for interstitial lung disease. Improved spatial resolution will also aid in characterization of lung nodules. With the elimination of electronic noise and improved dose efficiency of PCD-CT; early studies are showing is possible to substantially reduce radiation exposures in lung CT examinations, while still maintaining or improving image quality and preserving CT number accuracy.

Dual-source CT improves temporal resolution and acquisition speed, which is valuable in lung CT to reduce respiratory motion induced artefacts when imaging challenging patients such as pediatrics or uncooperative subjects. When dual-source is combined with PCD-CT, similar benefits apply and when used for contrast enhanced and angiography CT exams, enables the use of spectral applications such as iodine mapping to characterize lung perfused blood volume, VNC imaging or virtual monoenergetic images, without acquisition speed tradeoffs. As a result, it is possible to get high spatial resolution, excellent temporal resolution and spectral capabilities, all in the same examination.

With a larger number of detector elements to support improved resolution and with the use of two or more energy thresholds; the amount of information generated during a PCD-CT examinations grows substantially compared with standard CT. While in a research setting more information provides opportunities for investigation, efforts should be spent in the clinics to improve workflows harnessing the added information to benefit patients. And hopefully this will not come at the expense of increasing reading times for radiologists. Coincidentally, automation of workflows is an active area of focus in hospitals and by manufactures which should aid in the goal to maximize the benefits brought by PCD-CT.

End-to-end radiomics standardization framework

Grace J. Gang

Radiomics have demonstrated strong predictive ability for a range for clinical tasks related to disease diagnosis, treatment efficacy, patient prognosis, etc. The growing availability of large-scale image databases and advancement of artificial intelligence techniques further fueled interests in radiomics research. One of the main obstacles to such research is the lack of standardization between patient scans. For x-ray computed tomography (CT) in particular, varying image properties as a result of vendors, scanning protocols, reconstruction algorithms, and patient habitus introduce scanner-dependent variability that reduces the predictive power and generalizability of radiomics models. While these effects can be mitigated with careful data curation and standardization of imaging techniques, this is impractical for diverse sources of image data. In this work, we propose to extend traditional end-to-end imaging system models to include radiomics calculation as an explicit stage. Such models have traditionally been established to predict how spatial resolution and noise vary as a result of different imaging conditions; the extended step allows the prediction of radiomics variability in a similar manner. Furthermore, the forward model forms a basis for inverting the process to estimate the true underlying radiomics. Utility of the framework is demonstrated on histogram- and gray level co-occurrence matrix (GLCM) based radiomics features, where ground truth feature values are recovered under a range of radiation dose and reconstruction kernels. This framework has the potential to standardize radiomics across imaging conditions permitting more widespread application of radiomics models; larger, more diverse image databases; and improved diagnoses and inferences based on standardized radiomics values.

Hierarchical Phase Contrast Tomography: A Method for Imaging Multiscale Three-dimensional Structures in Whole Human Lung

Claire Walsh

Hierarchical-Phase Contrast Tomography (HiP-CT) is a new synchrotron X-ray tomography technique that spans a previously poorly explored scale in our understanding of human anatomy, the micron to whole intact organ scale. HiP-CT utilises the European Synchrotron radiation Facility, taking full advantage of the higher energy, greater beam coherence and small source size of the World's only 4th generation X-ray source the - ESRF's Extremely Brilliant Source (ESRF-EBS). With HiP-CT it is possible to scan intact human lungs (ex vivo) at 20-8um/voxel for the whole lung; down to 1um/voxel in selected local regions, without physically sectioning the organ[1]. The data produced are isotropic 3-dimensional and the higher resolution volume images are precisely registered to the lower resolution whole lung scans. This technology is transformative, particularly for the assessment of 3-dimensional and multiscale structures e.g. vascular networks. It's application to the pulmonary field is already demonstrating utility in understanding these structures in pathological cases.

The vascular architecture of the human lung is highly complex, with physiological and pathological vascular topologies, such as shunts, that cannot be assessed via classical 2D histology[2,3]. Much of the know vascular architecture is derived from older anatomical studies[3], or from newer methods e.g. light sheet microscopy or microCT but on smaller samples[4]. HiP-CT provides, for the first time, a technology that can be used to identify vascular anomalies at the microvasculature level and contextualise these within the whole lung, e.g. to hierarchically trace the vascular origins of these anomalies back to their source e.g. the bronchial, pulmonary or pleural supplies, or to correlate the microfeature to a clinical scale image correlate.

We have developed a protocol for lung inflation, fixation and dehydration and physical stabilisation that we have used to image 13 human lungs (both lobes and complete lungs), and 137 core biopsy samples. These samples cover a range of pathologies including Pleuroparenchymal fibroelastosis (PPFE), COVID-19 and Osler-Weber-Rendu disease.
Segmentation and or visualisation of the vascular networks within these lungs have revealed numerous pathological changes in vessel structures including increased broncho-pulmonary anastomosis in COVID-19, with concurrent expansion of the vasa vasorum [2,5], Vascular tree-in-bud in COVID-19, pulmonary-pleural anastomosis in PPFE lung biopsies and highly disordered vasculature in Osler-Weber-Rendu lungs.

Whilst we have demonstrated that these vascular abnormalities can be identified and quantified by HiP-CT, we are seeking to train the machine learning algorithms to automate the segmentation of these vascular networks. This will enable larger scale automated analyses of vascular network changes and potential automated identification of specific shunting or patterns of injury.

1. Walsh, C. L., et al. "Imaging intact human organs with local resolution of cellular structures using hierarchical phase-contrast tomography." *Nature methods* 18.12 (2021): 1532-1541.
2. Ackermann, Maximilian, et al. "The bronchial circulation in COVID-19 pneumonia." *American Journal of Respiratory and Critical Care Medicine* 205.1 (2022): 121-125.
3. Turner-Warwick, Margaret. "Precapillary systemic-pulmonary anastomoses." *Thorax* 18.3 (1963): 225.
4. Vasilescu, Dragoş M., et al. "Comprehensive stereological assessment of the human lung using multiresolution computed tomography." *Journal of Applied Physiology* 128.6 (2020): 1604-1616.
5. Ackermann, Maximilian, et al. "The fatal trajectory of pulmonary COVID-19 is driven by lobular ischemia and fibrotic remodelling." *EBioMedicine* 85 (2022): 104296.

Dissecting Pulmonary Gas Exchange and Hemodynamics with ^{129}Xe MRI

Bastiaan Driehuys
bastiaan.driehuys@duke.edu
Duke University Medical Center, Durham NC

Unexplained dyspnea poses a significant problem for both patients and healthcare systems and frequently leads to invasive diagnostic procedures. For example, patients may undergo surgical lung biopsy to diagnose interstitial lung disease, cardiopulmonary exercise testing, or right heart catheterization to detect pulmonary hypertension (PH). But addressing dyspnea may also be more readily achieved by exploiting the unique properties of hyperpolarized ^{129}Xe MRI. The technology has a long-standing history for assessing pulmonary ventilation, for which FDA approval has recently been granted. However, a more comprehensive picture can be obtained by exploiting ^{129}Xe solubility and chemical shift to image its uptake in the interstitial membrane tissues and its subsequent diffusive transfer into the pulmonary capillary red blood cells (RBCs).

Imaging these three compartments now allows us to decompose 3-dimensionally each of their contributions to gas exchange – accessible alveolar volume, membrane conductance and capillary blood volume conductance[1]. But beyond this, the RBC resonance, in particular, is even richer in information. The RBC signal exhibits cardiogenic amplitude oscillations that are diminished in pre-capillary PH and enhanced in post-capillary PH[2]. Thus, the combination of ^{129}Xe gas exchange MRI and ^{129}Xe-RBC cardiogenic oscillations has the potential to both detect and monitor different forms of pulmonary hypertension and their response to therapy. While such RBC oscillations were initially possible to observe only as a global metrics, recent advances in keyhole reconstruction have made it possible to map them regionally[3]. This, in turn, could become valuable for evaluating chronic thromboembolic pulmonary hypertension (CTEPH), detecting pre-capillary PH in patients with ILD, and detecting combined pre- and post-capillary PH (CPcPH).

And finally, we are starting to appreciate the insights gained from the RBC chemical shift, which is uniquely sensitive to pulmonary capillary blood oxygenation[4]. We can now show that this shift is variably diminished across pulmonary diseases, and yet preserved in certain forms of pulmonary hypertension like CTEPH. Thus, the RBC shift may be an early indicator of delayed blood oxygenation in patients; it can also help us identify patients with pre-capillary PH. In light of this, efforts to regionally measure the RBC shift using chemical shift imaging (CSI) become even more important.[5] In this talk, I will briefly review each of these interesting contrast mechanisms and outline steps needed to apply them to the study of dyspnea.

Funding: R01HL105643, R01HL126771, R01HL153872

1 Wang, Z. *et al.* Using hyperpolarized (129)Xe gas-exchange MRI to model the regional airspace, membrane, and capillary contributions to diffusing capacity. *Journal of applied physiology (Bethesda, Md. : 1985)* **130**, 1398-1409, doi:10.1152/japplphysiol.00702.2020 (2021).

2 Bier, E. A. *et al.* Noninvasive Diagnosis of Pulmonary Hypertension with Hyperpolarized 129Xe Magnetic Resonance Imaging and Spectroscopy. *ERJ Open Research*, 00035-02022, doi:10.1183/23120541.00035-2022 (2022).

3 Niedbalski, P. J. *et al.* Mapping cardiopulmonary dynamics within the microvasculature of the lungs using dissolved (129)Xe MRI. *Journal of applied physiology (Bethesda, Md. : 1985)* **129**, 218-229, doi:10.1152/japplphysiol.00186.2020 (2020).

4 Norquay, G., Leung, G., Stewart, N. J., Wolber, J. & Wild, J. M. (129) Xe chemical shift in human blood and pulmonary blood oxygenation measurement in humans using hyperpolarized (129) Xe NMR. *Magn. Reson. Med.* **77**, 1399-1408, doi:10.1002/mrm.26225 (2017).

5 Guan, S. *et al.* 3D Single-Breath Chemical Shift Imaging Hyperpolarized Xe-129 MRI of Healthy, CF, IPF, and COPD Subjects. *Tomography* **8**, 2574-2587 (2022).

Combining HP ^{129}Xe and UTE MRI with Proteomics to Phenotype Cystic Fibrosis Lung Disease

Zackary I. Cleveland[1], Abdullah S. Bdaiwi[1], Emily Skala[2], Matthew Siefert[2], and Assem G. Ziady[2]
[1]Center for Pulmonary Imaging Research, Division of Pulmonary Medicine and [2]Division of Bone Marrow Transplantation, Cincinnati Children's Hospital Medical Center, Cincinnati, OH 45229

Introduction: Cystic fibrosis (CF) is a genetic disease that involves progressive lung function loss and structural remodelling that historically led to lung transplant or death in early adulthood. However, the life expectancy in CF has increased substantially due to improved treatments. Following the introduction of highly effective modulator therapy (HEMT) (1), CF patients often present as spirometrically normal (e.g., forced expiratory volume in 1 second, FEV_1>85%). Still, pathological changes occur, and it is increasingly difficult to detect these early changes many patients. In contrast, ultra-short echo-time (UTE) and hyperpolarized (HP) ^{129}Xe MRI can detect pathology years before changes in FEV_1 are observed. Additionally, proteomic biomarkers from high-precisions mass spectrometry can accurately forecast CF lung disease progression. While robust and easily disseminated, these proteomic biomarkers have only been validated in patients with established lung disease. Here we use HP ^{129}Xe and UTE MRI to validate proteomic markers in early CF.

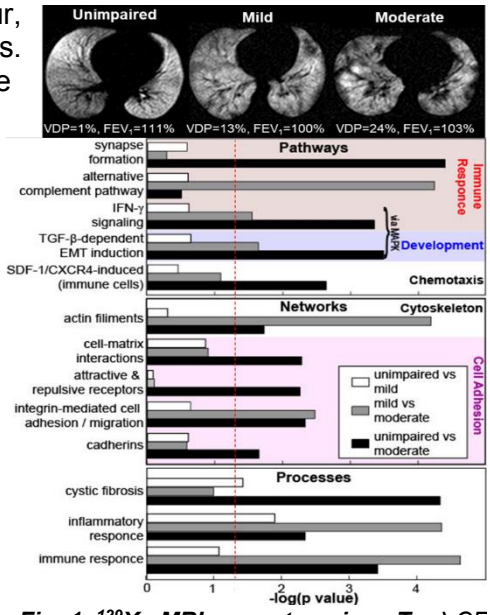

***Fig. 1**: ^{129}Xe MRI vs proteomics. **Top)** CF patients with FEV_1>100% and no, mild, and moderate ventilation impairment via ^{129}Xe MRI. **Bottom)** Proteomic differences in CF patient plasma. Cohort Comparisons are indicted. Vertical red line: p=0.05 (log scale).*

Methods: HP ^{129}Xe MRI, ventilation defect percentage (VPD) calculation, UTE MRI (2), Liquid Chromatography tandem Mass Spectrometry (LC-MS/MS) and bioinformatics (3,4) were performed as previously described. ^{129}Xe MRI (N=9) and UTE (N=8) were performed with same-day blood draws in CF patients with normal spirometry (FEV_1>85%). For comparison with ^{129}Xe, blood samples were grouped by functional impairment as ***no impairment*** (VPD<2, 2 male, 1 female), ***mild*** (5<VDP<15; 1 m, 2 f), and ***moderate*** (VDP>20, 2 m, 1 f). Bronchiectasis was scored by a trained reader with a simplified system (5). Lungs were divided into 6 regions (5 lobes plus lingula), and lobes were scored on a 0-3 scale: (0=not present; 1=present in <1/3 lobe; 2=present in <2/3 lobe; and 3 = present in >2/3 lobe). Lobar scores were summed to yield whole-lung scores. Samples were grouped by whole-lung severity score as ***mild*** (score≤3; 2 m, 2 f) or ***moderate*** (4≤score≤10; 2 m, 2 f). For UTE and VDP, group identities were blinded for non-biased proteomic analysis.

Results and Discussion: Using pathway, network and process analyses, the three disease severity groups defined by ^{129}Xe ventilation MRI (unimpaired, mild, and moderate) were successfully identified before the groups were unblinded. Proteomic analysis revealed differences in pro-inflammatory signaling, cytoskeletal rearrangement associated with remodeling, and cell adhesion associated with inflammatory cell activation (***Fig. 1***). Similarly, the groups segregated by structural UTE (mild or moderate) were readily identified before unblinding. Proteomic analysis revealed changes in pathways associated with CF disease (e.g. ENAC regulation), inflammatory signaling, remodeling, and cell adhesion (***Fig. 2***). These blinded studies provide compelling evidence that serum proteomics can detect the early and mild structural and ventilation abnormalities identified by MRI in spirometrically normal individuals, arguing that together these technologies yield robust and complimentary information about early remodeling and lung function impairment in CF.

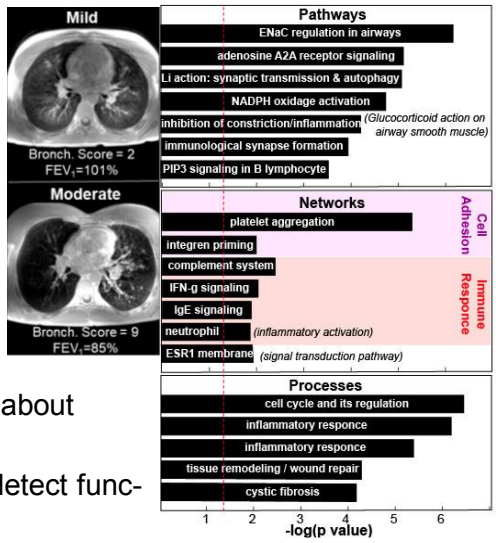

***Fig. 2: Structural UTE vs. proteomics. Left)** CF patients with mild (top) and moderate (bottom) remodeling via UTE. **Right)** Proteomic differences between patients with mild and moderate remodeling. Vertical red line: p=0.05.*

Conclusions: LC-MS/MS combined with ^{129}Xe and UTE MRI can detect functional, structural and molecular abnormalities in spirometrically norm CF patients. While the MRI modalities are available only in a few specialized centers, blood samples can be collected anywhere and shipped. Thus, MRI-validated proteomic could provide a powerful means to quantify disease trajectories in CF.

References:

1. Middleton PG, Mall MA, Dřevínek P, Lands LC, McKone EF, Polineni D, Ramsey BW, Taylor-Cousar JL, Tullis E, Vermeulen F, Marigowda G, McKee CM, Moskowitz SM, Nair N, Savage J, Simard C, Tian S, Waltz D, Xuan F, Rowe SM, Jain R. Elexacaftor–Tezacaftor–Ivacaftor for Cystic Fibrosis with a Single Phe508del Allele. N Engl J Med 2019;381(19):1809-1819.
2. Thomen RP, Walkup LL, Roach DJ, Cleveland ZI, Clancy JP, Woods JC. Hyperpolarized 129Xe for investigation of mild cystic fibrosis lung disease in pediatric patients. Journal of Cystic Fibrosis 2017;16(2):275-282.
3. Tucholska M, Bowden P, Jacks K, Zhu P, Furesz S, Dumbrovsky M, Marshall J. Human serum proteins fractionated by preparative partition chromatography prior to LC-ESI-MS/MS. J Proteome Res 2009;8(3):1143-1155.
4. Zhang R, Barker L, Pinchev D, Marshall J, Rasamoelisolo M, Smith C, Kupchak P, Kireeva I, Ingratta L, Jackowski G. Mining biomarkers in human sera using proteomic tools. Proteomics 2004;4(1):244-256.
5. Brody AS, Klein JS, Molina PL, Quan J, Bean JA, Wilmott RW. High-resolution computed tomography in young patients with cystic fibrosis: Distribution of abnormalities and correlation with pulmonary function tests. Journal of Pediatrics 2004;145(1):32-38.

Sensing the Heat with Spin Polarized ^{129}Xe

Rosa Tamara Branca

Absolute temperature measurements in tissues deep inside the body are extremely hard to perform non-invasively. Yet, for brown adipose tissue (BAT), a tissue specialized in heat production and capable of regulating energy expenditure, susceptibility to weight gain, and blood glucose, absolute temperature measurements would be extremely important to directly detect its thermogenic function. However, direct temperature measurements of BAT in humans are notoriously challenging. Optical techniques have a limited penetration depth and measurements of supraclavicular BAT temperature in humans during cold exposure have been confounded by vasoconstriction and subcutaneous fat thickness. Magnetic resonance (MR) thermometry techniques are commonly used for non-invasive tissue temperature measurements. The most widely used MR temperature probe is the water resonance frequency, which shifts linearly with temperature by -0.01ppm/°C. However, in fatty tissues, these measurements are notoriously confounded by temperature-dependent magnetic susceptibility gradients, which degrade the accuracy of both relative and absolute temperature measurements. For these reasons, in fatty tissues, MR thermometry methods based on the temperature-induced changes in the longitudinal magnetization of water and lipid protons are generally preferred, but these methods generally require a pre-calibration of the temperature dependence in the tissue of interest.

Here we report the first background-free detection of human brown adipose tissue and thermogenic activity by magnetic resonance with hyperpolarized xenon-129. We show that cold exposure in adult humans leads to a selective enhancement of the resonance frequency corresponding to xenon dissolved in the lipid compartment of brown fat. This selective enhancement enables background free detection of this tissue by MRI. We also show how the resonance frequency of xenon dissolved in lipids, along the temperature insensitive resonance frequency of nearby methylene protons, can be used for absolute temperature measurements. After calibration of this methodology in vitro in human adipose tissue samples and validation in vivo in rodents, this methodology is directly applied to measure human BAT temperature during cold exposure. Interestingly these measurements, performed in conjunction with ^{18}FDG-PET scans, reveal a thermogenically active BAT also in those healthy young subjects with a non-glucose avid BAT.

Finally, in an attempt to translate this methodology to ultralow field strengths, we show direct detection of polarization transfer from laser polarized xenon-129 spins to ^{1}H by simultaneous xenon-129 and ^{1}H NMR spectroscopy.

How to Capture an Atom: Developing Molecular Sensors with Useful Xenon-binding Properties

Zhuangyu Zhao,[1] Nathan A. Rudman,[1] and Ivan J. Dmochowski[1]

[1]Univ. Pennsylvania, Department of Chemistry, 231 South 34th St., Philadelphia, PA 19104 USA

With the recent FDA approval of Polarean's Xenoview, there is growing interest in performing void space imaging as well as molecular imaging in humans and animal models using this technology. ^{129}Xe is spin-1/2, and can be hyperpolarized to give a 10^4-10^5 signal enhancement over the room-temperature Boltzmann population of nuclear spins. Biology provides endogenous molecules, including lipid compartments and blood proteins, which bind xenon and provide specific Xe-129 nuclear magnetic resonance (NMR) chemical shifts. To visualize a much greater range of molecular targets, including disease biomarkers, there is the opportunity to deliver exogenous contrast agents that bind xenon with good affinity, label molecular targets of interest in vivo, and yield useful Xe-129 NMR signals. For the past two decades, our laboratory has developed water-soluble molecular capsules as xenon MR contrast agents, and explored their functionalization and biocompatibility. In 2020 we reported that very anionic tetrahedral capsules containing Co^{2+} at the vertices generate useful Xe-129 NMR signals.[1] Xenon diffuses through portals to access the capsule interior, and replacing paramagnetic Co^{2+} with smaller, diamagnetic Fe^{2+} cations tunes the Xe-129 NMR chemical shift, as well as portal size and Xe exchange rate.[2]

Since 2016 our laboratory has expanded this search to include genetically encoded proteins, and has identified several monomeric proteins of bacterial origin that yield unique Xe-129 NMR chemical shifts, either alone in solution (i.e., Xe-beta-lactamase, see Figure below) or upon binding a small molecule analyte, e.g., maltose-binding protein (MBP) and ribose-binding protein (RBP). These proteins (but not most proteins we have investigated) give significant saturation contrast at 100 nM using the hyper-CEST NMR technique. In recent breakthroughs, we identified a mechanism for controlling xenon exchange rate in MBP by gating access to a buried ~2-nm channel: Maltose binding stabilizes a salt bridge at the mouth of the channel, which slows xenon exchange.[3] Furthermore, we were able to modify the maltose binding site to introduce a zinc-binding motif and produce "turn on" Xe-129 NMR signal in the presence of micromolar zinc. The site was specific for Zn^{2+} over other physiologic cations, based on the histidine ligands introduced. This highlights the opportunity for engineering proteins for sensing different metal ions and small molecules using hp Xe-129 NMR.

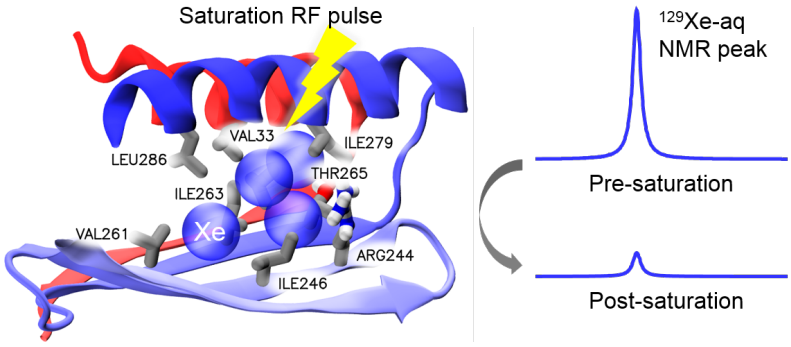

Cited References

[1]K. Du, S.D. Zemerov, S. Hurtado Parra, J.M. Kikkawa, I.J. Dmochowski, *Paramagnetic organocobalt capsule revealing xenon host-guest chemistry*, **Inorg. Chem.**, 59, 19, 13831-13844, 2020.

[2]K. Du, S.D. Zemerov, P.J. Carroll, I.J. Dmochowski, *Paramagnetic shifts and guest exchange kinetics in Co_nFe_{4-n} metal-organic capsules*, **Inorg. Chem.**, 59, 17, 12758-12767, 2020.

[3]Z. Zhao, N.A. Rudman, J. He, I.J. Dmochowski, *Programming xenon diffusion in maltose binding protein*, **Biophys. J.**, 121, 23, 4635-4643, 2022.

Role of ^{129}Xe MRI in Determining the Significance of Pulmonary Pathology in Challenging Cases (Examples of COPD, E-Cigarette, and Aging)

Y. Michael Shim

Years of international collaborations by multiple investigators have matured Hyperpolarized Xenon-129 MRI (HXeMRI) technology that has advantages over conventional methods.[1] The strength of HXeMRI is its ability to determine regional ventilation and gas exchange perturbations in various lung pathologies.[2-5] The continuum of these efforts has resulted in recent approval by the US FDA for the use of hyperpolarized Xenon-129 as oral inhalation contrast, and now the technology is posed to widely spread in clinical arenas. The primary goal of this talk is to discuss a synopsis of HXeMRI applications in three recent works by our group, which demonstrates the exciting future of HXeMRI technology to advance the field of pulmonary research.

Effects of aging on pulmonary airflow physiology: Aging is a well-known predictor of the loss of lung function measured by spirometry, but spirometry as a global measure of lung function cannot resolve the detailed physiology of aging.[6] HXeMR ventilation scans of subjects with normal spirometry reveal that the natural loss of spirometric lung function during aging is caused by airflow conduction in small airways. This aging process is different between non-smokers and smokers.

Effects of vaping on pulmonary gas exchange physiology: Vaping is anticipated to cause significant respiratory pathology early on in healthy young adults, but conventional methods have not demonstrated these early changes. HXeMRI dissolved phase scans reveal significant perturbations in the pulmonary interstitial tissue integrity and capillary blood flow in healthy young adults (younger than 30) with normal pulmonary function tests and CT imaging.

Previously underappreciated gas exchange pathology in Chronic Obstructive Pulmonary Disease (COPD): COPD is a syndrome in which airflow is irreversibly limited after noxious exposure or predisposed genetic risk. The airway pathology in chronic bronchitis and alveolar epithelial pathology in emphysema have been highlighted as two unique phenotypes of COPD. HXeMRI dissolved phase scans have revealed a third unique “vascular” phenotype in which capillary perfusion in the lung is significantly perturbed without emphysematous loss of alveolar epithelium. This study highlighted the previously underappreciated role of capillary vascular abnormalities in COPD patients.

In conclusion, these studies reveal the exciting strength and potential of HXeMRI technology to advance the field of respiratory science. These advances are anticipated to bring a new understanding of complex respiratory physiology in normal and diseased states.

1 Niedbalski, P. J. *et al.* Protocols for multi-site trials using hyperpolarized (129) Xe MRI for imaging of ventilation, alveolar-airspace size, and gas exchange: A position paper from the (129) Xe MRI clinical trials consortium. *Magn Reson Med* **86**, 2966-2986 (2021). https://doi.org:10.1002/mrm.28985

2 Teague, W. G., Tustison, N. J. & Altes, T. A. Ventilation heterogeneity in asthma. *J Asthma* **51**, 677-684 (2014). https://doi.org:10.3109/02770903.2014.914535

3 Myc, L. *et al.* Characterisation of gas exchange in COPD with dissolved-phase hyperpolarised xenon-129 MRI. *Thorax* **76**, 178-181 (2021). https://doi.org:10.1136/thoraxjnl-2020-214924

4 Mammarappallil, J. G., Rankine, L., Wild, J. M. & Driehuys, B. New Developments in Imaging Idiopathic Pulmonary Fibrosis With Hyperpolarized Xenon Magnetic Resonance Imaging. *J Thorac Imaging* **34**, 136-150 (2019). https://doi.org:10.1097/RTI.0000000000000392

5 Altes, T., Johnson, M., Mugler, J.P. Hyperpolarized H2-3 MRI detects the effects of a CFTR potentiator (ivacaftor) therapy in subjects with cystic fibrosis and the G551D mutation. *Proceedings of 20 ISMRM*, 1359 (2012).

6 Cooper, B. G. *et al.* The Global Lung Function Initiative (GLI) Network: bringing the world's respiratory reference values together. *Breathe (Sheff)* **13**, e56-e64 (2017). https://doi.org:10.1183/20734735.012717

129Xe MRI Phenotypes of Post-HSCT Pulmonary Complications

Laura L. Walkup, Ph.D.

As the use of hematopoietic stem-cell transplantation (HSCT) as a therapy for malignant and non-malignant conditions is expanding rapidly, so too is awareness that HSCT carries high risk of lung injury and pulmonary complications in as many as 50% of patients [1]. Clinical surveillance for late-onset (beyond day 100 post-HSCT) pulmonary complications relies upon pulmonary-function testing, specifically spirometry. For instance, bronchiolitis obliterans syndrome (BOS), the clinical description of the gold-standard histopathological diagnosis of BO, is diagnosed and staged by the degree of progressive airflow obstruction on repeated spirometry. However, spirometry is insensitive to early disease and difficult for young children. Pediatric HSCT patients are at known elevated risk for lung injury yet are challenging to monitor for early disease—the best window-of-opportunity for intervention to stabilize lung-function decline and improve outcomes.

We have shown ventilation magnetic-resonance imaging with inhaled hyperpolarized xenon-129 gas (Xe MRI) is feasible in young children, including those unable to perform spirometry, and is sensitive to subclinical, regional airflow obstruction in asymptomatic pediatric HSCT patients [2]. Building on this work, we recently have implemented Xe gas-exchange MRI—a technique that leverages the solubility and chemical shift of Xe gas in the pulmonary tissues to simultaneously assess the ventilation, interstitial, and diffusion (i.e., red-blood cell, RBC, uptake) compartments of pulmonary gas exchange—to describe lung complications in children post-HSCT [3]. In this presentation, Xe gas-exchange MRI in the context of pediatric HSCT will be discussed, including preliminary results suggesting that in addition to ventilation deficits and airflow obstruction, Xe gas-exchange MRI shows diffusion abnormalities in this population and how Xe MRI may be used to identify obstructive versus interstitial phenotypes of post-HSCT lung injury [4].

References

1. Bergeron, A. and G.S. Cheng, *Bronchiolitis Obliterans Syndrome and Other Late Pulmonary Complications After Allogeneic Hematopoietic Stem Cell Transplantation.* Clin Chest Med, 2017. **38**(4): p. 607-621.
2. Walkup, L.L., et al., *Xenon-129 MRI detects ventilation deficits in paediatric stem cell transplant patients unable to perform spirometry.* Eur Respir J, 2019. **53**(5): p. 1801779.
3. Willmering, M.M., et al., *Pediatric (129) Xe Gas-Transfer MRI-Feasibility and Applicability*. J Magn Reson Imaging, 2022. **56**(4): p. 1207-1219.
4. Plummer, J.W., et al., *Sensitivity and Specificity of ¹²⁹Xe-MRI as a Biomarker to Detect Bronchiolitis Obliterans Syndrome in Pediatric Post-Hematopoietic Stem-Cell Transplant Patients*, in *American Thoracic Society International Conference*. 2022. p. A2181-A2181.

Assessing Lung Structure via Hyperpolarized 129Xe MR Spectroscopy: Peeking into Peaks

Kai Ruppert

Hyperpolarized xenon-129 (HXe) MRI enables the characterization of regional lung structure and function by depicting ventilation patterns as well as the absorption of xenon gas by lung parenchyma and subsequent gas transport by the pulmonary circulation. Spectroscopy-based techniques, on the other hand, trade some or all of the spatial information provided by image encoding in exchange for more detailed signal frequency data and higher temporal resolution. As a result, spectroscopy offers additional lung function metrics inaccessible to imaging, or can serve as a guide for optimizing image acquisition parameters. To date, chemical shift saturation recovery (CSSR) spectroscopy has been shown to provide particularly valuable information about pathological changes in lung function as the apparent alveolar septal wall thickness increases with disease severity[1-3]. Nevertheless, existing spectroscopic techniques focus mostly on the peak areas of the two dominant dissolved-phase resonances in the lung that have been assigned to xenon bound to hemoglobin (203-230 ppm, depending on species and oxygenation level) and dissolved in lung tissue and blood plasma (~196 ppm). Here, we investigate variations in peak shape and frequency-dependent dynamics throughout the first tens of milliseconds of parenchymal gas exchange in order to draw additional conclusions about features of the underlying microscopic structures.

It has been previously demonstrated that the linewidth of the dissolved-phase resonances is decreased in interstitial lung disease patients compared to that in healthy control subjects, presumably due to an increase in magnetic homogeneity secondary to alveolar wall thickening[4,5]. Our preliminary findings indicate that the correlation between T2* and septal wall thickness is general in nature, extends to other lung pathologies such as COPD, and appears to be strongest for xenon accumulation times in the lung parenchyma below 10 ms. In fact, in the most severely diseased patients, the peak widths at very short accumulation times can narrow to the extent that additional, secondary dissolved-phase resonances are revealed. What is more, an analysis of the frequency-dependent gas uptake rates shows that the associated structural compartments of these resonances fill considerably faster than those of the dominant primary resonances.

Careful analysis of spectral peak shapes and dynamics obtained with HXe MR spectroscopy can provide additional information about the rapid gas-exchange processes between the alveolar volume and the parenchyma—information which might be more sensitive to pathological changes than the heavily temporally averaged signals employed for MR imaging.

1 Li, H. *et al.* Quantitative evaluation of radiation-induced lung injury with hyperpolarized xenon magnetic resonance. *Magn Reson Med* **76**, 408-416 (2016). https://doi.org:10.1002/mrm.25894

2 Stewart, N. J. *et al.* Reproducibility of quantitative indices of lung function and microstructure from 129 Xe chemical shift saturation recovery (CSSR) MR spectroscopy. *Magn Reson Med* **77**, 2107-2113 (2017). https://doi.org:10.1002/mrm.26310

3 Ruppert, K., Qing, K., Patrie, J. T., Altes, T. A. & Mugler, J. P., 3rd. Using Hyperpolarized Xenon-129 MRI to Quantify Early-Stage Lung Disease in Smokers. *Acad Radiol* **26**, 355-366 (2019). https://doi.org:10.1016/j.acra.2018.11.005

4 Kammerman, J. *et al.* Transverse relaxation rates of pulmonary dissolved-phase Hyperpolarized (129) Xe as a biomarker of lung injury in idiopathic pulmonary fibrosis. *Magn Reson Med* **84**, 1857-1867 (2020). https://doi.org:10.1002/mrm.28246

5 Mata, J. *et al.* Evaluation of Regional Lung Function in Pulmonary Fibrosis with Xenon-129 MRI. *Tomography* **7**, 452-465 (2021). https://doi.org:10.3390/tomography7030039

Data Harmonization on Large Cohorts of Lung CT Scans

Andrew F. Laine
Columbia University

Consistent imaging protocols will require normalization / harmonization of data sourced from multiple platforms, hospitals and vendors. AI has shown a remarkable ability to generalize and group / tease out patterns from high-dimensional data. Machine / deep learning algorithms should rely on mix-omics integration of imaging and physiological measures. There is an urgent need for new models of multi-modal transfer learning (e.g., understanding lung and heart functional interactions), and incremental learning as cohorts grow at an ever-faster face, combining data from states/countries.

We are in the process of developing harmonization methods that are applied to COPD patient imaging data. This phenotyping could lead to a better retrospective understanding of COPD disease pathways and prepare for future management of pulmonary-derived chronic pathologies. In addition, there are significant new chronic pathologies expected in COVID survivors (cardiomyopathy, pulmonary aspergillosis, hemoglobin / iron deficiencies) in the longer term, which will be challenging to treat and / or recognize. The harmonized baseline data during acute phases of disease would help tremendously in our ability to understand the implications of these pathologies.

The proposed harmonization platform would include normalization across vendors, sites, possible variations in protocols and patient size. We describe AI based harmonization methods to leverage a large number of baseline scans from existing and ongoing studies for density measures, texture and later airway topology. During this initial phase, the Columbia cohort would harmonize 2,500 subjects in total, sampling in proportion five distinct cohorts. In the long term we aspire to develop data sharing tools, with possible partnerships for long term / global infrastructure and computing, integrate expertise in multiple imaging modalities, lead an open AI approach to model, predict and understand stages of pulmonary disease including COPD.

Image-based Multiscale Modeling of the Lung to Quantify Regional Mechanical Stress In Vivo

Reza Avaz

There are several lung diseases that lead to diffuse inflammation, such as acute respiratory distress syndrome[1]. Diffuse inflammation leads to localized under-ventilation, which can lead to overdistension and, consequently, volutrauma of the surrounding healthy regions when the lungs are mechanically ventilated[2]. In addition to volutrauma, the lungs can also be damaged due to high settings of positive end-expiratory pressure during mechanical ventilation, which is termed barotrauma. Volutrauma and barotrauma conditions lead to damage in the alveolar septal walls through excessive changes in the homeostatic micromechanical environment, and the possibility of in-vivo estimation of wall stress and strain can significantly assist with diagnosis and treatment planning for these conditions. Although it is possible to quantify the strains in the alveolar septal walls through image registration processing dynamic imaging scans, including magnetic resonance imaging and dynamic computed tomography (CT), methods to quantify the level of stress experienced by the alveolar septal walls remain elusive.

In this study, we introduce a method to estimate the stress in the alveolar septal walls through a combination of dynamic imaging, image registration, and in-silico modeling. Briefly, we use dynamic CT scans of a rat with 16 image stacks over the course of one respiratory cycle. We perform non-linear non-rigid image registration[3] to obtain the displacement of each voxel. The in-silico model uses animal-specific airway reconstruction and lung pressure-volume measurements to estimate pressure distribution within the airway tree down to the alveoli. Once integrated with displacement quantifications, the in-silico model estimates the wall mechanical properties and wall stress while accounting for pulmonary surfactant. Our initial analysis demonstrates a high contribution of surfactant in modulating wall stress and strain. The proposed platform can be streamlined and integrated with dynamic imaging to quantify the regional micromechanical status of the lung in real time for individualized diagnosis and treatment of lung injury patients[4].

1 Aslan, A., Aslan, C., Zolbanin, N. M. & Jafari, R. Acute respiratory distress syndrome in COVID-19: possible mechanisms and therapeutic management. *Pneumonia* **13**, 1-15 (2021).

2 Gaver I, D. P., Nieman, G. F., Gatto, L. A., Cereda, M., Habashi, N. M., & Bates, J. H. The POOR get POORer: A hypothesis for the pathogenesis of ventilator-induced lung injury. *Am J Respir Critical Care Medicine* **202**, 1081–1087 (2020).

3 Keszei A. P., Berkels B., Deserno T. M. Survey of Non-Rigid Registration Tools in Medicine. *J Digit Imaging* **30** 102-116 (2017).

4 Neelakantan, S., Xin, Y., Gaver, D. P., Cereda, M., Rizi. R., Smith, B. J., Avazmohammadi, R. Computational lung modelling in respiratory medicine. *J R Soc Interface* **19**, 20220062 (2022).

Dynamic Hyperpolarized ^{129}Xe Imaging of Ventilation and Gas Exchange for Treatment Response Monitoring

Hooman Hamedani

While hyperpolarized ^{129}Xe MR imaging during a breath-hold is capable of regionally investigating lung function in terms of ventilation and gas exchange, lung function itself relies on dynamic aspects of gas mixing and blood redistribution in a constantly moving organ. Ventilation in the lung, for example, is driven by the resolution of differential pressures and concentration gradients over multiple timescales, and its relationship to breathing rate, volume, inflation level, depth, gas concentration, and diffusion was the subject of decades of theoretical study. It is also known that not every region of a compromised lung reaches its maximum volume change at end-inhale or its minimum at end-exhale[1]. Further, since ventilation inhomogeneity occurs in regions where local gas filling time-constants are comparable to or exceed inhalation time, artificially reducing breathing rate during a measurement via breath-hold fails to highlight regions that do not properly fill during normal breathing but do adequately fill during the measurement[2–4]. Similarly, pulmonary blood volume and flow are highly variable over both the breathing and cardiac cycles as capillaries and larger vessels distend, assist right heart activity and blunt pressure spikes that would otherwise be damaging. Both dynamical effects are critical to a healthy lung[5–9], but are not accessible to single-breath imaging. Restricting lung function imaging to a specific, artificially-induced state therefore inevitably fails to capture features crucial to maintaining organism homeostasis, making it difficult to compare measurements between subjects if the exact same state is not achieved.

Imaging respiratory dynamics without a breath-hold and during spontaneous breathing using a small dose of hyperpolarized gas *ad libitum* can therefore provide a better understanding of the pathophysiology of various lung diseases, as it can dynamically depict patients' true physiological gas flow and uptake without changing their breathing pattern. Extending the time of imaging also allows the use of signal averaging to estimate regional ventilation, gas mixing efficiency, and gas exchange at a steady-state-like condition, showing overall lung function during a relatively long period (approximately five minutes) of subjects' normal breathing. Identifying membrane-to-gas mixing efficiency in the acinar and its exchange with blood is central to understanding which aspects of a diseased lung are most tied to morbidity, as well as whether treatment can resolve those deficits. Diagnostic tests that aim to identify deficiencies linked to one or more of these processes are best approached by attempting to measure them, as quantitatively as possible, under physiologically relevant conditions. We, therefore, attempt to show that measuring these parameters of lung function simultaneously, dynamically, and regionally is crucial to understanding both the pathophysiology of different lung disorders and their responses to therapy. To emphasize the value of such local, multifaceted measurements, we highlight the outcomes of bronchoscopic lung volume reduction (LVR) procedure using endobronchial valves, an FDA-approved regional treatment for end-stage lung disease.

Reference:

1 Shao W, Patton TJ, Gerard SE, Pan Y, Reinhardt JM, Durumeric OC, *et al.* N-Phase Local Expansion Ratio for Characterizing Out-of-Phase Lung Ventilation. *IEEE Trans Med Imaging* 2020;39:2025–34. https://doi.org/10.1109/TMI.2019.2963083.

2 Kirby M, Svenningsen S, Kanhere N, Owrangi A, Wheatley A, Coxson HO, *et al.* Pulmonary ventilation visualized using hyperpolarized helium-3 and xenon-129 magnetic resonance imaging: differences in COPD and relationship to emphysema. *J Appl Physiol Bethesda Md 1985* 2013;114:707–15. https://doi.org/10.1152/japplphysiol.01206.2012.

3 Marshall H, Deppe MH, Parra-Robles J, Hillis S, Billings CG, Rajaram S, *et al.* Direct visualisation of collateral ventilation in COPD with hyperpolarised gas MRI. *Thorax* 2012;67:613–7. https://doi.org/10.1136/thoraxjnl-2011-200864.

4 Hamedani H, Clapp JT, Kadlecek SJ, Emami K, Ishii M, Gefter WB, *et al.* Regional Fractional Ventilation by Using Multibreath Wash-in (3)He MR Imaging. *Radiology* 2016;279:917–24. https://doi.org/10.1148/radiol.2015150495.

5 Rauwerda PE. *Unequal ventilation of different parts of the lung and the determination of cardiac output*. Thesis fully internal (DIV), Groningen: s.n.; 1946; 1946.

6 Bates JHT. *Lung Mechanics: An Inverse Modeling Approach*. Cambridge University Press; 2009.

7 Crawford AB, Makowska M, Paiva M, Engel LA. Convection- and diffusion-dependent ventilation maldistribution in normal subjects. *J Appl Physiol Bethesda Md 1985* 1985;59:838–46. https://doi.org/10.1152/jappl.1985.59.3.838.

8 Ugander M, Jense E, Arheden H. Pulmonary intravascular blood volume changes through the cardiac cycle in healthy volunteers studied by cardiovascular magnetic resonance measurements of arterial and venous flow. *J Cardiovasc Magn Reson Off J Soc Cardiovasc Magn Reson* 2009;11:42. https://doi.org/10.1186/1532-429X-11-42.

9 Brower R, Wise RA, Hassapoyannes C, Bromberger-Barnea B, Permutt S. Effect of lung inflation on lung blood volume and pulmonary venous flow. *J Appl Physiol Bethesda Md 1985* 1985;58:954–63. https://doi.org/10.1152/jappl.1985.58.3.954.

Airway Aerodynamics: MRI Based Modeling and Validation

Alister Bates PhD

Respiratory disease can occur in either the lungs, or in the central airways that carry air to and from the lungs. In many subjects, respiratory symptoms are caused by disease in both the lungs and major airways, but it can be difficult to assess the contribution of each aspect to symptoms. For example, many neonatal subjects with bronchopulmonary dysplasia have comorbid tracheomalacia. Some treatments aimed treating a particular lung disease (e.g., aerosolized albuterol for small airway obstruction) may exacerbate central airway disease (e.g. softer trachealis and increased tracheomalacia), so it is vital to understand whether each individual patient's symptoms are predominantly airway or lung related.

Subject-specific computational fluid dynamics (CFD) of respiratory airflow can assess the contribution of major airway disease to respiratory symptoms through calculation of metrics like the regional resistive work of breathing throughout the large airways. To create subject-specific airway models, high-resolution imaging is necessary to obtain anatomical boundary conditions. In diseases that involve airway motion, such as tracheomalacia and obstructive sleep apnea (OSA), cine imaging is required to capture the realistic changing position of the airway. Both computed tomography (CT) and magnetic resonance imaging (MRI) can be used to capture these boundary conditions depending on the required image resolution, field of view, cine time, and acceptability of patient exposure to ionizing radiation.

CFD in airways has not been clinically adopted at present, despite the useful metrics it can calculate. In part, this is due to the lack of *in vivo* validation. To rectify this, we aimed to validate the velocity field of inhaled gas produced by MRI-based CFD simulations through comparison to a velocity field created by phase-contrast (PC) MRI of inhaled gas contrast agent hyperpolarized ^{129}Xe.

Five pediatric patients with OSA underwent tidal-breathing proton MRI to create the boundary conditions for CFD simulations and also inhaled hyperpolarized ^{129}Xe PC MRI for two respiratory cycles. Patients were sedated with dexmedetomidine to create sleep-like airway muscle tone. 2D sagittal PC MRI data were acquired continuously during the two respiratory cycles, with acquisition parameters; spiral readout, in-plane spatial resolution: 2.5mm^2, slice thickness: 10 mm, velocity encoding: 200 cm/s, velocity encoding in either one (foot-head) or three spatial directions (right-left, anterior-posterior, foot-head); acquisition time for a single slice: ~0.5 or 1 s, respectively.

Comparing the velocity fields between CFD and PC-MRI revealed very similar airflow patterns. High-speed jets at the vocal folds and areas of subject-specific constriction occurred in the same places and to approximately the same magnitude in both CFD and PC-MRI, revealing that ^{1}H MRI-based CFD simulations can accurately calculate the velocity field of inhaled gases, including typical room air.

AI-based Detection of COPD using CT Images

Sandeep Bodduluri

Chronic obstructive pulmonary disease (COPD) is the third leading cause of death in the world, affecting over 392 million individuals, and is associated with a substantial economic burden. However, a substantial proportion of adults with COPD remain undiagnosed. The current diagnosis of COPD is made using spirometry, based on the ratio of the forced expiratory volume in one second (FEV_1) to the forced vital capacity (FVC). Although spirometry is safe and easy to perform, it is often underused in primary care settings due to poor access and lack of expertise in performing and interpreting spirometry. In this context, it is pertinent to note that approximately 70 million chest computed tomography (CT) scans are acquired each year in the US. These scans present opportunities to detect COPD in previously undiagnosed individuals.

The use of CT images to detect COPD is increasingly being studied utilizing rapid advances in image processing and deep learning algorithms. In this study, in a large multicohort of former and current smokers, we evaluated and compared the performance of traditional inspiratory CT-based radiomics (texture, shape, and density) features, CT density histogram as features, and 3D CT volumes towards the detection of COPD. The feature sets were trained and tested utilizing decision trees (for radiomics and histograms as input) and convolutional neural network architectures (for 3D CT volumes as input). Feature importance details were provided separately for the best radiomics features and best density threshold (Hounsfield Unit) and the class activation maps for 3D CNN architecture. We show that features from inspiratory CT alone can help accurately detect COPD across standard and low dose scans, and the traditional radiomics features can provide similar performance as deep learning models where pre-selection of either slices or regions of interest is required which may result in inefficiencies and hinder clinical translation.

Fluorine-19 Magnetic Resonance Imaging of the Lungs using Octafluorocyclobutane

Inert fluorinated gases are prominent novel inhalation agents for pulmonary functional magnetic resonance imaging (MRI)[1]. Numerous studies demonstrated feasibility of fluorine-19 (^{19}F) MRI of the lungs using perfluoropropane (PFP)[2,3] and sulfur hexafluoride (SF_6)[4] for diagnostics and the study of various lung disorders. The short T_1 relaxation times of fluorinated gases allow a high number of signal averages yielding sufficient lung image signal-to-noise ratio (SNR). Moreover, ^{19}F has a high natural abundance (~100%), a large gyromagnetic ratio, and is absent naturally in the living organism. These advantages result in the maximization of the ^{19}F MRI signal.

Despite most of the research being performed using PFP and SF_6, it is feasible to explore other inert fluorinated gases that can enhance the SNR level of ^{19}F pulmonary MRI. In this study, we explored the performance of octafluorocyclobutane (OFCB) as an inhalation agent for ^{19}F pulmonary MRI in healthy rats[5]. OFCB contains eight chemically equivalent fluorine atoms per molecule (which is a greater number of equivalent ^{19}F atoms compared to other fluorinated gases), and has a longer spin-spin relaxation time. We have also compared OFCB to PFP in order to determine the feasibility of using OFCB as a fluorinated gas for ^{19}F lung MRI by comparing its SNR to the SNR of PFP scans.

In vivo T_1 and T_2^* relaxation times of OFCB-O_2 mixture were measured to be equal to 17.77±1.5 ms and 3.4 ± 0.4 ms respectively. The gradient echo (GRE) lung images acquired in axial orientation using 70^o Ernst flip angle (FA) condition (TR = T_1) and averaged over either 11s (single breath-hold) or 185 s (continuous breathing) demonstrated the SNR of 9.72±2.1 and 14.48±4.51 respectively. The same images acquired using PFP gas demonstrated smaller SNR of 9.72±2.0 for single breath-hold protocol and of 12.68±4.09 for continuous breathing. OFCB images acquired using continuous breathing protocol and full longitudinal magnetization recovery condition (FA = 90^o, TR = 5T_1) showed the SNR equal to 10.23±0.7, whereas PFP images acquired using the protocol demonstrated lower SNR of 8.81±0.46.

OFCB significantly outperformed PFP in all three different imaging protocols ($p < 0.05$). The observed normalized SNR (normalized for the number of signal averages) advantage of OFCB agreed well with theoretical predictions for single breath-hold protocol and for continuous breathing with 90^o excitation FA. A slight deviation from theoretical values was observed for continuous breathing protocol with 70^o Ernst angle. This was potentially caused by slight mismatch between the OFCB T_1 *in vivo* and the TR value used during the scan. In addition, it could be explained by the absence of respiratory gating.

Overall, OFCB substantially outperforms PFP and the image quality of OFCB scans was significantly higher.

1. Couch, M. J. *et al.* 19F MRI of the Lungs Using Inert Fluorinated Gases: Challenges and New Developments. *J. Magn. Reson. Imaging* **49**, 343–354 (2018).
2. Neal, M. A., Pippard, B. J., Simpson, A. J. & Thelwall, P. E. Dynamic susceptibility contrast 19F-MRI of inhaled perfluoropropane: a novel approach to combined pulmonary ventilation and perfusion imaging. *Magn. Reson. Med.* **83**, 452–461 (2020).
3. Obert, A. J. *et al.* 1H-guided reconstruction of 19F gas MRI in COPD patients. *Magn. Reson. Med.* **84**, 1336–1346 (2020).
4. Adolphi, N. L. & Kuethe, D. O. Quantitative mapping of ventilation-perfusion ratios in lungs by 19F MR imaging of T1 of inert fluorinated gases. *Magn. Reson. Med.* **59**, 739–746 (2008).
5. Shepelytskyi, Y. *et al.* Evaluation of fluorine-19 magnetic resonance imaging of the lungs using octafluorocyclobutane in a rat model. *Magn. Reson. Med.* **85**, 987–994 (2021).

Imaging Change in Ventilation Properties with ^{19}F-MRI: Quantitative, Repeatable and Accessible Imaging of Lung Function

Pete Thelwall - Centre for In Vivo Imaging, Newcastle University, UK

Perfluoropropane (PFP) is an inert, inhalable gas that can be directly imaged by ^{19}F-MRI at thermal polarisation (1-7), enabling quantitative measurement of pulmonary ventilation properties without the need for gas hyperpolarisation equipment and expertise and without recourse to ionising radiation. We have assessed reproducibility of ^{19}F-MRI in healthy volunteers, performed studies to assess change in ventilation properties in patients with asthma and in patients with COPD on administration of a bronchodilator, and assessed impacts of chronic rejection on ventilation properties in lung transplant recipients.

We have employed 3D ^{19}F-MRI in healthy volunteers, patients with asthma, and in patients with COPD to visualise the distribution of inhaled PFP after three deep breaths of a gas mixture composed of 79% PFP and 21% oxygen gas. The proportion of the lung visible in these images was quantified and expressed as lung percentage ventilated volume (%VV). Change in patient %VV on administration of salbutamol was determined. In patients with COPD and in lung transplant recipients we have employed dynamic ^{19}F-MRI over multiple respiratory cycles. As ^{19}F-MRI of inhaled perfluoropropane does not employ hyperpolarisation, and so does not exhibit RF- and T_1-mediated loss of polarisation, tracer gas wash-in and wash-out can be monitored over minute timescales. Voxelwise analysis of dynamic ^{19}F-MRI data provided metrics of regional PFP wash-in and wash-out rate, providing a sensitive measure of regional ventilation properties with a broad dynamic range.

Our studies have demonstrated the high reproducibility of ^{19}F-MRI measurements of lung ventilation properties, with ability to characterise and quantify regional ventilation defects, with sensitivity to treatment response. PFP/oxygen gas mixture inhalation and the scan sessions were well tolerated by all participants. Lung %VV was 97.8 ± 1.4 for healthy volunteers, 87.2 ± 14.3 for patients with asthma, and 69.1 ± 16.6 for patients with COPD. A statistically significant increase in %VV was observed in patients with asthma. Positive correlations were observed between %VV and forced expiratory volume in 1 second (FEV_1), and between %VV and forced vital capacity (FVC). Dynamic ^{19}F-MRI data showed heterogeneous tracer wash-in and wash-out in patients with COPD and in lung transplant recipients with chronic tissue rejection.

^{19}F-MRI of inhaled PFP permits full-lung visualisation and quantitation of ventilation properties. Our studies demonstrate sensitivity to treatment response in patient cohorts. ^{19}F-MRI has lower barriers to entry than hyperpolarised noble gas MRI, and has potential to scale to use in clinical practice as a cost-efficient and valuable tool to image lung ventilation.

1) Halaweish AF et al. Chest. 2013;144:1300–1310. 2) Neal MA et al. Magn. Reson. Med. 2019;82:1301-1311. 3) Couch MI et al. J. Magn. Reson. Imaging. 2019;49(2):343-354. 4) Pippard BJ et al. Magn. Reson. Med. 2021;85:3343-3352. 5) Pippard BJ et al. European Respiratory Journal. 2019;54 (suppl 63) PA3160. 6) Goralski JL et al. JCI Insight. 2020 Jan 30;5(2):e133400. 7) Gutberlet M et al. Radiology. 2018;286(3):1040-1051.

Beyond FEV1: Dynamic Perfluorinated Gas MRI in Cystic Fibrosis

Jennifer L. Goralski, MD

The availability of highly effective CFTR modulators is revolutionizing the treatment of cystic fibrosis (CF) and drastically improving outcomes (1, 2). With this improvement comes a heightened need for sensitive and specific outcome measures that can detect and longitudinally track pulmonary disease, particularly in mild or early CF lung disease(3). One method that holds potential is the development of fluorine-enhanced MRI (^{19}F MRI) to characterize the regional kinetics of a tracer gas (perfluoropropane) wash-in and wash-out over serial breaths (4). When combined with ultrashort echo time (UTE) MRI, this approach provides unparalleled data on the structure and function of the lung. The recent approval of elexacaftor/tezacaftor/ivacaftor (E/T/I) for people with CF provided a unique opportunity to test the ability of ^{1}H UTE and ^{19}F MRI to spatially characterize changes in lung structure and ventilation kinetics, respectively, in response to this highly effective therapy. The study was designed to also assess the correlation between MRI-based descriptors of lung disease and established measures of lung function (FEV1 and LCI).

Adult CF patients were recruited from a single center prior to starting treatment with E/T/I. The following studies were obtained before starting E/T/I, and after one month on treatment: spirometry, multiple breath nitrogen washout (MBW), ^{1}H UTE MRI (structural images) and ^{19}F MRI (ventilation images). Changes between visits were calculated, as were correlations between FEV1, lung clearance index (LCI), MRI structural scores, and MRI-based ventilation descriptors.

8 subjects had complete datasets for evaluation. Consistent with prior clinical trial data, FEV1 and LCI improved after 28 days of E/T/I use. ^{1}H UTE MRI detected improvements in bronchiectasis/airway wall thickening score and mucus plugging score after 28 days of therapy. ^{19}F MRI demonstrated improvements in fractional lung volume with slow gas washout time (FLV↑tau2) and ventilation defect percentage (VDP). Improvements in FLV↑tau2 and VDP correlated with improvement in FEV1 ($r=0.81$ and 0.86, respectively, $p<0.05$).

This observational study establishes the ability of ^{19}F MRI and ^{1}H UTE MRI to detect improvements in lung structure and function after E/T/I treatment. This study supports further development of ^{19}F MRI and ^{1}H UTE MRI as outcome measures for cystic fibrosis research and drug development.

1. Middleton PG, Mall MA, Drevinek P, Lands LC, McKone EF, Polineni D, Ramsey BW, Taylor-Cousar JL, Tullis E, Vermeulen F, Marigowda G, McKee CM, Moskowitz SM, Nair N, Savage J, Simard C, Tian S, Waltz D, Xuan F, Rowe SM, Jain R, Group VXS. Elexacaftor-Tezacaftor-Ivacaftor for Cystic Fibrosis with a Single Phe508del Allele. *N Engl J Med* 2019; 381: 1809-1819.
2. Dave K, Dobra R, Scott S, Saunders C, Matthews J, Simmonds NJ, Davies JC. Entering the era of highly effective modulator therapies. *Pediatr Pulmonol* 2021; 56 Suppl 1: S79-s89.
3. Mayer-Hamblett N, Ramsey BW, Kronmal RA. Advancing outcome measures for the new era of drug development in cystic fibrosis. *Proc Am Thorac Soc* 2007; 4: 370-377.
4. Goralski JL, Chung SH, Glass TM, Ceppe AS, Akinnagbe-Zusterzeel EO, Trimble AT, Boucher RC, Soher BJ, Charles HC, Donaldson SH, Lee YZ. Dynamic perfluorinated gas MRI reveals abnormal ventilation despite normal FEV1 in cystic fibrosis. *JCI Insight* 2020; 5.

Next-generation Gas Hyperpolarization and HP Imaging on Point-of-Care MRI Scanners

Boyd Goodson, Ph.D., Southern Illinois University

MRI provides exquisite high-resolution images of anatomical features and organ function, without the use of ionizing radiation. However, until now the available clinical modalities have generally relied on ^{1}H spins from body water or fat—limiting the sources of contrast and corresponding applications. The recent FDA approval of hyperpolarized (HP) ^{129}Xe for use in pulmonary imaging empowers doctors with an entirely new clinical pulmonary MRI contrast agent, and represents the first approved hyperpolarized agent of any kind. As the demand for HP ^{129}Xe is likely to increase substantially, we will discuss the current status and recent advances of the third-generation clinical-scale XeUS ^{129}Xe hyperpolarizer,[1] including integrated *in-situ* NIR and NMR polarimetry that enables automated calibration and control of the device, and a pilot quality-assurance study.[1]

Next, the increasingly stronger magnets used in most clinical scanners (~1–7 T) are expensive, bulky, and immobile, and scans can be time-consuming and confining for many patients. Low-field (LF) MRI has gained renewed interest because it can potentially obviate such limitations; however, detection sensitivity and contrast limitations present ongoing challenges. Thus, the sensitivity boost and novel contrast provided by HP agents can be highly synergistic with low-field MRI, particularly if the hyperpolarization technique is itself low-cost, rapid, and portable.

Our collaboration is working to integrate multiple HP approaches (and prospective agents) with two different clinical low-field MRI platforms--a 0.35 T full-body scanner (Time Medical) and a 64 mT portable "point-of-care" scanner (Hyperfine) cited at WSU and SIUC, respectively. The 0.35 T system is the only commercial low-field clinical platform that is capable of both ^{1}H and ^{129}Xe MRI. With this system, we are currently working to integrate HP propane,[2] SABRE-hyperpolarized agents (including demonstration of MRS of HP [1-^{13}C]ketoisocaproate in a euthanized mouse[3]), and ^{129}Xe gas with this platform. The point-of-care 64 mT ^{1}H MRI scanner has already been demonstrated in clinical settings for bedside imaging, including of brain injury and cerebral hemorrhage (e.g. Ref. [4]). Here we are investigating the potential for adapting this type of scanner for use with HP substances in biomedical studies—with an ultimate goal of demonstrating utility for pulmonary imaging. We have recently demonstrated imaging of HP pyrazine and nicotinamide (via SABRE), with small-volume imaging performed in a head-coil with a resolution of $1\times1\times3.5$ mm^3 in <15 s.[5] We are currently working to integrate this platform with imaging of HP propane gas, with imaging enabled by partial spin-lock-induced crossing (SLIC)-modified sequences.[1]

Acknowledgements: NSF CHE-1905341, DOD CDMRP W81XWH-20-10578; ***COI Disclosure***: BMG declares stake ownership in XeUS Technologies LTD.

1 Birchall, J.R. et al., Pilot Quality-Assurance Study of a Third-Generation Batch-Mode Clinical-Scale Automated Xenon-129 Hyperpolarizer. *Molecules* **27**, 1327 (2022).

2 Ariyasingha, N.M. et al. Relaxation Dynamics of Nuclear Long-Lived Spin States in Propane and Propane-d6 Hyperpolarized by Parahydrogen. *J. Phys. Chem. C* **123**, 11734−11744 (2019).

3 Adelabu, I. et al., Efficient SABRE-SHEATH Hyperpolarization of Potent Branched-Chain-Amino-Acid Metabolic Probe [1-13C]ketoisocaproate. submitted (2023).

4 Mazurek, M. H. et al. Portable, bedside, low-field magnetic resonance imaging for evaluation of intracerebral hemorrhage, *Nature commun*. **12**, 1–11 (2021).

5 Iqbal, N. et al., Exploring SABRE-Enhanced Imaging with a Portable Clinical Low-Field MRI Scanner. In process (2023).

Next-generation Enabling Hyperpolarized Clinical Technologies

Ed Chekmenev, Ph.D., Wayne State University

The vast majority of emerging hyperpolarized MRI contrast agents employ heteronuclei (*e.g.* ^{13}C or ^{129}Xe) for transient storage of hyperpolarization and detection due to much longer lifetimes of the HP state and the lack of background signal from protons of water and fat. However, clinical MRI scanners are often poorly suited for excitation and detection of heteronuclei as they typically lack the corresponding RF hardware and software. While multi-nuclear detection capability exists on clinical research MRI scanners, to date their number (<0.1%) is inconsequential for the purpose of achieving widespread implementation of HP MRI.

Here, we will discuss our progress in developing four distinct approaches to enable detection of HP contrast media on clinical MRI scanners equipped with proton-only hardware and software. The first strategy employs *proton*-hyperpolarized propane gas[1] produced using a handheld disposable hyperpolarizer. The short lifetime of the HP state of HP propane is mitigated by the production immediately before read-out on a clinical 3 T MRI scanner or through the use of long-lived spin states in low magnetic fields: at 0.35 T and below. Our second approach employs ^{13}C-^{13}C singlet states created in HP [1,2-$^{13}C_2$]pyruvate, which can be detected using proton-only excitation.[2] This approach can be potentially extended to the detection of downstream metabolites, *e.g.* HP [1,2-$^{13}C_2$]lactate, paving the way to real-time metabolic imaging on a wide range of clinical MRI scanners. The third approach relies on the use of ultrafast electronics to "translate" excitation pulses at proton frequency to a given heteronuclear frequency. In this approach, a transmit-receive RF coil is required to transmit excitation pulses and detect the heteronuclear signal. The detected signal is then "translated" back to the proton frequency of the MRI scanner, and can be "fed" to the MRI scanner for image visualization or processed off-line. This approach becomes feasible as high-speed electronics is now a low-cost commodity enabling near-real time high-bandwidth data handling. Radiofrequency Amplification by Stimulated Emission of Radiation (RASER) is the fourth and most promising approach.[4] RASER signals are emitted spontaneously by negatively hyperpolarized spins without external radio-frequency excitation pulses (and thus not requiring the RF excitation coil and the pulse-sequence-synchronization) and without any background signal.[3] The recently demonstrated feasibility of RASER MRI[4] and ^{13}C RASER,[5] and the tracking of chemical transformation and chemical exchange, will be discussed. Together, these advances suggest the feasibility of ^{13}C and ^{129}Xe RASER imaging *in vivo*, as the only hardware requirement for RASER translation is the use of heteronuclear specialized (high Q) detection electronics.

Acknowledgements: NSF CHE-1904780, DOD CDMRP W81XWH-20-10576.
COI Disclosure: EYC declares stake ownership in XeUS Technologies LTD.

1) Kovtunov, K.; Koptyug, I.; Fekete, M.; Duckett, S.; Theis, T.; Joalland, B.; Chekmenev, E. Parahydrogen-induced Hyperpolarization of Gases. *Angew. Chem. Int. Ed.* **2020,** *59*, 17788-97.

2) Mandzhieva, I.; Adelabu, I.; Chekmenev, E.; Theis, T. Proton-only sensing of hyperpolarized [1,2-$^{13}C_2$]pyruvate. *ACS Sensors* **2022,** *7*, 3773–3781.

3) Joalland, B.; Theis, T.; Appelt, S.; Chekmenev, E. Background-Free Proton NMR Spectroscopy with Radiofrequency Amplification by Stimulated Emission Radiation. *Angew. Chem. Int. Ed.* **2021**, 26298-302.

4) Lehmkuhl, S.; et al. RASER MRI: Magnetic resonance images formed spontaneously exploiting cooperative nonlinear interaction. *Sci. Adv.* **2022,** *8*, eabp8483.

5) Nelson, C.; Schmidt, A.; Adelabu, I.; Nantogma, S.; Kiselev, V.; Abdurraheem, A.; de Maissin, H.; Lehmkuhl, S.; Appelt, S.; Theis, T.; Chekmenev, E. Parahydrogen-Induced Carbon-13 Radiofrequency Amplification by Stimulated Emission of Radiation. *Angew. Chem. Int. Ed.* **2023**, e202215678.

Mad Minute Poster Session

February 24th, 2023

6:00pm – 8:30pm

Table of Contents

15. **Andrew Lancaster** – Application of Pulmonary Perfusion Analysis via Magnetic Resonance Imaging to the Phenotyping of Long-COVID Cardiopulmonary Disease
16. **Ben Lavon** – Hilar Vessel Segmentation in Quantitative Chest Tomography Measurement of Pulmonary Vascular Volume Distribution Improves Detection of Pulmonary Hypertension Associated with COPD
17. **Daniel Li** – Serial Two-Photon Tomography of Fluoroscently-Labelled Alveolar-like Macrophages Instilled in Rat Lungs
18. **Luis Loza** – Feasability of 3D Dynamic Gas- and Dissolved-Phase Imaging of the Rodent Lung using Hyperpolarized 129Xe MRI
19. **Alexander Matheson** – 129Xe MRS Gas-Exchange Variability in Asthma: Demographics, Blood and Lung-Function
20. **David Mummy** – Estimating Physiological Values of Membrane and Red Blood Cell Conductance Using 129Xe gas Exchange MRI
21. **Samal Munidasa** – Free-breathing MRI for Monitoring Ventilation and Perfusion Changes Following Elexacaftor/Tezacaftor/Ivacaftor Treatment in Pediatric Cystic Fibrosis
22. **Joseph Plummer** – Compressed-sense reconstructions improve non-Cartesian hyperpolarized 129Xe MRI
23. **Matthew Thurston** – Automated Strategies to Derive Regional Perfusion Defects from Dynamic Contrast Enhanced Pulmonary MRI in Patients with COVID-19 Infection
24. **Andreas Voskrebenzev** – Emphysema Detection with PREFUL MRI Parametric Response Mapping
25. **Brandon Zanette** – 3D Stack-of-spirals Acquisition for 19F MRI of Perfluoropropane in the Human Lung

Hyperpolarized ^{129}Xe Multiple-Breath Washout MRI Shows Improved Ventilation and Reduced Ventilation Heterogeneity Up to 1 Year following Elexacaftor/Tezacaftor/Ivacaftor Treatment of Pediatric Cystic Fibrosis Lung Disease.

Faiyza Alam[1,2], Brandon Zanette[2], Sharon Braganza[2], Renee Jensen[3], Marie-Pier Dumas[3,4], Felix Ratjen[2,3], Giles Santyr[1,2]. *[1]Department of Medical Biophysics, University of Toronto, Toronto, ON, Canada,[2]Translational Medicine Program, The Hospital for Sick Children, Toronto ON, Canada, [3]Division of Respirology, The Hospital for Sick Children, Toronto, ON, Canada, [4]Clinical Epidemiology & Health Care Research, University of Toronto, Toronto, ON, Canada.*

PURPOSE: To evaluate the effectiveness of elexacaftor/tezacaftor/iva-caftor (ETI) therapy, sensitive tools to detect changes in early cystic fibrosis (CF) lung disease are needed. The lung clearance index (LCI) measured by multiple-breath washout (MBW) has been shown to detect treatment effects in pediatric CF [1], but only produces whole-lung averages of ventilation which fail to localize regional lung function. By contrast, hyperpolarized ^{129}Xe MRI conducted in a MBW fashion (MBW Xe-MRI) yields maps of fractional ventilation (FV), regionally quantifying gas clearance/breath. The coefficient of variation (CoV_{FV}) can be computed from FV maps to examine spatial ventilation inhomogeneity [2]. By considering both gas replacement and ventilation heterogeneity, MBW Xe-MRI potentially provides an alternate evaluation of therapy response to LCI. This work evaluates the capability of MBW Xe-MRI to monitor longitudinal changes in CF lung disease in pediatric subjects receiving ETI treatment.

METHODS: 11 subjects (median [IQR] age 15.5 [14-17] years) completed visits at baseline and one month post-ETI. Of these 11, 6 subjects were also evaluated at 6 months post-treatment and 4 were evaluated at 1 year post-treatment. On each visit, the lung clearance index (LCI) was measured with an Exhalyzer®D MBW device (EcoMedics, Duernten, Switzerland; Spiroware 3.3.1) and MBW Xe-MRI was performed in accordance with Couch et al. [3], using a ^{129}Xe dose of 10% TLC topped with N_2 up to 1/6th TLC. CoV_{FV} was determined by calculating the standard deviation over mean of FV using a 3x3 kernel across all voxels in the image. The Wilcoxon signed-rank test was used to identify significant changes between visits. Pearson's correlation was used to compare relative changes in mean FV and CoV_{FV} against relative changes in LCI.

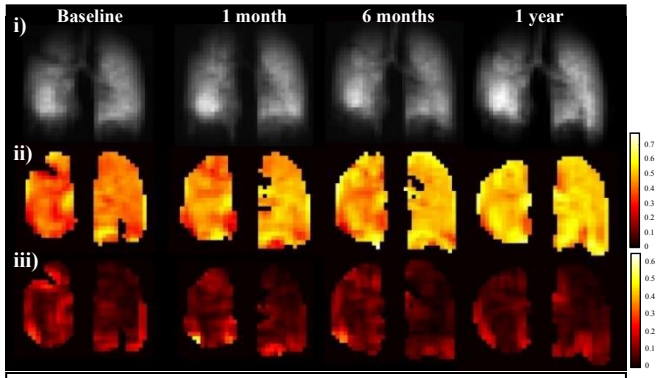

Figure 1: Representative subject (male, 18 yos) results from baseline, 1 month, 6 months and 1 year post-treatment with i) first breath signal intensity images, ii) FV maps, and iii) CoV_{FV} maps.

RESULTS: Xe-MRI (first breath), FV, and CoV_{FV} maps for a representative subject are shown in Figure 1. Figure 2 shows changes from baseline to 1 month, 6 months and 1 year post-treatment for both FV and CoV_{FV} for all subjects. Median (IQR) FV was significantly (P=.04) higher at 1-month (0.42 [0.41 0.45]) compared to baseline (0.37 [0.33 0.42]) and this change persisted between baseline and 6 months (P=.03). Median [IQR] CoV_{FV} was significantly (p=.002) lower at one-month (0.06 [0.05 0.07]) compared to baseline (0.10 [0.08 0.12]) and this change persisted between baseline and 6 months (P=.03). As well, relative changes in CoV_{FV} between baseline and 1 month were found to significantly (P<.001) and highly (R=0.94) correlate with relative changes in LCI (Fig. 3), but FV did not. Relative differences in FV, CoV_{FV} did not correlate with each other. FV, CoV_{FV} were not significantly different from 1 to 6 months.

DISCUSSION: This work demonstrates that MBW Xe-MRI can successfully detect longitudinal improvements in ventilation and ventilation heterogeneity in pediatric CF lung disease following ETI treatment. In most subjects, most of this improvement occurred immediately between baseline and 1-month and persisted up to 1 year. The plateau between 1 and 6 months may be indicative of the CF condition stabilizing, successfully delaying progression of disease. The correlation of relative differences in CoV_{FV} to LCI is consistent with previous findings, where CoV_{FV} correlated with LCI in healthy and stable CF cohorts (R=0.56, P<.001) [4]. This result suggests that these metrics reflect similar pathophysiological changes/improvements, i.e. in ventilation heterogeneity. Similarly, the ability of FV to significantly detect changes at 1 month that persist at 6 months despite its non-correlation to LCI suggests that FV is measuring a different aspect of treatment response compared to LCI and may be meaningful as a supplement for assessing CF lung disease progression. The lack of correlation between FV and CoV_{FV} despite these metrics being derived from the same data is interesting. In some individuals, an increased CoV_{FV} reflected a region of higher FV than the surrounding lung as opposed to lower. This may suggest a compensatory ventilation effect is present. Further investigation of FV skewness, spatial changes in FV/CoV_{FV} maps, and improving the resolution of these washout experiments may shed light on the treatment effect of ETI in pediatric CF lung disease.

CONCLUSION: Both FV and CoV_{FV} detect improvements in ventilation and ventilation homogeneity at one month following ETI treatment, and this change remained consistent from baseline to 6 months. Relative changes in CoV_{FV} correlated with relative changes in LCI. The ongoing study will help clarify the relationship between this novel measure and other imaging outcomes in capturing CF treatment response.

Acknowledgements: Funding by Canadian Institute for Health Research (CIHR), Cystic Fibrosis Foundation (CFF).

References: [1] Ratjen et al., Lancet Respir Med. (2017) Jul;5(7):557-567. [2] Horn et al., Proc Intl Soc Mag Reson Med. (2015) 23. [3] Couch et al., Magn Reson Med. (2020) 84:304–311. [4] Alam et al., ISMRM. (2022) [Abstract].

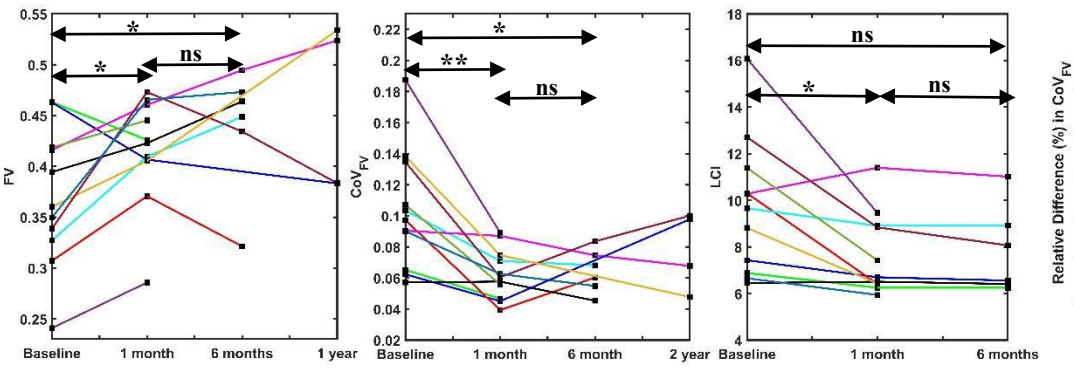

Figure 2: Treatment response to ETI in pediatric CF lung disease captured by FV, CoV_{FV} and LCI at baseline, 1 month, 6 month, and 1 year timepoints. Subjects in all three plots have the same-coloured lines.

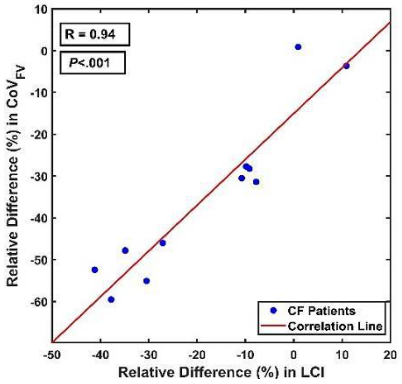

Figure 3: Correlation between relative differences in CoV_{FV}., LCI between baseline, 1 month.

Regional alterations in air-trapping associated with the early progression of COPD

Ryan Baron, Yi Xin, Hooman Hamedani, Mostafa Ismail, Faraz Amzajerdian, Stephen Kadlecek, Ian Duncan, Kai Ruppert, Rahim Rizi

Introduction: In smokers, COPD progression is thought to begin with the narrowing of small airways resulting in expiratory air trapping, followed by emphysematous destruction of the alveoli[1,2]. To study the regional alterations in lung density associated with COPD development and progression, we studied CT-derived ΔEE/ΔEI in the COPDGene cohort.

Methods: Subject data was obtained from the COPDGene Study: Phase-1 and Phase-2 end-expiratory and end-inspiratory CT images randomly selected from 50 never-smokers (Healthy), 50 early-stage COPD GOLD 0-2 subjects (Early), and 50 late-stage COPD GOLD 3-4 subjects (Late). Paired EE/EI images from Phase-2 were co-registered to their respective Phase-1 baseline image; ΔEE and ΔEI were calculated by subtracting the registered follow-up EE/EI images from the baseline EE/EI image. The lung was then divided into anterior, middle, and posterior regions based on pixel density, with parametric maps generated for each. Average change and standard deviation of ΔEE and ΔEI were calculated for all regions.

Results/Discussion: Figure 1A-C shows parametric maps from representative Early (A), Healthy (B), and Late (C) subjects. A qualitative comparison shows that Late and Healthy subjects experienced little change in ΔEE/ΔEI, as the voxel cluster is centered around the origin, while the Early subject experienced an overall loss of lung density at EE which was most pronounced in the posterior region. Bar graphs (Figures 1D&E) show that ΔEE decreased more significantly over the entire lung in the Early subjects (ΔEEmean=-46.2) compared to Healthy (ΔEEmean=-15.7) and Late (ΔEEmean=-6.24) ($p<0.01$), suggesting that the Early cohort developed more expiratory air trapping between Phase-1 and Phase-2. Surprisingly, Late subjects experienced less change in ΔEE compared to Healthy subjects, although this difference was not significant. Regionally, expiratory air trapping in the Early cohort was significantly higher in the posterior lung (ΔEEmean=-63.4) than in either the anterior (ΔEEmean=-34.1) or middle regions(ΔEEmean=-42.9)($p<0.01$), indicating a potential gradient in its development in the gravitationally dependent (posterior) vs. non-dependent (anterior) lung regions when positioned supine. Similar alterations in lung density were not seen at ΔEI, and no significant differences were observed between regions or cohorts.

Conclusion: ΔEE results suggest that Early COPD subjects experienced significantly greater tissue density loss associated with air trapping between study visits compared to Healthy or Late COPD subjects. Additionally, expiratory air trapping was significantly increased in the posterior, gravitationally dependent lung, suggesting a potential gradient in the development of altered lung mechanics associated with the early stages of COPD progression.

1.McDonough,NEJM(2011)
2.Bhatt,AJRCCM(2016)

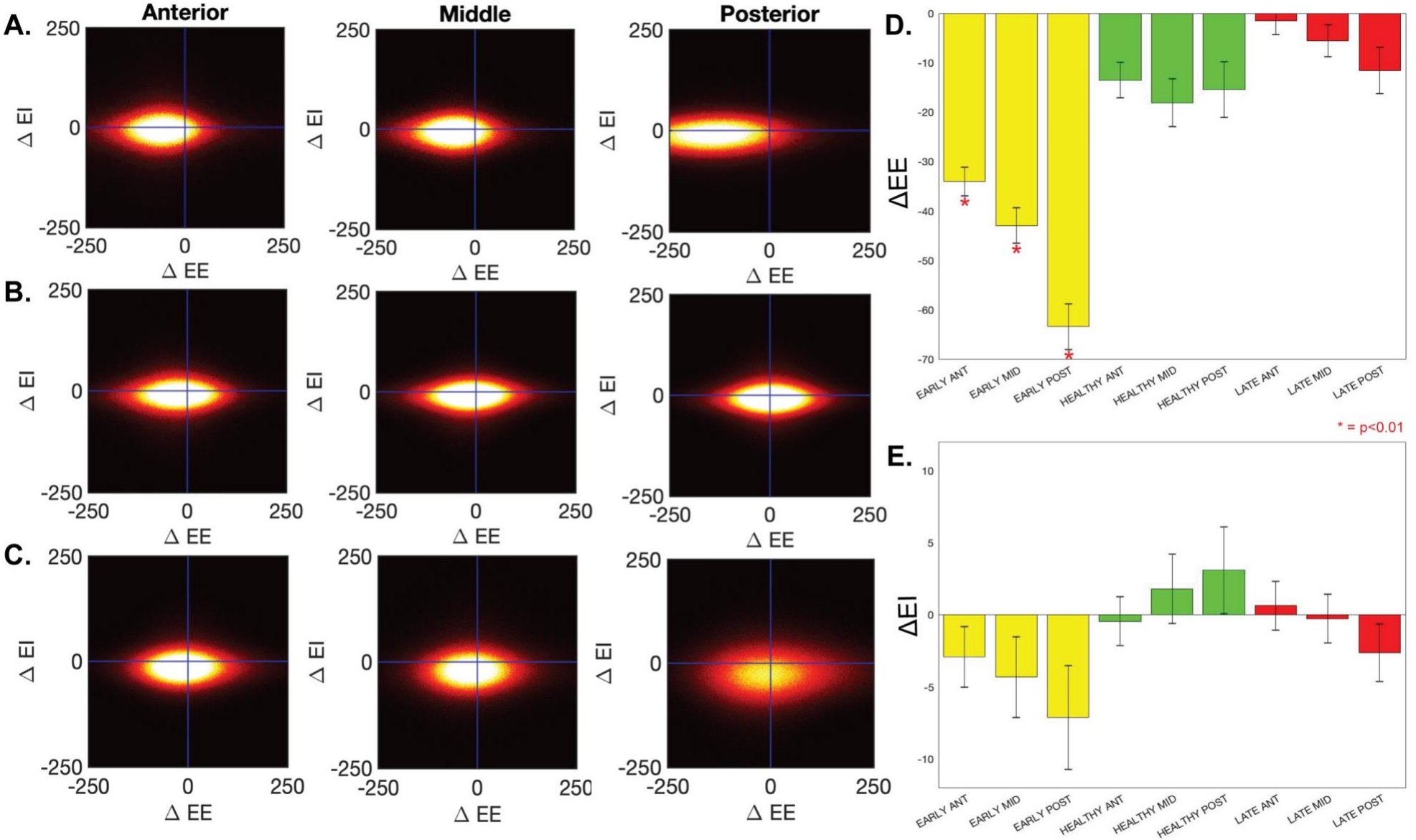

Figure 1: (A, B, C) Parametric maps from a representative Early COPD subject (A), Healthy subject (B), and Late COPD subject (C). The origin of the map represents 0 change at both ΔEE and ΔEI, while any shift toward negative or positive values indicates a decrease or increase in lung density between Phase 1 and Phase 2 CT imaging. (D & E) Bar graphs with standard error bars representing the average change in lung density shown as ΔEE and ΔEI from the anterior, middle and posterior regions in the Early COPD (yellow), Healthy (green), and Late COPD (red) cohorts.

Multiple-Breath Washout Ventilation Imaging Using Interleaved HP ^{129}Xe and ^{1}H 2D Spiral

Abdullah S. Bdaiwi, Joseph W. Plummer, Matthew W. Willmering, and Zackary I. Cleveland
Center for Pulmonary Imaging Research, Cincinnati Children's Hospital Medical Center, Cincinnati, OH 45229

Rationale: Hyperpolarized (HP) gas MRI is powerful method to assess lung function, with impaired ventilation typically defined via a defect (i.e., low signal) volume after a single inhalation. This binary quantification (ventilated or unventilated) obscures the dynamic nature of true physiology. To quantify ventilation dynamics, multiple-breath washout MRI with hyperpolarized (HP) gas (MBW) has been introduced [1,2] to measure fractional ventilation, r, (ratio of fresh gas entering a lung volume to end inspiratory volume) and has demonstrated sensitivity to impaired function in multiple diseases [2-5]. However, ^{129}Xe signal acquired during MBW, is affected by B_1-inhomgenites and spatially varying RF and T_1 decay, which must be corrected to yield accurate measures of ventilation. Further, it requires ^{129}Xe images with varying signal—and possible breath-to-breath variations in gas filling—to be coregistered, which could bias results. We propose a MBW method where images are corrected for B_1-field inhomogeneities and RF and T_1 signal decay, while facilitating image registration. The method employs rapid 2D spiral with interleaved ^{129}Xe—^{1}H—^{129}Xe acquisitions in each breath. This method enabled robust anatomical registration and accurately maps the temporal and spatial heterogeneity of ventilation.

Methods: Images were acquired from healthy subjects using breath-holds of 10s. Subject received 1-L dose of ^{129}Xe polarized to ~25% (Polarean, Durham, NC) inhaled from functional residual capacity. HP^{129}Xe images (~ 3.3s acquisition each) were separated by a ^{1}H acquisition (3.3s). The participant exhaled, inhaled room air, held their breath, and this procedure was repeated over 5 washout breaths. To confirm far off-resonant RF during ^{1}H imaging did not decay the ^{129}Xe signal, the sequence was examined by acquiring with and without ^{1}H acquisition. Images were acquired using a 3T Philips Ingenia scanner [resolution=3.5×3.5 mm^2, BW=285 Hz/pixel, TE/TR=1.6/8.9 ms, FOV=330x330 mm^2, 10 slices, slice thickness=15 mm, readout=3.5 ms, FA(^{129}Xe)=7.5°, FA(^{1}H)=5°] and reconstructed in MATLAB. Flip-angle (α) maps were extracted from Bloch Equation modeling and keyhole reconstruction [3]. T_1 map was calculated by a two-point fit of the decay between ^{129}Xe images. The first ^{129}Xe image in each breath, I, was corrected by:

$I_{Corrected} = I \times \frac{1}{\alpha}\frac{N_s}{sin(\alpha)} \left[\frac{1-[cos(\alpha)\, exp\left(-\frac{TR}{T_1}\right)]}{1-[cos(\alpha)\, exp\left(-\frac{TR}{T_1}\right)]^{N_s}}\right]$, where N_s is the number of spiral trajectories per slice. Fractional ventilation was calculated by fitting $I_{Corrected}(n) = I_{Corrected}(0)\,(1-r)^{n-1}$ to the washout images, where $I_{Corrected}(0)$ is the reference image (first breath) and n is number of breaths [4,5].

Results: Anatomical and ventilation images were successfully obtained and quantifiable ^{129}Xe signal (SNR ≥5) was observed out to 3 breaths. ^{129}Xe images showed perfect spatial overlap with same-breath ^{1}H images without registering images. Means of flip-angle and T_1 maps extracted from ^{129}Xe images acquired with and without ^{1}H imaging (same T_1 delay), were not statically different (Figure B), indicating any far off-resonant RF-induced decay was negligible. For MBW imaging, the extracted FA (mean = 7.4±2.7) and T_1 (Mean = 17.4±6) maps yield expected values and were consistent across breath. The resulting Fractional ventilation map (mean = 0.37±0.08) was consisted with previous observations and physiology expectations.

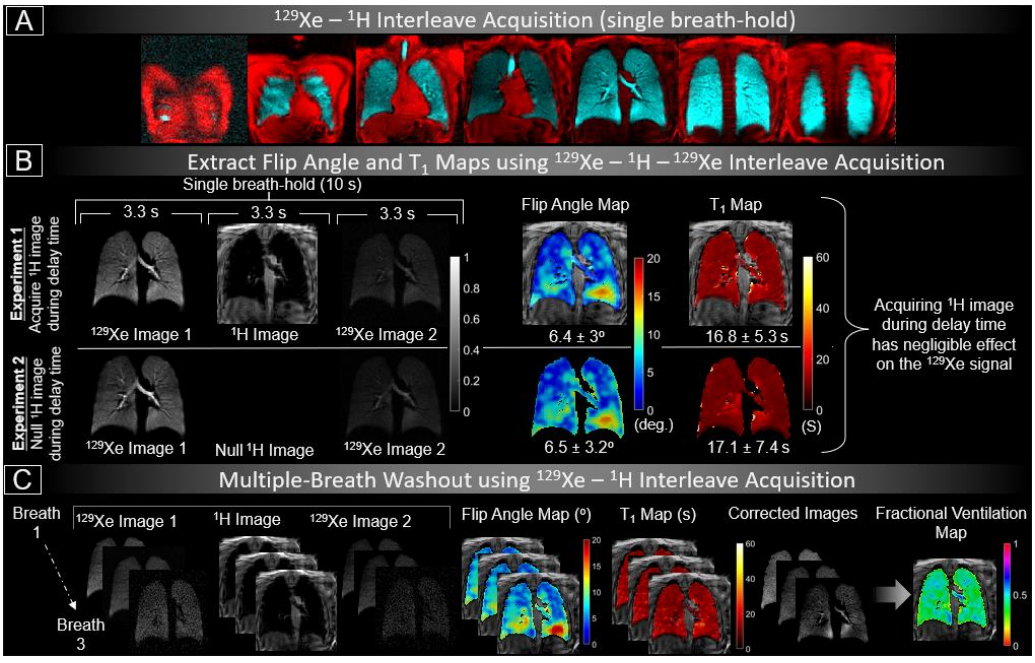

Conclusions: Improved ^{129}Xe MBW imaging was obtained using 2D spiral with an interleaved ^{129}Xe—^{1}H—^{129}Xe acquisition. Accurately mapping ventilation heterogeneity using ^{129}Xe MRI will provide a useful tool to detect functional changes that result from pulmonary disease progression and treatment response. Reducing FA and in-plane resolution ensure ≥5 images with acceptable SNR will be available for analysis, thus yielding more robust temporal dynamics.

References: [1] Horn, F. C, et al. *Journal of applied physiology* 116.2 (2014): 129-139. [2] Hamedani, H., et al. *Radiology* 279.3 (2016): 917. [3] Niedbalski, P. J, et al. *MRM* 82.1 (2019): 367-376. [4] Morgado, F, et al. *MRM* 80.6 (2018): 2670-2680. [5] Couch, M. J, et al. *MRM* 84.1 (2020): 304-311.

Funding: This study was supported by NIH (R01HL131012, R01HL143011, and R00HL138255).

Deep Learning-based Artifact Detection and Correction in Lung 4DCT

Joshua Carrizales, Mattison Flakus, Dallin Fairbourn, Gary E. Christensen, John E. Bayouth, Joseph M. Reinhardt

Purpose: Respiratory motion artifacts in four-dimensional computed tomography (4DCT) scans are often caused by inconsistent patient breathing patterns. Common artifacts include streaking, blurring, duplicated anatomy, missing anatomy, and incorrect reconstructions of patient anatomy[1]. Anatomical inaccuracies due to artifacts reduce the accuracy of metrics derived from 4DCT scans including calculated radiation therapy dose distributions and local lung function measurements, such as the Jacobian determinant[2]. The purpose of this work was to develop deep learning models that can automatically *detect* and *correct* motion artifacts in 4DCT scans.
Methods: We developed two separate convolutional neural networks (CNNs)[3,4]: one trained to *detect*[3] artifacts and another trained to *correct*[4] artifacts detected by the first network. The artifact *detection* dataset contained 26,710 2D coronal slices from 4DCTs of 28 lung cancer patients. Our dataset contained several types of artifacts manually segmented by an expert: duplication, incompletion, and interpolation. The *detection* model was developed using an 80/20 train/validation split, a learning rate of 0.00003, a batch size of 32, and 100 epochs[3]. Our model was tested using 5-fold cross validation on a hold-out dataset of 22 3D volumes, and receiver operating characteristic (ROC) analysis was performed. For the *correction* model, we augmented artifact-free 4DCT data with simulated artifacts to create our dataset. We used 50000 2D images for training and 900 2D images for validation. We tested the model on one hold-out image that contained a tumor and compared our model's prediction to the ground truth using the structural similarity index measurement (SSIM).
Results: Validation confirmed that the *detection* model performed at a high level with a mean true positive rate of 0.96 +/- 0.04 and a mean area under the curve (AUC) of 0.97+/- 0.03. The *correction* model obtained a SSIM of 0.89.
Discussion: Current methods of artifact *detection* are only able to identify a couple artifact types: diaphragm duplication artifacts or interpolation artifacts. Although duplication artifacts are the most common type of artifact, current artifact *detection* relies solely on artificially generated data[3,5] which makes their models biased. Our *detection* model was trained on manually segmented artifacts from 98 3D volumes and supplemented with artificially generated interpolation artifacts, making it more robust than current methods. Figure 1 shows the performance of the artifact *correction* network. We demonstrated how a simple CNN can synthesize structurally accurate images of the lung to repair detected artifacts. Although the prediction is convincing at a glance there is slight blurring that occurs in the predicted region. This is likely because of the perceptual loss function used during training.
Conclusion: Respiratory motion artifact *detection* and *correction* provides higher-quality image data to physicians for improvements in lung cancer radiation treatment. Our work could be easily implemented in a clinical environment because of its resistance to variance, fast run time, and minimum memory requirements. Future work should focus on improving the quality of lung structure and further validating our *correction* network.

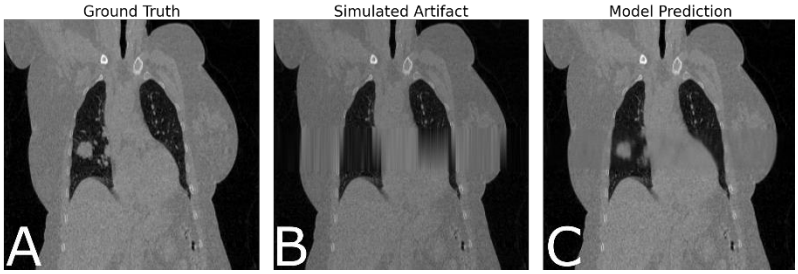

Figure 1. Images showing the impact artifacts have on 4DCT scans. A) Original image of lungs. B) Artificially generated artifact. C) Model prediction of lungs.

References:

1. Han D, Bayouth J, Bhatia S, Sonka M, Wu X. Characterization and identification of spatial artifacts during 4D-CT imaging. *Med Phys*. 2011;38(4):2074-2087. doi:10.1118/1.3553556

2. Yamamoto T, Langner U, Loo BWJ, Shen J, Keall PJ. Retrospective analysis of artifacts in four-dimensional CT images of 50 abdominal and thoracic radiotherapy patients. *Int J Radiat Oncol Biol Phys*. 2008;72(4):1250-1258. doi:10.1016/j.ijrobp.2008.06.1937

3. Shao W, Pan Y, Durumeric OC, et al. Geodesic density regression for correcting 4DCT pulmonary respiratory motion artifacts. *Med Image Anal*. 2021;72. doi:10.1016/j.media.2021.102140

4. Yan Z, Li X, Li M, Zuo W, Shan S. Shift-net: Image inpainting via deep feature rearrangement. In: *Proceedings of the European Conference on Computer Vision (ECCV)*. ; 2018:1-17.

5. Madesta F, Sentker T, Gauer T, Werner R. *Deep Learning-Based Conditional Inpainting for Restoration of Artifact-Affected 4D CT Images*.; 2022.

Quantitative CT and Computational Fluid Dynamics Show That Air Pollution Increases Airway Resistance Altering Regional Lung Structure and Function in COPD

Jiwoong Choi[1,2], In Kyu Lee[1,2], Mario Castro[1], Chang-Hoon Lee[3], Sunmi Choi[3], Hye-Ryun Kang[3], Kyoung-Nam Kim[4], Kyung-Shin Lee[3], Hongseok Ko[5], Kum Ju Chae[6], Ching-Long Lin[7], Eric A. Hoffman[7], Woo Jin Kim[5], Eun-Kee Park[8], Chang Hyun Lee[3,7]

[1]University of Kansas School of Medicine, Kansas City, KS, USA; [2]University of Kansas, Lawrence, KS, USA; [3]Seoul National University Hospital, Seoul, Korea; [4]Ajou University School of Medicine, Suwon, Korea;
[5]Kangwon National University Hospital; [6]Jeonbuk National University Hospital;
[7]The University of Iowa, Iowa City, IA, USA; [8]Kosin University College of Medicine, Busan, Korea.

Purpose: We investigated impact of air pollution exposure on regional airway and lung structure-function relationship in chronic obstructive pulmonary disease (COPD) patients and healthy adults, using quantitative computed tomography (QCT) and computational fluid dynamics (CFD) analysis.
Methods: Inspiratory and expiratory CTs, direct and address-based air pollution measurements, and pulmonary function test (PFT) results were prospectively collected (under IRB approval and with subject consent, using a common dose-reduced QCT protocol) enrolled in 5 institutions in South Korea [**1,2**], with healthy lungs (age=68±10, M:F=15:51) and COPD (age=69±7, M:F=66:10). We derived CT-based 185 structural and functional features from VIDA Vision (Coralville, IA) and in-house software, of which 72 air flow features of tidal breathing were computed from in-house one-dimensional (1D) CFD simulations in the entire conducting airway model [**2**]. ANOVA, post-hoc tests, and Pearson's correlation were used for analysis.
Results: Directly measured PM2.5 exposure was highly correlated with CFD-derived airway resistance (R) of the whole lung (r=0.63, p<0.001) at the peak inspiratory flow rate (hereafter). Air pressure drop (ΔP) to the terminal bronchiole was also associated with PM2.5 (r=0.49, p<0.001), particularly in the right lower lobe (RLL, r=0.60, p<0.001).

In the airways, normalized hydraulic diameter (D_h^*) of the right middle and lower lobes segmental airways, normalized wall thickness (WT^*) of the left lower lobe (LLL) and the right upper and middle lobes (RUL and RML), and luminal circularity (Cr) of the RUL were inversely associated with PM2.5 (r=-0.40, -0.35, -0.29, -0.50, -0.34, -0.63, p=0.004, 0.014, 0.038, <0.001, 0.016, <0.001, respectively). Among these, RUL segmental airway wall thinning ($-WT^*$) was highly correlated with R and ΔP (r=0.72, 0.43, p<0.001, 0.003). Segmental airway narrowing ($-D_h^*$) in the RML and RLL was correlated with ΔP (r=0.42, 0.47, p=0.003, 0.002).

PM2.5 exposure was also associated with alteration of regional ventilation. With more PM2.5 exposure, relative regional air volume change (RRAVC) [**3**] is smaller in the left upper and lower lobes and the RML yet greater in the RUL and the RLL (r=-0.61, -0.61, 0.62, -0.60, 0.61, p<0.001 for all).

PM2.5 exposure was also inversely correlated with CFD-derived transpulmonary pressure (P_{tp}) (r=-0.49, p<0.001), which may be contributable to reduced deformation indicated by inverse correlation of PM2.5 with volume expansion ratio (Jacobian determinant, *J*), anisotropic deformation index (ADI) (r=-0.36, -0.33, p=0.009, 0.018, respectively). PM2.5 was also correlated with functional small airway disease percent (fSAD%) (r=0.33, p=0.016).
Discussion: PM2.5 is associated with alteration of cross-correlated regional airway structure and lung function. Air pollution-induced thinning of airway wall may reduce circularity of airway lumen leading to decrease in minor diameter. Airway narrowing in the RLL may contributes to the greater pressure drop (r=-0.47 between D_h^* at RLL and ΔP, p=0.002). There are other strong association of residential and work address-based gaseous air pollutants exposure with the above-described features, for example NO2 and CO exposure and RUL WT* has strong inverse correlation (r=-0.74, -0.71, p<0.001, 0.017). Impact of PM10 was less significant than PM2.5.
Conclusion: QCT and CFD analysis associated air pollution exposure with increase in airway resistance along with regional alteration of airway structure and lung function features in COPD. QCT-CFD analysis may help unfold complicated functional mechanisms of air pollution impact in lung health and disease.
Funding: This work was supported in part by Korea Environmental Industry & Technology Institute (KEITI) grant 2018001360001 funded by Ministry of Environment (MOE), Republic of Korea.
References:
[1] Choi J, Lee IK, Lee C-H, Choi S, Ahn SY, Ko H, Kim KN, Lee KS, Lin CL, Hoffman EA, Castro M, Chae KJ, Kim WJ, Park EK, Lee CH. Quantitative CT Analysis of Ambient Particulate Matter Exposure-associated Multiscale Structure and Function Alteration in Asthma, COPD, and IPF Lungs. American Thoracic Society International Conference, San Francisco, CA, May 13-18, 2022. Am J Resp Crit Care Med 2022;205:A2544

[2] Choi J, Lee IK, Lee C-H, Choi S, Kang HR, Kim KN, Lee KS, Ko H, Chae KJ, Lin CL, Hoffman EA, Kim WJ, Park EK, Lee CH. Quantitative CT and Computational Fluid Dynamics Analysis of Air Pollution Impacts on Tidal Breathing in Asthma, COPD, and IPF Lungs. Radiological Society of North America Scientific Assembly and Annual Meeting, Chicago, IL, USA, November 27-December 1, 2022.

[3] Chae KJ, Choi J, Jin GY, Hoffman EA, Laroia AT, Park M, Lee CH. Relative regional air volume change maps at the acinar scale reflect variable ventilation in low lung attenuation of COPD patients. Acad Radiol 2020 Nov;27(11):1540-1548.

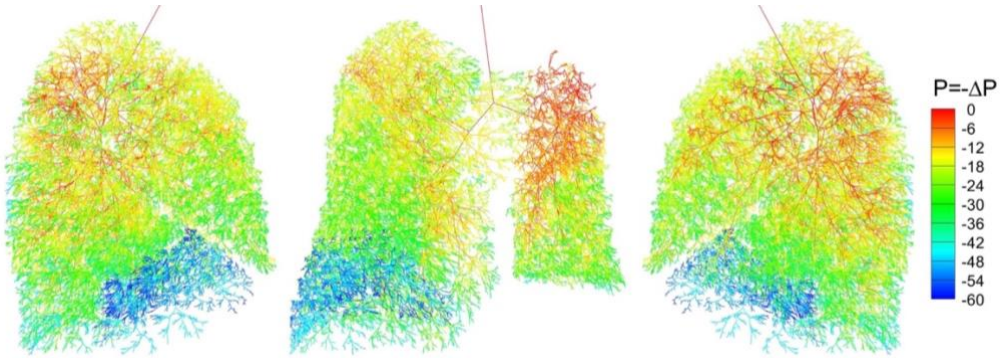

Figure. 1D CFD-derived pressure distribution through the entire conducting airway model from trachea to the terminal bronchioles in a representative COPD patient with high PM and CO exposure, correlated with greater ΔP in the right lower lobe (RLL) (see blue region).

Multiple breath wash-in/out time dynamics with sub 0.5 second scan time using 19F at 3.0T

Sang Hun Chung[1]; Khoi Minh Huynh, PhD[1]; Jennifer L. Goralski, MD[2,3,4]; Yong Chen, PhD[6]; Pew-Thian Yap, PhD[5]; Scott H. Donaldson, MD[2,3]; Yueh Z. Lee, MD/PhD[2,5]

[1]Department of Biomedical Engineering, University of North Carolina, Chapel Hill, USA, [2]Division of Pulmonary and Critical Care Medicine, UNC-Chapel Hill, [3]Marsico Lung Institute/UNC Cystic Fibrosis Center, UNC-Chapel Hill, [4]Division of Pediatric Pulmonology, UNC-Chapel Hill, [5]Department of Radiology and Biomedical Research Imaging Center, UNC-Chapel Hill, [6]Department of Radiology, Case Western Reserve University, Cleveland, USA

Purpose

Evaluate the feasibility of a sub 0.5 second scan time spiral magnetic resonance imaging (MRI) sequence for use in multiple wash-in/out ventilation time constant measurement in human lungs with fluorinated gas (^{19}F). A previously validated [1] 3D Volumetric interpolated breath-hold examination (VIBE) sequence is used as control.

Methods

8 participants with Cystic Fibrosis (CF) (ages 20-37 years, 6 female) and 5 healthy subjects (ages 22-27 years, 3 females) participated in this study. The study was approved by the local IRB, and informed consent was obtained from all participants prior to scans. Participants breathed in 10 wash-in breaths while scans were acquired every other breath at maximal inhalation breath-hold. Wash-out scans were repeated until no signal was visible. Corresponding VIBE (TE/TR, 1.61/13 ms; FA, 74°; resolution of 6.25 X 6.25 mm; slice thickness, 15 mm; number of slices, 18; acquisition matrix, 64 X 64; bandwidth, 130 Hz/pixel; averages, 2; partial Fourier, 6/8) and spiral (TE/TR, 0.48/11 ms; FA 74°; resolution of 6.25 X 6.25 mm; slice thickness, 15 mm; number of slices, 18; acquisition matrix, 64 X 64; bandwidth, 130 Hz/pixel; partial Fourier, 6/8) scans were acquired during the same breath-hold. The scans were performed on a Siemens Prisma (Siemens Medical Systems, Erlangen, Germany) 3.0T multinuclear capable scanner. The spiral scans were acquired as raw data and denoised [2]. The acquired data was fitted to exponential curves and the wash-out time constant was calculated. The ventilated Fractional Lung Volume (FLV) was calculated as the portion of the in-lung voxels with washout time constants below 163 seconds.

Results

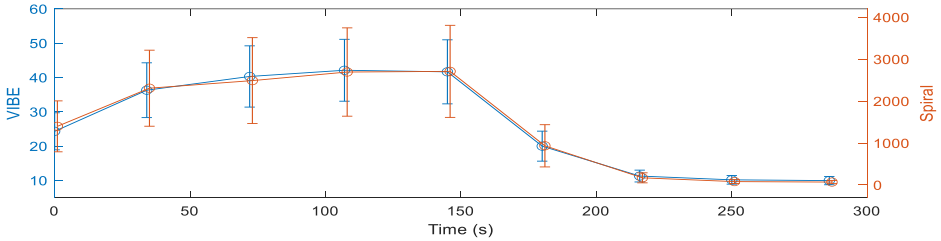

Figure 1. Whole lung signal average and error bars (± 1 standard deviation) for VIBE and Spiral

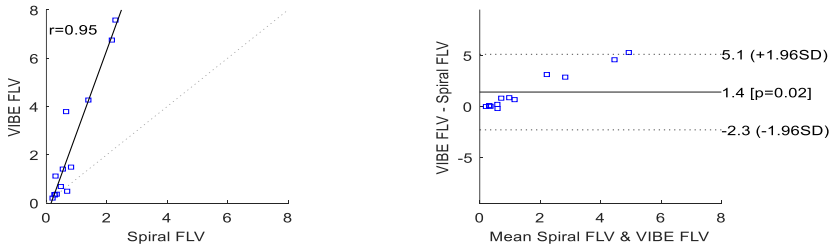

Figure 2. Bland-Altman plot of VIBE FLV and Spiral FLV

Discussion

The FLV scores were highly correlated (r=0.95) but with a systemic shift on the FLV magnitudes. The spiral data was acquired after the VIBE and had a noticeable higher standard deviation which might partially account for the shift in FLV values. Other sources of difference might be due to different sensitivities from the two tested sequences and the denoising process. Future work will be carried to understand the sources of variation and test for disease sensitivity in free-breathing subjects. This study is limited by the number of participants and the lack of standardization of breath size.

Conclusion

The high correlation indicates the possibility of using sub-0.5 second scans for multiple breath wash-in/out 19F ventilation imaging at 3.0T, opening the doors for free breathing 3D volumetric MRI ventilation imaging.

References

1. Goralski JL, Chung SH, Glass TM, et al. Dynamic perfluorinated gas MRI reveals abnormal ventilation despite normal FEV1 in cystic fibrosis. JCI Insight. 2020;5(2). doi:10.1172/jci.insight.133400
2. Huynh KM, Chang W-T, Chung SH, Chen Y, Lee Y, Yap P-T. Noise Mapping and Removal in Complex-Valued Multi-Channel MRI via Optimal Shrinkage of Singular Values. In: de Bruijne M, Cattin PC, Cotin S, et al., eds. Medical Image Computing and Computer Assisted Intervention – MICCAI 2021: 24th International Conference, Strasbourg, France, September 27–October 1, 2021, Proceedings, Part VI. Vol 12906. Lecture notes in computer science. Springer International Publishing; 2021:191-200. doi:10.1007/978-3-030-87231-1_19

Cardiogenic Oscillations in Mice via ^{129}Xe Gas Exchange Spectroscopy: The Effects of PEEP and Rocuronium

Mariah L. Costa[1, 2], Elizabeth M. Fugate[3], Stephanie A. Soderlund[1], Brice J. Albert[1], Diana M. Lindquist[3], Zackary I. Cleveland[1, 2, 3]

[1]Center for Pulmonary Imaging Research, Division of Pulmonary Medicine, Cincinnati Children's Hospital Medical Center, Cincinnati, OH 45229; [2]Department of Biomedical Engineering, University of Cincinnati, Cincinnati, OH 45221; [3]Imaging Research Center, Department of Radiology, Cincinnati Children's Hospital Medical Center, Cincinnati, Ohio 45229

Purpose: Hyperpolarized (HP) ^{129}Xe gas exchange MR spectroscopy (MRS) measures functional biomarkers of disease severity in a diverse set of cardiopulmonary disorders, because in humans, dissolved ^{129}Xe resonates at 198 ppm in the interstitial membrane and 217 ppm in red blood cells (RBCs). The RBC peak oscillates in magnitude, frequency, and phase during the cardiac cycle due to changes in pulmonary capillary blood volume, and may be impacted by capillary pressure, impedance, blood oxygenation, and vascular resistance. Oscillation amplitudes decrease relative to healthy subjects in chronic obstructive pulmonary disease, left heart failure, and pulmonary arterial hypertension, while increasing in idiopathic pulmonary fibrosis **[1]**. However, it has not been applied preclinically, because mice lack a unique RBC peak—instead displaying a combined membrane + RBC peak at ~198 ppm **[2]**. Here, ^{129}Xe MRS was used to investigate cardiogenic oscillations in mice ventilated at standard pressure, high positive end-expiratory pressure (PEEP), and standard pressure under rocuronium bromide paralytic.

Methods ***Animal handling:*** C57BL/6J mice were anesthetized with ketamine/xylazine/acepromazine and ventilated at 100 bpm (70% ^{129}Xe, 30% O_2). The standard pressure group (n=3) was ventilated at a peak inspiratory pressure of 16±1cmH_2O and the high pressure group (n=3) at 20±2cmH_2O and PEEP of 8±2cmH_2O. 3 animals were administered rocuronium bromide and scanned at standard pressure. Heart rate (HR) was sampled at 1 Hz via EKG. ***MRS:*** was performed with an NSPECT sequence on a 7T Bruker BioSpin (ParaVision 6.0.1). ^{129}Xe was polarized to >30% (Model 9820, Polarean Plc). Spectra were acquired over 83 breaths (50s scan) [1000 FIDs, 512 points/FID, TR=50ms, dwell time= 25μs; RF: 0.59ms 3-lobe sinc, α=90°; bandwidth=10.5kHz] at 198 ppm. ***Analysis*****:** Spectra were processed in MATLAB (**Fig. 1A**) and the amplitude of the dissolved peak (**Fig.1B**) was detrended by fitting to a double exponential and filtered (0.5 Hz high-pass; 0.16 Hz band-pass window was applied to remove the respiratory frequency). After iFFT across the indirect dimension, the average change in peak amplitude and area were quantified relative to the maxima from the first pulse.

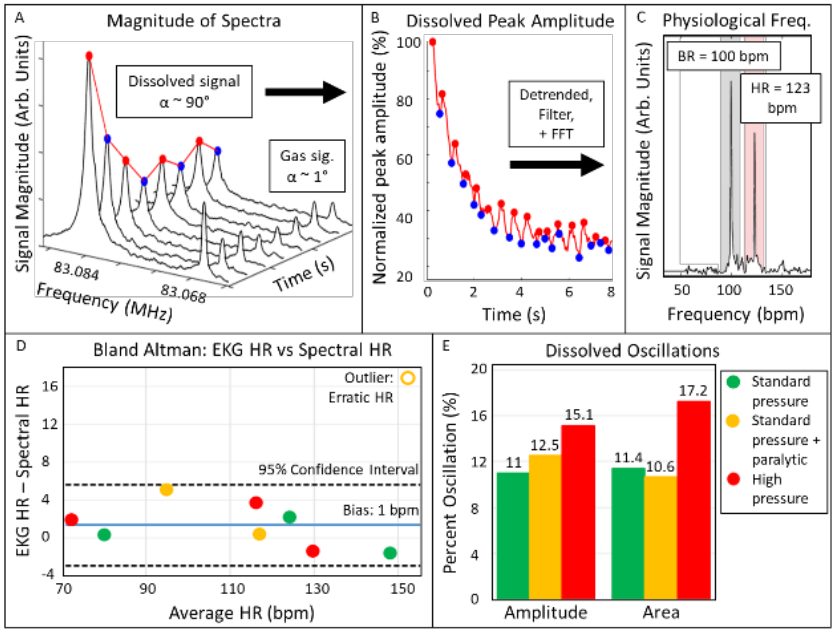

Fig. 1. *Magnitude spectra (**A**) showing oscillations due to ventilation and pulsatile capillary blood volume (**B**). Detrended, high-pass filtered, iFFT of (**A**) reflecting BR and HR (**C**). There was good agreement (within 1 bpm) between EKG and spectral HR, with most data falling within the 95% confidence interval. In one case, an erratic HR (range: 121–192 bpm), resulted in poor agreement (**D**). Oscillations in dissolved amplitude and area (**E**) increased in magnitude when PEEP was applied due to capillary compression. Paralytic rocuronium bromide did not noticeably change the oscillation magnitude.*

Results: While the human membrane peak does not exhibit cardiogenic oscillations, the similar frequency mouse dissolved peak oscillated due to the contribution from the RBCs. Distinct respiratory and HR peaks were identified (**Fig. 1C**), with the spectral HR agreed well with EKG. The magnitude of the amplitude oscillations was 11% for the standard pressure group, 12.5% for the standard pressure with paralytic group, and 15.1% for the high pressure group. The magnitude of area oscillations was 11.4% for the standard pressure group, 17.2% for the high pressure group, and 10.6% for the standard pressure with paralytic group (**Fig. 1D**).

Discussion: Cardiogenic oscillations have been observed from dissolved ^{129}Xe spectra in mice. Oscillation magnitude closely aligns with those seen in humans (~10% in healthy adults) **[3]**. High PEEP compressed the capillaries and increased the pressure at systole, thereby causing a large drop in pressure between systole and diastole – generating increased oscillation amplitude. Rocuronium increases compliance with mechanical ventilation and did not appear to affect cardiogenic oscillations, but did increase HR variability.

Conclusions: Dissolved ^{129}Xe MRS can evaluate cardiogenic oscillations in mice, and these oscillations are sensitive to hemodynamic changes caused by PEEP. This technique can be extended to a diverse set of mouse models to better understand lung microvasculature pathophysiology and hemodynamics, providing new insight into human lung disease.

References: **[1]** Wang, Z, et al., *Eur Respir J* 2019; 54: 1900831. **[2]** Freeman, MS, et al., *MRM* 2013, 70:1192–1199. **[3]** Bier, EA, et al., *NMR Biomed*. 2019 Jan;32(1):e4029.

Acknowledgements: NHLBI R01HL143011.

Hyperpolarised helium MRI in direct and indirect asthmatic airway challenge

Chuan T Foo[1,2], Kris Nilsen[3,4], Bruce R Thompson[5], Francis Thien[1,2]

[1]Box Hill Hospital, Melbourne, Victoria
[2] Monash University, Melbourne, Victoria
[3] Alfred Hospital, Melbourne, Victoria
[4] Swinburne University of Technology, Melbourne, Victoria
[5] Melbourne University, Melbourne, Victoria

Introduction/Aim: MRI ventilation defects in acute asthma are not homogeneous, but regionally heterogeneous. We assessed topographical ventilation differences following direct (methacholine) and indirect (mannitol) inhalational challenges in mild asthma, to improve understanding of their pathophysiology.

Methods: Asthmatic subjects underwent spirometry and hyperpolarised helium MRI (He3MRI) ventilation scans pre and post inhalation of either methacholine or mannitol (at their known provocative concentration/dose) with repeat scans using alternate challenge test on a separate day. He3MRI ventilation was quantified using previously established k-means segmentation.

Results: 8 subjects were studied. Mean age was 35.9±9.8 years and 75% were females. Baseline FEV1 was 95.3±12.8% and fell by 24±7% post methacholine challenge. Post mannitol challenge, FEV1 fell by 18±11% from a baseline of 94.0±12.4%. For all patients, ventilation abnormalities seen at baseline were worse post-challenge. New areas of ventilation defects were also observed with regions of poor ventilation increasing from 10.3% to 17.8% with methacholine and from 11.9% to 15.1% with mannitol. Considerable overlap between regions affected by either challenge test was also noted.

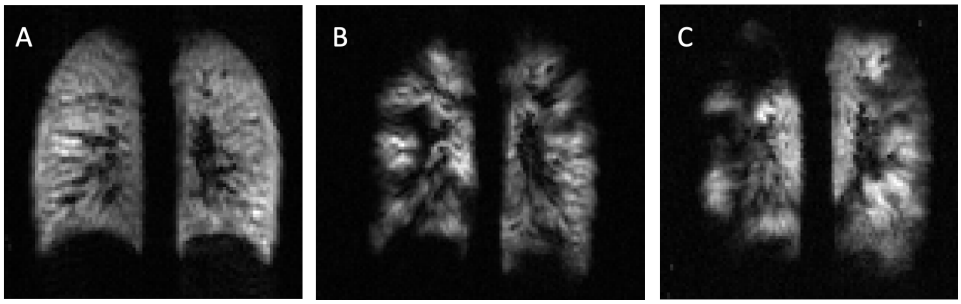

He3MRI scan from a representative subject. A: Baseline. B: Post-methacholine (FEV1 reduced by 33%) C: Post-mannitol (FEV1 reduced by 33%)

Conclusion: Direct and indirect airway challenges have different topographical distributions in ventilation defects despite a similar fall in FEV1. Certain airways also appear to be more susceptible to bronchial provocation regardless of the challenge method. This reinforces the notion that asthma is a heterogeneous disease.

Grant Support: CASS Foundation Grant

Lung Lobar Sliding Reduces Parenchymal Distortion During Breathing

Adam Galloy, Joseph Reinhardt, Suresh M. L. Raghavan

Introduction

Understanding the mechanics of breathing can lead to better diagnosis and treatment of lung diseases. One source of complexity in lung mechanics comes from sliding between the lung lobes along the lobar fissures during breathing [1]. However, some subjects having missing or incomplete lobar fissures [2] which can limit or prevent lobar sliding. Little is known about the role lobar sliding (or the lack thereof) plays in lung mechanics. Rodarte et al. postulated that lobar sliding can help the lungs reduce parenchymal distortion and stress concentrations by giving the lung tissue additional degrees of freedom to adapt to changes in thoracic cavity shape throughout the breathing cycle [3]. The objective of this study was to test the hypothesis that lobar sliding helps reduce distortion in the lung parenchyma during breathing. We used finite element (FE) models of left lungs from eight human subjects to perform a paired comparison of the amount of distortion present in simulations that allowed and disallowed sliding.

Methods

We acquired 4DCT scans of eight subjects with lung cancer during tidal breathing following a procedure approved by our institutional review board [4]. The two left lung lobes (upper and lower) and thoracic cavity were segmented from the images. From the segmentations at end inhale, solid FE meshes representing the lung lobes were generated along with a surface FE mesh of the thoracic cavity. Exhalation was simulated by prescribing displacements to the thoracic cavity surface to drive deformation of the lobar tissue with contact constraints. Subject specific thoracic cavity displacements were derived by registering the thoracic cavity mask at end exhale to the mask at end inhale. We assumed that contact between the lobes and thoracic cavity allowed for frictionless sliding. For each subject two simulations were performed: one where frictionless sliding was allowed between lobes and one where a large friction coefficient prevented sliding between lobes. This contact mechanics model of lobar sliding has been described in detail in Galloy et al. [5].

Results and Discussion

Distortion was quantified for each simulation using the mean anisotropic deformation index (ADI) [6] for the left lung as whole, the lower lobe, and the upper lobe. Consistent with the hypothesis, we found a significant median decrease in distortion (mean ADI) between sliding and non-sliding simulations of 5.3% for the whole left lung ($p = 0.008$) and 8.0% for the lower lobe ($p = 0.008$). On the other hand, for the upper lobe we found an insignificant median decrease in distortion between simulations of 1.8% ($p = 0.078$). This suggests subjects with incomplete or missing lobar fissures may experience more parenchymal distortion during breathing than subjects with complete lobar fissures. The lower lobe may stand to benefit more from lobar sliding than the upper lobe because of its proximity to the diaphragm and heart cavity where the most drastic shape changes occur in the thoracic cavity.

In addition to paired intra-subject comparisons, we looked at inter-subject trends by quantifying the amount of lobar sliding that occurred in each sliding simulation using the max shear metric developed by Amelon et al. [1]. We found that the reduction in whole lung distortion for a subject between the sliding and non-sliding simulations was positively correlated with the amount of lobar sliding that occurred during the sliding simulation (Pearson's correlation coefficient of 0.95). This trend is consistent with the hypothesis and reinforces the previous findings. It also suggests that in addition to the presence of lobar sliding the amount of lobar sliding in a subject can have an impact on their lung mechanics.

References

[1] Amelon, R. E., Cao, K., Reinhardt, J. M., Christensen, G. E., and Raghavan, M. L., 2014, "A Measure for Characterizing Sliding on Lung Boundaries," Ann Biomed Eng, **42**(3), pp. 642–650.

[2] Koster, T. D., and Slebos, D.-J., 2016, "The Fissure: Interlobar Collateral Ventilation and Implications for Endoscopic Therapy in Emphysema," Int J Chron Obstruct Pulmon Dis, **11**, pp. 765–773.

[3] Rodarte, J. R., Hubmayr, R. D., Stamenovic, D., and Walters, B. J., 1985, "Regional Lung Strain in Dogs during Deflation from Total Lung Capacity," Journal of Applied Physiology, **58**(1), pp. 164–172.

[4] Du, K., Bayouth, J. E., Cao, K., Christensen, G. E., Ding, K., and Reinhardt, J. M., 2012, "Reproducibility of Registration-Based Measures of Lung Tissue Expansion," Medical Physics, **39**(3), pp. 1595–1608.

[5] Galloy, A. E., Amelon, R. E., Reinhardt, J. M., and Raghavan, M. L., 2022, "Contact Mechanics Model of Lung Lobar Sliding," Applications in Engineering Science, **10**, p. 100098.

[6] Amelon, R., Cao, K., Ding, K., Christensen, G. E., Reinhardt, J. M., and Raghavan, M. L., 2011, "Three-Dimensional Characterization of Regional Lung Deformation," Journal of Biomechanics, **44**(13), pp. 2489–2495.

Hyperpolarized ^{129}Xe in a large animal model of acute Pulmonary Embolism – initial findings

Mattias H. Kristensen[1], Michael Vaeggemose[1,2], Esben S. S. Hansen[1], Mohsen Redda[1], Jacob Valentin Hansen[3,4], Asger Andersen[3,4] Rolf F. Schulte[5], Oliver Rodgers[6], Guilhem J. Collier[6], Graham Norquay[6], Jim M. Wild[6], Christoffer Laustsen[1]

[1] Aarhus University, Department of Clinical Medicine, The MR Research Centre, Aarhus, Denmark
[2] GE HealthCare, Brøndby, Denmark
[3] Aarhus University, Department of Clinical Medicine, Aarhus Denmark
[4] The Department of Cardiology Research Aarhus University Hospital, Aarhus Denmark
[5] GE HealthCare, Munich, Germany
[6] POLARIS, Department of Infection, Immunity and Cardiovascular Disease, University of Sheffield, Sheffield, UK

Purpose/Introduction

Pulmonary embolism (PE) is a serious pathophysiological event that affects millions of people every year (1). Hyperpolarized (HP) ^{129}Xe gas MR has been proposed as a useful tool in characteristics of the pulmonary physiology in PE (2). The aim of our study is to investigate the use of HP ^{129}Xe MRI in a large animal model (porcine) of PE reassembling human physiology. There is a growing interest in imaging of PE, where this is first of its kind with xenon in a porcine model (3, 4, 5).

Methods

MRI was performed on 60 kg pigs (n=4) on a 3T MRI scanner (MR750, GE Healthcare, Waukesha, WI, USA) with a ^{129}Xe transmit-receive vest coil (Clinical MR Solutions, Brookfield, WI, USA). For all experiments ^{129}Xe gas was polarised using SEOP with a custom-built polariser (POLARIS, University of Sheffield) (6) and cryogenically separated and collected in its frozen state over a time of 9min (xenon ~ 800mL).

The PE were introduced though a jugular catheter on an on-site well-established model of acute pulmonary embolism (7), inducing haemodynamic response corresponding to patients with intermediate-high risk PE. Mean time to xenon imaging was 4 hours.

A 3D coronal steady-state free precession (SSFP) sequence was used for ventilation imaging (8); voxel size of 5x5x10mm, matrix size of 80x80x30, repetition time (TR) = 3.2ms, echo time (TE) = minimum (~1ms), flip angle (FA) = 10^0, bandwidth = 31.25kHz, total acquisition time of 6sec.

A 3D Cartesian MRSI trajectory with a resolution of 1x1x2cm^3, 28x28x6 matrix size and FOV = 28x28x12cm requiring a total of 2416 excitations was applied to acquire dissolved phase images. Dissolved phases and gas phase FA where 10^0 and 0.1^0, respectively. In the spectral dimension, 88 sampling points were acquired with a bandwidth of 20kHz. TR was set to 7.4ms resulting in a total acquisition time of 18s. Gas, tissue, and blood phases and their chemical shifts were determined with Advanced Method for Accurate, Robust, and Efficient Spectral (AMARES) fitting using OXSA (9).

Blood flow was evaluated by dynamic contrast enhanced (DCE) MRI with i.v. gadolinium, 0.2 ml/kg, using a standard TRICKS sequence (10). Embolized (PE) and non-embolized (No PE) areas of the lung were identified in the DCE. Regions of interests (ROIs) were co-registered to the HP ^{129}Xe ventilation and dissolved phase images. Representative examples are shown in fig. 1. Image analysis included mean values from embolized areas and non-embolized areas in DCE and normalized ventilation and dissolved phase images. Statistical analysis for significant mean differences were performed using Students paired t-test.

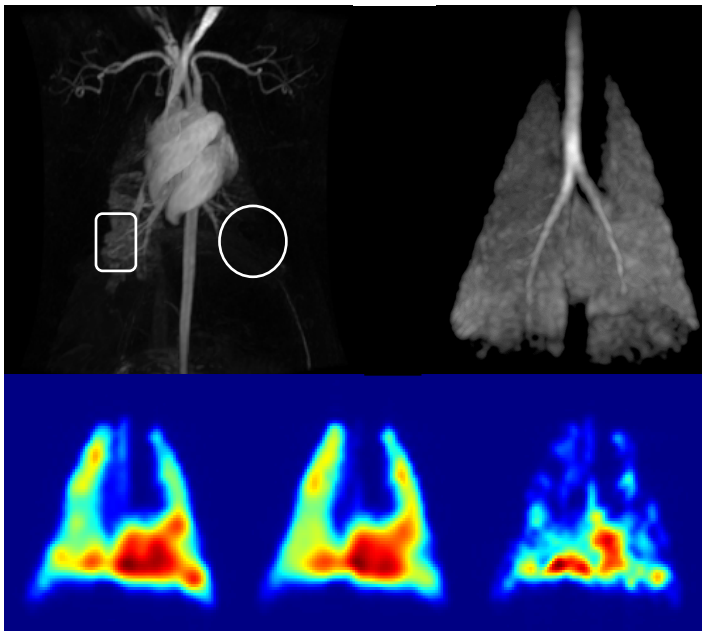

Figure 1 – Top row: Dynamic contrast enhanced (DCE) MRI of pulmonary blood flow, note embolised area bottom right in the lungs (white circle) and normally perfused area (rounded square); Top right: Ventilation distribution of ^{129}Xe. Bottom row, dissolved phases from left to right: gas, barrier, and red blood cell.

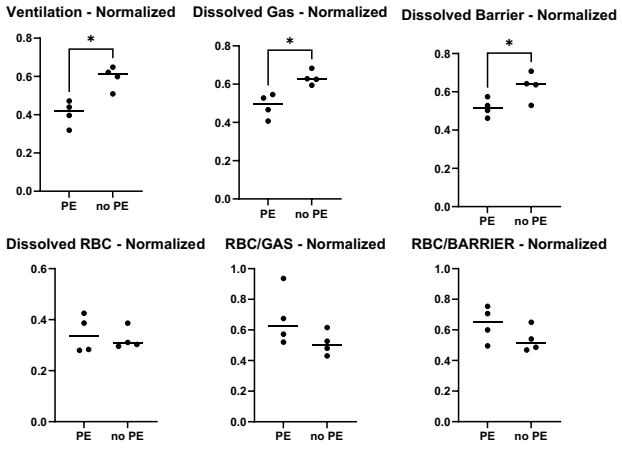

Figure 2 - Mean difference plots of HP 129Xe parameters. Abbreviations: RBC Red Blood Cell; PE Pulmonary emboli. * Denotes significance p<0.05

Results

By visual inspection 3-4 embolized areas were clearly depicted in each of the pigs (Fig 1). The differences in blood flow between embolized and non-embolized are significant (8.0 ml/100ml/s ± 0.19, p=0.003). HP ^{129}Xe show changes in ventilation (1.5 ± +0.1, p=0.04), dissolved phase barrier signal (1.2 ± 0.1, p=0.04) and dissolved phase gas signal (1.3 ± 0.1, p=0.02), the red blood cell signal (RBC) was decreased in 2 out of the 4 pigs.

Discussion

Applying HP ^{129}Xe MRI on PE shows a decrease in ventilation and dissolved phase barrier (membrane) and gas signals. The decrease in ventilation and dissolved gas is unexpected as guidelines for diagnosing acute PE expect preserved ventilation (11). It could be explained by the mechanism of hypocapnic bronchoconstriction, which increases regional airway resistance particularly at the lower volumes of vital capacity (12). This effect has been shown to be significant in the pig (13), but will require further investigations. The difference in dissolved phase barrier signal disappears when normalizing to gas signal. This could be another indicator of insufficient ventilation as the primary cause. We also theorize that the hypoperfused areas could be accumulating infiltration as the pig is mechanically ventilated for 6-8 hours before HP ^{129}Xe MR investigations.

Conclusion

Hyperpolarized ^{129}Xe MR is a unique method for determination of physiological lung properties. The technique could assist in understanding ventilation and perfusion mismatch caused by acute pulmonary emboli. In our large animal model, we find decrease in ventilation as well as perfusion in areas with embolies. Results which could benefit future understanding and treatments for acute and chronic pulmonary embolism.

References

1. Turetz M, Sideris AT, Friedman OA, Triphathi N, Horowitz JM. Epidemiology, Pathophysiology, and Natural History of Pulmonary Embolism. Semin Intervent Radiol. 2018;35(2):92-8.
2. Cleveland ZI, Cofer GP, Metz G, Beaver D, Nouls J, Kaushik SS, et al. Hyperpolarized Xe MR imaging of alveolar gas uptake in humans. PLoS One. 2010;5(8):e12192.
3. Lipson DA, Roberts DA, Hansen-Flaschen J, Gentile TR, Jones G, Thompson A, et al. Pulmonary ventilation and perfusion scanning using hyperpolarized helium-3 MRI and arterial spin tagging in healthy normal subjects and in pulmonary embolism and orthotopic lung transplant patients. Magn Reson Med. 2002;47(6):1073-6.
4. Rizi RR, Saha PK, Wang B, Ferrante MA, Lipson D, Baumgardner J, et al. Co-registration of acquired MR ventilation and perfusion images--validation in a porcine model. Magn Reson Med. 2003;49(1):13-8.
5. Chang Y, Mata JF, Bozlar U, Altes T, Brookeman JR, Hagspiel KD, et al. Detecting Simulated Pulmonary Embolism in a Rabbit Model with Hyperpolarized Xenon-129 Uptake Spectroscopy. Proc Intl Soc Mag Reson Med; Toronto2008.
6. Norquay G, Collier GJ, Rao M, Stewart NJ, Wild JM. 129Xe-Rb Spin-Exchange Optical Pumping with High Photon Efficiency. Phys Rev Lett. 2018;121(15):153201.
7. Schultz J, Andersen A, Gade IL, Ringgaard S, Kjaergaard B, Nielsen-Kudsk JE. A porcine in-vivo model of acute pulmonary embolism. Pulm Circ. 2018;8(1):2045893217738217.
8. Stewart NJ, Norquay G, Griffiths PD, Wild JM. Feasibility of human lung ventilation imaging using highly polarized naturally abundant xenon and optimized three-dimensional steady-state free precession. Magn Reson Med. 2015;74(2):346-52.
9. Purvis LAB, Clarke WT, Biasiolli L, Valkovic L, Robson MD, Rodgers CT. OXSA: An open-source magnetic resonance spectroscopy analysis toolbox in MATLAB. PLoS One. 2017;12(9):e0185356.
10. Korosec FR, Frayne R, Grist TM, Mistretta CA. Time-resolved contrast-enhanced 3D MR angiography. Magn Reson Med. 1996;36(3):345-51.
11. Bajc M, Neilly JB, Miniati M, Schuemichen C, Meignan M, Jonson B. EANM guidelines for ventilation/perfusion scintigraphy. European Journal of Nuclear Medicine and Molecular Imaging. 2009;36(8):1356-70.
12. O'Cain CF, Hensley MJ, McFadden ER, Jr., Ingram RH, Jr. Pattern and mechanism of airway response to hypocapnia in normal subjects. J Appl Physiol Respir Environ Exerc Physiol. 1979;47(1):8-12.
13. Langer T, Castagna V, Brusatori S, Santini A, Mauri T, Zanella A, et al. Short-term Physiologic Consequences of Regional Pulmonary Vascular Occlusion in Pigs. Anesthesiology. 2019;131(2):336-43.

Fractional Ventilation Mapping of the Rat Lung using Multiple Breath Washout Hyperpolarized ^{129}Xe and Perfluoropropane MRI. Shaelyn Horvath[1,2], Brandon Zanette[2], Daniel Li[2], Faiyza Alam[1,2], Stephen Kadlecek[3] and Giles Santyr[1,2]. *[1]Department of Medical Biophysics, University of Toronto, Toronto, ON, Canada,[2]Translational Medicine Program, The Hospital for Sick Children, Toronto ON, Canada, [3]Department of Radiology, University of Pennsylvania, Philadelphia, PA, USA.*

Purpose: Cystic fibrosis (CF) is an incurable systemic disease in which declines in lung function are the primary cause of mortality. To improve quality and length of life for these patients, thorough treatment and monitoring is vital. Multiple breath washout (MBW) hyperpolarized ^{129}Xe MRI (HP Xe-MRI) acquires images as a function of gas washout breath allowing mapping of regional ventilation by extracting fractional ventilation (FV), a unitless parameter reflecting gas replacement per breath. It is a promising method for monitoring treatment of pediatric CF[1,3], however, HP gas is not widely available and requires an anoxic breath-hold, limiting clinical accessability[2]. Fluorinated gases such as perfluoropropane (PFP) are thermally polarized with recoverable signal allowing for normoxic breath-holds (79% PFP, 21% O_2), making this technique more accessible to children. In addition, it allows for a potential capability to probe long-term gas replacement and gas trapping in the lungs, not possible with Xe-MRI due to irrecoverable signal decay[3]. MBW PFP-MRI has been previously studied in adults to distinguish health from CF[4], however, comparison of PFP to HP ^{129}Xe for FV mapping has yet to be shown. We hypothesize that PFP will yield FV maps that are similar to those produced with HP ^{129}Xe under the same ventilation and similar washout conditions. In this work, FV maps derived from MBW Xe-MRI and MBW PFP-MRI in mechanically ventilated healthy rats using similar washout paradigms are compared.

Methods: All methods followed animal use protocols approved by The Hospital for Sick Children's Laboratory Animal Services. Healthy Sprague-Dawley rats (mean mass 350g) were prepared as previously described[5]. Each rat was intubated and connected to a custom MR-compatible mechanical ventilator (Spinhance, Philadelphia PA) using a ventilatory rate of 50 breaths per minute and a tidal volume of 8 mL/kg. MBW Xe-MRI was conducted using 6 pre-breaths of HP ^{129}Xe (Polarean Inc., Durham, NC) to introduce the gas to the lungs, followed by an 8s breath-hold during which calibration images were acquired[2,3]. The ventilator then delivered a washout breath of room air, followed by a 2s breath-hold at peak inspiration during which image acquisition was preformed using a 2D GRE sequence and repeated for a total of 6 washout breaths/images. A similar procedure was performed with PFP (79% PFP, 21% O_2; Airgas, Radnor, PA), except using a 10s breath-hold for imaging. Additionally, due to the short T_2^* of PFP, 10 averages were acquired for each washout image. This process was repeated 20 times for each rat for further signal averaging. Data analysis was performed using MATLAB to perform signal averaging (for PFP-MRI), correct for flip angle and T_1 induced signal losses (for Xe-MRI), and calculate FV maps as previously reported[2,3]. FV maps calculated from PFP-MRI and Xe-MRI were then compared based on image-wide mean ± standard deviation of FV values.

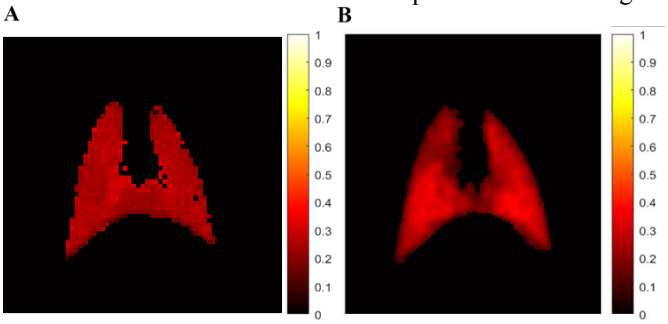

Figure 1. A: FV map extracted from MBW Xe-MRI. Mean FV=0.22±0.03. B: FV map extracted from MBW PFP-MRI. Mean FV=0.24±0.07.

Results: Ventilation and imaging procedures were well-tolerated by the rats, including the switching of gases. Figure 1A shows an FV map from a representative rat using MBW Xe-MRI (mean FV of 0.22±0.03). Figure 1B shows an FV map from the same rat using MBW PFP-MRI (mean FV of 0.24±0.07).

Discussion: Mean FV measured with MBW MRI in mechanically ventilated rats are comparable between PFP and HP ^{129}Xe. The absolute mean FV values found in this study are lower than expected for a healthy rat under the same washout paradigm, imaging, and analysis (0.3-0.4)[2]. This may be explained as an effect of the mechanical ventilator (e.g., variations in timing and/or dead-space contributions), or by the occurrence of obscured complex gas dynamics. Nevertheless, the effects caused by these limitations would be consistent for both gases. Therefore, the relative agreement confirms that PFP yields similar FV maps to HP ^{129}Xe in ventilated rats. Future work will investigate 3D UTE MRI sequences to increase SNR and reduce image acquisition time as well as study the ability of PFP to probe longer-term gas replacement compared to HP ^{129}Xe.

Conclusion: This study demonstrates the feasibility of MBW PFP-MRI in rats, providing FV maps comparable to those produced with MBW Xe-MRI. This should help pave the way for clinical translation of MBW PFP-MRI in pediatric CF, as well as other lung diseases.

References: [1] Alam et al. ISMRM. 2022; Abstract #1177. [2] Morgado et al. MRM. 2018;80(6) [3] Couch et al. MRM. 2012; 68(5). [4] Goralski et al. JCI Insight. 2020; 5(2). [5] Santyr et al. MRM. 2008;59(6):1304–1310.

Acknowledgements: This work is supported by an NSERC Alliance partnership with Siemens Healthiness. Shaelyn Horvath recognises the support of Temerty Faculty of Medicine QEII-GSST.

Assessment of Thoracic Insufficiency Syndrome Using Dynamic Hyperpolarized ^{129}Xe MRI

Mostafa K. Ismail, H. Hamedani, F. Amzajerdian, R. Baron, L. Loza, I. Duncan, S. Kadlecek, K. Ruppert , R. Rizi

INTRODUCTION: Restrictive and obstructive lung diseases are characterized by abnormal air flow into and out of the lungs, increasing the difficulty of respiration due to abnormal airway resistance, lung and chest wall compliance, and ventilation rate. In some diseases like thoracic insufficiency syndrome (TIS), treatment effectiveness can only be evaluated through pulmonary function tests which are difficult to acquire pre-intervention and only provide global measures of lung function. Lung transplant provides a final therapeutic option for end-stage disease, but post-transplant mortality rates remain high due to graft failure, which is still poorly understood. Non-invasive measurements of compromised pulmonary air flow might enable the early detection and assessment of obstructive and restrictive disease states. Here, we developed a dynamic hyperpolarized 129Xe MR imaging technique to measure regional ventilation changes in the lungs, using it to produce dynamic ventilation maps in a preclinical model of thoracic insufficiency syndrome (TIS) as well as three lung transplant (LTX) recipients.

METHODS: Two healthy subjects, one right-lung unilateral, and two bilateral lung transplant recipients were imaged; in another set of experiments, two Yucatan miniature pigs: one healthy and one underwent rib tethering on the right side (T3-9) at 6 weeks-old (TIS model) were imaged at 5 months-old). All images were acquired on 1.5T Siemens scanner using an 8-channel 129Xe-coil during free breathing. A pneumotach flow sensor and 129Xe injection (about 2.5L) were timed synchronously with inhalation. 3D-spiral interleaves were acquired continuously over four minutes of imaging with TR/TE = 7.63/0.62 ms, flip angle of 4°, and reconstructed onto 80×80x80 grids with FOV of 150 mm isotropic for pigs and 350 mm for humans. The diaphragm position over time was used to retrospectively bin each image into 16 phases of a representative breathing cycle. Symmetric image normalization (Syn) with cross-correlation metric in the ANTs toolbox was used to co-register all frames to the end-inhale frame to allow voxel-wise analysis. Registered voxel regions, nominally corresponding to the same tissue volume at each bin time tn, were then characterized by signal intensities Sn. A model was then fit to Sn to derive the local volumes Vn, subject to the constraints that: 1) local volume increases during inhalation result in the addition of gas with a fixed HP magnetization (S0), 2) new gas mixes with residual gas, 3) volume decrease during exhalation results in signal loss proportional to the fractional reduction in local gas volume, and 4) gas is continuously relaxed at rate G due to the combined effects of RF excitation, collisions with O2 molecules and uptake, and this rate is approximately constant during the breathing cycle. We then solve for the set of local Vn and FRC consistent with differential equations describing this model: $\frac{\dot{S}}{S} = \frac{\dot{V}}{V}\left(\frac{S_0}{S} - 1\right) - \Gamma$ (inhale) and $\frac{\dot{S}}{S} = \frac{\dot{V}}{V}\left(\frac{V}{V-1+FRC} - 1\right) - \Gamma$ (exhale) and fit to sigmoid curves describing local expansion, contraction rate and timing: $V_n = \frac{TV}{1+e^{-S_I(t_n - t_I)}} + FRC$ (inhale) and $V_n = \frac{TV}{1+e^{S_E(t_n - t_E)}} + FRC$ (exhale). The resulting "sI and sE" describe the local rate of volumetric expansion, while tI and tE correspond to the times of peak flow into and out of the local region, respectively. Moreover, the first derivative of the volume flow over time gives the gas flow rate, allowing us to calculate the maximum flow rate $Max\ flow\ rate = \frac{-TV \cdot s}{4}$.

Results/Discussion: Figure 1 shows separate sigmoid fits for exhalation/inhalation. Three parameters were obtained for each breathing phase: maximum flow rate, time of maximum flow rate relative to the trachea, and the local rate of volumetric expansion, s. The color scale for the dynamic maps is not fixed since all these parameters depend on subjects' different breathing patterns, but still shows local changes within subjects. While not observed in the healthy pig, Figure2 shows a contrast between the right, tethered lung and the left lung in the TIS pig, where lower inhale s indicates less efficient gas replacement in the right lung, perhaps due to restriction associated with tethering. Interestingly, similar effects are seen in the ADC maps (white arrows), indicating that regions with high s might also have high diffusion, due to reduced microstructure size in the restricted lung and/or compensatory expansion in the contralateral lung. Figure 3 shows these maps for the human dataset, in which a superior-to-inferior gradient is noticeable for the flow rate parameters for all subjects except for the native left fibrotic lung of the unilateral LTX patient, analogous to the loss of ventilation gradients in severe emphysema. There was also a noticeable posterior-to-anterior gradient in the arrival/departure time in one of the bilateral LTX subjects (red arrows) consistent with expectations based on previous measurements of gravity-dependent sequential filling and emptying. This gradient was not seen in the other LTX subject. More work is required to understand these gradients and the correlation of s with ADC for the lung parenchyma.

Conclusion: Dynamic HXe MR images can be analyzed to yield information about altered ventilation dynamics resulting from TIS and LTx, suggesting that these ventilation maps obtained during free breathing can assess the abnormal air flow and potentially allow for an improved assessment of altered lung dynamics associated with TIS and LTX.

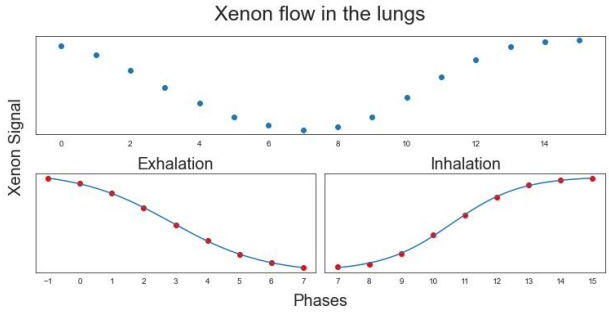

Figure 1: Average gas flow in the lung for the 16 phases representing the breathing curve. A sigmoid fit is applied separately for the exhalation and inhalation parts, with average r-squared values of 1.

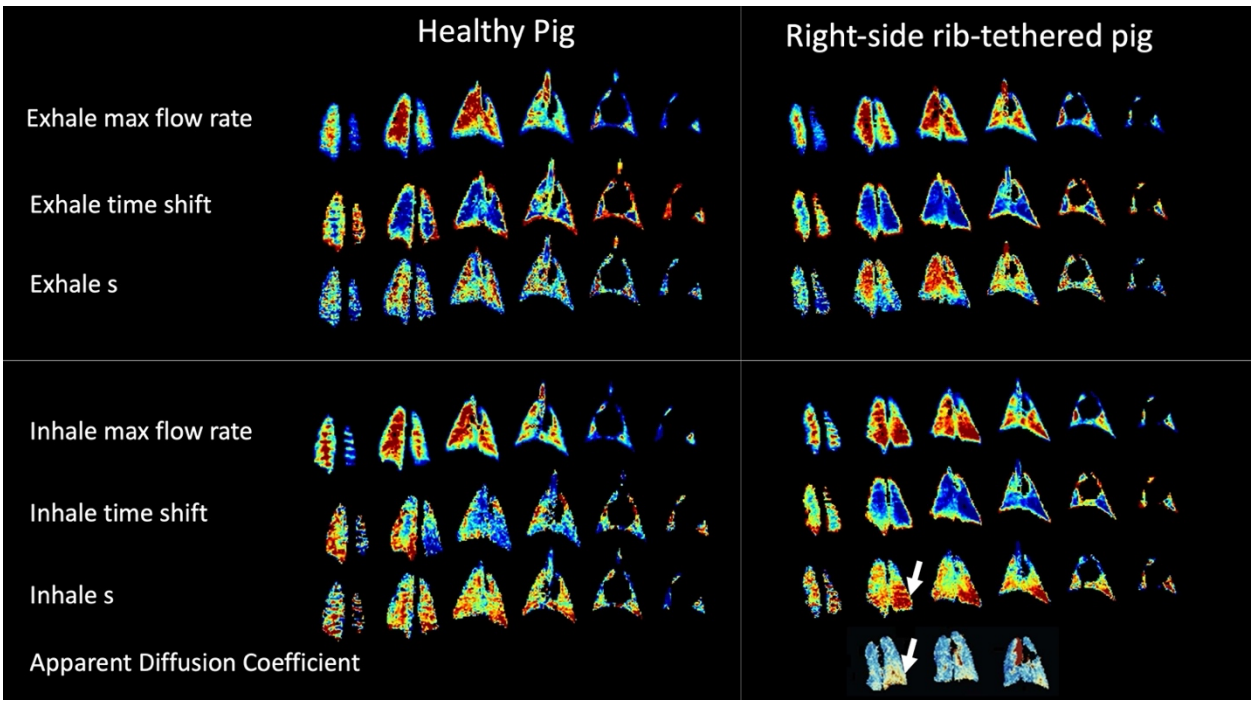

Figure 2: Ventilation maps and ADC for the healthy pig and the right-side rib-tethered pig showing contrast between the left and right lungs in the s parameter in the TIS pig not seen in the healthy pig as well as a correlation between the inhale s map and the ADC map in the lung parenchyma of the TIS pig. This indicates that regions with s, which means high change of Xenon per unit volume, or normalized maximum flow rate, might also have high diffusion. More work is required to evaluate this correlation

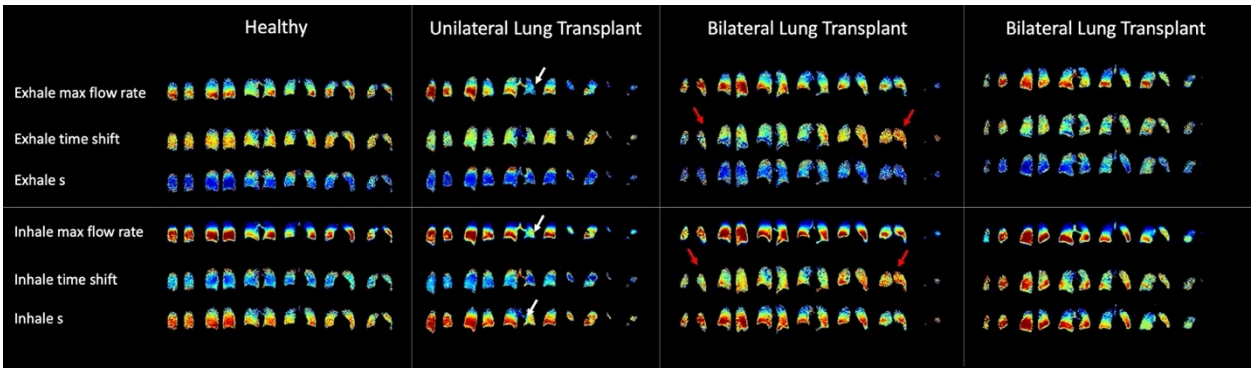

Figure 3: Ventilation maps for the human subjects showing a vertical gradient in the maximum flow rates and s parameters for all the subjects except for the left fibrotic lung of the unilateral lung transplant patient (white arrows). Red arrows show a gradient from anterior to posterior part of the lung in the time shift in the bilateral LTX indicating that air enters and exists the posterior part earlier than the anterior part of the lung. Moreover, we speculate that regions in one lobe might have same s, which is governed by the airway's resistance leading to that lobe and is different between lobes??? More work is needed to understand the clinical significance of these findings.

Using chest CT with spirometry to distinguish pulmonary hypertension phenotypes in patients with connective tissue disease-related ILD

Sarah L. Khan, MD, Kevin J. Psoter, PhD, MPA, Cheng Ting Lin, MD, Sonye K. Danoff, MD, PhD, Stephen C. Mathai, MD, MHS

Purpose

Pulmonary hypertension (PH) associated with connective tissue disease-related interstitial lung disease (CTD-ILD) may arise from fibrosis-induced ablation of pulmonary blood vessels as seen in WHO Group 3 PH or from endovascular dysfunction caused by the chronic inflammation of CTD as seen in Group 1 PH[1,2]. Determining the cause of PH is crucial for disease management[3]. However, there are no guidelines for making this distinction in CTD-ILD patients, so it is left to clinician discretion[4,5]. Previously, a validated severity-staging system based on chest imaging (computed tomography [CT]) and spirometry was developed to differentiate ILD phenotypes in patients with systemic sclerosis[6]. We conducted a feasibility study to examine the agreement of this phenotyping system with clinician discretion, the standard approach for phenotyping PH associated with CTD-ILD (CTD-ILD-PH), and spirometry.

Methods

We randomly selected 50 patients with CTD-ILD and PH in the Johns Hopkins PH, Myositis, and ILD registries and used chest CTs and spirometry to systematically classify them as having either a parenchymal or vascular phenotype (Figure 1). We also used spirometry to group patients based on their degree of forced vital capacity (FVC) limitation with one group having a FVC greater than or equal to 70% and the other, less than 70%. For comparison, the parenchymal phenotype correlated with Group 3 PH and FVC < 70% while the vascular phenotype correlated with Group 1 PH and FVC ≥ 70%. Overall and positive percent agreement of the CT- and spirometry-guided classification was compared to clinically-assigned and FVC-determined groups. Phenotype-concordant PH therapy receipt was assessed based on systematic phenotyping.

Results

Among 50 patients with CTD-ILD-PH, 30 had clinically-assigned Group 3 PH and 20 had Group 1 PH. After systematically-classifying patients' phenotypes, there were 29 patients with the parenchymal phenotype and 21 with the vascular phenotype. Overall, 17 patients were reclassified to the opposite phenotype (34.0%, 95% CI: 21.2, 48.8%). Nine of the patients with Group 3 PH were reclassified to the vascular phenotype (30.0%; 95% CI: 14.7, 49.4%) while eight of the patients with Group 1 PH were reclassified to the parenchymal phenotype (40.0%; 95% CI: 19.1, 63.9%). There was 86% (95% CI: 73.3, 94.2%) overall agreement between FVC groups and clinically-assigned WHO Groups, but only 52.0% (95% CI: 37.4, 66.3%) agreement between the FVC groups and the systematically-assigned phenotypes. With regard to PH therapies, 32 patients received medications discordant with their phenotype (64.0%, 95% CI: 49.2, 77.1%). None of the patients with a parenchymal phenotype received medications concordant with their phenotype (0.0%; 95% CI: 0.0, 11.9%) while 18 of the patients with a vascular phenotype received concordant therapy (85.7%; 95% CI: 63.7, 97.0%).

Discussion

In this study, we found that it is feasible to use chest CTs and spirometry to systematically classify CTD-ILD-PH patients as having a parenchymal or vascular phenotype. Our preliminary findings suggest that classification of PH phenotypes in this population differs significantly between a formalized CT- and PFT-driven approach and clinical discretion. The high level of agreement between spirometry and clinically-assigned WHO Groups suggests that clinicians rely heavily on the degree of FVC limitation to make these decisions. The reclassification of PH phenotypes had a significant impact on the appropriateness of clinical management strategies employed as 64% of patients did not receive phenotype concordant therapy. Future studies will assess the prognostic utility and impact on clinical management of this standardized approach to PH phenotyping in patients with CTD-ILD-PH.

Conclusion

Chest imaging and spirometry can be used to systematically classify CTD-ILD-PH patients as having either a parenchymal or vascular phenotype which may have prognostic and therapeutic utility.

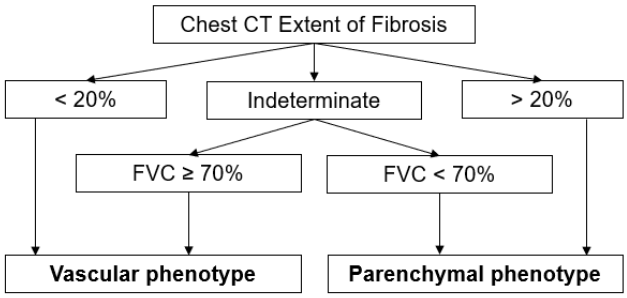

Figure 1. Chest CTs and spirometry have been used to stage the severity of ILD in scleroderma[6]. We adapted this system to distinguish vascular and parenchymal phenotypes of CTD-ILD-PH. The percent of lung involved based on chest CTs was visually assessed at five levels (1) origin of the great vessels, 2) main carina, 3), pulmonary venous confluence, 4) halfway between points 3 and 5, and 5) top of the right hemidiaphragm) and averaged. FVC was assessed based on the percent predicted.

References

1. King CS, Nathan SD. Pulmonary hypertension due to interstitial lung disease. *Curr Opin Pulm Med*. 2019;25(5):459-467. doi:10.1097/MCP.0000000000000599

2. King CS, Nathan SD. Idiopathic pulmonary fibrosis: effects and optimal management of comorbidities. *Lancet Respir Med*. 2017;5(1):72-84. doi:10.1016/S2213-2600(16)30222-3

3. Thomas CA, Anderson RJ, Condon DF. Diagnosis and Management of Pulmonary Hypertension in the Modern Era : Insights from the 6th World Symposium. *Pulm Ther*. 2020;6(1):9-22. doi:10.1007/s41030-019-00105-5

4. Galiè N, Simonneau G. The Fifth World Symposium on Pulmonary Hypertension. *J Am Coll Cardiol*. 2013;62(25):D1-D3. doi:10.1016/j.jacc.2013.10.030

5. Seeger W, Adir Y, Barberà A, et al. Pulmonary Hypertension in Chronic Lung Diseases. *J Am Coll Cardiol*. 2013;62(25):D109-D116. doi:10.1016/j.jacc.2013.10.036

6. Goh NSL, Desai SR, Veeraraghavan S, et al. Interstitial lung disease in systemic sclerosis: A simple staging system. *Am J Respir Crit Care Med*. 2008;177(11):1248-1254. doi:10.1164/rccm.200706-877OC

Repeatability and reproducibility of oxygen-enhanced MRI of the lung at 3 tesla: cross-centre, cross-vendor evaluation

Mina Kim[1], Sarah H. Needleman[1], Josephine H. Naish[2,3], Yohn Taylor[1], Marta Tibiletti[2], James P. B. O'Connor[4,5], Geoff J. M. Parker[1,2]

[1]Centre for Medical Image Computing (CMIC), Department of Medical Physics & Biomedical Engineering, University College London, London, UK; [2]Bioxydyn Limited, Manchester, UK; [3]BHF Manchester Centre for Heart and Lung Magnetic Resonance Research (MCMR), Manchester University NHS Foundation Trust, Manchester, UK; [4]Division of Cancer Sciences, University of Manchester, Manchester, UK; [5]Division of Radiotherapy and Imaging, Institute of Cancer Research, London, UK

Purpose: Oxygen-enhanced MRI (OE-MRI) can provide information on regional lung function [1]. Despite technical challenges of OE-MRI in the lung at higher magnetic field, we have recently shown its feasibility at 3 T and signal enhancement behaviour in the lung using a dual echo RF-spoiled gradient echo acquisition [2]. This method enables measurement of dynamic OE signal change with either T_1-weighting or T_2*-weighting, and for monitoring of dynamic ΔR_2* [2,3]. The purpose of this work was to evaluate repeatability and reproducibility of the proposed method across two sites, vendors and time points.

Methods: Following research ethics approval and written informed consent, we recruited 16 healthy volunteers with no previous record of lung diseases. Of these, 8 travelling subjects (3 males, age range = 26-54 years, median = 39.5) underwent lung MRI on a 3 T whole-body scanner from two vendors in different cities (Philips Ingenia in London, UK and Siemens MAGNETOM Vida in Manchester, UK) at a 4 week interval. Eight separate subjects (4 males, age range = 23-51 years, median = 27) were scanned twice for a scan-rescan test at a 4-6 week interval using the Philips scanner. Parameters for the RF-spoiled dual gradient echo acquisition for Philips 3 T and simulation are listed in [2] (TR = 16 ms). Where possible, protocols for the two different scanner manufacturers utilized similar acquisition parameters, though some options required manufacturer-specific parameters. Site-dependent parameters included: full echo, bandwidth 4488 Hz/Px for Philips (L) vs. half echo, bandwidth 2000 Hz/Px for Siemens (M). The shortest TE available for the chosen acquisition were selected for each scanner: TE_{1L} = 0.71 ms, TE_{2L} = 1.2 ms for Philips; TE_{1M} = 0.81 ms, TE_{2M} = 1.51 ms for Siemens. Selection of flip angle (FA) was optimized through simulation of expected signal change over a range of TE [2,4]. Subjects breathed medical air (21% O_2) and 100% O_2 via non-rebreathing face mask (Intersurgical Ltd., Wokingham, UK) at a flow rate of 15 $Lmin^{-1}$. Images were acquired during free breathing. Data analysis was performed in MATLAB R2022b (MathWorks, Natick, MA). After non-linear image registration using ANTs [5,6], the lung parenchyma, excluding central major vasculature, was manually segmented from registered images and a voxel-wise tissue density correction was applied. Subsequently, the dynamic data points in the masked lung were fitted using exponential functions for the O_2 wash-in and wash-out for each voxel. Percent signal enhancement (PSE) maps were produced by the subtraction of the fitted baseline normoxia intensity from the fitted hyperoxia intensity, normalized to the fitted normoxia intensity. Mean and standard deviation (std) were calculated for PSE values at each TE over the 2 most posterior slices for TE_{1L}, TE_{1M}, TE_{2L} and TE_{2M} due to poor signal to noise ratio (SNR) in the anterior slices at TE_{2M}. Mean ΔR_2* maps were calculated by the subtraction of averaged normoxia R_2* maps (30th to 60th time series acquisitions) from averaged hyperoxia R_2* maps (120th to 180th). Intra-class correlation coefficient (ICC) was calculated using SPSS v28.0 (SPSS Inc, Chicago, IL).

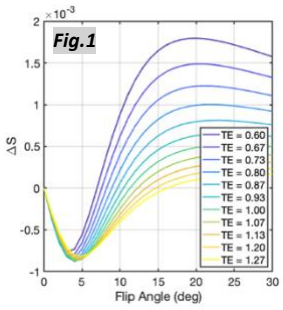

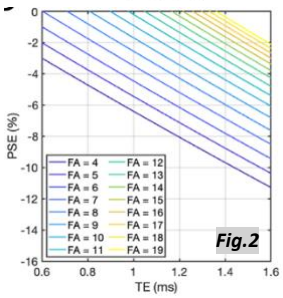

Results: Simulations show that T_2*-induced negative enhancement (ΔS) is maximum at 3° < FA < 5° over the TE range evaluated (Fig. 1) and negative PSE increases with lower FA and longer TE (Fig. 2). Table 1 shows excellent intra-scanner, intra-subject repeatability for PSE and ΔR_2*, and good inter-scanner reproducibility for ΔR_2*, confirmed by Bland-Altman (BA) analysis and ICC. Plots of the combined PSE values at four separate TEs from two MRI systems display TE dependence of the signal (Fig. 3) similar to simulated results (Fig. 2).

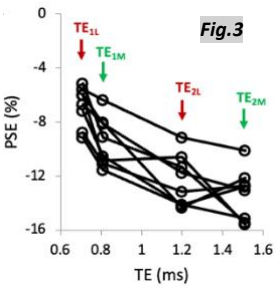

Discussion: Our results show that the proposed protocol with the dual echo spoiled gradient echo acquisition at 3 T yields excellent PSE and ΔR_2* intra-scanner repeatability. They also demonstrate that comparable OE-MRI protocols of the lung can be implemented at 3 T across different sites and scanners with excellent repeatability and good reproducibility for ΔR_2*. Although matching TE between scanners is challenging, the expected trend of PSE with TE is observed between sites.

Conclusions: We have evaluated repeatability and reproducibility of OE-MRI of the lung at 3 T across two sites, vendors and time points using the dual echo RF-spoiled gradient echo acquisition. Our results demonstrate good repeatability for the quantitative and semi-quantitative indices across time points, consistent signal behaviour and repeatable ΔR_2* across two sites and vendors, suggesting potential utility in multi-centre clinical studies. However, substantial impact of TE should be considered when interpretating PSE.

References: 1. Edelman RR et al., Nat Med. 1996; 2: 1236–1239; 2. Kim M et al., Proc Intl Soc Magn Reson Med. 2022; 1481; 3. Needleman SH et al., Proc Intl Soc Magn Reson Med. 2022; 658; 4. Kruger SJ et al., NMR Biomed. 2014; Dec;27(12):1535-41; 5. Avants BB et al., Med Image Anal. 2008;12(1):26-41; 6. Avants BB et al., NeuroImage. 2011;54(3):2033-2044.

Acknowledgements: CRUK NCITA award (C1519/A28682; C19221/A28683), EPSRC-funded UCL CDT in Medical Imaging (EP/L016478/1; EP/S021930/1), EPSRC Industrial CASE award (V20000074), GSK R&D Ltd (BIDS3000035683), Innovate UK award (104629). We thank Lucy Caselton, Sumandeep Kaur and David M. Higgins of Philips Healthcare for technical assistance.

Table 1	Mean (%) ± std (%)	Coefficient of variation	Mean difference		BA bias (bias ± 95% LOA)		ICC_{inter}	ICC_{intra}
			Inter-scanner	Intra-scanner	Inter-scanner	Intra-scanner		
TE_{1L} PSE	7.59 ± 1.60	21.06		-0.51		(-2.36, 1.33)		0.77
TE_{2L} PSE	13.98 ± 2.66	19.04		-0.57		(-2.99, 1.84)		0.92
ΔR_2*	0.14 ± 0.03	24.63	0.00	0.00	(-0.06, 0.06)	(-0.05, 0.04)	0.70	0.94

TITLE: Application of Pulmonary Perfusion Analysis via Magnetic Resonance Imaging to the Phenotyping of Long-COVID Cardiopulmonary Disease

AUTHORS: Andrew C. Lancaster[1], Yoko Kato[2], Chia-Ying Liu[3], Yoshimori Kassai[3], Jaclyn Sesso[2], Joao A.C. Lima[2,4], Bharath Ambale-Venkatesh[4]

[1]School of Medicine, Johns Hopkins University, Baltimore, MD, United States
[2]Division of Cardiology, Department of Medicine, Johns Hopkins University School of Medicine, Baltimore, MD, United States
[3]Canon Medical Systems Corporation, Otawara, Japan
[4]Department of Radiology and Radiological Sciences, Johns Hopkins University School of Medicine, Baltimore, MD, United States

PURPOSE:
Viral SARS-CoV-2, which causes COVID-19, has been implicated in multiple cardiopulmonary diseases [1-6]. Much remains to be learned regarding the long-term sequelae in patients who recover incompletely from COVID-19, termed long-COVID. Magnetic resonance imaging (MRI) studies have proven useful in the evaluation of patients with several cardiopulmonary diseases [7-14] including COVID-19. Methods for assessing lung perfusion via MRI may aid in phenotyping patients with advanced disease [15-21]. In a similar effort to that by Hueper et al. [22], we sought to derive a robust methodology for assessing quantitative pulmonary perfusion parameters from dynamic contrast-enhanced (DCE) MRI and to use this methodology to characterize sequelae of COVID-19 among patients who receive similar care related to disease severity and duration in a single health care system. A history of pulmonary diseases affecting lung perfusion, such as COPD [23], has been reported as a risk factor for hospitalization and poor prognosis/outcomes in COVID-19. Therefore, we sought to investigate the associations between pulmonary perfusion parameters, clinical data, and cardiac functional data in an effort to better phenotype the long-COVID phenomenon.

METHODS:
In a single-center analysis, patients who were diagnosed with COVID-19 after March 2020, who were 3-6 months post-discharge for confirmed COVID-19 illness at a Johns Hopkins institution, and who were 18 years of age or older were screened. Included patients underwent comprehensive cardiopulmonary imaging evaluation and phenotyping, including a cardiac MR imaging study (Canon Galan 3T scanner) with 4D lung perfusion images obtained after 0.04 mmol/kg Dotarem contrast at 5 mL/sec was administered. Using QMass 8.1 (Medis Medical Imaging Systems, Leiden, Netherlands), pulmonary perfusion was assessed. A representative coronal image of the lungs within the anterior 1/3 of the chest was selected, such that the pulmonary artery trunk proximal to its bifurcation and the trachea could be visualized. Using QMass 8.1's Time Signal Intensity analysis, the arterial input function (AIF) was assessed by creating a circular region of interest (ROI) around the middle of the pulmonary artery trunk blood pool, sparing adjacent areas of the vessel wall such that measurements would be robust against motion during the cardiac cycle and to avoid bias from the turbulence of blood flow. Pulmonary parenchymal ROIs were drawn on the lung peripheries to ensure they excluded the larger pulmonary arterial vasculature and allowed for positioning throughout the image acquisition phases. Right lung was consistently labeled as ROI1 and left lung as ROI2. ROIs were propagated to each phase in image acquisition. Perfusion data was automatically collected, and the time-signal intensity (SI) curves of each ROI were investigated. The initial timing of the SI upslope was set as T0 and the timing of the end of the first-pass was set as TEnd. For each of the three ROIs, amplitude (au), max upslope (au/s), time max upslope (s), mean intensity (au), time 50% max (s), T0 intensity (au), baseline intensity (au), and relative upslope (%) were collected, where "au" stands for arbitrary unit.

Additionally, cardiac functional analysis was performed on the MRI studies and data for the following variables were recorded: myocardial native T1 (ms), myocardial ECV (%), myocardial T2 (ms), late-gadolinium enhancement (LGE) presence/absence, LGE scar quantification (%), left ventricle (LV) mass index (LVMI, g/m^2), LV end-diastolic volume index (LVEDVI, ml/m^2), LV end-systolic volume index (LVESVI, ml/m^2), LV ejection fraction (LVEF, %), LV longitudinal strain by biplane assessment (%), right ventricle (RV) mass index (RVMI, g/m^2), RV end-diastolic volume index (RVEDVI, ml/m^2), RV end-systolic volume index (RVESVI, ml/m^2), RV ejection fraction (RVEF, %), RV free wall longitudinal strain (%), left atrium (LA) maximum volume index by biplane assessment (ml/m^2), LA minimum volume index by biplane assessment (ml/m^2), LA total ejection fraction (%), LA ejection fraction of booster pump function (LAEF Booster) (%), and LA biplane reservoir strain (%). Statistical regression analysis was performed to assess relationships between perfusion parameters (particularly time to max upslope [s], time to 50% max intensity [s], and relative upslope [%]); clinical characteristics (age, sex, BMI, whether hospitalized for COVID, whether reported any post-COVID symptoms, whether had a history of pulmonary disease prior to COVID diagnosis, and whether was a past smoker), and cardiac functional parameters. T-tests were performed between the right and left lung perfusion parameters to assess for consistency in measurement.

RESULTS:
54 patients met inclusion criteria. Average age was 55.2 ± 12.4 years. Average BMI was 29.5 ± 6.0 kg/m^2. 8 patients (15%) had a history of pulmonary disease, including COPD, asthma, or obstructive sleep apnea. There were no statistically significant differences between the lungs in terms of perfusion parameters: Right relative upslope vs left relative upslope (t-test, p = 0.80); right time 50% max vs left time 50% max (t-test, p = 0.92); right time max upslope vs left time max upslope (t-test, p = 0.34).

Regression analysis was performed between perfusion parameters and clinical characteristics. Analysis revealed direct correlation between time to 50% max and hospitalization (blood pool time 50% max and hospitalization, p=0.027; right lung time 50% max and hospitalization, p=0.003); a direct correlation between time to max upslope of the right lung and age (p=0.012); an inverse correlation between blood pool relative upslope and hypertension (p=0.05); a direct correlation between right lung time to 50% max and rheumatoid arthritis (p=0.046); and inverse correlations between perfusion and the presence of long-COVID symptoms (left lung relative upslope vs. dyspnea on exertion/exercise intolerance, p=0.011; left lung relative upslope vs. brain fog, p=0.036; right lung relative upslope vs. dyspnea on exertion/exercise intolerance, p=0.03; right lung relative upslope vs. headache, p=0.049).

Regression analysis was also performed between perfusion parameters and cardiac functional parameters. Analysis revealed an inverse correlation between blood pool relative upslope and LVEDVI (p=0.037) and direct correlations between blood pool relative upslope vs. LVESVI (p=0.015) and LVEF (p=0.023); an inverse correlation between left lung relative upslope and LAEF Booster (p=0.047) and between right lung relative upslope and LAEF Booster (p=0.026); an inverse correlation between blood pool time max upslope and LA biplane reservoir strain (p=0.05); a direct correlation between left lung time max upslope and LGE scar quantification (p=0.024); direct correlations between right lung time max upslope vs. RVESVI (p=0.009) and RVEF (p=0.010); a direct correlation between blood pool time 50% max vs. myocardial native T1 (p=0.048) and LA biplane reservoir strain (p=0.019); and a direct correlation between right lung time 50% max and RVEF (p=0.045).

DISCUSSION:
This study of pulmonary perfusion in post-COVID patients and its association with demographic variables, clinical characteristics, and functional cardiac measurements revealed important insights. Older patients and those who required hospitalization for COVID-19 illness may have worse pulmonary perfusion following their illness. Patients with comorbidities at the time of COVID diagnosis, particularly hypertension and rheumatoid arthritis, and those who experience certain post-COVID symptoms, such as dyspnea, exercise intolerance, and brain fog may have associated lung perfusion abnormalities post-COVID. Additionally, there are several cardiac functional parameters that correlate with lung perfusion. A limitation of our study is that we cannot definitively conclude whether the worse pulmonary perfusion is a consequence of COVID-19 or the reason for severe COVID-19 and/or hospitalization.

CONCLUSION:
Pulmonary perfusion analysis of cardiopulmonary magnetic resonance imaging in patients with previous COVID-19 may help phenotype advanced disease. Preliminary analysis revealed important associations between demographics, clinical characteristics, and cardiac functional parameters with pulmonary perfusion.

REFERENCES:

[1] Chung MK, Zidar DA, Bristow MR, Cameron SJ, Chan T, Harding CV 3rd, Kwon DH, Singh T, Tilton JC, Tsai EJ, Tucker NR, Barnard J, Loscalzo J. COVID-19 and Cardiovascular Disease: From Bench to Bedside. Circ Res. 2021 Apr 16;128(8):1214-1236. doi: 10.1161/CIRCRESAHA.121.317997. Epub 2021 Apr 15. PMID: 33856918; PMCID: PMC8048382.

[2] Clerkin KJ, Fried JA, Raikhelkar J, Sayer G, Griffin JM, Masoumi A, Jain SS, Burkhoff D, Kumaraiah D, Rabbani L, Schwartz A, Uriel N. COVID-19 and Cardiovascular Disease. Circulation. 2020 May 19;141(20):1648-1655. doi: 10.1161/CIRCULATIONAHA.120.046941. Epub 2020 Mar 21. PMID: 32200663.

[3] Cenko E, Badimon L, Bugiardini R, Claeys MJ, De Luca G, de Wit C, Derumeaux G, Dorobantu M, Duncker DJ, Eringa EC, Gorog DA, Hassager C, Heinzel FR, Huber K, Manfrini O, Milicic D, Oikonomou E, Padro T, Trifunovic-Zamaklar D, Vasiljevic-Pokrajcic Z, Vavlukis M, Vilahur G, Tousoulis D. Cardiovascular disease and COVID-19: a consensus paper from the ESC Working Group on Coronary Pathophysiology & Microcirculation, ESC Working Group on Thrombosis and the Association for Acute CardioVascular Care (ACVC), in collaboration with the European Heart Rhythm Association (EHRA). Cardiovasc Res. 2021 Dec 17;117(14):2705-2729. doi: 10.1093/cvr/cvab298. PMID: 34528075; PMCID: PMC8500019.

[4] Doerschug KC, Schmidt GA. Pulmonary Aspects of COVID-19. Annu Rev Med. 2022 Jan 27;73:81-93. doi: 10.1146/annurev-med-042220-014817. PMID: 35084996.

[5] Çakır Edis E. Chronic Pulmonary Diseases and COVID-19. Turk Thorac J. 2020 Sep;21(5):345-349. doi: 10.5152/TurkThoracJ.2020.20091. Epub 2020 Sep 1. PMID: 33031727; PMCID: PMC7544403.

[6] Guan WJ, Ni ZY, Hu Y, Liang WH, Ou CQ, He JX, Liu L, Shan H, Lei CL, Hui DSC, Du B, Li LJ, Zeng G, Yuen KY, Chen RC, Tang CL, Wang T, Chen PY, Xiang J, Li SY, Wang JL, Liang ZJ, Peng YX, Wei L, Liu Y, Hu YH, Peng P, Wang JM, Liu JY, Chen Z, Li G, Zheng ZJ, Qiu SQ, Luo J, Ye CJ, Zhu SY, Zhong NS; China Medical Treatment Expert Group for Covid-19. Clinical Characteristics of Coronavirus Disease 2019 in China. N Engl J Med. 2020 Apr 30;382(18):1708-1720. doi: 10.1056/NEJMoa2002032. Epub 2020 Feb 28. PMID: 32109013; PMCID: PMC7092819.

[7] Busse A, Rajagopal R, Yücel S, Beller E, Öner A, Streckenbach F, Cantré D, Ince H, Weber MA, Meinel FG. Cardiac MRI-Update 2020. Radiologe. 2020 Nov;60(Suppl 1):33-40. English. doi: 10.1007/s00117-020-00687-1. PMID: 32385547.

[8] Bauer WR. Was kann die kardiale MR-Bildgebung heute leisten? [Cardiac MRI today]. Dtsch Med Wochenschr. 2021 Mar;146(5):344-350. German. doi: 10.1055/a-1239-5068. Epub 2021 Mar 1. PMID: 33648004.

[9] Vitrella G, Faganello G, Morea G, Pagnan L, Belgrano M, Cova MA. Role of Cardiac Imaging: Cardiac Magnetic Resonance and Cardiac Computed Tomography. 2019 May 18. In: Sinagra G, Merlo M, Pinamonti B, editors. Dilated Cardiomyopathy: From Genetics to Clinical Management [Internet]. Cham (CH): Springer; 2019. Chapter 8. PMID: 32091727.

[10] Lima JA, Desai MY. Cardiovascular magnetic resonance imaging: current and emerging applications. J Am Coll Cardiol. 2004 Sep 15;44(6):1164-71. doi: 10.1016/j.jacc.2004.06.033. PMID: 15364314.

[11] Kato S, Azuma M, Fukui K, Kodama S, Nakayama N, Kitamura H, Hagiwara E, Ogura T, Horita N, Namkoong H, Kimura K, Tamura K, Utsunomiya D. Cardiac involvement in coronavirus disease 2019 assessed by cardiac magnetic resonance imaging: a meta-analysis. Heart Vessels. 2022 Mar 16:1–13. doi: 10.1007/s00380-022-02055-6. Epub ahead of print. PMID: 35294611; PMCID: PMC8925980.

[12] Ojha V, Verma M, Pandey NN, Mani A, Malhi AS, Kumar S, Jagia P, Roy A, Sharma S. Cardiac Magnetic Resonance Imaging in Coronavirus Disease 2019 (COVID-19): A Systematic Review of Cardiac Magnetic Resonance Imaging Findings in 199 Patients. J Thorac Imaging. 2021 Mar 1;36(2):73-83. doi: 10.1097/RTI.0000000000000574. PMID: 33306666.

[13] Puntmann VO, Carerj ML, Wieters I, Fahim M, Arendt C, Hoffmann J, Shchendrygina A, Escher F, Vasa-Nicotera M, Zeiher AM, Vehreschild M, Nagel E. Outcomes of Cardiovascular Magnetic Resonance Imaging in Patients Recently Recovered From Coronavirus Disease 2019 (COVID-19). JAMA Cardiol. 2020 Nov 1;5(11):1265-1273. doi: 10.1001/jamacardio.2020.3557. Erratum in: JAMA Cardiol. 2020 Nov 1;5(11):1308. PMID: 32730619; PMCID: PMC7385689.

[14] Atri L, Morgan M, Harrell S, AlJaroudi W, Berman AE. Role of cardiac magnetic resonance imaging in the diagnosis and management of COVID-19 related myocarditis: Clinical and imaging considerations. World J Radiol. 2021 Sep 28;13(9):283-293. doi: 10.4329/wjr.v13.i9.283. PMID: 34630914; PMCID: PMC8473436.

[15] Ohno Y, Hatabu H, Murase K, Higashino T, Kawamitsu H, Watanabe H, Takenaka D, Fujii M, Sugimura K. Quantitative assessment of regional pulmonary perfusion in the entire lung using three-dimensional ultrafast dynamic contrast-enhanced magnetic resonance imaging: Preliminary experience in 40 subjects. J Magn Reson Imaging. 2004 Sep;20(3):353-65. doi: 10.1002/jmri.20137. PMID: 15332240.

[16] Risse, F & Fink, Christian & Ley, S & Kauczor, Hans-Ulrich & Schad, Lothar. (2004). Perfusion quantification of the whole lung using singular value decomposition with optimized threshold.

[17] Ley S, Ley-Zaporozhan J. Pulmonary perfusion imaging using MRI: clinical application. Insights Imaging. 2012 Feb;3(1):61-71. doi: 10.1007/s13244-011-0140-1. Epub 2011 Dec 29. PMID: 22695999; PMCID: PMC3292645.

[18] Hatabu H, Ohno Y, Gefter WB, Parraga G, Madore B, Lee KS, Altes TA, Lynch DA, Mayo JR, Seo JB, Wild JM, van Beek EJR, Schiebler ML, Kauczor HU; Fleischner Society. Expanding Applications of Pulmonary MRI in the Clinical Evaluation of Lung Disorders: Fleischner Society Position Paper. Radiology. 2020 Nov;297(2):286-301. doi: 10.1148/radiol.2020201138. Epub 2020 Sep 1. PMID: 32870136.

[19] Schiwek M, Triphan SMF, Biederer J, Weinheimer O, Eichinger M, Vogelmeier CF, Jörres RA, Kauczor HU, Heußel CP, Konietzke P, von Stackelberg O, Risse F, Jobst BJ, Wielpütz MO; COSYCONET study group. Quantification of pulmonary perfusion abnormalities using DCE-MRI in COPD: comparison with quantitative CT and pulmonary function. Eur Radiol. 2021 Sep 22. doi: 10.1007/s00330-021-08229-6. Epub ahead of print. PMID: 34553255.

[20] Ingrisch M, Maxien D, Schwab F, Reiser MF, Nikolaou K, Dietrich O. Assessment of pulmonary perfusion with breath-hold and free-breathing dynamic contrast-enhanced magnetic resonance imaging: quantification and reproducibility. Invest Radiol. 2014 Jun;49(6):382-9. doi: 10.1097/RLI.0000000000000020. PMID: 24473368.

[21] Hatabu, Hiroto, et al. "Quantitative assessment of pulmonary perfusion with dynamic contrast-enhanced MRI." Magnetic Resonance in Medicine: An Official Journal of the International Society for Magnetic Resonance in Medicine 42.6 (1999): 1033-1038.

[22] Hueper K, Parikh MA, Prince MR, Schoenfeld C, Liu C, Bluemke DA, Dashnaw SM, Goldstein TA, Hoffman EA, Lima JA, Skrok J, Zheng J, Barr RG, Vogel-Claussen J. Quantitative and semiquantitative measures of regional pulmonary microvascular perfusion by magnetic resonance imaging and their relationships to global lung perfusion and lung diffusing capacity: the multiethnic study of atherosclerosis chronic obstructive pulmonary disease study. Invest Radiol. 2013 Apr;48(4):223-30. doi: 10.1097/RLI.0b013e318281057d. PMID: 23385398; PMCID: PMC3952075.

[23] Halpin DMG, Rabe AP, Loke WJ, Grieve S, Daniele P, Hwang S, Forsythe A. Epidemiology, Healthcare Resource Utilization, and Mortality of Asthma and COPD in COVID-19: A Systematic Literature Review and Meta-Analyses. J Asthma Allergy. 2022 Jun 17;15:811-825. doi: 10.2147/JAA.S360985. PMID: 35747745; PMCID: PMC9211747.

Hilar vessel segmentation in quantitative chest tomography measurement of pulmonary vascular volume distribution improves detection of pulmonary hypertension associated with COPD

Ben R. Lavon[1], Joana Costa[1], Patrick Muchmore[1], Hector Cajigas[2]
[1] Fluidda Inc. NY, NY USA
[2] Division of Pulmonary and Critical Care, Mayo Clinic Rochester MN

Introduction

Detection of pulmonary hypertension (PH) in subjects with COPD is often challenging. Quantitative CT (qCT) methods for segmenting the intraparenchymal pulmonary vasculature can distinguish PH from non-PH cohorts by analyzing its volume distribution across vessels of various size ranges, with PH subjects having less pulmonary vascular volume contained in smaller vessels than non-PH subjects.[1] Previous methodology did not include analysis of large proximal pulmonary arteries. Dilation of central, proximal vessels has prognostic significance in patients with COPD.[2] We sought to develop a method for segmenting hilar vessel structures and to examine their diagnostic implications for PH in a cohort of COPD subjects with and without known PH.

Methods

We previously described a retrospective cohort of subjects with COPD with or without known PH collected from 3 centers.[1] PH subjects had RHC-confirmed PH within 30 days of the CT. Scans were processed with Functional Respiratory Imaging, a qCT platform (FLUIDDA, Kotnich, BE). First, a deep learning-based algorithm identified a lung region of interest which excluded the hilum. Next, manual post-processing was performed to identify the hilar vessels lateral from the azygos arch in the right lung and distal to the line drawn tangent to the lateral most excursion of the heart and perpendicular to the centerline of the left PA in the left lung. Finally, an automated algorithm identified all vessel-like structures in the scans with and without inclusion of the hilum to measure the volume and volume fraction of segmented pulmonary vasculature contained in structures smaller than 5 mm^2 (BV5 and BV5Pr, respectively) and in structures larger than 10mm^2 (BV10 and BV10Pr, respectively). We then compared the volume of hilar tissue segmented between PH and non-PH groups, as well as the magnitude of difference in BV5Pr and BV10Pr between PH and non-PH groups with and without the hilum using two-sample t-tests.

Results

A total of 87 subjects were included (45 without PH, 42 with PH). Inclusion of the hilum resulted in substantial increases in BV10and small increases in the volume (BV5). The increases in total vascular volume, BV5, and BV10 were significantly larger for the PH group than the non-PH group, reflecting the impact of dilated proximal vessels. The volume fraction contained in BV5 decreased for all subjects with the inclusion of the hilum, and the volume fraction contained in BV10 increased for all subjects, as expected. The magnitude of this change was larger in the PH group than the non-PH group, although the difference was statistically significant only for BV10

	PH (mean ± SD)	No PH (mean ± SD)	P value
Total volume hilar vessels	85.31 ± 26.05	70.61 ± 22.97	0.006
Volume hilar BV5	2.95 ± 1.62	2.28 ± 1.09	0.024
Volume hilar BV10	79.54 ± 23.75	66.08 ± 21.50	0.007
BV5Pr without hilum	40.89 ± 9.29	46.66 ± 8.39	0.003
BV5Pr with hilum	31.55 ± 8.51	37.94 ± 7.17	<0.001
BV10Pr without hilum	37.02 ± 9.38	30.45 ± 8.43	0.0009
BV10Pr with hilum	51.14 ± 9.52	43.10 ± 7.68	<0.0001
Change in BV5Pr with hilum	-9.33 ± 2.69	-8.71 ± 2.17	0.237
Change in BV10Pr with hilum	14.13 ± 3.44	12.65 ± 2.59	0.012

Conclusion

Inclusion of the hilum increases the statistical power of qCT measures of pulmonary vascular volume distribution as a diagnostic tool for detection of PH in patients with COPD. Additional research will examine the impact of these updated measurements on survival and other clinical outcomes in this cohort, and additional validation will be needed to establish their use as clinical decision-making tools in practice.

References

1. Cajigas, H, et al. COPD-associated pulmonary hypertension detected by novel pulmonary blood vessel quantification system. Impact on clinical characteristics and outcomes. Poster presented at 2022 PVRI Congress; June, 2022, Athens.
2. Wells JM, Washko GR, Han MK, et al. Pulmonary arterial enlargement and acute exacerbations of COPD. N Engl J Med. 2012;367(10):913-921. doi:10.1056/NEJMoa1203830
3. Lins M, Vandevenne J, Thillai M, et al. Assessment of Small Pulmonary Blood Vessels in COVID-19 Patients Using HRCT. Acad Radiol. 2020;27(10):1449-1455. doi:10.1016/j.acra.2020.07.019

Feasibility of 3D Dynamic Gas- and Dissolved-Phase Imaging of the Rodent Lung using Hyperpolarized 129Xe Magnetic Resonance Imaging

Luis Loza, Tahmina Achekzai, Stephen Kadlecek, Hooman Hamedani, Faraz Amzajerdian, Mostafa Ismail, Ryan Baron, Ian Duncan, Kai Ruppert, Rahim Rizi

Introduction

Hyperpolarized 129Xe (HXe) magnetic resonance imaging (MRI) of pulmonary ventilation and gas exchange offers useful assessments of functional impairment, disease progression, and treatment response, and its application in preclinical lung disease models can help improve our understanding of the mechanisms driving disease onset and progression. Yet traditional HXe MR imaging is typically performed during end-inspiration (EI) breath holds, thus failing to capture pulmonary ventilation and gas exchange under true physiological conditions. Here, we demonstrate the feasibility of dynamically acquiring high-resolution 3D gas- (GP) and dissolved-phase (DP) images under mechanical ventilation in a healthy rat.

Methods

One male Sprague Dawley rat (340g) was anesthetized, intubated, and ventilated with air, switching to a HXe gas mixture (21% O2, 79% N2/xenon) during imaging in a 3T horizontal-bore MRI system (1L enriched HXe per imaging session). 3D images were acquired continuously during normal breathing over the course of 400–500 breaths using a customized spiral-like k-space trajectory, reconstructed offline, averaged and placed into 10 bins to produce distinct image sets at different points in the breathing cycle. Imaging parameters were as follows: MS = 64×64, FOV = 50mm × 50mm, FA = 3°, TR = 10ms, BW = 200kHz.

Results

Figure 1 shows coronal GP (top) and DP (bottom) EI images from anterior-to-posterior in a healthy rat. For each successive GP slice, the splitting of the airway tree is visible, from the trachea to the secondary and tertiary bronchi. Signal is primarily observed in the lung parenchyma in DP images, with signal voids within the parenchyma corresponding to the major airways.

Discussion and Conclusions

This study is the first to acquire high-resolution isotropic 3D GP images in a healthy rat lung (in-plane resolution = 0.5208mm, slice thickness = 0.5208mm). While DP images were acquired in the same manner, their resolution is inherently lower due to the short T2* at 3T (~ 1ms), so they are not isotropic. Nevertheless, the ability to dynamically acquire high-resolution HXe images significantly improves upon traditional breath-hold imaging techniques, allowing us to capture

the full extent of ventilation and gas exchange heterogeneity occurring over the breathing cycle. Analyzing changes in GP and DP signal dynamics over the breathing cycle enables a qualitative assessment of gas distribution and exchange, respectively. In future, mathematical models can be constructed to yield quantitative measures of ventilation and perfusion, enabling a more direct assessment of disease-related functional changes in the lung.

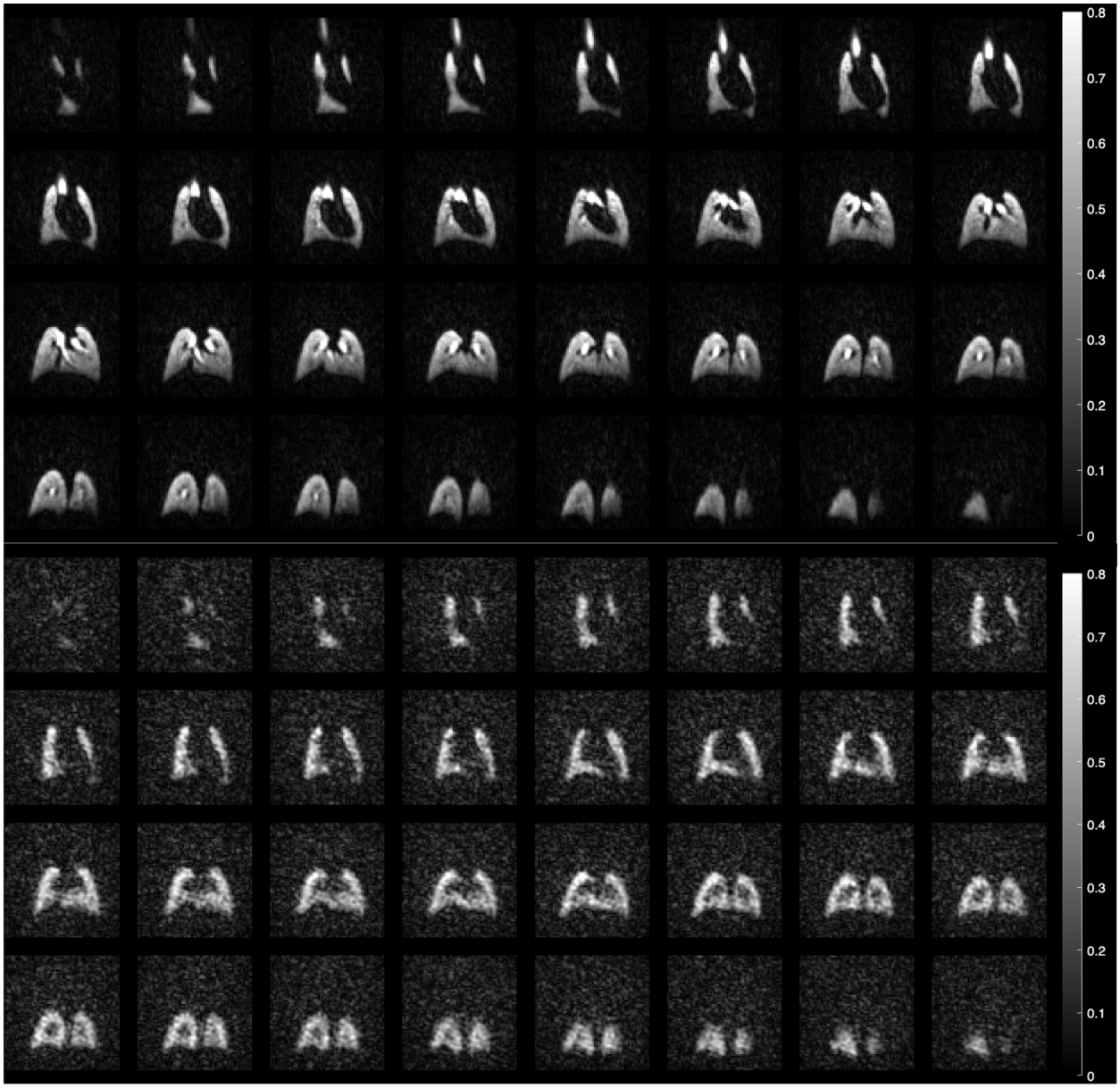

Figure 1: GP (top) and DP (bottom) EI coronal images in a healthy rat, normalized to their respective maximum signal intensity to enable relative comparison between the two image sets. As expected, there is a drastic difference in image SNR between GP and DP images.

^{129}Xe MRS Gas-Exchange Variability in Asthma: Demographics, Blood and Lung-Function

Alexander M Matheson[1,2], Marrissa J McIntosh[1,2] Narinder Paul[3] Anurag Bhalla[4] Cory Yamashita[4] and Grace Parraga[1-4]

[1]Robarts Research Institute, [2]Department of Medical Biophysics, [3]Department of Medical Imaging, [4]Division of Respirology, Department of Medicine, Western University London, Canada

PURPOSE: In patients with asthma, lung findings include airway wall thickening, and smooth muscle dysfunction. Other abnormalities have been observed, including collagen deposits in alveolar walls in uncontrolled asthma[1] and pulmonary vascular pruning.[2] ^{129}Xe MRS can probe the alveolar-capillary interface where these abnormalities may be occurring. The temporal variability of the RBC and alveolar membrane ^{129}Xe MRS signal, referred to as cardiogenic oscillations, are thought to be driven by blood pulsation.[3] Research in patients with COPD have uncovered RBC:membrane differences and oscillation amplitude differences compared to healthy participants[4] but such investigations have not been undertaken in asthma. Clinical measures of gas exchange are affected by age, sex, height, and hemoglobin[5, 6] and but contributions to ^{129}Xe spectral measurements are still under investigation. Therefore, we examined both static and dynamic spectroscopy measurements in people with asthma and healthy volunteers and to compare them with clinical measurements.

METHODS: Participants with severe asthma were recruited from a quaternary care Asthma clinic and provided written informed consent to an approved protocol (NCT02351141 or NCT 03733535) to undertake pulmonary function tests, blood tests, ^{129}Xe MRI, and static and dynamic MRS. Healthy volunteers were recruited from the local general population and performed static and dynamic MRS and fingertip hemoglobin measurements. ^{129}Xe MRS peaks were fit to a three-component Lorentzian model in Matlab (2021a, Mathworks) to determine component magnitude, phase, and frequency. Each peak was then fit to sinusoids to measure cardiogenic oscillations in peak magnitude, phase and frequency. Oscillations were normalized to initial peak height. RBC:membrane ratio was calculated as the ratio of areas-under-the-curve.

RESULTS: 22 participants with asthma (age=60±15, 18/22 female) and 16 healthy volunteers (age=37±17 years, 5/16 female) were enrolled. RBC:membrane and RBC:Gas measurements were significantly lesser in participants with asthma (0.29±0.08) compared to healthy volunteers (0.44±0.09, p<.001), however there was no significant difference in membrane:gas (healthy=0.93±0.26, asthma=0.94±0.18, p=.93). Figure 1 shows age and sex effects on RBC:membrane. Multivariate models were constructed for both groups: sex, age and hemoglobin were common sources of variance and weight contributed to healthy participants. Height and BMI were not significant contributors to either model. In addition to RBC oscillations, we observed oscillations in the membrane and gas signals in both healthy volunteers and participants with asthma. There were no significant differences between oscillation amplitudes in healthy participants (12±5%) and participants with asthma (15±12%, p=.33).

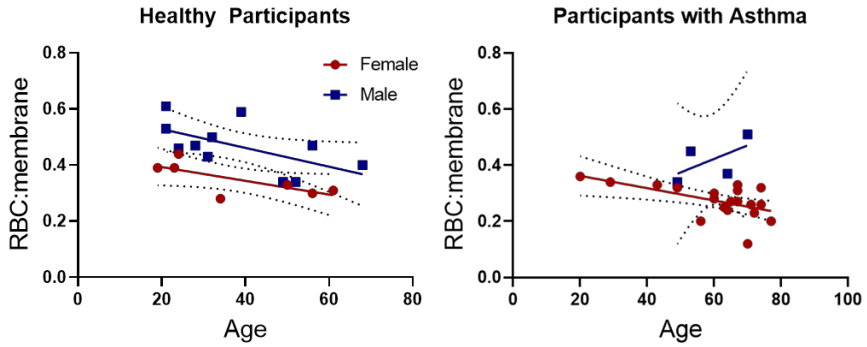

Table 1: Multivariate model in healthy participants

Variable	β	Standardized β	Significance p
Constant	-1.094		.02
Sex	.12	1.35	.03
Age	-.001	-.44	.02
Weight	-.004	-.25	.004
Hemoglobin	.13	-.56	.006

Table 2: Multivariate model in participants with asthma

Variable	β	Standardized β	Significance p
Constant	.17		.14
Sex	.14	.60	<.001
Age	-.002	-.36	.01
Hemoglobin	.17	.318	.04

Figure 1 Multivariable models of RBC:membrane in healthy participants and participants with asthma. RBC:membrane neared significant correlation with age in both groups for women (healthy: r=72, p=.07 asthma: r=.56, p=.01) and healthy men (r=.60, p=.05). Age, sex, and hemoglobin levels were significant contributors to multivariable models of RBC:membrane.

DISCUSSION: The RBC:membrane ratio was diminished in participants with asthma and appeared to be driven by RBC, as there was no difference in membrane:gas observed. We uncovered a correlation between RBC:membrane and age in both groups, however this was not enough to explain differences between them. Multivariable models indicated that a combination of age, sex and hemoglobin measurements contributed to RBC:membrane measurements. The presence of both sex and hemoglobin in models was surprising, as it may suggest physiological sex differences beyond hemoglobin can affect RBC:membrane. Whether demographic differences are sufficient to explain gas exchange measurements in people with asthma is still unclear. In addition to RBC oscillations, we observed membrane oscillations and novel gas oscillations, however these were not different between cohorts.

CONCLUSIONS: Participants with severe asthma exhibited significantly lower RBC:membrane ratios compared to healthy volunteers. Differences in group demographics may contribute, as multivariable models in both healthy participants and participants with asthma showed age, sex and hemoglobin contributing to measurements. Cardiogenic oscillations were observed in all spectral peaks in both healthy participants and participants with asthma.

REFERENCES:1. Weitoft, M, et al. *Respir Res* 2014. 2. Ash, SY, et al. *Am J Respir Crit Care Med* 2018. 3. Bier, EA, et al. *NMR Biomed* 2019. 4. Wang, Z, et al. *Eur Respir J* 2019. 5. Yang, SC, et al. *Am Rev Respir Dis* 1993. 6. Marrades, RM, et al. *Am J Respir Crit Care Med* 1997.

Estimating Physiological Values of Membrane and Red Blood Cell Conductance Using ^{129}Xe Gas Exchange MRI

David Mummy, Ph.D.[1], Shuo Zhang, M.S.,[1], Aryil Bechtel, B.S.[1], Bastiaan Driehuys, Ph.D.[1]
[1]*Department of Radiology, Duke University, Durham NC, USA*

Purpose. ^{129}Xe gas exchange MRI can be used to estimate values of diffusing capacity of the lung for carbon monoxide (DL_{CO}) and the carbon monoxide transfer coefficient (KCO) using the equations of Roughton and Forster.[1,2] Specifically, a patient's relative ^{129}Xe membrane uptake and RBC transfer are multiplied by model coefficients to estimate KCO. ^{129}Xe ventilation imaging is then used to estimate accessible alveolar volume and thereby generate DLCO (Figure, A). Previously, these model coefficients were estimated by Wang et al. using empirical statistical fitting.[2] However, these model-fit coefficients do not provide physiologically valid values for the volume-independent specific conductance coefficients of the membrane and RBC compartments. Here, we replace the curve-fit coefficients with *a priori* physiological estimates of volume-independent specific conductance calculated from the recently published reference equations of Munkholm et al. and compare the resulting DL_{CO} estimates to those of the Wang model.[3]

Methods. Healthy subjects (N=33, 12F/21M, age 41.7±16.7yrs) with no history of pulmonary disease, less than 5 pack-years smoking history, and no smoking history within the last 5 years underwent hyperpolarized ^{129}Xe MRI. Measures of ^{129}Xe signal from the membrane and RBC compartments were hemoglobin-corrected using the method proposed by Bechtel et al.[4] Values of DL_{CO} estimated using volume-independent specific conductance coefficients from Munkholm et al. were compared with analogous results obtained using the Wang method.[1–3] Finally, the Munkholm-based DL_{CO} estimates were compared with DLCO values obtained clinically.

Results. The coefficients derived from Munkholm et al. for the membrane and RBC compartments were 22.3 and 8.0 mL/min/mmHg/L, respectively. This is compared with 11.2 and 14.6 mL/min/mmHg/L in the model of Wang et al. DL_{CO} estimates from both models were tightly correlated ($p < 0.001$, $r = 0.97$), with the DL_{CO} values estimated using the Munkholm coefficients showing a modest downward bias of 2 mL/min/mmHg (Figure, B). DL_{CO} estimates using the Munkholm coefficients were strongly correlated with clinical DL_{CO} (Figure, C; $p < 0.001$, $r = 0.58$).

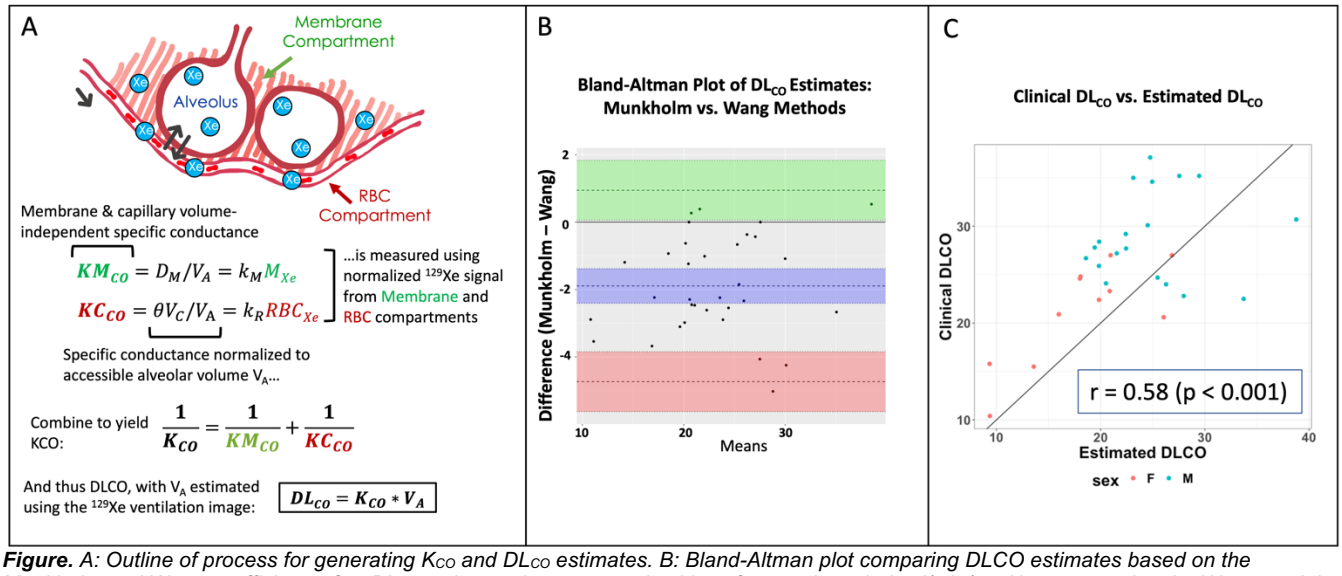

Figure. *A: Outline of process for generating K_{CO} and DL_{CO} estimates. B: Bland-Altman plot comparing DLCO estimates based on the Munkholm and Wang coefficients. Our DL_{CO} estimates have a negative bias of approximately 2 ml/min/mmHg compared to the Wang model but are well correlated ($p < 0.001$, $r = 0.97$). C. Image-based estimates of DLCO vs. clinical DLCO are well correlated ($r = 0.58$, $p < 0.001$). The 45 degree line indicates perfect agreement.*

Discussion. ^{129}Xe-based DL_{CO} predictions using physiological parameters were relatively consistent with estimates generated using the Wang model curve-fits, despite the disparity between the two sets of coefficients used in the models. Estimates of DL_{CO} using this method were well correlated with clinical DL_{CO}. Importantly, the use of physiology-based estimates rather than curve fits resulted in individual estimates of membrane and RBC volume-independent specific conductance coefficients that are consistent with published reference equations for healthy subjects.

Conclusion. ^{129}Xe gas exchange MRI may enable physiologically meaningful quantitative assessment of the independent contributions of the membrane and RBC compartments to DLCO and KCO abnormalities observed clinically.

References

1. Roughton FJW, Forster RE. *J Appl Physiol* 1957;11(2):290–302.
2. Wang Z, Rankine L, Bier EA, et al. *J Appl Physiol* 2021;
3. Munkholm M, Marott JL, Bjerre-Kristensen L, et al. *Eur Respir J* 2018;52(1).
4. Bechtel AL, Bier E, Lu J, et al. Establishing a hemoglobin correction for 129 Xe gas exchange MRI. ISMRM 2022.

Free-breathing MRI for Monitoring Ventilation and Perfusion changes following Elexacaftor/Tezacaftor/Ivacaftor Treatment in Pediatric Cystic Fibrosis

Samal Munidasa[1,2], Brandon Zanette[1], Marcus Couch[3], Marie-Pier Dumas[4], Wallace Wee[4], Michelle Shaw[1], Renee Jensen[4], Daniel Li[1], Sharon Braganza[1], Felix Ratjen[1,4], Giles Santyr[1,2]

[1]Translational Medicine Program, The Hospital for Sick Children, Toronto, ON, Canada.
[2]Department of Medical Biophysics, University of Toronto, Toronto, ON, Canada.
[3]Siemens Healthcare Limited, Montreal, QC, Canada.
[4]Division of Respiratory Medicine, The Hospital for Sick Children, Toronto, ON, Canada.

Purpose: Cystic Fibrosis (CF), caused by mutations in the CF transmembrane conductance regulator (CFTR) gene family is characterized by an aberrant build-up of sticky mucus within the lungs that leads to airway plugging, damage and inflammation [1]. Hyperpolarized (HP) 129-Xenon MRI (Xe-MRI), which involves inhaling a gas and holding one's breath, has been found to be sensitive to early CF lung disease as compared to traditional lung function measures, such as forced expiratory volume in one second (FEV_1) [2]. But Xe-MRI is not widely available and involves a lengthy breath-hold which can be challenging to perform in very sick or young children. Alternatively, free-breathing lung MRI does not require special equipment (i.e. polarizer or contrast agents) or a breath-hold and uses ^{1}H signal variations associated with the cardiorespiratory motion to derive ventilation and perfusion weighted maps. Phase-resolved functional lung (PREFUL) MRI is a specific free-breathing MRI technique that sorts images acquired during natural breathing into complete respiratory and cardiac cycles in the time domain, enabling the evaluation of both static and dynamic ventilation and perfusion parameters, respectively [3]. PREFUL MRI has been used to assess ventilation/perfusion abnormalities in adults with CF, chronic obstructive pulmonary disease (COPD), and chronic thromboembolic hypertension (CTEPH) [3]. Additionally, PREFUL MRI derived ventilation distributions have been shown to be responsive to the treatment of pulmonary exacerbations in pediatric CF [4] and has shown good repeatability [5]. However, PREFUL MRI has not been used to monitor changes in ventilation and perfusion following CFTR-modulator treatment, specifically the combination of elexacaftor/tezacaftor/ivacaftor (ETI). As part of an ongoing, multi-site study (HyPOINT), we assessed the responsiveness of free-breathing MRI derived ventilation and perfusion parameters to ETI treatment compared to Xe-MRI and pulmonary function tests in children with CF.

Methods: 13 CF subjects (6 females & 7 males) aged 16±2 years were recruited in accordance with ethics approval at The Hospital for Sick Children. Participants performed spirometry and N_2 multiple breath-washout (FEV_1 and lung clearance index, respectively) as well as Xe-MRI and free-breathing MRI at 3T as previously described [5], prior to and following ETI treatment. The follow-up visits occurred 1-month (n=13), 6-months (n=8), 1-year (n=5) after the initiation of ETI treatment. Regional ventilation (RV) and normalized perfusion (Q) maps were calculated from the free-breathing images using the PREFUL method [3]. Ventilation Defect Percentage was calculated for each subject from the RV maps using k-means clustering (VDP_{RV}) and perfusion defect percentage was calculated using a threshold 2% of the normalized perfusion signal (QDP) [6]. Ventilation-perfusion matching (VQM) distributions were determined by combining VDP and QDP maps within the thoracic cavity where regions containing both or neither ventilation or perfusion defects represented VQM [6]. VDP derived from Xe-MRI ventilation distributions (VDP_{Xe}) were calculated based on a threshold of 60% of the mean xenon ventilation signal [5]. Treatment effects observed by VDP_{RV}, QDP, VQM, VDP_{Xe} and FEV_1 were determined using a Wilcoxon's ranked sign test and absolute/percent changes of each were correlated using a Spearman ranked correlation test.

Results: Figure 1a shows VDP_{RV} and QDP maps for a representative CF patient at baseline and three timepoints post-treatment. Figure 1b shows the individual absolute changes in VDP_{Xe}, VDP_{RV}, QDP, VQM, and FEV_1 for all CF patients. All parameters significantly decreased between the baseline and 1-month follow-up (all $p<0.01$) as well as between the baseline and 6-months follow-up (all $p<0.05$). Across all time-points and parameters, only the absolute changes in the baseline vs. 1-month VDP_{Xe} and VDP_{RV} were significantly correlated ($\rho=0.62$, $p= 0.02$), while percentage change in VDP_{Xe} and VDP_{RV} did not significantly correlate ($p>0.05$). Whereas, of all timepoints and parameters, the percentage changes in the baseline vs. 1-month VDP_{RV} and QDP ($\rho=0.74$, $p= 0.003$) and VQM and FEV_1 ($\rho=0.74$, $p= 0.003$) significantly correlated.

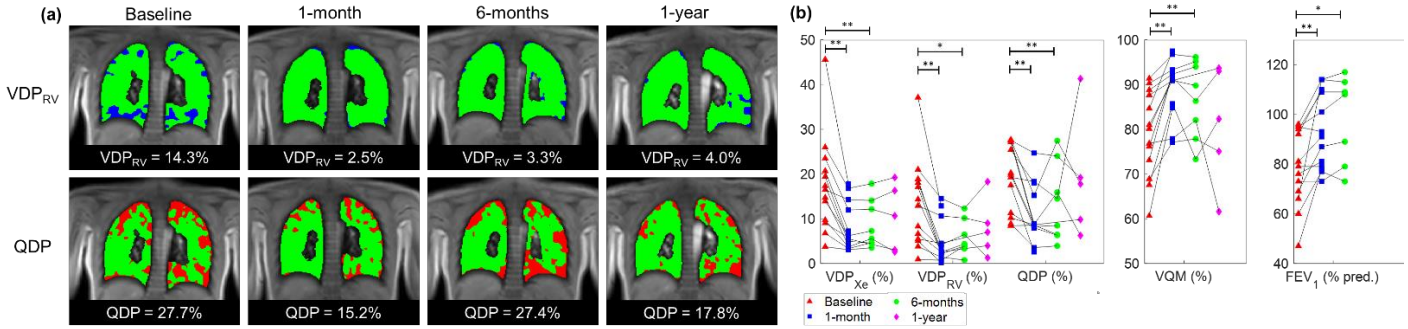

Figure 1. (a) PREFUL MRI derived (top) regional ventilation (RV) ventilation defect percentage (VDP_{RV}) and (bottom) perfusion defect percentage (QDP) maps for a representative pediatric CF patient at baseline, 1-month, 6-months, and 1-year following initiation of ETI treatment. Blue and red areas indicate regions of ventilation and perfusion defects, respectively, and the green regions indicate healthy ventilation/perfusion. (b) Individual percent changes in VDP_{Xe}, VDP_{RV}, QDP, VQM, and FEV_1 for all CF patients at four time-points. A statistically significant change of $p<0.05$ is denoted by a single asterisk, and $p<0.01$ is denoted by two asterisks.

Discussion: Free-breathing MRI with PREFUL was able to detect a significant improvement in ventilation, perfusion, and ventilation/perfusion matching following elexacaftor/tezacaftor/ivacaftor treatment, similarly to Xe-MRI. The ventilatory change with intervention is consistent with previous work showing that PREFUL and Xe-MRI significantly decreased in pediatric CF children undergoing intravenous antibiotic treatment for a pulmonary exacerbation [7]. Whereas ventilation defects determined by both PREFUL MRI, and Xe-MRI appeared to plateau following the 1-month visit, perfusion defects found in several CF patients showed notable increases at 6-months an/or 1-year post-treatment. In a similar study of CF patients treated with ETI, lung MRI morphological scores showed significant improvement at 8-16 week follow-ups, whereas PREFUL MRI perfusion scores did not significantly change [8]. Thus, the change in PREFUL MRI derived perfusion defects may be less sensitive to early ETI treatment relative to the ventilatory changes. Although, acquisition of additional 6-month/1-year datapoints will be necessary to support this finding. In future work, perfusion-weighted PREFUL MRI could be compared to traditional perfusion MRI techniques such as gadolinium-enhanced dynamic contrast enhanced MRI as described in previous work [3]**.** Additionally, multi-slice PREFUL MRI acquisitions would improve assessment of ventilation and perfusion across the entire lung.

Conclusion: Free-breathing MRI provides a responsive pulmonary ventilation and perfusion measure for following CFTR-modulator treatment in CF lung disease.

Acknowledgements: The authors would like to thank the following sources of funding: The Hospital for Sick Children, Natural Sciences and Engineering Research Council of Canada (NSERC) Discovery grant (RGPIN 217015-2013), the Cystic Fibrosis Foundation (Grant Number: WOODS19A0), Canadian Institutes of Health Research (CIHR) operating and project grants (MOP 123431, PJT 153099). Samal Munidasa would like to thank Restracomp and NSERC for their support.

References:

1. Cutting. G.R. Nat Rev Genet. 2015;16(1) 45-56.
2. Santyr G. et al. Acad. Radiol. 2019;26(3):344-354
3. Voskrebenzev A. et al. Magn Reson Med. 2018;79(4):2306-2314.
4. Munidasa S. et al. Eur. Respir. J. 2020;59(3): 2003104
5. Munidasa S. et al. Magn. Reson. Med. 2022;epub doi: 10.1002/mrm.29566
6. Zanette B. et al. J Magn Reson Imaging. 2022; 55(6):1696-1707.
7. Couch M.J. et al. Acad Radiol. 2021; 28(8):e209-e218.
8. Graeber S.Y. et al. Am J Respir Crit Care Med. 2022; 1;206(3):311-320.

Title: Compressed-sense reconstructions improve non-Cartesian hyperpolarized ^{129}Xe MRI

Authors: ***J. W. Plummer[1,2]***, A. S. Bdaiwi[1,2], S. A. Soderlund[2], M. M. Willmering[2], J. C. Woods[1,2,3,4,5], Z. I. Cleveland[1,2,3,4], L.L. Walkup[1,2,3,4]

[1]Department of Biomedical Engineering, University of Cincinnati, United States; [2]Center for Pulmonary Imaging Research, Cincinnati Children's Hospital Medical Center, United States; [3]Department of Radiology, Cincinnati Children's Hospital Medical Center, United States; [4]Department of Pediatrics, University of Cincinnati, United States; [5]Department of Physics, University of Cincinnati, United States.

Purpose: Hyperpolarized ^{129}Xe MRI is a powerful imaging modality often used to assess pulmonary gas-uptake. Scans are typically performed within a ≤16-second breath-hold[1], limiting the attainable SNR, resolution, and dynamic information. Non-Cartesian sequences, including 2D-spiral and 3D-FLORET, have improved ^{129}Xe MRI sampling efficiency[2]; but are yet to be combined with compressed sense (CS) reconstruction methods[3]. Here, we demonstrate CS reconstructions in a range of non-Cartesian ^{129}Xe MRI sequences, and show that SNR, image quality, and imaging speed are improved.

Methods: In this work, two reconstruction approaches are compared: i) *gridded reconstruction* (A^{-1}) and ii) *CS with wavelet and total-variation regularization*. Gridded reconstruction is akin to solving the *forward model* MRI problem: $Ax = b + \varepsilon$, by matrix inversion, where A is the measurement matrix ($A = DF$), composed of linear operators for density composition, D, and non-uniform fast Fourier transform[4], F; x is the reconstructed image; b is the k-space data; and ε is the additive noise. The CS approach recasts the forward model as a regularized least squares problem, and solves:

$$x^* = \left\{ \min_x \frac{1}{2} \|Ax - b\|_2 + \lambda_1 \|W(x)\|_1 + \lambda_2 \|G(x)\|_2 ,\right.$$

for the reconstructed image, x^*, by regularizing (λ_i) for both wavelet-transform energy ($W(x)$; efficient for preserving edges and low contrast information) and total variation ($G(x)$; efficient at suppressing noise/streaking). CS images were reconstructed using the *alternating direction method of multipliers* algorithm[5] in SigPy[6]. λ_1 and λ_2 ranged from 1x10^{-5} to 1x10^{-3}.

Human participants (healthy) were imaged per a protocol approved by our local Institutional Review Board (2014-5279 with FDA IND-123,577). Hyperpolarized ^{129}Xe images were collected on a Philips 3T-Ingenia scanner with a single channel custom chest coil. Simulated point-spread functions (PSF) and ventilation imaging sequences included: **(A)** 2D-radial (projections=246, TR/TE=4.25/0.85ms; flip angle=2º); **(B)** 2D-spiral (variable-density, interleaves=24, TR/TE=10.1/1.53ms; flip angle=20º); **(C)** 3D-radial (projections=3670, TR/TE=4.00/0.04ms; flip angle=1º); and **(D)** 3D-FLORET (interleaves=1134, TR/TE=13.13/0.08ms; flip angle=1.5º) sequences. Matrix size=100; resolution=3x3x15 mm^3 (2D) and 3x3x3 mm^3 (3D); FOV=300^3 mm^3. SNR and structural similarity index (SSIM; between fully-sampled A^{-1} and CS reconstructions).

Results: Figure 1 examines noise incoherence in acquisitions with 100% (acceleration factor, R=1) and 50% (R=2) sampling of the Nyquist limit. PSFs for radial sequences exhibited largely incoherent noise with 2-fold under-sampling (Figure 1A,C). Spiral under-sampling produced similar patterns, with coherent noise at the edges of the FOV (Figure 1B,D). The same settings were demonstrated in ventilation imaging for A^{-1} and CS reconstructions. In all cases, CS increased SNR (up to 3-fold), even with 2-fold acceleration, while preserving high SSIM against the fully-sampled A^{-1} reconstruction (>0.98).

Discussion: CS enhances reconstructed image quality of non-Cartesian ^{129}Xe acquisitions, as demonstrated in 2D/3D-radial and 3D-FLORET sequences. The high number of excitations and small flip angles lead to poor SNR; however, this is largely improved with CS.

CS most benefits under-sampled acquisitions that exhibit incoherent noise, as is the case for the 2-fold under-sampled acquisitions presented here. All cases exhibit an incoherent noise structure, which CS suppresses, delivering an SNR on par with fully-sampled acquisitions while maintaining high SSIM.

Such 2-fold accelerations also permit larger flip angles due to fewer required RF-excitations, thus boosting attainable SNR. Of clinical importance, it halves the required breath-hold duration, making ^{129}Xe MRI more feasible for children and advanced lung disease patients. Many ^{129}Xe applications that utilize 3D-radial/FLORET[7] sampling may benefit from CS reconstructions, particularly diffusion-weighted[8] and gas-exchange MRI[9] that suffer from low SNR and long breath-holds.

Conclusion: This work demonstrates that CS reconstruction improves SNR and image quality while reducing the scan duration of commonly used non-Cartesian ^{129}Xe MRI sequences. This work extends into many ^{129}Xe applications, and can be improved further following implementation of CS methods such as locally low-rank or deep-learning supervised regularization.

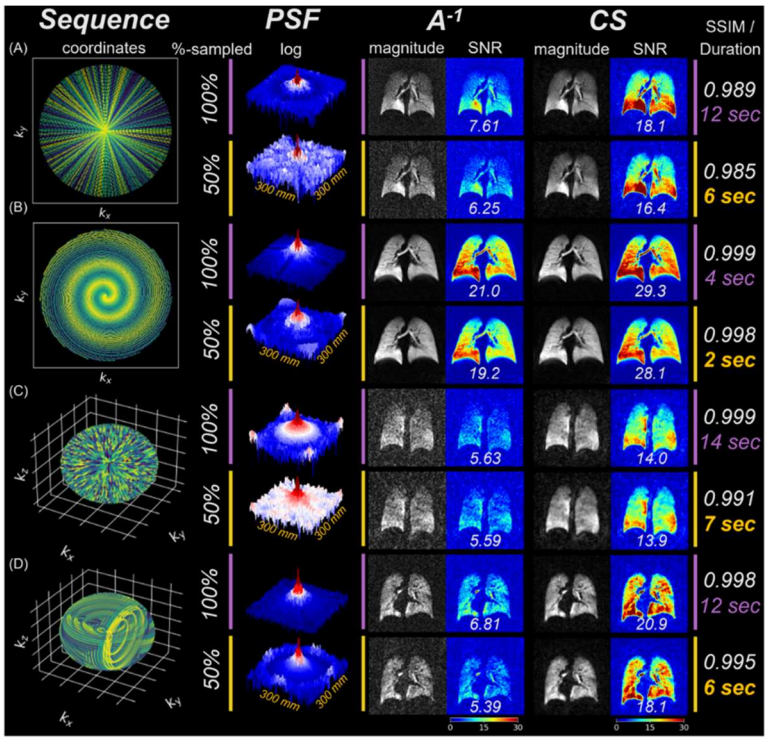

***Figure 1**: Sequence (A: 2D-radial, B: 2D-spiral, C: 3D-radial, D: 3D-FLORET), point-spread functions (PSF) and ventilation images reconstructed using density compensated gridded reconstruction (A^{-1}) and compressed sense (CS) for R=1 (100%-sampled) and R=2 (50%-sampled) acceleration factors. SNR = signal-noise ratio (mean value located at bottom of panels); SSIM = structural similarity index; duration = total scan duration (seconds) for 300^3 mm^3 FOV.*

References:

1. Niedbalski, P.J., *Protocols for multi-site trials using*… 2020.
2. Willmering, M.M., *Improved pulmonary ^{129}Xe ventilation*... 2020.
3. Lustig, M., *Sparse MRI: The application of compressed*… 2007.
4. Fessler, J.A. and Sutton, B.P., *NUFFT-based gridding*… 2007.
5. Parikh, N. and Boyd, S., *Proximal Algorithms*. 2014.
6. Ong, F. and Lustig, M. *SigPy: a python package*... 2019.
7. Niedbalski, P.J., *Utilizing flip angle/TR equivalence*… 2022.
8. Bdaiwi, A.S., *Diffusion weighted hyperpolarized ^{129}Xe*... 2022.
9. Kaushik, S.S., *Probing the regional distribution of*… 2015.

Automated Strategies to Derive Regional Perfusion Defects from Dynamic Contrast Enhanced Pulmonary MRI in patients with COVID-19 infection

Authors:

Matthew D. Thurston[1], Ahsan Javed[1], Shreya M. Kanth[2], Julio A. Huapaya[2], Christine Mancini[1], Kendall J. O'Brien[1], Amanda Potersnak[1], Haiyan Wang[1], David Regenold[2], Scott Baute[1], Marcus Y Chen[1], Anthony F. Suffredini[2], and Adrienne E. Campbell-Washburn[1]

[1]Cardiovascular Branch, Division of Intramural Research, National Heart, Lung, and Blood Institute, National Institutes of Health

[2]Critical Care Medicine Department, Clinical Center, National Institutes of Health

Purpose: Quantitative perfusion, as assessed by dynamic contrast enhanced (DCE) MRI and pharmacokinetic modelling, is used routinely in several organs, including the brain and heart (1-2), and has been used for research applications in the lung (3). Automated identification of regional lung perfusion defects could be valuable to characterize various pulmonary pathologies. Analogously, a variety of methods have been validated to characterize ventilation defects in hyperpolarized gas MRI, including thresholding and k-means clustering (4-5). In this study we sought to develop a method to automatically detect regional perfusion defects using DCE MRI, and apply our method in both patients with COVID and healthy volunteers.

Methods: This study was approved by the local Institutional Review Board and all study participants provided written informed consent for research MRI. We performed 153 lung DCE exams in patients with a history of COVID-19 infection, with 116 exams in patients with mild infections and 38 exams in patients with moderate or severe infections (hospitalized). We also performed lung DCE exams on 7 healthy volunteers. Imaging was performed on a 0.55 T MRI system via dynamic 3D Cartesian gradient echo acquisition with a frame rate of 1.5s/volume (breath held, resolution = 3.75x3.75x20mm^3, TE/TR = 0.76/2.5ms, FA = 31°). Gadolinium contrast was injected (2ml at 4ml/s) to image the first pass of contrast through the pulmonary tissue. Perfusion modelling was performed using the open-source ROCKETSHIP software package (6) with the two-compartment exchange model and the main-pulmonary artery used for the arterial input function.

Regional perfusion defect analysis was compared between two methods: thresholding and k-means clustering. For both, perfusion values were clipped ± 1 standard deviation from the mean. Thresholding was applied by dividing pixel-wise lung perfusion into 10 equal histogram bins, and the lowest bin was selected as the regional perfusion defects. For k-means clustering, 10 clusters were used with the lowest-value cluster being defined as the regional perfusion defect map. We compared the following measurements: the two methods to detect percent perfusion defect, global perfusion between patients and healthy volunteers, global perfusion between mild vs. moderate/severe infections, and percent defect between mild and moderate infection patients (using thresholding). Statistical testing was conducted using R software (version 4.2.1).

Results: Figure 1 shows a quantitative perfusion map in a patient with perfusion defects and the results of the thresholding and k-means methods for automated detection of perfusion defects. We found no statistically significant difference between thresholding (mean ± standard deviation = 15.6 ± 7.4 %) and k-means (16.2 ± 6.2 %) in our patient group, $t(152) = 1.25$ $p = 0.21$. There was no significant difference in mean global perfusion between patients (4.8 ±2.6 ml/g/min) and healthy volunteers (5.1 ±1.8 ml/g/min), $t(158) = 0.48$, $p = 0.64$, but there was a significant difference in mean global perfusion between patients with mild infection (5.1 ±2.7 ml/g/min) and patients with moderate infection (3.7 ±1.9 ml/g/min), $t(151) = 3.74$, $p < 0.001$, $d = 0.59$. There was no significant difference in percent defect (thresholding method) between patients with mild infection (15.5 ±7.1 %) and patients with moderate infection (15.7 ±8.4 %), $t(151) = 0.10$, $p = 0.92$. However, we observed 17 exams in patients with significant perfusion defects (>25%), and three examples are provided in Figure 2.

Discussion and Conclusion: Quantitative pulmonary perfusion measured by MRI may be a useful metric to study patients with COVID-19 infection. We demonstrated two methods to automatically detect perfusion defects and observed significant perfusion defects in a subset of patients. Future studies could test an adaptive k-means method to further refine the detection of perfusion defects based on classification of disease severity, and test clinical correlates to better understand the clinical presentation in patients with observed percent defects.

References: 1. Franks R., Plein S., Chiribiri A.(2021). Clinical application of dynamic contrast enhanced perfusion imaging by cardiovascular magnetic resonance. *Front Cardiovasc Med. 29*;8:768563. doi: 10.3389/fcvm.2021.768563, **2.** Ibrahim M., Ghazi T.U., Bapuraj J.R., Srinivasan A. (2021). Contrast pediatric brain perfusion: dynamic susceptibility contrast and dynamic contrast-enhanced MR imaging. *Magn Reson Imaging Clin N Am; 29*(4):515-526. doi: 10.1016/j.mric.2021.06.004, **3.** Torres L.A., Lee K.E., Barton G.P., Hahn A.D., Sandbo N., Schiebler M.L., Fain S.B. (2022). Dynamic contrast enhanced MRI for the evaluation of lung perfusion in idiopathic pulmonary fibrosis. *Eur Respir J ;60*(4):2102058. doi:10.1183/13993003.02058-2021, **4.** He M., Zha W., Tan F., Rankine L., Fain S., Driehuys B. (2019). A comparison of two hyperpolarized Xe MRI ventilation quatification pipelines: The effect of signal to noise ratio. *Acad Radiol, 26*(7), 949-959**. 5.** Zha W., Niles D.J., Kruger S.J., Dardzinski B.J., Cadman R.V., Mummy D.G., Nagle S.K., Fain S.B. (2016). Semi-automated ventilation defect quantification in exercise-induced bronchoconstriction using hyperpolarized helium-3 magnetic resonance imaging: a repeatability study. *Acad Radiol, 23*(9), 1104-1114

6. Barnes S.R., Ng T.S., Santa-Maria N., Montagne A., Zlokovic B.V., Jacobs R.E. (2015). ROCKETSHIP: a flexible and modular software tool for the planning, processing and analysis of dynamic MRI studies. *BMC Med Imaging 15:19*

Figure. 1: Example of Perfusion map, lung segmentation (red) and perfusion defect (red). **Figure. 2**: Subjects with >25% perfusion defect (red).

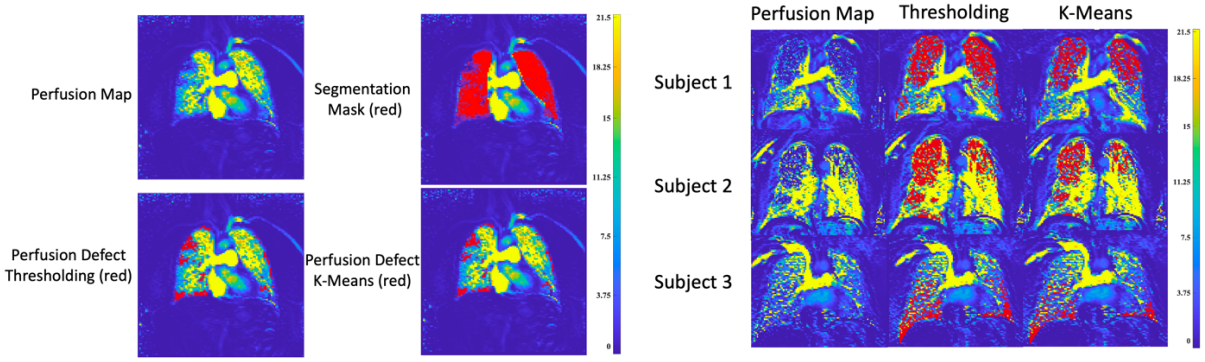

Emphysema Detection with Proton PREFUL MRI Parametric Response Mapping

Voskrebenzev A[1,2], Kaireit TF[1,2], Gutberlet M[1,2], Klimeš F[1,2], Behrendt L[1,2], Shin H[1,2], Kauczor HU[3,4], Welte T[2,5], Wacker F[1,2], and Vogel-Claussen J[1,2]

[1]Institute of Diagnostic and Interventional Radiology, Hannover Medical School, Hannover, Germany
[2]German Centre for Lung Research, Hannover, Germany
[3]Department of Diagnostic and Interventional Radiology, University Hospital of Heidelberg, Heidelberg, Germany
[4]Translational Lung Research Center Heidelberg (TLRC), Member of the German Lung Research Center (DZL), Heidelberg, Germany
[5]Clinic of Pneumology, Hannover Medical School, Hannover, Germany

PURPOSE

Ventilation measurements using signal differences between expiratory and inspiratory respiration states gained popularity as a biomarker for ventilation abnormalities. One method, which incorpartes such measurements is Phase-resolved functional lung imaging (PREFUL)[1]. A further classification of abnormalities such as emphysema and air-trapping beyond the current gas-exchange measurement is desirable. Considering that for CT, a threshold based method, parametric response mapping (PRM), is successfully used to distinguish between different lung ventilation abnormalities[2], the aim of this study was to establish an analogous MRI method and compare to CT_{PRM}.

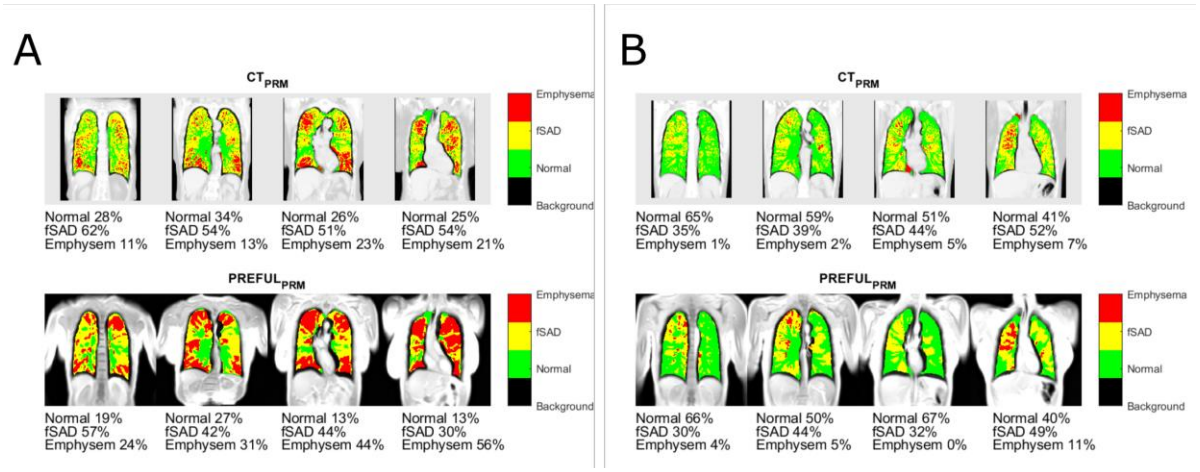

Figure 1: *Examplary results for two cases (A, female 70, Gold IV; B, female 42, Gold III) showing the Parametric Response Mapping (PRM) based on CT (1st row) and proton MRI PREFUL (2nd row). Please note the regional correspondence of functional small airways disease (fSAD) and Emphysema classification.*

METHODS

A retrospective analysis[3] of 34 subjects (20 female, median age 63 (42-76), GOLD status I (9), II (9), III (12), IV (4)) from the COSYCONET study was performed. PRM_{PREFUL} was calculated for four coronal slices acquired with a spoiled gradient echo sequence during free breathing: Field-of-view 500x500 mm^2, matrix 128x96, slice thickness 15 mm, echo time/repetition time 0.82 ms/3 ms, flip angle 5°, bandwidth 1500 Hz/px, imaging-time/slice ~1 minute and a temporal resolution of 288 ms. Post-processing was as follows:

1. PREFUL provided one respiration cycle, which includes registered averaged images during expiration and inspiration[1].
2. The N4ITK algorithm was used to correct for field inhomogeneities[4].
3. A region of interest (ROI) was automatically constructed in the liver using a lung boundary ROI, which was derived with a convolutional neuronal network[5].
4. The images were normalized to have the same mean signal in the liver for all four slice positions and for both respiration states.
5. Average T2* values from literature were used to correct for signal decay inside the lung[6].
6. Known Hounsfield Units (HU) in the liver (58 HU)[7] and in the air (-1024 background) were used to scale MR-signals to pseudo HU.
7. Analogous to CT, values above -856 HU in inspiration and below -950 HU in expiration were defined as regions of airtrapping due to functional small airways disease (fSAD) and values below -856 HU in inspiration and below -950 HU in expiration were defined as emphysema. Otherwise lung voxel were considered normal.

For PRM_{CT}, images in full in- and expiration acquired on a 64-slice scanner were downsampled (factor 2) and registered to expiration. CT slices were matched and averaged to MRI and used for PRM[2]. Finally, PREFUL lung volumes were registered to CT.
For regional comparison, the overlap coefficient regarding normal, fSAD, and emphysema (three classes) was calculated. The total lung percentages of the different classes were assessed with a paired Wilcoxon signed rank test, Pearson correlation and Bland-Altmann plots.

RESULTS

The visual agreement (Figure 1) of exemplary maps was confirmed by good regional correspondence (overlap normal: 91(83 - 99)%; fSAD 47(29 - 58)%; emphysema 17(3 - 29)%). Both PRM methods provided correlated total percentages ($r>=0.86$) in a similar range, but with significantly different ($P<0.001$) median values (Figure 2) with a mean bias: CT/PREFUL Normal: 73.50%/80.77%, bias -7.58; fSAD: 24.11%/18.31%, bias 6.39; Emphysema: 1.74%/0.23%, bias 1.19.

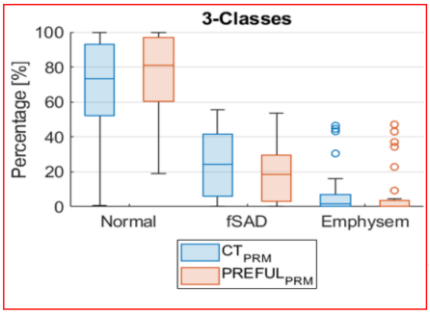

Figure 2: *Boxplot for number of voxels of the normal, fSAD and emphysema class in relation to total lung voxels as obtained with PRM based on CT and PREFUL.*

DISCUSSION

Detection of fSAD and emphysema similar to CT using PREFUL MRI is presented. For total-lung-values high correlations were found for all three classes. The regional comparison revealed lower consensus. The low overlap for emphysema can be explained by low amount of such regions. Furthermore, differences between MRI and CT can be caused by different respiration maneuvers (free-breathing vs. breath-hold).
Unlike RVent, which is a pure functional gas exchange measurement, PRM_{PREFUL} considers also the functional parenchyma tissue density changes. Since gas exchange and lung tissue changes are probably highly correlated, ventilation defects are similar for both methods (not shown here). Nevertheless PRM_{PREFUL} may provide additional information by emphysema classification.
Improvements can be achieved in regard to acquisition (ultra-short TE), bias field correction and HU mapping, which can e.g. be replaced by deep-learning[8].

CONCLUSION

A novel processing pipeline can classify three ventilation states (normal, fSAD, emphysema) with a high agreement to CT and may provide added value to functional lung MRI.

REFERENCES

1. Voskrebenzev A et al. *Magn Reson Med*. 2018;79(4):2306-2314. doi:10.1002/mrm.26893
2. Galbán CJ et al. *Nat Med*. 2012;18(11):1711-1715. doi:10.1038/nm.2971
3. Kahnert K et al. *Respir Res*. 2020;21(1):28. doi:10.1186/s12931-020-1293-6
4. Tustison NJ et al. *IEEE Trans Med Imaging*. 2010;29(6):1310-1320. doi:10.1109/TMI.2010.2046908
5. Ronneberger O et al. In: Navab N et al., *MICCAI 2015*. doi:10.1007/978-3-319-24574-4_28
6. Yu J et al. *Magn Reson Med* 2011;66(1):248-254. doi:10.1002/mrm.22829
7. Tisch C et al. *Int J Legal Med*. 2019;133(6):1861-1867. doi:10.1007/s00414-019-02016-1
8. Nie D et al. *MICCAI 2016 Proc*. 2016;2016:170-178. doi:10.1007/978-3-319-46976-8_18

3D Stack-of-Spirals Acquisition for ^{19}F MRI of Perfluoropropane in the Human Lung

Brandon Zanette[1], Faiyza Alam[1,2], Mary A Neal[3,4], Peter E Thelwall[3,4], Felix Ratjen[1,5], Giles Santyr[1,2]

1.Translational Medicine Program, The Hospital for Sick Children, Toronto, ON, Canada 2. Department of Medical Biophysics, University of Toronto, Toronto, ON, Canada 3.Translational and Clinical Research Institute, Newcastle University, Newcastle upon Tyne, United Kingdom 4.Newcastle Magnetic Resonance Centre, Campus for Ageing and Vitality, Newcastle University, Newcastle upon Tyne, United Kingdom 5.Division of Respiratory Medicine, The Hospital for Sick Children, Toronto, ON, Canada

Purpose: Inert fluorinated (^{19}F) gas MRI is an emergent technology with potential to be a lower cost, reduced infrastructure alternative to hyperpolarized (HP) gas MRI for functional lung imaging[1], providing similar and/or complementary information[2,3]. Fluorinated gases, such as perfluoropropane (PFP; C_3F_8), are biologically inert and, most importantly, do not require hyperpolarization. Instead, these gases rely on a relatively high number of ^{19}F nuclei per molecule as well as signal averaging, permitting imaging at thermal equilibrium[1]. Additionally, fluorinated gases may be freely mixed with oxygen, unlike HP gases where non-equilibrium magnetization is significantly reduced by relaxation due to paramagnetic O_2, typically necessitating anoxic administrations. Normoxic mixtures of fluorinated gases that are not reliant on hyperpolarized magnetization enable extended, multi-breath experiments that permit more comprehensive investigation of gas washin and washout kinetics in the lungs[4–6], while improving the overall tolerability of imaging experiments, especially in challenging populations such as children.

Decreasing the scan time associated with ^{19}F acquisitions is of great importance for shortening necessary breath-hold durations and/or enabling increased signal averaging per unit time. Increasing the number of achievable signal averages per unit time is expected to improve image quality of either static breath-hold or multi-breath ^{19}F MRI. Spiral non-Cartesian imaging trajectories sample k-space more efficiently than Cartesian sequences, reducing overall scan durations[7]. Furthermore, so-called 'spiral-out' trajectories sample the centre of k-space immediately before sampling higher spatial frequencies. Thus, these sequences are well-suited for ultra-short echo time (UTE) acquisitions, which will assist in mitigating the short T_2^* of fluorinated gases.

The purpose of this preliminary work was to explore the feasibility of a 3D stack-of-spirals (3D-SoS) sequence for ventilation imaging using ^{19}F MRI in-vivo and assess image quality and SNR compared to a conventional 3D gradient recalled echo (3D-GRE) sequence.

Methods: One participant (female, age=48 years) with no history of lung disease was recruited and imaged in accordance with institutional ethics and Health Canada approval. Imaging was performed on a clinical 3T system (Siemens Prisma^{fit}, Erlangen, Germany) with a ^{19}F rigid elliptical birdcage transmitter and 8-channel receive array (Rapid Biomedical, Rimpar, Germany). The participant was instructed to take 5 breaths from a 5 L reservoir of gas (21% O_2/79% PFP) (AirGas, Radnor, PA) to saturate the lungs with the gas mixture, then inhale to total lung capacity and hold their breath for the duration of the imaging sequence. A 3D-GRE acquisition guided by previous literature was implemented[8,9] with the following imaging parameters: FOV=360×480×260 mm^2, acquisition matrix=36×48×26, TE=1.67 ms, TR=8.7 ms, BW=24 kHz, Navg=3, and scan duration=17 sec. A second administration of gas was performed and the participant was imaged with a custom 3D-SoS sequence adapted for ^{19}F imaging[7,10]. The imaging parameters were: FOV=480×480×260 mm^2, Cartesian equivalent matrix=48×48×26, Nspiral=10, Readout time= 1.86 ms, BW=100 kHz, Navg=8, scan duration=18 sec. Both sequences used an 800 μs hard pulse and flip angle=45º for excitation. All images were reconstructed to an isotropic resolution of 5×5×5 mm^3. A 40×40 mm^2 ROI was used to measure mean signal in a central slice of each dataset, with an identically sized ROI used to measure background noise. SNR was calculated as mean signal divided by standard deviation of background noise.

Results: Figure 1 shows images acquired with both the 3D-GRE and 3D-SoS sequences. Qualitative improvements to SNR and overall image quality were observed in the 3D-SoS images compared to the 3D-GRE images. The SNR for the 3D-GRE and 3D-SoS image datasets were 19.4 and 27.8, respectively. The SNR improvement associated with spiral imaging was ~44% for this participant.

Discussion: In this preliminary work, the feasibility of rapid spiral imaging k-space acquisition is demonstrated for improvement of ^{19}F MRI image quality of the human lung in a breath-hold. The scan time reduction afforded by the efficient coverage of k-space allowed for increased signal averaging with a breath-hold duration that was nearly equivalent to the 3D-GRE acquisition. Alternatively, the efficiency of this acquisition may be used to reduce necessary breath-hold durations or improve achievable spatial resolution per unit time, but these require further exploration in-vivo.

This 3D-SoS sequence may also yield additional benefits to image quality in future. Spiral-out trajectories are readily amenable to shortened or ultra-short echo times. Reducing the 3D-SoS TE from that performed in this work should be reasonably achievable, helping to mitigate signal losses associated with the short T_2^* of PFP (~2 ms at 3T)[1,11]. Furthermore, non-Cartesian acquisitions lend themselves well to incoherent undersampling and reconstruction with compressed sensing[8] and parallel imaging[12] techniques to further accelerate imaging. This will be especially important for pediatric subjects who may be unable to tolerate lengthy breath-holds, or in dynamic multi-breath or extended free-breathing experiments to probe the kinetics of gas washin and washout.

Conclusion: 3D-SoS imaging of inert fluorinated gases is feasible in-vivo, enabling increased signal averaging in the same scan duration, thereby improving image quality and SNR.

Acknowledgements: The authors thank Sharon Braganza, Daniel Li, Leslie Burns, Tammy Rayner, and Ruth Weiss for assistance with imaging experiments. Special thanks to Dr. Tobias Wichmann for technical assistance with calibration and deployment of the ^{19}F hardware used in this work. This work was supported by CIHR, NSERC Alliance, Canada Foundation for Innovation, and Siemens Healthineers.

References: 1. Couch MJ, Ball IK, Li T, et al. J Magn Reson Imaging. 2019;49(2):343-354. 2. Obert AJ, Gutberlet M, Kern AL, et al. Magn Reson Med. 2020;84(3):1336-1346. 3. McCallister A, Chung SH, Antonacci M, et al. Magn Reson Med. 2021;85(2):1028-1038. 4. Gutberlet M, Kaireit TF, Voskrebenzev A, et al. Radiology. 2018;286(3):1040-1051. 5. Goralski JL, SH C, Glass T, et al. JCI Insight. 2020;5(2):e133400. 6. Obert AJ, Kern AL, Gutberlet M, et al. J Magn Reson Imaging. 2022. 7. Zanette B, Friedlander Y, Couch MJ, Santyr G. Proc Intl Soc Mag Reson Med. 2021;29:3228. 8. Pippard BJ, Neal MA, Maunder AM, et al. Magn Reson Med. 2021;85(6):3343-3352. 9. Neal MA, Pippard BJ, Hollingsworth KG, et al. Magn Reson Med. 2019;82(4):1301-1311. 10. Zanette B, Munidasa M, Friedlander Y et al. Mag Reson Med. 2023;83(3):1083-1091. 11. Couch MJ, Ball IK, Li T, et al. Radiology. 2013;269(3):903-909. 12. Lustig M, Pauly JM. Magn Reson Med. 2010; 64(2):457-471.

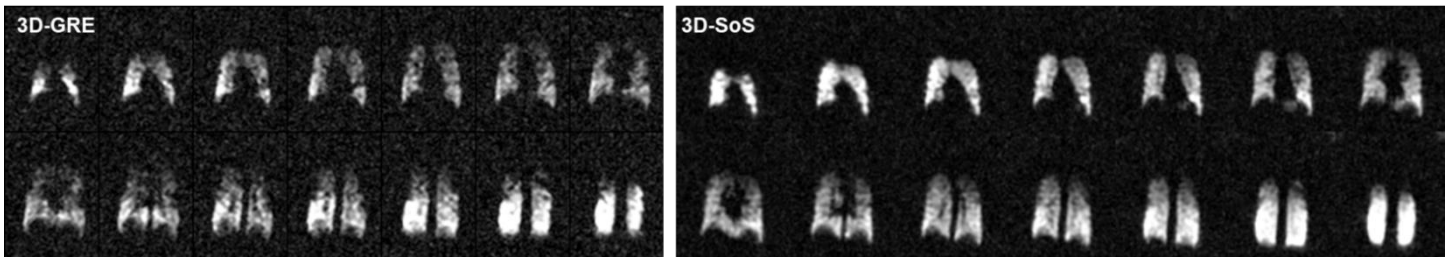

Figure 1: Images acquired in the coronal plane at 10 mm intervals for the 3D-GRE and 3D-SoS sequences.

Notes:

Notes:

Notes:

Notes:

Notes:

Notes:

Notes:

Notes:

Notes:

Notes:

Workshop Evaluation Form

Please fill out the following survey and return it to the front desk. Thank you!

On a scale of 1 to 5 (1 being the worst and 5 being the best) how would you rate the following?

Organization of the conference:

1 2 3 4 5 Comments:

Organization and usefulness of the program book:

1 2 3 4 5 Comments:

Did you find the speakers well prepared and engaging?

1 2 3 4 5 Comments:

Did you find the topics covered by the talks to be relevant and interesting?

1 2 3 4 5 Comments:

Were there any speakers/topics that were not featured but that you wish had been included? If yes, please list.

Yes No Comments:

Did you feel that speakers were allotted an appropriate amount of time for their presentations?

Yes No Comments:

Did you feel that there were enough opportunities for discussion sessions?

Yes No Comments:

What did you find to be the most beneficial aspect of the conference?

Comments:

What did you find to be the least beneficial aspect of the conference, and how do you think this aspect could be improved?

Comments:

Do you have any overall comments, feedback, or suggestions?

Comments: